

Physical processes of the CO₂ hydrate
formation and decomposition at conditions
relevant to Mars

Dissertation
zur Erlangung des Doktorgrades
der Mathematisch-Naturwissenschaftlichen Fakultäten
der Georg-August-Universität zu Göttingen

vorgelegt von

Georgi Yordanov Genov

aus Varna, Bulgarien

Göttingen 2005

D 7

Referentin/Referent: Prof. Dr. W. F. Kuhs

Korreferentin/Korreferent: Prof. Dr. S. Webb

Tag der mündlichen Prüfung: 14.01.2005

Abstract

This thesis is concerned with the formation and decomposition kinetics, as well as with the microstructure of CO₂ hydrate at conditions relevant to those on the Martian surface and in the Martian interior. It was conducted in the framework of DFG-project Ku 920/11 – part of the larger German research initiative (Schwerpunktprogramm 1115) “Mars and the terrestrial planets”.

Here, the results from neutron diffraction and gas consumption measurements of the CO₂ hydrate growth in the temperature range 185 K – 272 K are gathered and checked for consistency. Also first data from *in situ* neutron diffraction runs on CO₂ hydrate decomposition are presented. A sigmoid reaction development (higher order kinetics) was observed in a number of runs in both – formation and dissociation, suggesting for concomitant nucleation and growth processes taking place. The asymmetry, found in the sigmoid shape of the reaction curves, suggests that diffusion also plays an appreciable role. A new two-stage method for data interpretation (stage **A** – nucleation-and-growth transformation and stage **B** – diffusion controlled transformation), trying for the first time to unify the theoretical description of both – formation and decomposition processes on macroscopic level is suggested. The previously reported anomalous preservation for the CO₂ hydrate case is confirmed and first hints to explaining this problem are given. Thus, valuable information on the physics of the CO₂ hydrate formation and dissociation is obtained. On this basis it can be calculated that a volume of ice with a specific surface area of around 0.1 m²/g, exposed to Martian conditions, i.e. temperatures of about 150 K and pressures around 6 mbar, will be half transformed into CO₂ hydrate in approximately 10 000 yr and fully transformed in approximately 90 000 yr, disregarding the initial reaction-controlled part and allowing only the diffusion to control the transformation. For its part, the anomalous preservation may, on one hand, serve as an inhibitor or at least as a slow-down factor for some catastrophic processes involving CO₂ hydrate decomposition; on the other hand it may cause such processes, once the ice-hydrate phase boundary is crossed.

Special attention is paid to the hydrate microstructure. For the first time an attempt for its quantification is presented on the basis of a partly-open 3D clathrate foam structure. An estimate of the connectivity between the foam cells (bubbles), important for different model simulations, is also given. Moreover, a general image processing algorithm, allowing for fast quantification of foam structures established by SEM is outlined.

Auszug

Diese Doktorarbeit befasst sich mit der Kinetik der Bildung und der Zersetzung sowie mit der Mikrostruktur von CO₂-Hydrat unter p-T Bedingungen der Marsoberfläche und des Marsinneren. Sie wurde im Rahmen des DFG Projektes Ku 920/11 als Teil einer DFG-finanzierten Forschungsinitiative "Mars und die terrestrischen Planeten" (Schwerpunktprogramm 1115) durchgeführt.

Die Wachstumskinetik wurde mit Neutronenbeugungs- und Gasverbrauchs-Messungen im Temperaturbereich von 185 K bis 272 K untersucht und die Ergebnisse der beiden Methoden auf Konsistenz geprüft. Darüber hinaus werden erste Ergebnisse von *in situ* Neutronbeugungsmessungen der CO₂-Hydrat-Zersetzung präsentiert. Eine sigmoide Reaktionsentwicklung (Kinetik höherer Ordnung) wurde mehrfach sowohl bei der Bildung, als auch bei der Zersetzung beobachtet. Diese weist darauf hin, dass teilweise gleichzeitig Keimbildungs- und Wachstumsprozesse stattfinden. Die Asymmetrie der sigmoiden Form der Reaktionskurven zeigt zudem, dass Diffusionsprozesse eine wesentliche Rolle spielen. Mit einer erstmals hier vorgeschlagenen zweistufigen Methode für die Dateninterpretation (Stufe A: Kernbildung- und Wachstumstransformation und Stufe B: Diffusionskontrollierte Transformation) wird zum ersten Mal versucht, die theoretische Beschreibung von Bildungs- und Zersetzungsprozessen auf phänomenologischem Niveau zu vereinheitlichen. Die von anderen Autoren berichtete „anormale Erhaltung“ von CO₂-Hydrat wird bestätigt und erste Überlegungen zur Erklärung dieses Phänomens werden gegeben. Die experimentellen Untersuchungen erlauben erstmals Vorhersagen des Umwandlungsverhaltens von CO₂-Hydraten unter Marsbedingungen. So kann berechnet werden, dass ein Volumen von Eis mit einer spezifischen Oberfläche von ca. 0.1 m²/g bei Marsbedingungen, d. h. bei Temperaturen von 150 K und einem Druck um 6 mbar, in ca 10 000 J. zur Hälfte in CO₂-Hydrat umgewandelt sein wird und in ca 90000 J. völlig transformiert. Im wesentlichen ist die Umwandlungskinetik dabei von der Diffusion der Bestandteile durch das kristalline Gashydrat bestimmt. Die „anormale Erhaltung“ steht zwar zunächst den mehrfach zur Erklärung geomorphologischer Strukturen herangezogenen katastrophalen Zersetzungsprozessen von Gashydraten entgegen, der Effekt kann andererseits aber auch solche katastrophalen Prozesse fördern, indem er großen Mengen von Gashydraten metastabil erhält, die sich dann beim Überschreiten des Eisschmelzpunkts in katastrophaler Weise zersetzen.

Spezielle Aufmerksamkeit wird in der Arbeit auch auf die Mikrostruktur der Gashydrate gerichtet. Zum ersten Mal wird ein Versuch für die Quantifizierung der Mikrostruktur basierend auf einer Beschreibung als teilweise offen-porigem Schaum präsentiert. Außerdem wird ein allgemeiner Bildverarbeitungsalgorithmus, der die schnelle Quantifizierung von im Rasterelektronenmikroskop beobachteten Schaumstrukturen zulässt, entworfen.

Table of contents

Abstract	i
Table of contents	iii
Chapter I – CO ₂ clathrate hydrates on Mars	I-1
§ 1. A few words about Mars	I-1
1.1. Martian atmosphere	I-1
1.2. Martian inner structure	I-4
§ 2. Ice and clathrate hydrates	I-6
2.1. Ice Ih	I-6
2.2. Hydrate structures and phase diagram	I-7
2.3. Hydrate formation and decomposition kinetics	I-10
§ 3. CO ₂ hydrates on Mars	I-13
Chapter II – Methods and instrumentation	II-1
§ 1. Neutrons – basic physics and instruments	II-1
1.1. Neutrons – basic physical properties	II-1
1.2. Neutron interactions	II-3
1.3. Neutron production	II-10
1.4. Neutron detection	II-13
1.5. D 20 – a high-intensity 2-axis neutron diffractometer	II-14
1.6. Radiation protection	II-16
§ 2. pVT method	II-18
2.1. Main principles	II-18
2.2. Experimental setups	II-20
§ 3. Field Emission Scanning Electron Microscopy (FE-SEM)	II-22
3.1. Electron – basic physical properties	II-22
3.2. Principles of the scanning electron microscopy	II-23
3.3. LEO 1530 Gemini – one FE-SEM with cryo stage	II-25
§ 4. BET method	II-27
Chapter III – Modeling approaches	III -1
§ 1. Multistage Model of Gas Hydrate Growth from Ice Powder	III -1
1.1. The model	III -1
§ 2. JMAKGB – a combined Avrami-Erofeev and Ginstling-Brounshtein way of data interpretation	III -12
2.1. The approach	III -12
Chapter IV – Experiments, results and conclusions	IV-1
§ 1. Experiments on CO ₂ hydrate formation	IV-1
1.1. The starting material	IV-1
1.2. The experiments	IV-2
1.3. Data analyses and discussion	IV-4
§ 2. Experiments on CO ₂ hydrate decomposition	IV-18
2.1. Starting material and experiments	IV-18
2.2. Data analyses and discussion	IV-19
§ 3. Topological observations – hydrate foam structure	IV-22
CO ₂ clathrate hydrates on Mars - yes or no?	1
References	5

Appendix I	15
Appendix II	Sheet 1
Appendix III	24
Acknowledgements	39
Lebenslauf	40

Chapter I

CO₂ clathrate hydrates on Mars

The aim of this chapter is to give the reader a general idea about the planet of Mars with its atmosphere and inner structure, since the atmospheric conditions and the vertical thermal profile of the Martian interior are of major importance for the existence of CO₂ hydrates on the Red Planet (see § 2 and § 3). Also the ice Ih, as well as the clathrate hydrates with their structure and thermodynamics are conversed. The possible significance of the gas hydrates for the Universe, the Solar system, and certainly for our target – Mars is being discussed. Of course, this cannot be done in very detail for the reason of limited space. Nevertheless, this is supposed to be one enjoyable reading.

§ 1. A few words about Mars¹

1.1. Martian atmosphere

Being the fourth planet in the Solar system, Mars is the last of the inner planets, characterized by their rocky composition, unlike the gaseous and icy outer ones. The history of Mars exploration starts in the year 1608 with the first observations of Galilei. In 1659 Huygens saw a dark area on its surface (*Syrtis Major*). It helped for defining the Martian rotation period. In 17th and 18th century were found the polar ice regions and their seasonal variations, as well as the giant dust storms. The attempts to map the Martian surface date from the 1830 when Mars was close to the Earth. In 1877 Schiaparelli, using the 22-cm refractor in Milan, observed and mapped his famous “canale” (**Fig.I.1**). He had won his fame first showing that the Perseides were linked to the Swift-Tuttle comet, a discovery that earned him his own observatory. Therefore his peculiar Martian map was taken seriously and that was the beginning of the speculations for the existence of intelligent life there. Some people even went further as for instance Clara Goguet Guzman, a French widow, who established the “Guzman Prize” (100 000 FFr) for the one who first established a contact with another civilization. By that time the scientific community got divided into two fractions - “canalists” and “anticanalists”. This delusion lasted till the beginning of the XXth century when better telescopes with higher resolution appeared.

Since 1960, 36 unmanned missions were sent to Mars, 20 of them by USSR/Russia, one by Japan, one by EU and the rest by USA. A huge amount of climate data, spectroscopic observations, pictures etc was gathered.

¹ More information can be found for instance in the book “Towards Mars!” – Edited by R. Pellinen & P. Raudsepp – Oy Raud Publishing Ltd. Helsinki, 2000

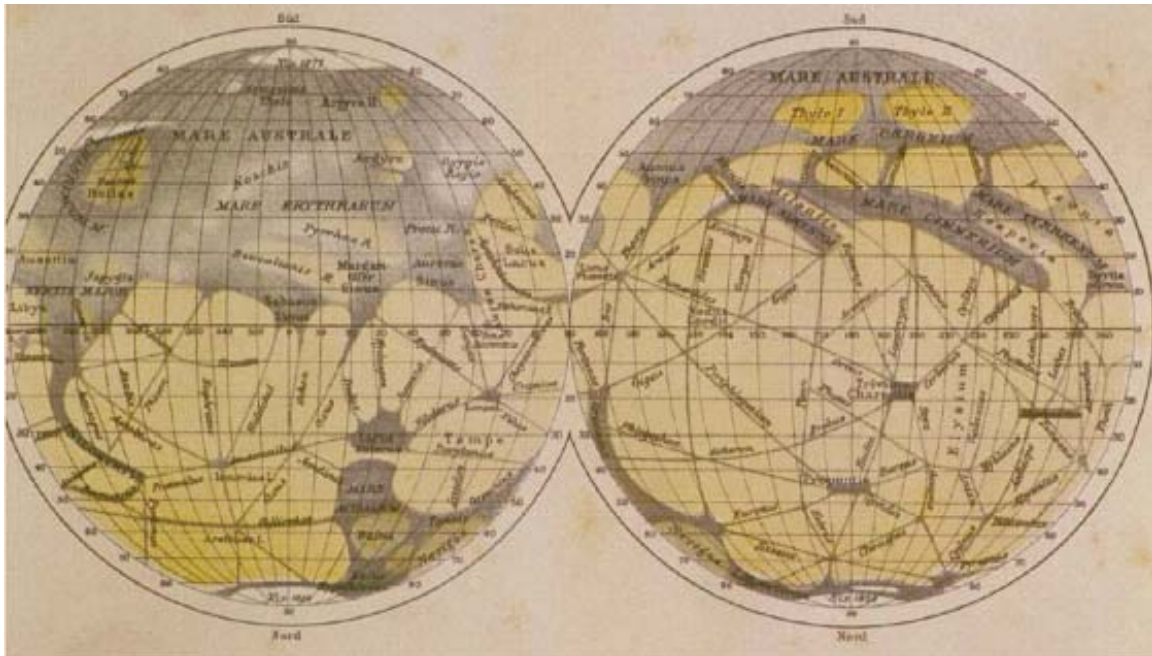


Fig.I.1 The map of Giovanni Schiaparelli. He called the straight lines canals, and found out that the patterns on the surface changed with the seasons. He attributed this to the seasonal vegetation changes.

As mentioned above, Mars, just like Earth, has polar ice caps. Today they are assumed to consist of CO₂ and water ices (including CO₂ hydrate), as well as dust in unknown proportions, overlying the bedrock. The caps have two components – permanent and seasonal. The permanent component consists mainly of water ice. The seasonal one is composed of dry ice and due to deposition (during the autumn and winter) and sublimation of CO₂ (during the spring and summer) considerably varies in size. The permanent northern cap (**Fig.I.2**) consists mainly of water ice. The data recently received from Mars Express suggest that the southern cap consists mainly of dry ice but also contains significant amounts of water ice (**Fig.I.12**). In some years the southern cap vanishes completely, during others a small residual cap can be seen.

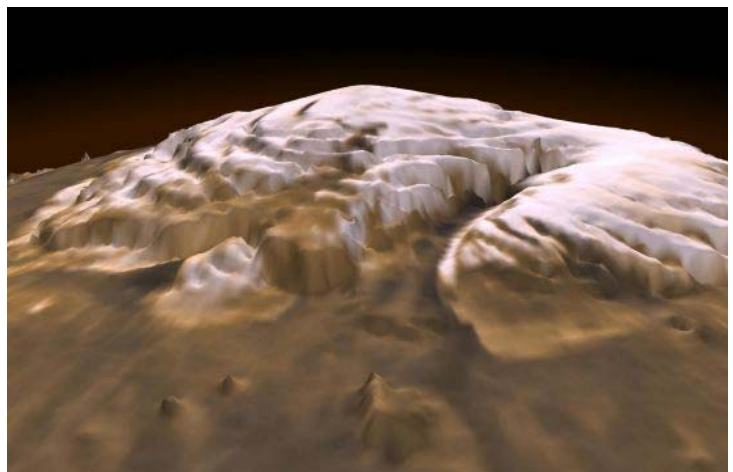


Fig.I.2 3D Mars' North Pole

Courtesy: MOLA Team, MGS Project, NASA. Image: Greg Shirah (SVS)

The atmosphere on Mars consists mainly of CO₂ (**Appendix I**) and is extremely dry. If all atmospheric water is deposited on the surface it will make a layer $\approx 100 \mu\text{m}$ thick. The pT conditions there are often close to the water saturation ones. This leads to cloud formation early in the morning as near-surface fog, and in the afternoon as high condensation clouds. If Mars did not have atmosphere its average temperature would be determined by the radiation balance between the incoming solar radiation, the outward thermal radiation from the surface and the heat coming from the planet interior. Mars receives

slightly more than 44 % of the solar radiation received by Earth. The heat conducted from the Martian interior is 10^{-4} times the solar heating and is insignificant from a climatic point of view. That means the first two factors play the principal role. The atmosphere itself significantly affects the average planet temperature, since gases are poor absorbers of visible light but often absorb well the thermal radiation, causing a greenhouse effect. CO₂ is a good greenhouse gas. The increase of the temperature due to it is about 11°C on Earth and represents almost 30 % of the total greenhouse effect here. On Mars it warms up with about 7°C.

Dust and water ice particles can also strongly affect the atmospheric absorption and scattering of the visible and thermal radiation and thus to modify the atmospheric circulation. These effects are most common around the large volcanoes, the winter polar cap and globally, during dust storms (**Fig.I.3**). Although, the atmosphere always contains enough aerosols (dust and ice particles) to scatter ~ 40 % of the incoming solar radiation. The net atmospheric effects depend on the physical properties (such as size and optical properties) and on the spatial and temporal distributions of the aerosols. The aerosols cause a strong decrease of the surface and near-surface daily temperatures as well as a reduction in the vertical rate of change in temperature².

The Martian near-surface atmospheric temperatures have been measured at the three landing sites in the northern hemisphere: predominantly at the two Viking Lander sites³ for one or more Martian years and by Pathfinder⁴ for about 1/8 Martian year during the summer. Elsewhere the surface temperatures have been measured from orbit. The lowest surface temperatures occur in the southern polar region during the winter. There they can go down to 148 K. The highest observed surface temperature have been measured in the summer in northern mid-latitudes and goes up to 293 – 298 K. In the Polar Regions the annual mean-surface temperature is between 158 and 163 K and at the equator, between 218 and 223 K. The typical diurnal temperature variations as measured by the Viking Landers at 1.5 m height above the surface showed values of around 70 K (Tillman et al. 1979). The Mars Pathfinder performed these measurements at three heights (0.25, 0.5, 1 m) and found the temperature to change very rapidly with height. The reason for that is the thin atmosphere. But during dust storms the difference of 70 K can be reduced to 6 K or even less. One very useful link is: http://www-mars.lmd.jussieu.fr/mars/live_access.html. It gives the opportunity to make a coarse forecast of the weather on Mars as well as the thickness of the dry ice coverage at different places, using the Martian Global Circulation Model linked to the Mars Climate Database.

² A serious book, dealing with the Martian atmosphere, far not suitable for everybody is the one of Read & Lewis (2004). It can be described with four words “dynamic meteorology of Mars”

³ VL1 landed at *Chryse Planitia* (22.48° N, 49.97° W planetographic, 1.5 km below the datum and 6.1 mbar elevation). VL2 landed at *Utopia Planitia* (47.97° N, 225.74° W, 3 km below the datum elevation)

⁴ Mars Pathfinder landed at 19.3°N and 33.6°W.

The atmospheric pressure on Mars is between 5 and 10 mbar. In the absence of a natural reference (like the sea level on Earth), the pressure reference level there is the altitude, on which the annual mean pressure is 6.1 mbar (the triple point of water). The surface pressure on Mars exhibits significant spatial and temporal variations. During the winter the surface temperature at the Mars Polar Regions is low enough to cause the deposition of the atmospheric CO₂ directly on the polar cap. During spring and summer some of the dry ice sublimates directly back into the atmosphere. The seasonal exchange of CO₂ between the caps and the atmosphere causes seasonal surface pressure variations of about 30 %. The pressure decrease with the altitude there is at about 63 % per 10.8 km. Hence, the surface pressure varies substantially due to the large variations in the Martian topography. The difference in altitudes of the highest and the lowest points there is more than 30 km. The pressure at the highest peaks is around 1 mbar and in the deepest valleys – approximately 12 – 14 mbar.

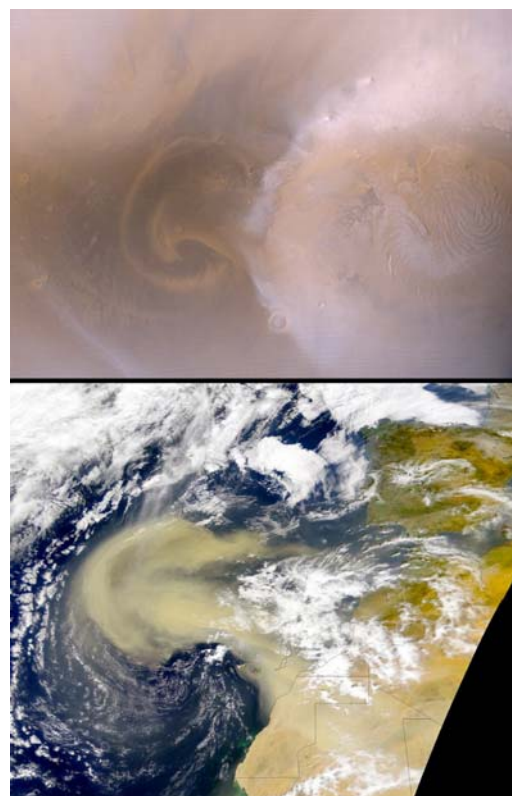


Fig.I.3 TOP Mars Dust Storm; MOC image: NASA/JPL/Malin Space Science Systems. BOTTOM Earth Dust Storm; SeaWiFS image: Provided by NASA/GSFC and ORBIMAGE/SeaWiFS Project.

1.2. Martian inner structure

Undoubtedly the best method for determining the inner structure of a planet is seismology. Basically no information about the seismic structure was returned from the Viking seismic experiment, which was too sensitive to the wind and the pressure fluctuations. Other previous spacecrafts have measured the gravity field, but this primarily provides information about the outmost layers of the planet, and it has proven difficult to choose among several reasonable models even for the lithosphere itself. Thus, the inner structure of Mars remains almost completely unknown. Nevertheless, a large number of models are trying to describe it⁵. On **Fig.I.4** one of the present models of the Martian interior can be seen. Presently the most popular modeling approach is based on thermal convection of an infinite Prandtl number fluid with strongly temperature dependent viscosity. The main differences between those and previous models include the definition of the lithosphere; an early thermal history, which cannot be described by stationary scaling laws; high mantle temperature, and some predictions concerning the formation of hot plumes at the core-mantle boundary.

⁵ The overview of the models is after Sotin & Lognonné (1999)

As a result of the application of these models the internal structure of Mars can be divided into: conductive crust at the top, which includes the thermal lithosphere; convective mantle with unstable top and lower thermal boundary layers at the crust-mantle and core-mantle boundaries respectively; iron-rich core, whose radius is a free parameter and which eventually sets apart into inner maybe solid core. The problems with the determination of its radius and state are debated by Schubert & Spohn (1990). Important parameters here are initial temperature of the mantle, radius of the core-mantle interface, and viscosity law of the mantle.

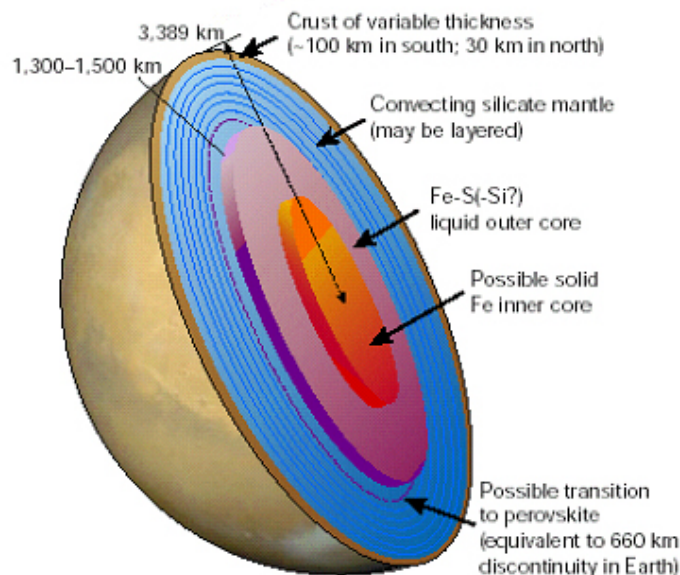


Fig.I.4 Cutaway view of the Martian interior (Stevenson 2004).

The initial temperature of the mantle must be larger than the iron alloys melting temperatures. The different models run with different initial temperatures and end up with very similar ones. If the temperature is initially too high, then the viscosity is low, the convection is more efficient and the cooling rate is fast and vice versa. Usually the models use an Earth-like viscous law for the Martian mantle viscosity, assuming it equal to 1021 Pa.s for temperature of 1350°C. Viscosity is assumed to be Newtonian and different values of the activation energy are used to study the viscous law influence on the mantle temperature and the planet cooling rate. The first numerical models showed that, if chondritic radiogenic heating rate was assumed, the temperature of the mantle would remain much higher than the peridotites' melting point and a large partial melt zone would still be present in the Martian bowels at present. Alternatively, if one assumes that radiogenic elements have been segregated into the crust early enough in the Martian history, the mantle temperature would be lower than the solidus one. One major question still remains despite the efforts and the data of the MGS – the question about the possibility of plate tectonics (e.g. Sleep 1994) that would allow for a much faster cooling of the planet.

The presence of volcanoes (e.g. *Elysium*, *Olympus Mons*, *Tharsis* area) suggests that the lower thermal boundary layer at the core-mantle interface has been unstable during the Martian thermal history (Parmentier, Sotin & Travis 1994 and Sotin & Labrosse 1999). Although, it is known that thermal convection of a fluid heated from within is driven by downwellings. Hot upwelling can appear if the temperature difference across the lower thermal boundary layer is large enough. In the models, this case occurs when a solid inner core forms at the center of the planet. Additional models are being

conducted to investigate the range of parameters that lead to the formation of hot plumes at the core-mantle boundary.

§ 2. Ice and clathrate hydrates

2.1. Ice Ih

The ice is quite abundant on Earth, in the Solar system, and in the interstellar medium (see Chapter I, § 3). If all the ice presently existing on Earth melts, the sea level will increase with about 70 m. In some planets and in most of the satellites, the ice is the major constituent. For instance, Pluto consists of 80% ice; Ganymede, Callisto and Titan – of 40%. It is also present in many other moons, in the planetary rings, and in the comets.

The ice consists of water molecules. The oxygen atom in one water molecule is connected to two hydrogens by covalent bonds. Hydrogen bonds connect each water molecule with four others in a tetrahedral framework. They have electrostatic character. The hydrogen bond binds the hydrogen nucleus belonging to one molecule (hydrogen donor) to the lone-pair electrons of the oxygen from another molecule (hydrogen acceptor). Each oxygen atom uses two of the six outer electrons to make the covalent bonds and four (two lone-pairs) to make two hydrogen bonds. Each hydrogen atom participates in one covalent and one hydrogen bond.

The ice can form different crystallographic structures depending on the thermodynamic conditions. The pT conditions of stability of the different crystalline phases of ice are shown on the phase diagram (**Fig.I.5**). The ice phase, used to form gas hydrates during these kinetic experiments, was ice Ih, stable at temperatures below 273 K and ambient pressures.

The oxygen atoms of the water molecules in ice Ih are arranged in layers of hexagonal rings. The atoms of each hexagonal ring are displaced with respect to each other alternately in two planes. The resulting hexagonal channels make ice Ih an open structure (see **Fig.I.6**). Its space group is $P6_3/mmc$. In reality the water molecules experience small displacements from the shown positions. Therefore, the arrangement on **Fig.I.6** should be regarded as an averaged over space and time formation. More details about the hexagonal ice structure and its properties can be found in Kuhs & Lehmann (1986), Petrenko & Whitworth (1999). The water molecules on the ice surface are poorly bound because they interact with other molecules only from one side. It makes the structure of the free

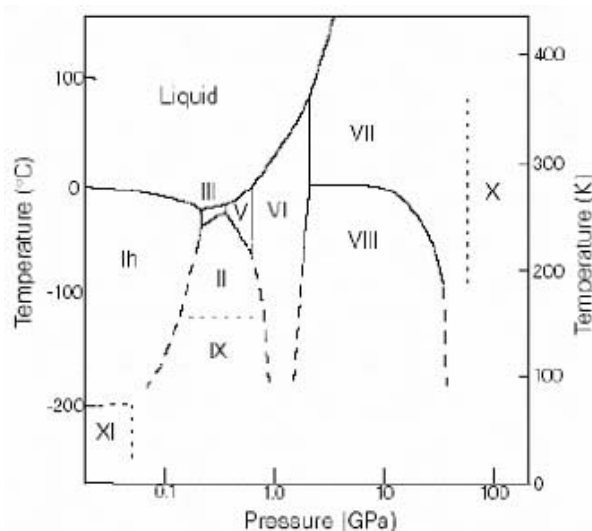


Fig.I.5 Ice phase diagram (Lobban et al. 1998). Solid lines represent measured transitions; dashed lines - transitions extrapolated to low temperatures; dotted lines - predicted transitions.

surface to some extent different from the one of the bulk. A number of experimental and theoretical studies on the structure and the physical properties of the ice surface (e.g. Petrenko and Whitworth 1999) showed the importance and complexity of such investigations, especially close to the ice melting point. Dash (1995) and Wettlaufer (1997) discussed theoretically the phenomenon of surface premelting or the existence of a quasi-liquid layer at temperatures and pressures below the melting point. Bluhm et al. (2002) presented experimental observations on the premelting of ice showing the existence of a quasi-liquid layer at temperatures between -20°C and 0°C . When the temperature approached the ice melting point the film was about 30 \AA thick and at 253K it became insignificant.

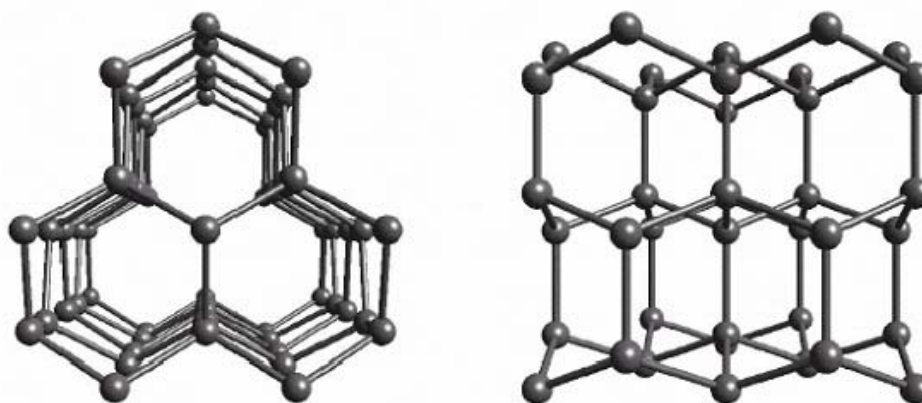


Fig.I.6 Structure of ice Ih (taken from Lobban 1998). The right and the left pictures show the structure as seen parallel and perpendicular to the hexagonal channels, respectively.

2.2. Hydrate structures and phase diagram

Clathrate hydrates comprise a class of ice-like solids in which, usually apolar guest molecules occupy, fully or partially, cages in the host structure formed by H-bonded water molecules. Different people give different names to this structure – gas clathrates, gas hydrates, clathrates, hydrates etc – but they all mean the same. They exist as stable compounds at high pressure and/or low temperature (van der Waals and Platteeuw, 1959).

The gas hydrates (hence this will be the name most frequently used in this work) usually form two crystallographic cubic structures – structure (Type) I and structure (Type) II (von Stackelberg & Müller, 1954) of space groups $Pm\bar{3}n$ and $Fd\bar{3}m$ respectively. Rather seldom a third hexagonal structure of space group $P6/mmm$ maybe observed (Type H).

The unit cell of Type I consists of 46 water molecules, forming two types of cages – small and large (see **Fig.I.7**). The small cages in the unit cell are two against six large ones. The small cage has the shape of pentagonal dodecahedron (5^{12}) (see **Fig.I.7**) and the large one that of tetrakaidecahedron ($5^{12}6^2$). Typical guests forming Type I hydrates are CO_2 and CH_4 .

The unit cell of Type II consists of 136 water molecules, forming also two types of cages – small and large. In this case the small cages in the unit cell are sixteen against eight large ones. The

small cage has again the shape of pentagonal dodecahedron (5^{12}) but the large one this time is hexakaidecahedron ($5^{12}6^4$). Type II hydrates are formed by gases like O_2 and N_2 .

The unit cell of Type H consists of 34 water molecules, forming three types of cages – two small of different type and one huge. In this case, the unit cell consists of three small cages of type 5^{12} , twelve small ones of type $4^35^66^3$ and one huge of type $5^{12}6^8$. The formation of Type H requires the cooperation of two guest gases (large and small) to be stable. It is the large cavity that allows structure H hydrates to fit in large molecules (e.g. butane, hydrocarbons), given the presence of other smaller help gases to fill and support the remaining cavities. Structure H hydrates were suggested to exist in the Gulf of Mexico. There thermogenically-produced supplies of heavy hydrocarbons are common.

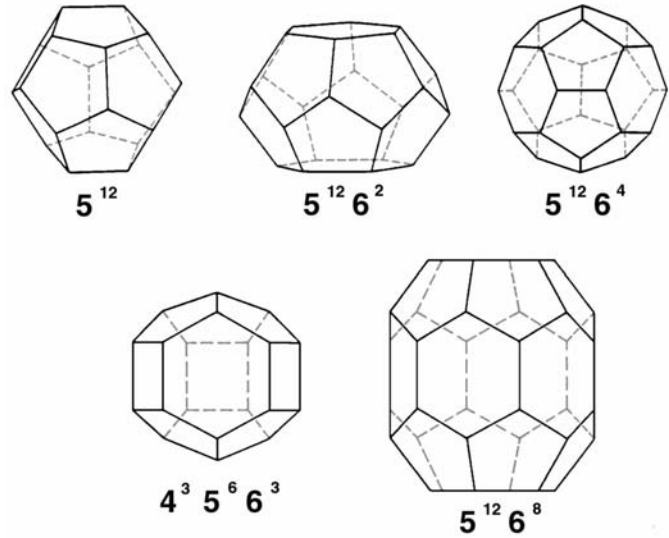


Fig.I.7 Schematic of the cages, building the unit cells of the different hydrate structures

The importance of the gas hydrates here on Earth is out of any doubt. The kinetics of their formation and decomposition, as well as their physical properties are of a significant importance for the gas industry, economy and ecology. Anyway, the topic of this work is the gas hydrates on Mars; therefore I am not going to enter into a detailed discussion about their role on our planet. But their importance in cosmic scale and especially for Mars will be debated in the next paragraph.

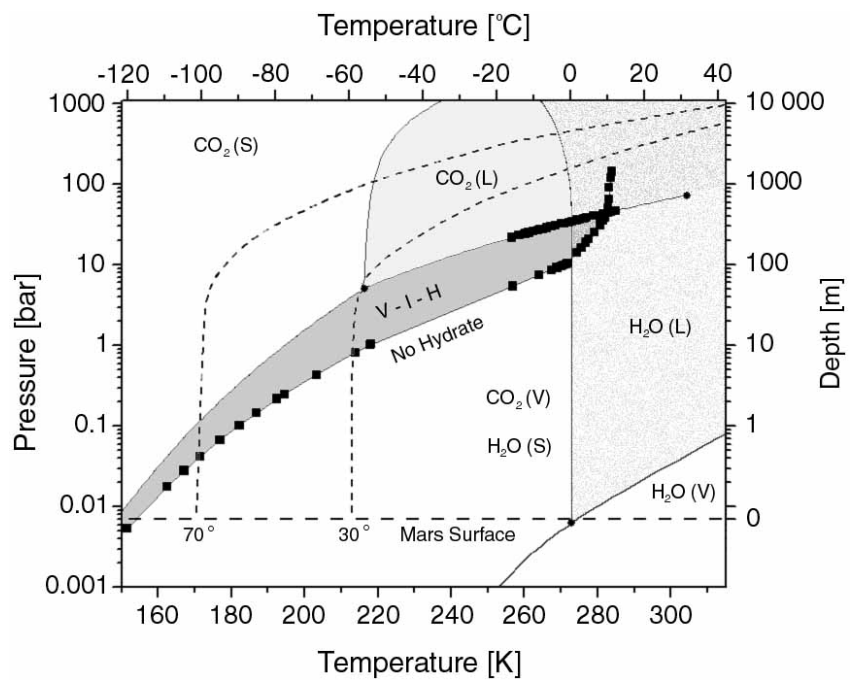


Fig.I.8 CO_2 hydrate phase diagram. The black squares show experimental data (after Sloan, 1998). The lines drawing CO_2 phase boundaries are calculated according to the Intern. thermodyn. tables (1976). The water phase boundaries are only guides to the eye.

The hydrate structures are stable at different pressure-temperature conditions depending on the guest molecule. Here one Mars related phase diagram of the CO_2 hydrate combined with those of pure

CO₂ and water is given (**Fig.I.8**). The CO₂ hydrate has two quadruple points: (I-Lw-H-V) ($T = 273.1$ K; $p = 12.56$ bar) and (Lw-H-V-LHC) ($T = 283.0$ K; $p = 44.99$ bar) (Sloan, 1998). The CO₂ itself has a triple point at $T = 216.58$ K and $p = 5.185$ bar and a critical point at $T = 304.2$ K and $p = 73.858$ bar. The dark gray region (V-I-H) represents the conditions at which the CO₂ hydrate is stable together with gaseous CO₂ and water ice (below 273.15 K). On the horizontal axes the temperature is given in Kelvin and Celsius (down and up respectively). On the vertical ones the pressure (left) and the depth in the Martian regolith (right) are given. The horizontal dashed line at zero depth represents the average surface conditions. The two bent dashed lines show two calculated Martian geotherms after Stewart & Nimmo (2002) at 30° and 70° latitude. I will come back to this phase diagram several times later on.

As a matter of fact, probably the first evidence for the existence of CO₂ hydrates dates back to the year 1882, when Wroblewski (1882a, b and c) reported clathrate formation while studying carbonic acid. He noted that the gas hydrate was a white material resembling snow and could be formed by raising the pressure above certain limit in his H₂O – CO₂ system. He was the first to estimate the CO₂ hydrate composition, finding it to be approximately CO₂·8H₂O. He also mentions that “...the hydrate is only formed either on the walls of the tube, where the water layer is extremely thin or on the free water surface...” This already indicates the importance of the surface available for reaction, i.e. the larger the surface the better. Later on in 1894, Villard deduced the hydrate composition as CO₂·6H₂O. Three years later, he published the hydrate dissociation curve in the range 267 K – 283 K (Villard 1897). Tamman & Krige (1925) measured the hydrate decomposition curve from 253 K down to 230 K and Frost & Deaton (1946) determined the dissociation pressure between 273 and 283 K. Takenouchi & Kennedy (1965) measured the decomposition curve from 45 bars up to 2 kbar. For the first time the CO₂ hydrate was classified as a Type I clathrate by von Stackelberg & Muller (1954).

2.3. Formation and decomposition kinetics

Since the 1950s, a large number of gas hydrate systems have been studied but still many of their physico-chemical properties as well as their formation and decomposition kinetics are not well understood, despite their importance for a number of reasons (e.g. Sloan 1998).

A review of the kinetics of gas hydrate formation in aqueous laboratory systems can be found in Sloan (1998). The nucleation and the induction period of the gas hydrate formation in aqueous solutions are described within the frames of the General Nucleation Theory in the papers of Kashchiev and Firoozabadi (2002, 2003). Also a hypothetical microscopic mechanism for the nucleation of hydrate from ice with an emphasize put on the role of the quasi-liquid layer can be found in Sloan and Fleyfel (1991). Schmitt (1986) performed experimental measurements of the induction period of the CO₂ hydrate formation at low temperatures. No clear dependence on the temperature and the

overpressure was observed. A strong dependence of the transformation rates on the surface area of the gas-ice contact was demonstrated by Barrer and Edge (1967). Later, Hwang et al. (1990) studied the methane-hydrate growth on ice as a heterogeneous interfacial phenomenon and measured the clathrate formation rates during ice melting at different gas pressures. Sloan and Fleyfel (1991) discussed molecular mechanisms of the hydrate-crystal nucleation on ice surface, emphasizing the role of the quasi-liquid-layer (QLL). Takeya et al. (2000) made *in-situ* observations of the CO₂-hydrate growth from ice-powder for various thermodynamic conditions using laboratory X-ray diffraction. They distinguished the initial ice-surface coverage stage and a subsequent stage, which was assumed to be controlled by gas and water diffusion through the hydrate shells surrounding the ice grains. The process was modeled following Hondoh and Uchida (1992) and Salamatin et al. (1998) in a single ice particle approximation. The respective activation energies of the ice-to-hydrate conversion were estimated to be 19.2 and 38.3 kJ/mol. The first *in-situ* neutron diffraction experiments on kinetics of the clathrate formation from ice-powders were presented by Henning et al. (2000). They studied the CO₂-hydrate growth on D₂O ice Ih, using the high intensity powder diffractometer HIPD at Argonne National Laboratory for temperatures from 230 to 263 K at a gas pressure of approximately 6.2 MPa. The starting material was crushed and sieved ice with unknown but most likely irregular shape of the grains. To interpret their results at a later stage of the hydrate formation process, the authors applied a simplified diffusion model of the flat hydrate-layer growth, developed for the hydration of concrete grains (Berliner et al. 1998; Fujii and Kondo 1974), and determined the activation energy of 27.1 kJ/mol. This work has been continued by Wang et al. (2002) to study the kinetics of CH₄-hydrate formation on deuterated ice particles. A more sophisticated shrinking-ice-core model (Froment and Bischoff 1990; Levenspiel 1999) actually reduced to the diffusion model of Takeya et al. (2000; 2001) has been used to fit the measurements. Higher activation energy of 61.3 kJ/mol was deduced for the methane hydrate growth on ice. Based on Mizuno and Hanafusa (1987), the authors suggested that the quasi-liquid layer of water molecules at the ice-hydrate interface may play a key role in the (diffusive) gas and water redistribution although a definite proof could not be given.

One of the recent and most intriguing findings is that, at least in cases where the guest species are available as excess free gas, some gas hydrate crystals grow with a nanometric porous microstructure. Using cryo field-emission scanning electron microscopy (FE-SEM), direct observations of such sub-micron porous gas hydrates have now repeatedly been made (Klapproth 2002; Klapproth et al. 2003; Kuhs et al. 2000; Staykova et al. 2002; Staykova et al. 2003; Genov et al. 2004). Hwang et al. (1990) reported that the methane hydrates formed from ice in their experiments were bulky and contained many voids. Rather interestingly, there is evidence that besides dense hydrates, some natural gas hydrates from the ocean sea floor also exhibit nanometric porosity (Suess et al. 2002). Based on experimental studies (Aya et al. 1992; Sugaya and Mori 1996; Uchida and Kawabata 1995) of CO₂ and fluorocarbon hydrate growth at liquid-liquid interfaces, Mori and

Mochizuki (1997) and Mori (1998) had already proposed a porous microstructure of the hydrate layers intervening the two liquid phases and suggested a phenomenological capillary permeation model of water transport across the films. Although general physical concepts of this phenomenon in different situations may be quite similar, still there are no sufficient data to develop a unified theoretical approach to its modeling (Mori 1998).

In accordance with numerous experimental observations (Henning et al. 2000; Kuhs et al. 2000; Staykova et al. 2002; 2003; Stern et al. 1998; Takeya et al. 2000; Uchida et al. 1992; 1994), a thin gas hydrate film rapidly spreads over the ice surface at the initial stage of the ice-to-hydrate conversion (stage I after Staykova et al. 2002, 2003). Subsequently, the only possibility to maintain the clathration reaction is the transport of gas molecules through the intervening hydrate layer to the ice-hydrate interface and/or of water molecules from the ice core to the outer hydrate-gas interface. As mentioned above, a diffusion-limited clathrate growth was assumed for this second stage described by Takeya et al. (2000), Henning et al. (2000), and Wang et al. (2002) on the basis of the shrinking-core models formulated for a single ice particle, in their treatment without taking explicitly account of a surface coverage stage. Salamatina and Kuhs (2002) suggested in the case of porous gas hydrates, the gas and water mass transport through the hydrate layer becomes much easier, and the clathration reaction itself together with the gas and water transfer over the phase boundaries may be the rate-limiting step(s) of the hydrate formation that follows the initial coverage and this process should be modeled simultaneously with the ice-grain coating (stage II after Staykova et al. 2002, 2003). Still they expect an onset of a diffusion-limited stage (stage III in this nomenclature) of the hydrate formation process completely or, at least, partly controlled by the gas and water diffusion through the hydrate phase. The values for the activation energies for the CH₄ hydrate formation case they obtained were 39.9 kJ/mol (with D₂O ice) and 34 kJ/mol (with H₂O ice) for the reaction-limited stage and 59.9 kJ/mol for the diffusion limited one. Later on, to improve the fit of the initial part of the reaction, the first stage was divided into two sub stages (Genov et al. 2004) – stage Ia and stage Ib. Stage Ib was the previously mentioned surface coverage, preceded by a crack filling stage Ia. In the case of CO₂, hydrate they reported activation energies for stage I 5.5 kJ/mol at low temperatures and 31.5 kJ/mol above 220 K; 42.3 kJ/mol for stage II and 54.6 kJ/mol for stage III.

The anomalous preservation is a well established but little-understood phenomenon of a long-term stability of gas hydrates outside their stability field. It occurs after some initial hydrate decomposition into ice in certain temperature range. It is a very interesting phenomenon of substantial scientific and practical interest. Davidson et al (1986) performed early observations of this effect. Such were made independently in more detailed, by Yakushev & Istomin (1992). These authors observed an unexpected perseverance when gas hydrates were brought outside their stability field at temperatures below the ice melting point. More recently, Stern et al. (2001) and Takeya et al. (2001) investigated the temperature dependency of the effect in the methane hydrate case and found that the effect also

had a lower limit. According to Stern et al. (2001) the “anomalous preservation window” is between 240K and the ice melting point, while at temperatures below 240K the decomposition is rapid and appears to be thermally activated. Within this window the decomposition rates vary considerably by several orders of magnitude in a reproducible way (see **Fig.I.9**) with two minima at around 250 and 268 K. Takeya et al. 2002 confirmed this effect and

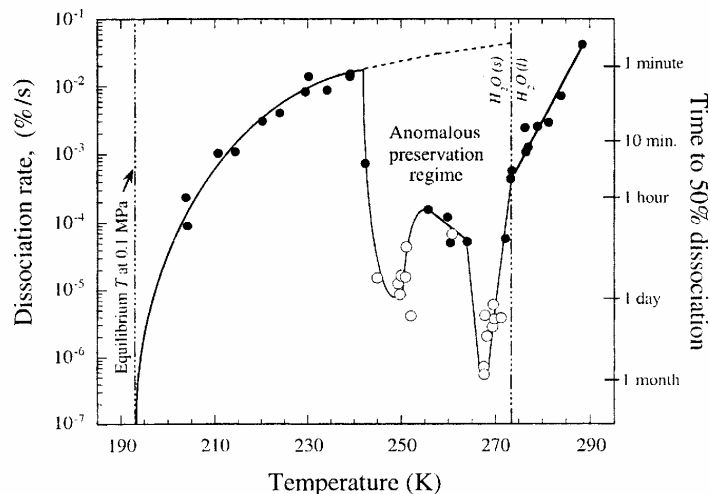


Fig.I.9 Self-preservation of CH₄. (Stern et al. 2001)

suggested diffusion limitation for explaining the slow decomposition kinetics within the anomalous preservation window. A similar, but not identical behaviour was observed for CO₂ hydrate (Stern et al. 2003). Still, the deeper physical origin of “anomalous preservation” remains obscure and the controlling parameters elusive (Wilder & Smith 2002, Stern et al. 2002, Circone et al. 2004). This effect may lead to a revision of the existing ideas about the importance of the CO₂ decomposition for the processes running on Mars (see § 3).

§ 3. CO₂ hydrates on Mars

Iro et al. (2003), trying to interpret the nitrogen deficiency in comets, discussed in detail the conditions needed to form clathrate hydrates in the proto-planetary nebulae, surrounding the pre-main and main sequence (MS) stars. They stated most of the conditions for hydrate formation were fulfilled, despite the rapid grain growth to meter scale. The key was to provide enough microscopic ice particles exposed to a gaseous environment. *De facto*, observations of the radiometric continuum of circumstellar discs around τ -Tauri and Herbig Ae/Be stars suggest massive dust disks consisting of millimeter-sized grains, which disappear after several millions of years (e.g. Beckwith et al. 2000, Natta et al. 2000). A lot of work on detecting water ices in the Universe was done on the Infrared Space Observatory (ISO). For instance, broad emission bands of water ice at 43 and 60 μm were found in the disk of the isolated Herbig Ae/Be star HD 100546 in the constellation Musca. The one at 43 μm is much weaker than the one at 60 μm , which means the water ice, is located in the outer parts of the disk at temperatures below 50 K (Malfait et al. 1998). There is also another broad ice feature between 87 and 90 μm , which is very similar to the one in NGC 6302⁶ (Barlow 1997). Crystalline ices were also detected in the proto-planetary disks of ϵ -Eridani and the isolated Fe star HD 142527 (Li, Lunine

⁶ The Butterfly nebula in Scorpius.

& Bendo 2003, Malfait et al. 1999) in Lupus. 90 % of the ice in the latter was found crystalline at temperature around 50 K. HST demonstrated that relatively old circumstellar disks as the one around the 5 million year old B9.5Ve (Jaschek & Jaschek 1992) Herbig Ae/Be star HD 141569A are dusty (**Fig.I.10**) (Clampin et al. 2003). Li & Lunine (2003) found water ice there. Knowing the ices usually exist at the outer parts of the proto-planetary nebulae, Hersant et al. (2004) proposed an interpretation of the volatile enrichment, observed in the four giant planets of the Solar System, with respect to the Solar abundances. They assumed the volatiles had been trapped in the form of hydrates and incorporated in the planetesimals flying in the proto-planets' feeding zones. Obviously, the idea that the gas hydrates may play a role in a cosmic scale starts to gain in popularity. Nevertheless, the pressure and temperature conditions in the outer space and on Mars are distinctly different.

There is a well-known meteorological phenomenon called diamond dust production. At temperatures below -18°C , ice Ih crystals may form as irregular hexagonal plates or non-branched ice needles or columns directly from water vapor in the air, through a process called deposition. Their size may go below $20\text{ }\mu\text{m}$ across, which may result in "snow" with a very high specific surface area. The ice existing and forming on Mars is most likely ice Ih in the shape of diamond dust.

CO_2 is an abundant volatile on Mars. It dominates in the atmosphere and covers the polar ice caps much of the time. In the early seventies, the possible existence of CO_2 hydrates on Mars was proposed (Miller & Smythe 1970). Recent consideration of the temperature and pressure of the regolith and of the thermally insulating properties of dry ice and CO_2 clathrate (Ross and Kargel, 1998) suggested that dry ice, CO_2 clathrate, liquid CO_2 , and carbonated groundwater are common phases even at Martian temperatures (Lambert and Chamberlain 1978, Hoffman 2000, Kargel et al. 2000).

What if CO_2 hydrates are present in the Martian polar caps as some authors suggest (e.g. Clifford *et al.* 2000, Nye *et al.* 2000)? Clifford (1980a, 1980b, 1993) first proposed that *Chasma Boreale* and *Chasma Australe* were possibly formed by a jökulhlaup-type event. He noted the large size of these reentrants and the fact that they crosscut typical polar channels and are geomorphologically similar to *Ravi Vallis* – an outflow channel with a flood origin (**Fig.I.11**). Clifford (1980b) hypothesized a basal melting in the past history of the polar cap was possible and that melt water could collect within and be catastrophically released from craters beneath the cap, resulting in a jökulhlaup. Heat generated by turbulence and viscous dissipation within the flowing water and by friction between the flowing water and surrounding ice could then serve to enlarge the drainage tunnel.

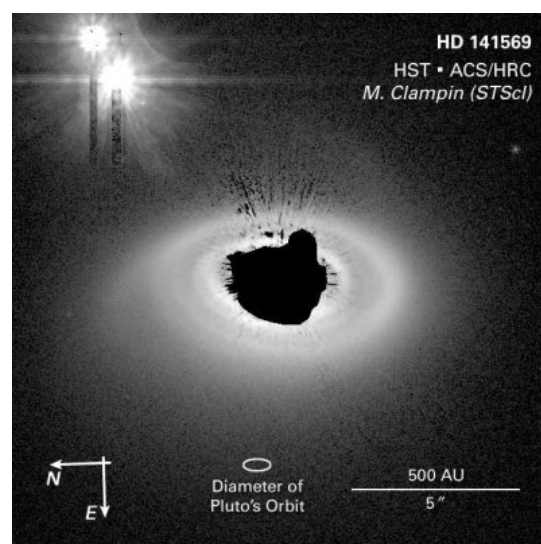


Fig.I.10 Coronagraphic image of HD 141569

But if the polar caps contain significant amounts of CO₂ hydrate mixed with water ice (Jakosky et al. 1995, Hoffman 2000), then the cap will not melt as readily as it would if consisting only of water ice, because of the clathrate's lower thermal conductivity, higher stability under pressures and higher strength (Durham 1998), compared to the pure water ice. Thus, obtaining an accurate estimate of the amount of CO₂ clathrate in the layered deposits is of major importance. Mellon (1996) studied this

problem and found that the polar deposits probably contain relatively small amounts of CO₂. However, if the polar deposits contain significant amounts of CO₂ clathrate, this would affect the behavior of the melted polar material. Under constant pressure but increasing temperature beneath the cap, the decomposed CO₂ clathrate would release liquid CO₂ (soluble in water at low temperatures and high pressures), liquid water and excess, gaseous CO₂ (Hoffman 2000). When this melt mixture reaches the cap periphery, and pressure is therefore greatly reduced, the water would readily freeze and CO₂ would now be nearly completely insoluble, leaving unstable pockets of

CO₂ gas within the ice which would be likely to burst (Hoffman 2000).

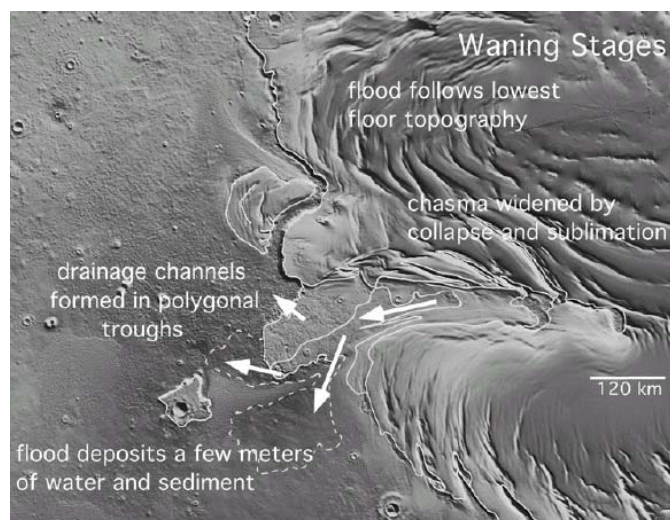


Fig.I.11 Formation of Chasma Boreale by an outflow of melt water (from Fishbaugh & Head 2002).

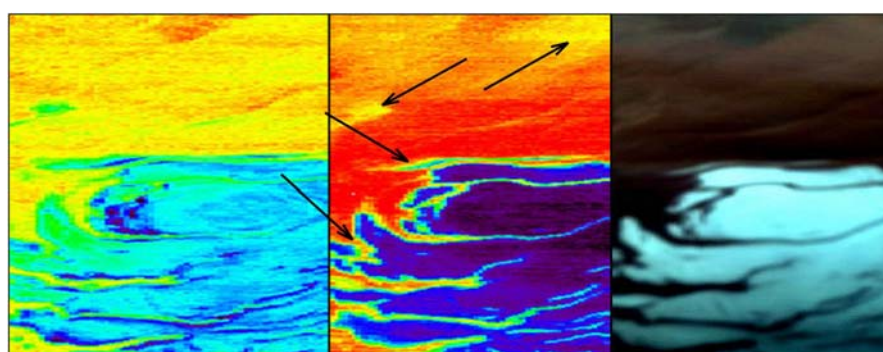


Fig. I.12 The Martian South Polar Cap as seen in terms of H₂O (left), CO₂ (middle) and normally (right). The arrows show the suspected clathrate containing regions. Courtesy: Mars Express, OMEGA team. Image Number: SEMVMA4740D

The question of a possible diurnal and annual CO₂ hydrate cycle on Mars also stays, since the large temperature amplitudes observed there cause leaving and reentering the clathrate stability field on daily and seasonal basis. The question is can the gas hydrate be detected by any means, being deposited on the surface. Probably yes. The OMEGA spectrometer on board of Mars Express returned some data, which were used by the OMEGA team to produce images of the south polar cap, as it was visible in terms of CO₂ and H₂O (**Fig.I.12**). The arrows assign areas where the existence of dry ice is not very likely but still it is visible and a strong water ice signal can be detected. If one looks back at the phase diagram from **Fig.I.8** will see that dark gray p-T region where the water ice coexists with gaseous CO₂ and CO₂ hydrate. It is not clear if this is hydrate, because the images are in a rainbow

scale, which is not published yet and will not be available before the beginning of the year 2005 due to technical problems (OMEGA team private communication April 2004). Otherwise, one approach to see if this is hydrate or not is to try to find there the “golden ratio” of $\approx 6:1$ water to CO₂ molecules. In any case this is still an open question.

The decomposition of CO₂ hydrate is believed to play a significant role in the terra-forming processes on Mars. Many of the observed surface features are partly attributed to it. For instance, Musselwhite et al. (2001) argued that the Martian gullies (**Fig.I.13**) had been formed not by liquid water but by liquid CO₂ since the present Martian climate does not allow liquid water existence at the surface in general. Especially this is true for the southern hemisphere where most of the gully structures occur. However, water can be present there as ice Ih, CO₂ hydrates or hydrates of other gases (e.g. Max & Clifford 2001, Pellenbarg et al. 2003) or liquid water at depths below 2 km under the surface (see geotherms in the phase diagram **Fig.I.8**). With the present obliquity, the slopes where the gullies occur remain generally shaded during most of the year and are among the coldest spots on the planet. At such conditions, any dry ice just below the surface and in diffusive contact with the surface should remain stable and act as a dam trapping gas hydrate, water ice and liquid CO₂ underneath. In case of temperature increase the dry ice dam will get molten and the liquid CO₂ will drain out. It will rapidly vaporize. Some of the vapor may snow out, but the rapid expansion should be enough to create a fluidized suspended flow of CO₂ gas along with some entrained debris. The clathrate hydrate will dissociate into CO₂ vapor plus water ice and the additional gas release should help to maintain the flow. Gully formation by this process can be in single or multiple episodes depending on the rate of replenishment of the liquid-CO₂ aquifer and the formation of a new dry-ice plug. It is believed that the melting of ground-ice by high heat flux has formed the Martian chaotic terrains (Mckenzie & Nimmo 1999). Milton (1974) suggested the decomposition of CO₂ clathrate had caused rapid water outflows and formation of chaotic terrains. When sediment saturated with water becomes subjected to a stress, a loosely packed grain framework suddenly collapses and the grains become temporarily suspended in the pore fluid (liquefaction) (see **Fig.I.14**). If water flows fast enough so that it balances with the settling velocity of grains, the grains are suspended in the stream and the water-sediment mixture behaves like fluid (fluidization). These two processes may have

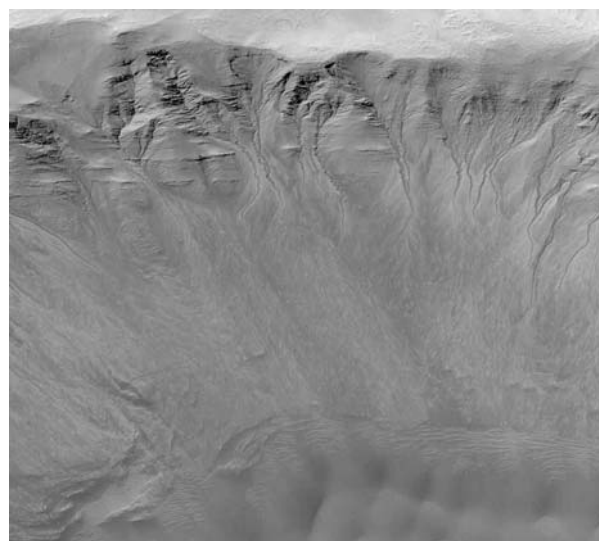


Fig.I.13 Gullies on a Crater Wall in Newton Basin
MGS MOC Release No. MOC2-317, 8 August 2002

played important roles in the chaotic terrain formation (Ori & Mosangini 1997). If the amount of gas derived from clathrate is large enough and conditions for gas build-up under an impermeable layer

exist, the pressure release of gas can play a major role in pulverizing rocks and remaining ices. Furthermore fragmented rocks by gas explosion can liquefy easily. Once liquefied and fluidized the mobilized water-sediment mixture flows out catastrophically. In some cases, ponds of water may have occurred in the depressions inside the chaotic terrain (Ori & Mosangini 1998). Ness & Orme (2002) gave a similar explanation of the formation of the Martian spiders. In their interpretation the process did not reach the stage of catastrophic flooding but stopped after intensive out-gassing and several other events linked in one or another way with the CO₂ hydrate formation and decomposition.

Cabrol et al. (1998) proposed that the physical environment and the morphology of the south polar domes on Mars suggest for possible cryovolcanism. The surveyed region consisted of 1.5-km thick-layered deposits covered seasonally by CO₂ frost (Thomas et al. 1992) underlain by H₂O ice and CO₂ hydrate at depths > 10m (Miller and Smythe, 1970). When the pressure and the temperature are raised above the stability limit, the clathrate is decomposed into ice and gases, resulting in explosive eruptions. Cabrol et al. observed these pancake-shaped domes only in impact structures and suggested morphogenic processes associated with high pressure and high temperature conditions, created by meteorite impacts that can generate eruptive conditions for clathrates. All the domes are observed at the bottom of impact craters, and range between 40 - 50-km in diameter, with a few larger or smaller exceptions. They are round at their base and show concentric rings. This observation rules out the possibility of an aeolian construct. Their comparison illustrates a process of dome formation most likely by the emergence of underground material, which can be compared to the formation of terrestrial volcanic lava domes.

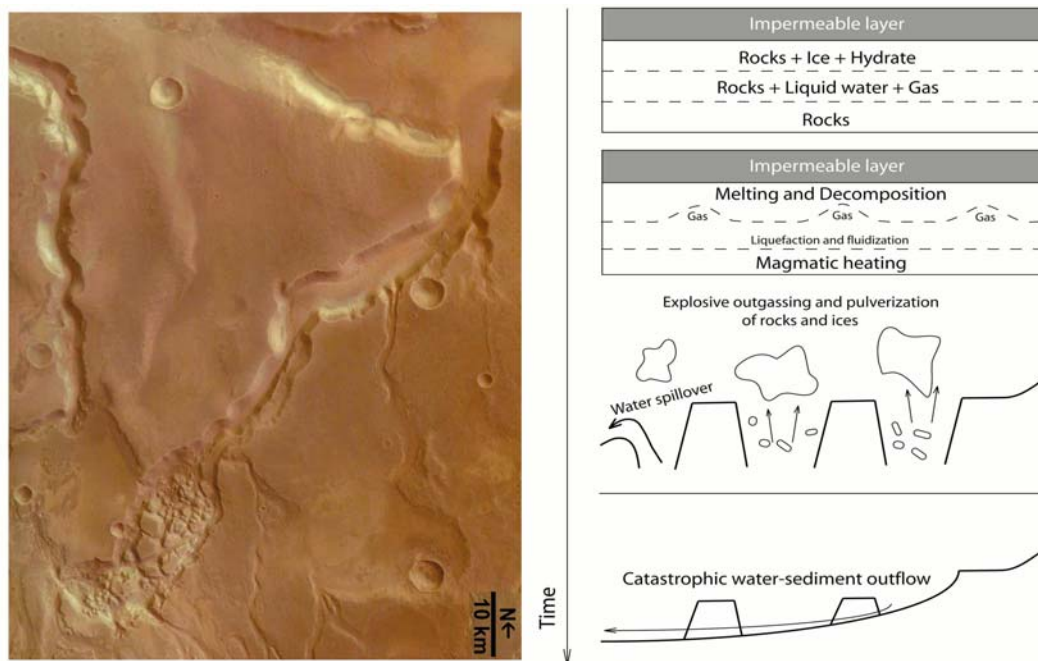


Fig.I.14 Chaotic terrain (left: Courtesy ESA Mars Express 2004) and a possible mechanism of its formation (right: after Komatsu et al. (2000)).

Still a lot more examples of the possible importance of the CO₂ hydrate on Mars can be given. One thing remains unclear: is it really possible to form hydrate there? Kieffer (2000) suggests no

significant amount of clathrates could exist near the surface of Mars. Stewart & Nimmo (2002) find it is extremely unlikely that CO₂ clathrate is present in the Martian regolith in quantities that would affect surface modification processes. They argue that long term storage of CO₂ hydrate in the crust, hypothetically formed in an ancient warmer climate, is limited by the removal rates in the present climate. Other authors (e.g. Baker et al. 1991) suggest that, if not today, at least in the early Martian geologic history the clathrates may have played an important role for the climate changes there. Since not too much is known about the CO₂ hydrates formation and decomposition kinetics, their physical and structural properties, it becomes clear that all the above mentioned speculations rest on extremely unstable basis. How fast do CO₂ hydrates form? What limits their growth? What controls the hydrate decomposition? Is a catastrophic decomposition likely? Are the physics behind the hydrate formation and decomposition similar? Can we describe better the hydrate microstructure, which certainly affects its physical and mechanical properties? This work comes to try to throw more light upon these issues.

Chapter II

Methods and instrumentation

In this chapter will be discussed the basic physics of the neutrons, such as their physical properties and interactions in which they play a role. A special emphasize will be put on the neutron scattering, neutron production and detection. Some other processes involving neutrons, which do not have a direct impact on the present studies will be mentioned very briefly. Also will be given a description of the instrument used in these studies – D20 – and certain issues of the radiation protection will be conversed. Later on the pVT system used in the in-house work will be described and its main ideology discussed. Then, the main principles of the electron microscopy will be introduced, together with some basic information on the physics of the electrons and a description of LEO 1530 Gemini – the cryo FE-SEM used here. At the end of the chapter, the BET method for measuring specific surface area will be briefly described.

§ 1. Neutrons – basic physics and instruments

1.1. Neutrons – basic physical properties

In the year 1930 Bothe and Becker performed an experiment on bombardment of beryllium with alpha particles. They detected highly penetrating radiation, which they identified as γ -rays. Frederic and Irene Joliot-Curie realized the considered radiation ejects protons out of paraffin target and obtained the velocity of the ejected protons $\approx 3.3 \times 10^7$ m/s. This was explained as a Compton scattering of γ -rays from protons.

In 1932 James Chadwick (a student of Rutherford) carried out a series of experiments to define the real nature of the “beryllium” rays. He investigated them passing not only through paraffin but also through some other especially N-containing materials. Thus, he obtained the velocity of the ejected nitrogen nuclei ($\approx 4.7 \times 10^6$ m/s). He rejected the hypothesis of the electromagnetic nature of this radiation and assumed it to consist of neutral particles with a steady state mass close to that of the proton (Chadwick 1932) – the neutron. For this, in 1935 he obtained the Nobel Prize in physics.

Let us have a fast look at the main properties of the neutrons as well as the interactions they take part in.

Mass: Estimation about the mass of these particles could be done on the basis of the conservation laws assuming them to be non-relativistic (with an accuracy of 1 %).

$$\left| \begin{array}{l} \frac{mv_0^2}{2} = \frac{mv^2}{2} + \frac{M_x V_x^2}{2} \\ mv_0 = mv + M_x V_x \end{array} \right. \quad (\text{II. 1})$$

m and M_x are the masses of the unknown particle and the recoil nucleus respectively, v_0 and v – the velocity of the particle before and after the collision, V_x – the velocity of the nucleus. By solving system (II.1) Chadwick got:

$$V_x = \frac{2m}{m + M_x} v_0 \quad (\text{II.2})$$

As a result, the neutron mass $m_n = 939.57 \text{ Mev}$ or $1.15 m_p$ was found.

In the same year Ivanenko and Heisenberg suggested that the atomic nucleus consists of neutrons and protons.

Electric Charge: In the elementary particle physics as an electric charge of a particle is understood a discrete whole quantum number, whose conservation limits the possible kinds of transformations of the particle. All elementary particles carry an elementary charge, equal either to $0 e$ or to $\pm 1 e$. As a unit electric charge is taken the charge of the electron ($1 e = 1.6 \times 10^{-9} \text{ C}$).

From the other site, the electric charge is a quantitative measure for the interaction between the particles and the electric fields. The new theories unifying the forces require the neutron to be exactly neutral. In this sense its charge is less than $10^{-21} e$.

Spin: In the quantum mechanics is shown that the square magnitude of the orbital angular momentum has a quantized spectrum of eigenvalues:

$$|\vec{l}|^2 = l(l+1)\hbar^2 \quad \text{or} \quad |\vec{l}| = \hbar\sqrt{l(l+1)} \quad (\text{II. 3})$$

where l is the azimuthal quantum number and for given principal quantum number n gets values $l = 0, 1, 2, \dots, n-1$. The spectrum of the possible values of the projection of \vec{l} over a given direction z has $(2l+1)$ values: $\pm l\hbar; \pm(l-1)\hbar; \dots, 0$. In the quantum physics only the maximum projection of \vec{l} equal to $\hbar l$ is measured.

The experiments have shown that the elementary particles have inner angular momentum, which has a quantum nature and is not connected with their orbital motion. It is called spin. Analogously to the former may be shown that the eigenvalues of the square of the operator of the spin are:

$$|\vec{s}|^2 = s(s+1)\hbar^2 \quad \text{or} \quad |\vec{s}| = \hbar\sqrt{s(s+1)} \quad (\text{II. 4})$$

The projection of \vec{s} over a given direction z has $(2s+1)$ different values. The neutrons have a spin quantum number $s = \frac{1}{2}$. Thus, they follow the statistics of Fermi – Dirac and obey the principle of

Pauli, which states that in a quantum system two particles of the same type cannot be in the same condition at the same time.

Magnetic momentum: From the classical electrodynamics is known that a particle with charge e and mass m , has also a magnetic momentum μ . In the quantum mechanics is shown that the magnetic momentum, which is due to the orbital motion of the particle, is equal to:

$$\vec{\mu}_l = \frac{e}{2m} \hbar \sqrt{l(l+1)} \quad (\text{II. 5})$$

and the one due to the spin is:

$$\vec{\mu}_s = g \frac{e}{2m} \hbar \sqrt{s(s+1)} \quad (\text{II. 6})$$

where g is the gyro magnetic ratio.

According to the equation of Dirac, a particle with spin equal to $\frac{1}{2}$ should have a magnetic momentum - one magneton, if the particle is charged and 0 magneton if it has a zero charge. The experiments have shown anomalously high biases from the calculated values for the protons and neutrons:

$$\begin{aligned} \mu_p &= 2.792763 \mu_0 \\ \mu_n &= -1.91315 \mu_0 \end{aligned}$$

where μ_0 is the nuclear magneton and is equal to $\mu_0 = e\hbar / 2m_p$. This showed those particles had much more complicated structure, impossible to be explained with simple assumptions. According to the quantum chromodynamics, the hadrons (including the neutrons) consist of quarks, which together with the leptons are the building units of the whole material world. They are fermions (spin $1/2$) and have non-zero steady state mass. The quarks interact between themselves with strong interactions carried by the gluons - neutral bosons (spin 1), with a zero steady state mass. According to the fragrance (their main characteristic) there are six quarks: u, d, s, c, b, t. The neutron has a udd structure.

1.2. Neutron interactions

1.2.1. Strong (nuclear) interactions

There are three types of strong interactions for the neutrons:

1. Neutron – proton interactions.
2. Neutron – neutron interactions.
3. Neutron – nucleus interactions.

The reaction cross-sections for the neutron case significantly depend on its energy. The classification of the neutrons according to their energies is given in Table II.1.

Name		Energy [eV]
	Cold	0 – 0.005
Slow	Thermal	0.005 – 0.5
	Resonant	0.5 - 10^3
Intermediate		10^3 – 10^5
Fast		10^5 – 5×10^7
Super fast		$> 5 \times 10^7$

Table II.1 Neutron energy classification

The nuclear interaction is, however weak in an absolute scale, and therefore the neutrons can penetrate the sample and investigate the bulk properties

1.2.2. Weak interactions

On the first place it appears with its beta decay:

$$n \rightarrow p + e^- + \tilde{\nu}_e \quad t_{1/2} = 10.2 \text{ min} \quad (\text{II. 7})$$

The neutron takes part in many other weak interactions, which will not be considered here.

1.2.3. Electromagnetic interactions

The neutrons that have wavelengths of the order of or bigger then the atomic dimensions ($E_n < 10 \text{ eV}$) take part in the electromagnetic interactions of the magnetic momentum of the neutron with those of the electron layers of the atoms. These interactions can be used in a large number of investigations in the field of the solid-state physics. The neutron can interact with the electric fields of the nuclei as well as (n, e^-) scattering is possible.

1.2.4. Radiative capture $((n, \gamma) \text{ reactions})$

This is one of the most common reactions of the neutrons with the matter. It follows the scheme,

$${}_0^1n + {}_Z^AX \rightarrow {}_Z^{A+1}X + \gamma \quad (\text{II. 8})$$

The latter nucleus is usually β -active. This type of reactions is typical for the slow and intermediate neutrons and is widely used for their detection. It is also the main responsible for the activation of the experimental equipment.

1.2.5. (n, p) reactions

It is typical for the fast neutrons.

$${}_0^1n + {}_Z^AX \rightarrow {}_1^1p + {}_{Z-1}^AY \quad (\text{II. 9})$$

This is an exothermal reaction because $m_n > m_p$. It cannot take part at low energies because the ejected proton needs energy to jump over the Coulomb barrier.

1.2.6. (n, α) reactions

This is a reaction of the type,

$${}_0^1n + {}_Z^AX \rightarrow {}_2^4He + {}_{Z-2}^{A-3}Y \quad (\text{II. 10})$$

It is typical mainly for the fast neutrons but in many cases the coulomb barrier of the nuclei for α particles is too low and the reaction can happen even with thermal neutrons. Thus, for registration of thermal neutrons the reaction,

$${}_0^1n + {}_5^{10}B \rightarrow {}_2^4He + {}_3^7Li + 2.8 \text{ MeV} \quad (\text{II. 11})$$

is used.

Reactions resulting in producing more then one nucleon are also possible but will not be considered here.

1.2.7. Neutron scattering¹

¹ This overview is based on: Pynn (1990) and Squires (1997)

When neutrons are scattered by matter, the process can change the momentum and the energy of the neutrons and the matter. The scattering is not necessarily elastic because the atoms in the matter can move to some extent. Therefore, they can recoil during a collision with a projectile, or if they are moving when the neutron arrives, they can pass on or absorb energy.

The total momentum and energy are conserved. When a neutron is scattered it loses energy ε . Knowing that

$$\hbar \vec{k} = m \vec{v} \quad (\text{II. 12})$$

it is easy to see that the amount of momentum given up by the neutron during its collision, or the momentum transfer, is

$$\hbar \vec{Q} = \hbar(\vec{k} - \vec{k}') \quad (\text{II. 13})$$

where \vec{k} is the wave vector of the incident neutrons and \vec{k}' is that of the scattered neutrons. The quantity $\vec{Q} = \vec{k} - \vec{k}'$ is the scattering vector, and the vector relationship between \vec{Q} , \vec{k} , and \vec{k}' can be displayed in the scattering triangle (**Fig.II.1**). This triangle also emphasizes that the magnitude and direction of \vec{Q} are determined by the magnitudes of the wave vectors for the incident and scattered neutrons and the deflection (scattering) angle 2θ . For elastic scattering (**Fig.II.1a**) $\vec{k} = \vec{k}'$, so $\varepsilon = 0$ and applying a bit of trigonometry to the scattering triangle leads to $Q = 4\pi \sin \theta / \lambda$.

In the neutron-scattering experiments, are measured the intensity of the scattered neutrons (per incident neutron) as a function of Q and ε . This scattered intensity $I(\vec{Q}, \varepsilon)$ is often referred to as the neutron scattering law for the sample.

In a complete and elegant analysis, van Hove showed in 1954 that the scattering law could be written exactly in terms of time-dependent correlations between the positions of pairs of atoms in the sample. His result is that $I(\vec{Q}, \varepsilon)$ is proportional to the Fourier transform of a function giving the probability to find two atoms at a certain distance apart. Lets have a more detailed look at this.

He used the observation of Fermi that the actual interaction between a neutron and a nucleus may be replaced by an effective potential, much weaker than the actual interaction. This pseudo-potential causes the same scattering as the actual interaction but it is weak enough to be used in Born's perturbation expansion. The Born approximation says the probability an incident plane wave with a wave vector \vec{k} scattered by a weak potential $V(\vec{r})$ to become an outgoing plane wave with a wave vector \vec{k}' is:

$$\left| \int e^{i\vec{k} \cdot \vec{r}} V(\vec{r}) e^{-i\vec{k}' \cdot \vec{r}} d^3 r \right|^2 = \left| \int e^{i\vec{Q} \cdot \vec{r}} V(\vec{r}) d^3 r \right|^2 \quad (\text{II. 14})$$

where the integration is over the volume of the scattering sample. Even though individual nuclei scatter spherically, $V(\vec{r})$ represents the potential due to the entire sample, and the resulting disturbance for the assembly of atoms is a plane wave.

The potential to be used in (II. 14) is the Fermi's pseudo-potential, which for a single nucleus is given by $b_j \delta(\vec{r} - \vec{r}_j)$, where b_j is the scattering length of a nucleus labeled j at position \vec{r}_j and δ is the delta function of Dirac that is zero unless the position vector \vec{r} coincides with \vec{r}_j . Thus, for an assembly of nuclei, such as a crystal, the potential $V(\vec{r})$ is the superposition of individual neutron-nuclei interactions:

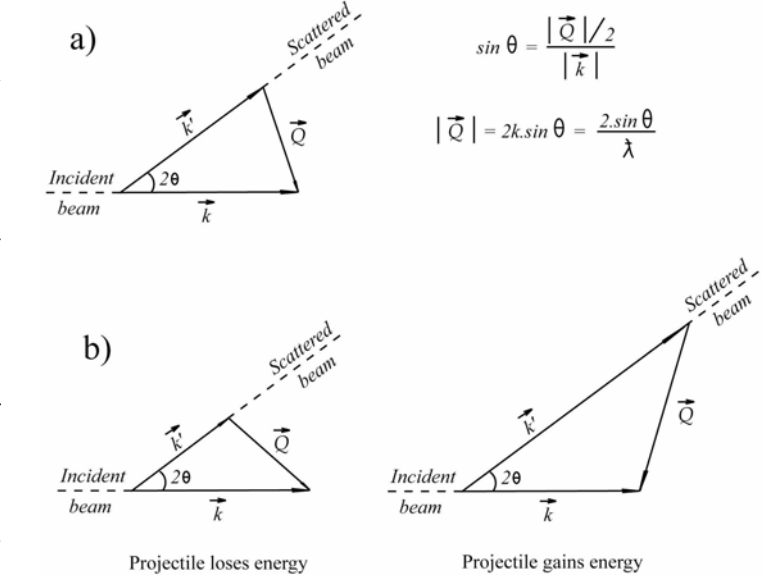


Fig. II. 1 Scattering triangles of (a) elastic scattering ($k' = k$) and (b) inelastic scattering with gain ($k' > k$) and loss ($k' < k$) of energy from the projectile.

$$V(\vec{r}) = \sum_j b_j \delta(\vec{r} - \vec{r}_j) \quad (\text{II. 15})$$

The summation is over all nuclear sites in the crystal.

Using (II. 14) and (II. 15) van Hove showed that the number of neutrons scattered per incident neutron is (van Hove's neutron-scattering law):

$$I(\vec{Q}, \epsilon) = \frac{1}{h} \frac{k'}{k} \sum_{j,l} b_j b_l \int_{-\infty}^{\infty} \left\langle e^{-i\vec{Q} \cdot \vec{r}_l(0)} e^{i\vec{Q} \cdot \vec{r}_j(t)} \right\rangle e^{-i\epsilon t} dt \quad (\text{II. 16})$$

The summation is over pairs of nuclei j and l and the nucleus labeled j is at position $\vec{r}_j(t)$ at time t , while the nucleus labeled l is at position $\vec{r}_l(0)$ at time $t = 0$. The angular brackets denote averaging over all starting times for observations of the system, which is equivalent to an average over all possible thermodynamic states of the sample. Let us treat equation (II. 16) as if it described a classical mechanics system in order to clarify its physical meaning. The sum over atomic sites in (II. 16) can then be rewritten as:

$$\sum_{j,l} b_j b_l \left\langle e^{-i\vec{Q} \cdot [\vec{r}_l(0) - \vec{r}_j(t)]} \right\rangle = \sum_{j,l} b_j b_l \int_{-\infty}^{\infty} \delta(\vec{r} - [\vec{r}_l(0) - \vec{r}_j(t)]) e^{-i\vec{Q} \cdot \vec{r}} dt \quad (\text{II. 17})$$

Lets suppose for a second that the scattering lengths of all the atoms in the sample are the same ($b_j = b_l = b$). The scattering lengths in (II. 17) can be removed from the summation, and the right-hand side becomes:

$$Nb^2 \int_{-\infty}^{\infty} G(\vec{r}, t) e^{-i\vec{Q}\cdot\vec{r}} d^3r$$

$$G(\vec{r}, t) = \frac{1}{N} \sum_{j,l} \langle \delta(\vec{r} - [\vec{r}_l(0) - \vec{r}_j(t)]) \rangle \quad (\text{II. 18})$$

N is the number of atoms in the sample. The delta function in the definition of $G(\vec{r}, t)$ is zero except when the position of an atom l at time zero and the position of atom j at time t are separated by the vector \vec{r} . $G(\vec{r}, t)$ is equal to the probability an atom to be at the origin of a coordinate system at time zero and an atom to be at position \vec{r} at time t , because the delta functions are summed over all possible pairs of atoms. $G(\vec{r}, t)$ is generally referred to as the time dependent pair-correlation function because it describes how the correlation between two particles develops with time. (II. 16) can be written as:

$$I(\vec{Q}, \varepsilon) = \frac{Nb^2}{h} \frac{k'}{k} \int_{-\infty}^{\infty} G(\vec{r}, t) e^{-i\vec{Q}\cdot\vec{r}} e^{-i\varepsilon t} d^3r dt \quad (\text{II. 19})$$

Thus, $I(\vec{Q}, \varepsilon)$ is simply proportional to the Fourier transform of a function giving the probability to find two atoms at a certain distance apart. By inverting (II. 19), information about the structure and dynamics of condensed matter may be obtained.

Actually, Van Hove's formalism can be modified to expose two types of scattering effects. The first is coherent scattering. Here the neutron wave interacts with the whole sample as a unit, thus scattered waves from different nuclei interfere with each other. This type of scattering depends on the relative distances between the constituent atoms and consequently gives information about the structure. Elastic coherent scattering tells about the equilibrium structure, while inelastic coherent scattering provides information about the collective motions of the atoms. The second type is the incoherent scattering. Here the neutron wave interacts independently with every nucleus in the sample in order that the scattered waves from different nuclei do not interfere but the intensities from each nucleus just add up. For instance, the incoherent scattering may, be a result of the interaction of a neutron wave with the same atom but at different positions and times, thus providing information about diffusion.

Even for a sample made of a single isotope, the scattering lengths emerging in (II. 16) will not be equal. This is because the scattering length of a nucleus depends on its spin. There is no correlation between the spin and the position of a nucleus. Therefore, the scattering lengths from (II. 16) can be averaged over the nuclear spin states without affecting the thermodynamic average (in the angular brackets). After introducing a nuclear spin averaging the sum in (II. 16) becomes:

$$\sum_{j,l} \overline{b_j b_l} A_{jl} = \sum_{j,l} (\overline{b})^2 A_{jl} + \sum_j (\overline{b^2} - (\overline{b})^2) A_{jj} \quad (\text{II. 20})$$

A_{jl} replaces the integral from (II. 16). The first term in the right-hand side of (II. 20) represents the coherent scattering, and the second one corresponds to the incoherent one. Consequently, one can define the coherent and incoherent scattering lengths as:

The expression for the coherent scattering law is a sum over j and l and thus involves correlations between the position of an atom j at time zero and this of an atom l at time t . Though j and l may sporadically be the same atom, in general they are not because of the large number N of nuclei in the sample. Therefore, one can say coherent scattering basically describes interference between waves produced by the scattering of a single neutron from all nuclei in a sample.

The incoherent scattering involves correlations between the position of an atom j at time zero and the position of the same atom at time t . Consequently, here the scattered waves from different nuclei do not interfere. Most often, the incoherent scattering intensity is the same for all scattering angles, adding intensity to the background.

The simplest type of coherent neutron scattering is diffraction. Assume the atoms are arranged at fixed positions in a lattice and a neutron beam is shooting at it. Let also the value of the incident wave vector, \vec{k} is the same for all neutrons, i.e. they fly in parallel and have equal velocities. Because the atoms and their associated nuclei are fixed by default, there is no change in the neutron's energy during the scattering and the scattering is elastic. When a projectile neutron wave arrives at each atom, the atom becomes a center of a scattered spherical wave and interference will take place. As the waves originate from a regular array of sites, the individual disturbances will reinforce each other only in particular directions. These directions are closely related to the symmetry and spacing of the scattering sites and can be used to deduce the symmetry of the lattice and the distances between the atoms.

Though, the diffraction is an elastic scattering process ($\varepsilon = 0$), the diffractometers integrate over the scattered neutrons energies. Therefore, rather than setting $\varepsilon = 0$ in (II. 16), to calculate the diffracted intensity one integrates the equation over ε . This makes sure the effect of the atomic vibrations is taken into account in the diffraction cross-section. The integration gives another delta function, suggesting that the pair correlation function $G(\vec{r}, t)$ has to be evaluated at $t = 0$. Thus the result for a single isotope crystal is:

$$I(\vec{Q}) = b_{coh}^2 \sum_{j,l} \left\langle e^{-i\vec{Q} \cdot (\vec{r}_j - \vec{r}_l)} \right\rangle \quad (\text{II. 22})$$

If the atoms in the sample were really stationary, the thermodynamic averaging brackets could be removed from (II. 22) since r_j and r_l would be constant. But *de facto*, the atoms oscillate around their equilibrium positions. When this is taken into account, the thermodynamic average introduces the Debye-Waller factor, and (II. 16) becomes:

$$\begin{aligned} b_{coh} &= \bar{b} \\ b_{inc} &= \sqrt{b^2 - (\bar{b})^2} \end{aligned} \quad (\text{II. 21})$$

$$I(\vec{Q}) = b_{coh}^2 \sum_{j,l} e^{i\vec{Q} \cdot (\vec{r}_j - \vec{r}_l)} e^{-\frac{1}{2}Q^2 \langle u^2 \rangle} \equiv |S(\vec{Q})|^2 \quad (\text{II. 23})$$

where $\langle u^2 \rangle$ is the average of the square of the displacement of an atom from its equilibrium position; $S(\vec{Q})$ is the structure factor.

One can determine \vec{Q} at which $S(\vec{Q})$ is nonzero and at which diffraction occurs. Presume \vec{Q} is perpendicular to a plane of atoms and if it is any integer multiple of $2\pi/d$, (d is the distance between parallel, neighboring planes of atoms) then $\vec{Q} \cdot (\vec{r}_j - \vec{r}_l)$ is a multiple of 2π and $S(\vec{Q}) \neq 0$ because each exponential term in the sum in (II. 16) is unity. Thus, \vec{Q} must be perpendicular to planes of atoms in the lattice and must not satisfy the condition, $S(\vec{Q}) = 0$, and there will be no scattering. If one applies the condition described above

$$Q = n(2\pi/d), \quad n - \text{integer} \quad (\text{II. 24})$$

to the scattering triangle for elastic scattering and then uses the relationship between Q , θ and λ , will obtain:

$$n\lambda = 2d \sin \theta \quad (\text{II. 25})$$

This equation, called Bragg's law, relates the scattering angle 2θ , to the interplanar spacing in a crystalline sample. Bragg's law can also be understood in terms of the path-length difference between waves scattered from neighboring planes of atoms (**Fig.II.2**). Diffraction (or Bragg scattering) may occur for any set of atomic planes one can imagine in a crystal, providing the wavelength λ and the angle θ between the projectile neutron beam and the planes satisfy (II. 25). Bragg scattering from a particular set of atomic planes resembles reflection from a mirror parallel to those planes: the angle between the incident beam and the plane of atoms equals the angle between the scattered beam and the plane. If a beam of neutrons of a particular wavelength shoots on a single crystal, there will be no diffraction. To obtain diffraction for a set of planes the crystal must be rotated to the correct orientation so that Bragg's law is satisfied.

To this moment only a simple type of crystal that can be built of unit cells, each containing one atom was discussed. On the

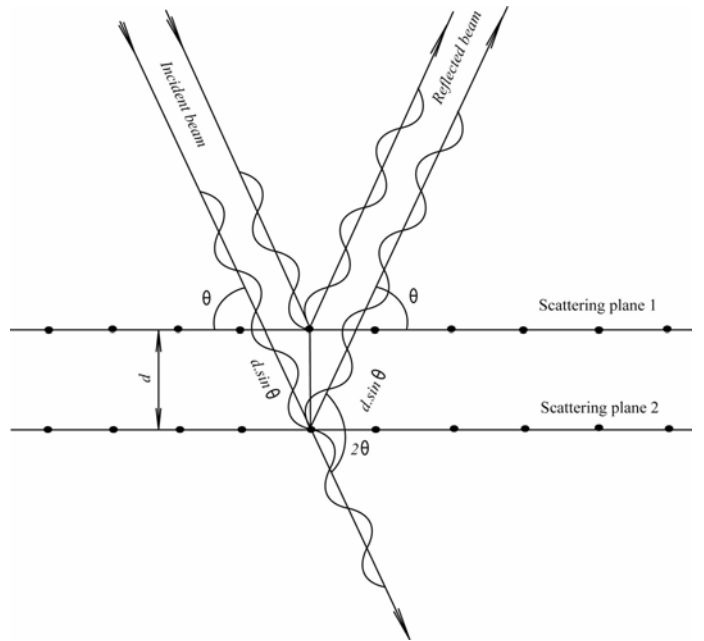


Fig. II. 2. The extra distance passed by the wave reflected by the second scattering plane is $2d \sin \theta$. When this distance is set to be equal to $n\lambda$ the result is again the Bragg's law.

other hand, polycrystalline powders, which consist of many randomly oriented single-crystal grains, will diffract neutrons whatever the orientation of the sample relative to the incident beam of neutrons is. There will always be grains in the powder that are correctly oriented to diffract. Thus, whenever the scattering angle, 2θ , and the wavelength λ satisfy the Bragg equation for a set of planes, a reflection independent of the sample orientation will be detected. This observation is the basis of the powder diffraction.

1.3. Neutron production

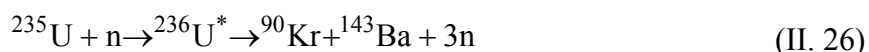
1.3.1. Neutrons from nuclear fission (Balabanov 1998)

The process of decay of the excited nuclei into 2 (rarely 3 or 4) pieces with comparable masses is called fission. O. Hahn, F. Strassmann, L. Meitner and O. Frisch discovered it in 1938 by bombardment of uranium-235 with neutrons.

The energetic instability of the heavy nuclei follows from the relatively small mass defects and the coulomb forces cause the fission. The fission of the heavy nuclei can be spontaneous or provoked by collisions with neutrons, protons, γ -rays etc and brings some energy gain.

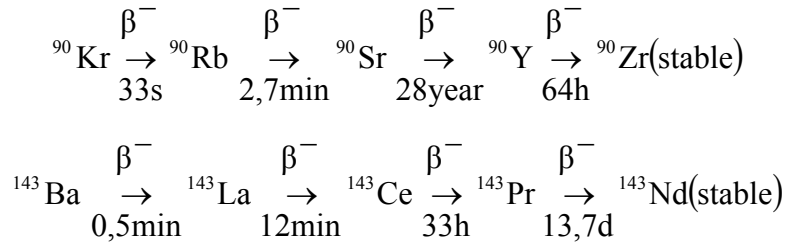
To split a nucleus a certain amount of energy is needed to deform it. If a spherical nucleus ($\alpha = 0$) is deformed to ellipsoidal its volume will not change because the nuclear matter is not deformable but its surface will increase. From one side, this will cause an increase of the surface energy and the nucleus will tend to recover its initial shape ΔE_{attr} . From the other side, this deformation will lead to decreasing the coulomb repulsion energy ΔE_{rep} . Obviously, if $\Delta E_{rep} > \Delta E_{attr}$ the nucleus will start to increase its deformation and eventually split (**Fig.II.3**). The maximum of the curve on **Fig.II.3b** corresponds to the state when the nucleus splits into two. The difference between the energy of the non-excited state and the maximal one is the activation energy, E_a . It is equal to the kinetic energy of the adsorbed neutron plus the binding energy f_n of the neutron in the nucleus. If the binding energy is bigger then the activation one the fission may take place even with thermal neutrons. This is the case with ^{235}U , where $E_a = 5.8 \text{ MeV}$ and $f_n = 6.4 \text{ MeV}$.

During the fission the ^{235}U nucleus first absorbs a neutron, and a ^{236}U compound nucleus is formed in an excited state. It is unstable, and splits into two fragments² (Keepin, 1969) (rarely more). There are several hundred variants of splitting of ^{236}U compound nucleus. Here is one of them:



² The nuclei formed within 10^{-14}s are fission fragments. These fast nuclei slow down by colliding with the atoms of the fuel material, then pick-up electrons, and finally become neutral atoms. Since they are radioactive, they undergo several decay processes, and form the fission products.

The primary fission fragments have more neutrons than the stable nuclei with the same atomic number. In most cases they undergo several successive β^- -transitions for „adjusting” their neutron/proton ratio. As an example, the fragment-pair from (II. 26) decays as follows:



Additionally, a number of neutrons are emitted (2,47 for ${}^{235}\text{U}$ with energy 1 - 2 MeV), more than 99% of them within 10^{-12} s after the fission. These are the prompt neutrons and originate from fission fragments that usually have much higher excitation energy than the neutron separation one.

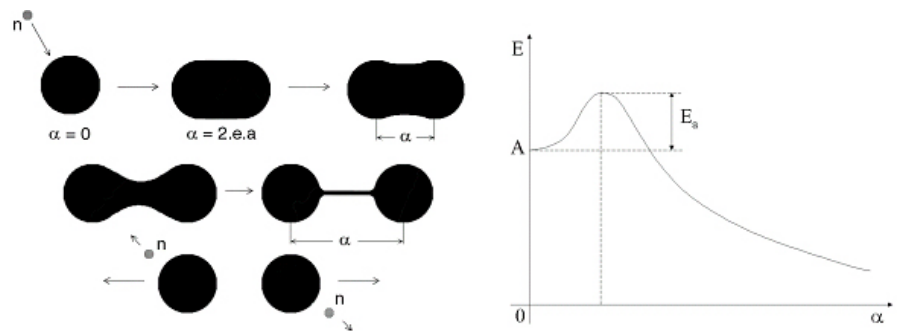
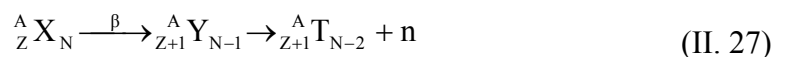


Fig. II. 3 Schematic drawing of the nuclear fission (left); The parameter α characterizes the degree of deformation of the nucleus. $\alpha = 0$ corresponds to a spherical non-deformed nucleus (point A) (right). For slightly deformed nuclei α is equal to the distance between the foci of the ellipsoid. Bigger values of α have the meaning of distance between the secondary nuclei.

The half-life of neutron-emission of these highly excited states is in the order of 10^{-15} s or even shorter. However, not all fission fragments emit neutrons. Some of them relax by emitting prompt γ -rays. It is possible 10 to 20 % of the prompt neutrons to be emitted during the deformation stage of the splitting nucleus.

Usually there is no neutron emission after the prompt neutrons. The fission products undergo several successive β -decays to reduce the neutron-excess. However, in some cases a daughter nucleus is formed after a β -decay, where the excitation energy is higher than the neutron binding one. This nucleus will emit a delayed neutron, nearly promptly after its formation. They are approximately 0,64% of the emitted neutrons and may come sometimes several minutes (on average 12 s) after the fission. The decay chain is:



The “X” nucleus is called a delayed-neutron precursor; the “Y” nucleus is a delayed-neutron emitter. Obviously, for these neutrons the “delay time” is determined by the half-life of the precursor (X), which can be quite large, since the β -decay is governed by the weak interaction. The delayed neutrons play a major role in the nuclear reactors control.

1.3.2. Neutron production via spallation

Another way of neutron production is to use an accelerator instead of a reactor. The neutrons obtained that way are called spallation neutrons. This is done by letting high-energy protons (or, less effectively, electrons) collide with a heavy-metal target, made of tungsten or uranium (**Fig.II.4**). When a fast particle, such as the high-energy proton, bombards a heavy atomic nucleus, some neutrons are “spalled”, or knocked out, in a nuclear reaction called spallation. Other neutrons are “boiled off” as the bombarded nucleus heats up. It is something like when a bad Snooker player breaks the balls at the start of the game using all the force he has. The result is that a few balls are immediately ejected and many more will just start mooching around. For every proton striking the nucleus, 20 to 30 neutrons are expelled. The accelerator coupled with a proton storage ring produces the protons in bursts lasting for less than a microsecond. One of the advantages of a spallation source is that only a small amount of energy (about 27 MeV per neutron) is deposited in the spallation target by the protons. Nuclear fission produces at about four to five times more energy in generating each of its neutrons. However, the price of producing the high-energy protons (electricity) is very high.

Neutrons from a spallation source arrive in pulses rather than continuously as they do at the reactor. This means the monochromator crystal needed at reactors, for instance, can be avoided and all the neutrons can be used. The trick allowing for this is that one can measure the time of flight of each detected neutron between the moderator and the detector. From this time its velocity and wavelength can be determined. Therefore, generating a monochromatic beam is unnecessary.

A thermal neutron with energy of 25 MeV flies with a speed of about 2.2 km/s (Mach 7). A typical neutron spectrometer is about 10 m long, so the neutron travels from the moderator to the detector in about 5 ms. Since the duration of the neutron pulse emerging from the moderator

of a pulsed source is typically a few tens of microseconds, the time of flight of the neutron can be determined with high relative precision.

1.4. Neutron detection

The neutron detection is based on the registration of the products of the nuclear reactions they cause. The neutron detector is an ordinary charged particle (or γ -quantum) detector whose working media is rich in a solution reacting intensively with the neutrons. The large variety of nuclear reactions caused by the neutrons and the different dependence of the reaction cross-sections on their energy

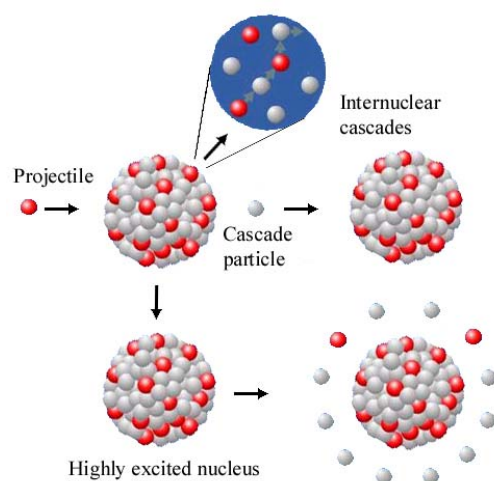


Fig. II. 4 Mechanism of the neutron production via spallation

gives the opportunity different types of detectors to be constructed. All the methods for neutron detection can be combined in several groups, briefly described below.

1.4.1. Radiative capture method

It is based on the registration of the γ -quanta coming from the radiative capture (n, γ) reactions, charged particles or fission products. One very convenient reaction for detecting low-energy neutrons is (II. 11). The Boron has a unique feature – the law “ $1/v$ ”³ holds for it in a very broad energy interval. Moreover, in such reactions α -particles are emitted, which makes the registration easier. Usually (a) ionization cameras full of BF_3 gas or with walls covered by a chemical compound rich in Boron; (b) proportional counters full of BF_3 ; (c) scintillators rich in B or Li; (d) nuclear photo emulsions etc are used for neutron detection. Sometimes the reactions



are used. The second one⁴ is actually implemented in the detecting system of D20 (see Chapter II §1, 1.5).

1.4.2. Method of the recoiled nuclei

It is based on registering the recoiled nuclei (most frequently H_2) as a result of elastic collisions between the fast neutrons and the detector’s active medium. Proportional counters full of hydrogen are used, as well as, Wilson and diffusion cameras full of gaseous or liquid hydrogen. Measuring the trace length one can deduce the neutron energy. Organic scintillators and nuclear photo emulsions with high hydrogen content are also utilized for this business.

1.4.3. Activation (method of the indicators of radioactivity)

The production of radioactive nuclei by bombarding a stable target with neutrons is activation. By measuring the intensity of the artificially created radioactivity (resulting in β or γ emission) the intensity of the neutron flux can be deduced. Unfortunately, this method does not give any immediate information on the neutron fluens. It is used for measuring constant fluxes and is useless for variable ones (as those during starting or stopping a reactor). It also plays a role for the radiation protection and health physics.

1.5. D 20 – a high-intensity 2-axis neutron diffractometer

Now it is time to have a look at the neutron facility used in this work. Some of the *in-situ* kinetic experiments on the CO_2 hydrate formation and decomposition were performed using neutron powder diffraction at the High-Intensity 2-Axis Neutron Diffractometer D20 (**Fig. II. 5**), at Institute Laue-Langevin (ILL), Grenoble, France. A detailed description of the instrument can be found at <http://www.ill.fr/YellowBook/D20> and in Convert et al. (1998, 1999).

³ The neutron capture cross-section at energies smaller than the energy of the first resonance is described as: $\sigma \approx \text{const}/v$

⁴ Here the reaction products, a 191 keV triton and a 573 keV proton, are emitted in opposite directions.

A monochromatic neutron beam reaches the sample, located at 3200 mm from the monochromator. A large-area ^3He Position Sensitive Detector (II.30) registers the diffracted by the sample neutrons. It covers part of a circle with center in the sample position. D20 uses a monochromatic thermal neutron beam with a very high flux. A monochromator of pyrolytic graphite HOPG (002) in reflection position with a fixed vertical focusing, giving wavelength of 2.4 \AA at a take-off angle of 42° , was chosen for the kinetic experiments, presented in this work. The beam flux, coming after the monochromator, is about $4.2 \cdot 10^7 \text{ n.cm}^{-2}.\text{s}^{-1}$. The position sensitive detector, used on D20, provides a detection zone of around 4 m by 150 mm. It is filled with 3.1 bar ^3He and 0.8 bar CF_4 . A micro-strip gas chamber technology (MSGC) has been used in its construction. A thin chromium layer has been deposited on the polished surface of electronically conducting glass plates. Then the chromium has been etched to create conductive micro-strip electrodes (4 cathodes and 4 thin anodes per detector cell). The small distance between the anode and cathode ($170 \text{ }\mu\text{m}$) provides fast evacuation of the positive ions, and allows for very high counting rates. Each detection plate, consisting of 32 cells, covers 3.2° (0.1° per cell). The position sensitive detector covers 153.6° with 48 plates mounted at a distance of 1471 mm from the sample. The 32 cells of one plate have 32 independent outputs. Each of the 1536 cells has individual amplifier and anti-coincidence logic unit. After the amplifier the signal coming from the cell is thresholded by the discriminator. Its neighboring cells are switched off for $1.5 \text{ }\mu\text{s}$, thus, preventing counting the same event twice. $2.5 \text{ }\mu\text{s}$ after having passed the threshold a cell may count again. The limit of the counting rate is around 50000 s^{-1} per cell. This micro-strip detection system has a precise and very stable geometry.

D20 is also equipped with a fast data acquisition system, which has a parallel input for up to 1600 cells. The instrument allows measuring of series of short histograms to observe irreversible kinetic phenomena, each lasting typically for a few seconds. In addition D20 is equipped with Silicon Graphics workstations for instrument and acquisition control, as well as with Large Array Manipulation Program (LAMP) - for data correction and 2 and 3D plots of the data (http://www.ill.fr/data_treat/lamp/front.htm).

The high flux at the sample position, the large stationary position sensitive detector and the fast data acquisition system make D20 an ideal tool for studying gas hydrate kinetics.

The proper p-T conditions for gas hydrate formation and decomposition are provided by high, low pressure or vacuum equipment together with cryogenic equipment. The required pressure at the

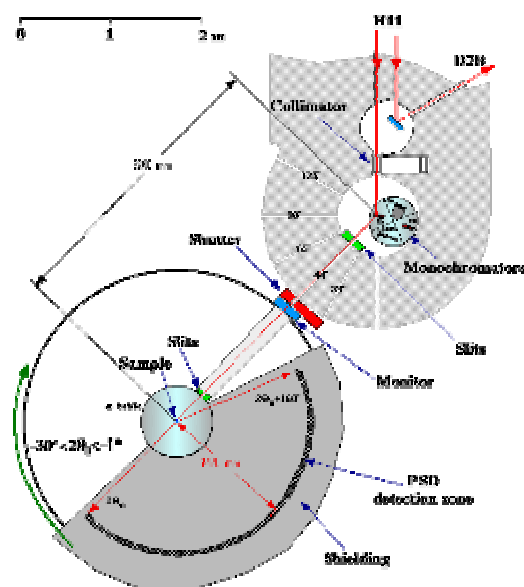


Fig. II.5 D20 – schematic

sample was supplied by gear built in Göttingen. Detailed descriptions of the used setups here and in the lab will be given in the next subsection.

A calibrated temperature sensor fixed to the hull of the sample cell was reading the probe temperature. In addition, the pressure stick was equipped with a heating coil, controlling the temperature of the stick tube close to the one of the reaction. The aluminum sample cells used in the neutron diffraction experiments were also manufactured in GZG, Göttingen.

A Helium Flow Cryostat (“Orange cryostat”), specially modified for D20, was providing the temperature control during the *in situ* kinetic experiments. The pressure cell, mounted on the pressure stick, was placed in a chamber with 10-20 mbar of He exchange gas, thus, giving the thermal contact between the cell and the surrounding sample chamber. Here is good to mention that if the pressure of the exchange gas is too high then the heat exchange between the stick and the cryostat becomes very strong. If this is the case, the heating coil cannot cope with it and the stick becomes overcooled. In the CO₂ case this may lead to blockage due to dry ice formation.

Opening the “cold” valve, which changed the helium gas flow through the chamber, controlled coarsely the chamber temperature. The heating coil of the cryostat heat exchanger provided the fine temperature control. In addition a thermocouple was placed at the cryostat’s sample-chamber wall to provide a reference temperature reading. The DTI temperature control interface adjusts automatically the cryostat temperature with precision of a fraction of the degree, using the previously mentioned reference temperature or the temperature measured on the hull of the sample cell, depending on the needs. Details on the cryostat construction can be found in Staykova (2004).

1.6. Radiation protection

The only aspects of the radiation protection debated here will be the activation of the experimental equipment used in this work. There are two types of interactions between the neutrons and the structuring materials in the beam, which can lead to activation – the radiative capture and the (n, α) reactions, described in subsection 1.1 of this chapter. Following the ALARA⁵ principle, when building such equipment, materials with as low as possible interaction cross-sections must be used, thus to reducing the degree of activation. Also as little as possible material should be placed in the beam.

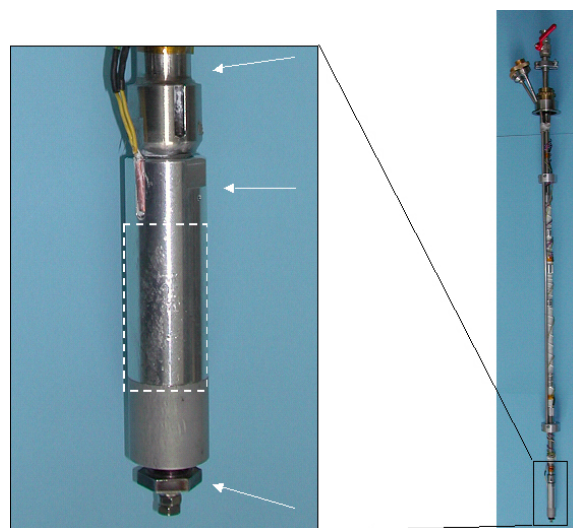


Fig. II. 6 The stick (right) and the part closest to the beam (left). The white rectangle shows approximately the target of the direct beam.

⁵ ALARA – As Low As Reasonably Achievable – the main principle of the radiation protection.

Fig.II.6 shows the sample stick and a zoom-in of the part with the sample cell attached to it. The zoomed parts have been either in the beam or in some close vicinity. The three white arrows assign three different regions of interest. The topmost one points to the welding, connecting the main stick tube to the adapter for attaching the cell. It is a gas welding made with some composite containing Cu. The arrow in the middle shows the cell, made of high-strength Al alloy. It has also a Cd shield for reducing the scattering from the Bridgman seal. The third arrow points to the Bridgman seal, consisting mainly of Co and steel. On **Fig.II.7** the spectra measured at these three places are shown.

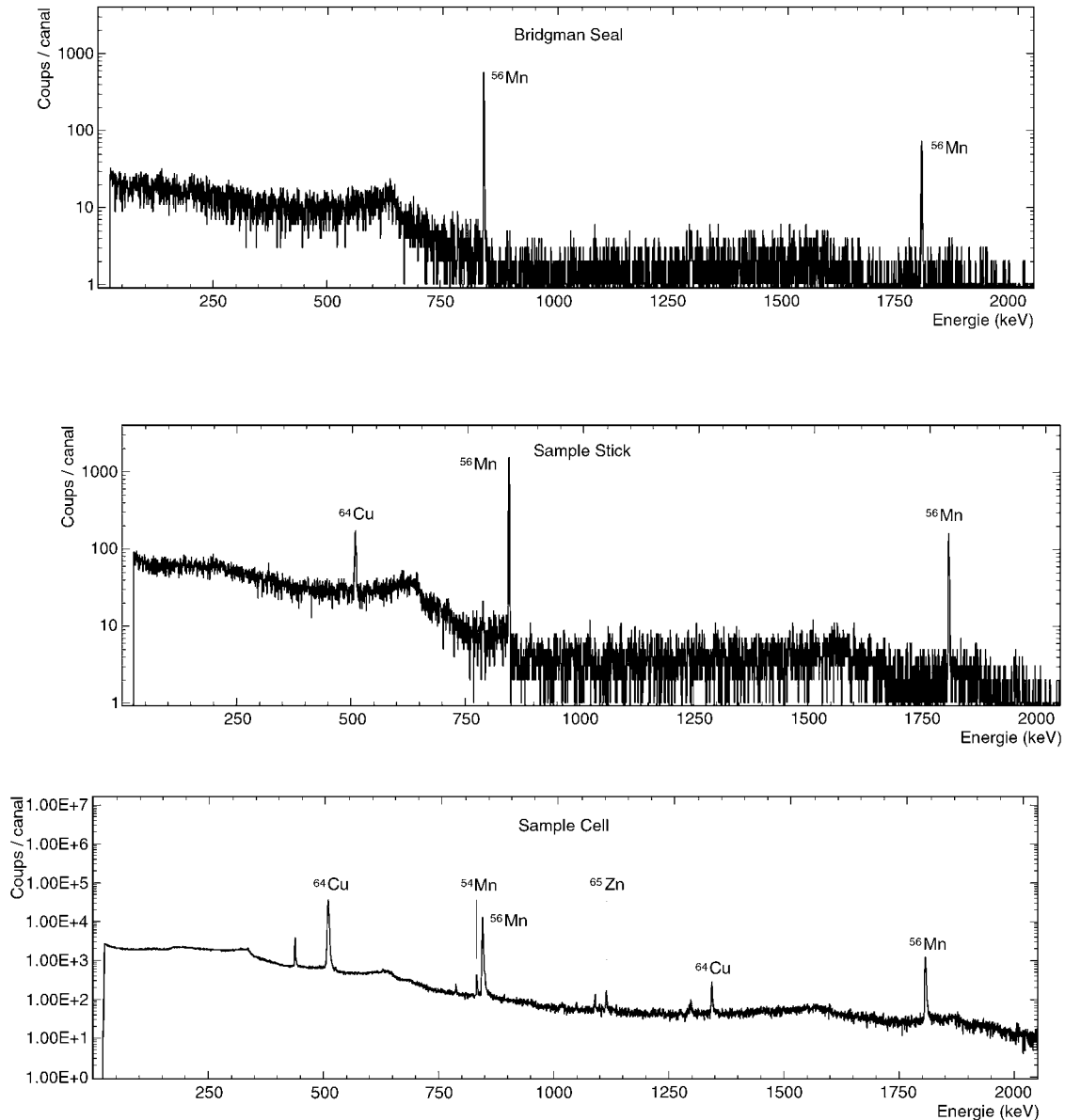


Fig. II. 7. The spectra taken at the positions of the three arrows from **Fig. II. 6**: the Bridgman seal (top), the welding (middle), the sample cell (bottom).

Looking at the Bridgman seal spectrum, one can see only ^{56}Mn in it. It has been produced by neutron (radiative) capture from the stable ^{55}Mn following the scheme $^{55}\text{Mn}(n, \gamma)^{56}\text{Mn}$. For $t_{1/2} = 2.5785$ h it decays via β to the ground state of ^{56}Fe . ^{56}Mn is present also in the other two spectra. This is quite well understandable because Mn is one of the very important additives in different alloys. It is

added to steel to improve rolling and forging qualities, strength, toughness, stiffness, wear resistance, hardness, and hardenability. With aluminum and antimony, and especially with small amounts of copper, it forms highly ferromagnetic alloys. It is also used in small amounts in the high-strength aluminum alloys together with silicon, magnesium and copper – the so-called silumins, as well as with Zn in the deformable alloys. Let us consider the spectrum around the welding. Together with the ^{56}Mn some ^{64}Cu appears. This is normal again knowing there is some Cu in the welding composite. It had been produced again after neutron capture, according to the scheme $^{63}\text{Cu}(n, \gamma)^{64}\text{Cu}$. ^{64}Cu has $t_{1/2} = 12.7$ h and has two decay channels: via electronic capture or β^+ to ^{64}Ni with an overall probability of 61 %, or via β^- to ^{64}Zn with probability 39 %. Both products are stable. In the sample cell two other isotopes are presented: ^{65}Zn and ^{54}Mn . The presence of ^{65}Zn is not surprising, since ^{64}Zn is one of the components of the alloy, which again via neutron capture has been transformed to ^{65}Zn . On the other hand ^{65}Zn undergoes electron capture to ^{65}Cu with $t_{1/2} = 244.26$ d. But what does this exot ^{54}Mn do here? There are two explanations. The first and most likely explanation is the peak is weak and the program may have gotten confused. The second possibility is just for some reason ^{53}Mn to be mixed in this alloy. This is a radioactive isotope, which via electron capture decays to ^{53}Cr with $t_{1/2} = 3.74\text{E}6$ y. If any ^{53}Mn is present in the alloy it will stay there for quite some time before decaying completely and during this time it may eventually capture some neutron and transform to ^{54}Mn , which decays in a way very similar to the one of ^{64}Cu to ^{64}Cr or ^{64}Fe with probabilities 100 % or $< 2.9\text{E-}4$ % respectively.

Up to here I discussed only the “long living” activation products. Just to make the story more complete I will mention one last activation possibility. The aluminum in the structuring materials is 100 % ^{27}Al . It transforms to ^{28}Al according to the well known already scheme $^{27}\text{Al}(n, \gamma)^{28}\text{Al}$. Later on ^{28}Al undergoes β^- decay to ^{28}Si . The half-life of ^{28}Al is only 2.2414 min and this is the reason not to see it in the spectra.

Unfortunately, for proper analysis of the activation and extraction of the activities due to every single constituent a much more precise work is needed. In any case the activation levels are low enough and after several days out of the beam most of the ^{64}Cu and almost all of the ^{56}Mn will be gone. Anyway, these are the main contributors to the total activity of the materials I used. There will be still ^{65}Zn and ^{54}Mn (if any ^{54}Mn at all), but the experience shows in a few days the emitted radiation is at background levels.

§ 2. pVT method

2.1. Main principles

The gas hydrate formation or decomposition can be observed *in situ* either by diffraction or by continuous pressure recording during the reaction. The first method (already discussed in the previous

paragraph) is very accurate in terms of statistical precision, temporal resolution etc but is too expensive. Usually the beam time at the diffraction facilities as this in Grenoble, for instance, is very much limited and requires traveling together with the experimental setup, which the reader will probably agree, is quite heavy and voluminous. So, it is necessary to find a way to do experiments in the lab, and this way is exactly the implementation of pVT rigs.

Let us make one imaginary experiment. Suppose an isolated thermodynamic system at certain temperature T , volume V and pressure p . If the system is really isolated, i.e. there is no gas supply from outside or change in the temperature, the pressure measured by the imaginary pressure gauge of this imaginary system will show the same pressure till the end of the Universe. Now let us put some normal ice in the system and provide such thermodynamic conditions that make sure no kind of reaction whatsoever can run in there. Again the pressure measured by the imaginary pressure gauge will be absolutely stable with time. Now let us make the system enter into the gas hydrate stability field by readjusting p , T or both to some new level. The ice lattice starts to rearrange and to arrest gas molecules thus forming the clathrate structure. These gas molecules will no longer be giving any contribution to the overall pressure in the system. Thus, by reducing the number of free gas molecules, the pressure will start dropping. Then obviously, the pressure drop in the system, being proportional to the number of the gas molecules trapped by the forming new phase, will be relative to the amount of hydrate formed. It has already become clear that just by recording the pressure drop in the system with time then transforming it into pressure accumulated in the hydrate phase and finally normalizing the whole reaction data set to the final amount of hydrate in the sample, one will get the hydrate fraction change with time.

This is in fact exactly how our lab pVT rigs work. The later normalization is done in a way that after stopping the reaction and recovering the sample, the specimen is measured on the X-ray powder diffractometer in the lab. The diffraction data, as always, are analyzed with GSAS (see Appendix V).

Up to now everything seems clear and straightforward but there is one problem and it is that one can never achieve perfectly isolated system. Especially this is true when measuring very low pressures, which is exactly my case in this work. Actually the diurnal temperature cycle made me think of a number of improvements of the pVT rig I used. The evolution of the setup helped but did not cure the problem completely. This will be discussed in the following subsection. In any case, at the end the setup became so good that the temperature fluctuations were negligible in most of the cases except during high summer when the air-conditioner was unable to cope with the heat. For this reason the High-Summer Correction (HSC) was invented. In reality the measured reaction sometimes comes out quite wavy, as one can see schematically on **Fig.II.8**. But this profile appears to be a superposition of the pure reaction + pressure fluctuations due to the temperature changes. In order to get the pure reaction out of this measured wavy chaos one needs only to subtract the background of the pressure fluctuations. Unfortunately, the real temperature-pressure changes do not show such nice regular

behavior as the ones on the figure. It is basically impossible to simulate them with any reasonable function. The way out of the mess is to generate the background using a record of the temperature during the reaction, and applying the Charles's law, to simulate the pressure variations. For a reference pressure the one at the beginning of the reaction is to be taken. Obviously, to simulate the background this way an assumption that it has been produced in a system exactly as the one used but in which no reaction takes place and the pressure change is only due to the temperature variations is needed. Sometimes due to the imperfection of the thermodynamic boundary conditions, this treatment may result in an over- or under correction. To avoid this, a fetch factor can be introduced to enhance or suppress the pressure/temperature fluctuations (W. F. Kuhs private communication). Finally one can say that the combination between the improved system and the HSC gives really good data at the end.

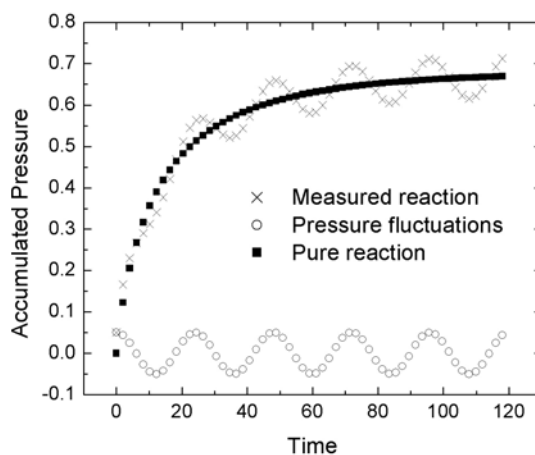


Fig.II.8 Schematic of how the HSC correction works.

2.2. Experimental setups

First this is the place to mention that for the experiments on CO₂ hydrate formation and decomposition above 2 bar the setup of Staykova (2004) was used. For the low-pressure neutron and in-house experiments, purpose built hardware was employed and it was generally the same for both cases. Here only the low-pressure setup will be discussed, since information on the high-pressure one can be found in Staykova (2004). The main difference between the neutron and the in-house setups was the sample stick (**Appendix II** Sheet 5), which was quite long in order to be able to place the sample in the orange cryostat at D20 at the level of the beam. Initially the idea was to make the setup absolutely identical using the same sample stick in the lab and at the neutron facility. The low-temperature baths used in the lab are relatively shallow and one could not expect to succeed to fit the whole stick into the cooling tank. There was only place to submerge the cell. That meant the whole stick was supposed to stay outside the coolant exposed to all possible temperature effects from the environment. The first trials, of course, confirmed this suspicion by recording nothing but the temperature diurnal variations. This suggested a reduction of the active volume and placing as much of it as possible in the coolant. The result, I will later on refer to this setup as to Evolution 1 (E1), can be seen in **Appendix II** Sheet 7. All the volume below the pressure gauge there is submerged. This put the pVT system light years closer to what was needed and already reactions could be observed without any problem. Of course the problems did not end here. The CO₂ gas cylinder is stored at room temperature next to the pVT rig. That means when one wants to introduce the gas into the system,

where the ice is placed in order to start the hydrate formation, this gas will be at room temperature while the ice is at the temperature of the reaction (220 K for instance). Would this affect the reaction? Actually E2 showed a dramatic change in the hydrate formation behavior. But this will be discussed in the experimental chapter. Now, what was E2? It can be subdivided into E2a and E2b. E2a was when in the system a high-precision dosing valve Pfeiffer EVN 116 was introduced. It allowed extremely slow inflow of gas in the beginning of the reaction. Thus the gas would have all the time necessary to cool down to the targeted temperature before the start of the reaction. Firstly, if one has a look again at **Appendix II** Sheet 7 will realize that the surface available for the heat exchange and cooling the gas is not very large. The diameter of the tube above the sample cell is 12 mm. That means the starting ice will provide the main contribution to the cooling surface. Secondly, even if one decides to compensate this effect by lowering the gas flux into the system (easily possible with the dosing valve), he will enter into another trouble. It is that applying pressure from vacuum conditions at some stage one will reach the ice-to-hydrate phase transition boundary. But the required reaction pressure is well beyond this boundary. Until it is reached the system will be at conditions of hydrate formation and if it takes too long the initial part of the reaction will not be recorded on one hand, and on the other hand the formation will proceed at undefined conditions. To reduce these risks one needs to accelerate the gas filling. This is already a real vicious circle. To get out of it I came up with E2b, which was to fill this 12 mm of diameter tube mentioned above with 1 mm in diameter bare-balls up to the top. Once they are cooled well the gas is introduced at low rate and cools down wandering between the bare-balls. Their existence already allows for much faster filling of the system with gas.

A thermocouple was installed in the gas volume, next to the pressure gauge from Sheet 7 in **Appendix II** to read the gas temperature during the reaction. This temperature was used if needed for the HSC.

Thus the system reached quite reasonable thermodynamic quality at relatively low price. The next evolutionary step will be just to try to cool down the incoming gas more effectively either by cooling the whole gas supply system including the gas cylinder or by introducing a small receiver submerged in the cooling tank.

Now let us have a brief look at the technical specification of the used hardware (**Fig.II.9**). The low temperature bath is NESLAB ULT-80 with temperature range between 193 K to 283 K and temperature stability $\pm 0.03^\circ$. The vacuum was produced by a vacuum pump Pfeiffer DUO 5, with capacity of 5 m³/h and max vacuum 10^{-3} mbar read with Pfeiffer Compact Pirani Gauge TPR 265. Its measurement range is 5×10^{-4} - 1000 mbar with accuracy of $\approx 10\%$ of the reading in the range of 10^{-3} - 100 mbar (outside of this range up to factor 2). The reaction pressure was followed by Pfeiffer Compact Piezo Gauge APR 262. Its measurement range is 0.2 - 2200 mbar with accuracy of 2 % F.S. both gauges were connected to a Pfeiffer Dual-Channel Measurement and Control Unit for Compact Gauges TPG 262. An EXTECH 421508 thermometer with a K-type thermocouple read the

temperature in the system. Both the thermometer and the TPG 262 have RS 232 serial interface. Through it the data were transferred to a PC using Windmill 5 with COMIML commercial software. At the experiments above 2 bars the pressure was followed with 10 bar piezoelectric pressure sensor ASHCROFT Type KXD.

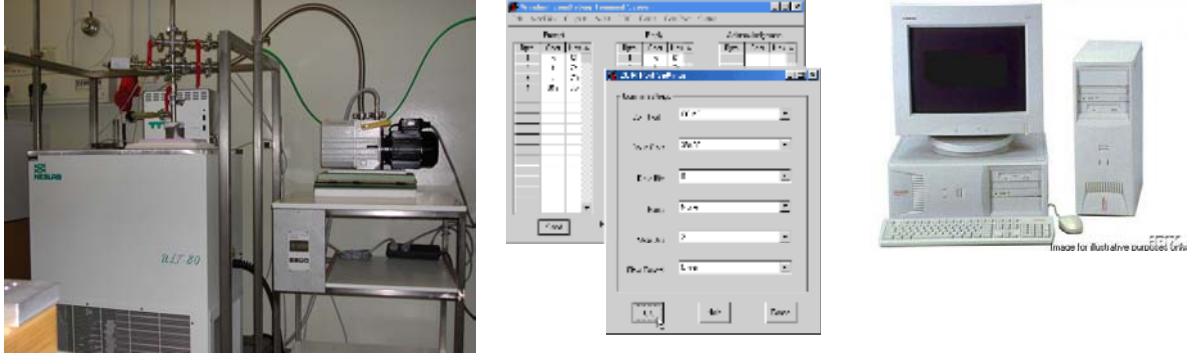


Fig.II.9 The pressure changes in the system were transferred and stored on the PC using Windmill 5

§ 3. Field Emission Scanning Electron Microscopy (FE-SEM)

3.1. Electron – basic physical properties

In the year 1897, Joseph John Thomson proclaimed that cathode rays were negatively charged particles, which he called “corpuscles”. He claimed that these corpuscles were the things from which atoms were built up. This was much beyond what he had actually discovered. Even British scientists did not generally accept Thomson’s corpuscle hypothesis, until he spoke of it again in 1899. By this time, the Irish physicist George Francis Fitzgerald had suggested that Thomson’s “corpuscles” making up the cathode ray were actually free electrons.

Let us summarize here the main electron properties. Its mass is $m_e = 9.1 \times 10^{-31}$ kg = 0.511 MeV, which is about three orders of magnitude less than those of the proton and the neutron. Its electric charge and magnetic momentum are $e = 1.6 \times 10^{-19}$ C and $\mu = 1.00116 \mu_B$, respectively. The electrons, having a spin $s = \frac{1}{2}$, obey the statistics of Fermi – Dirac and follow the principle of Pauli as in the case of protons and neutrons. The electron’s classical radius is $r_e = 2.8 \times 10^{-15}$ m. In the classical electrodynamics the electron is considered as a particle whose motion is described by the equations of Lorenz-Maxwell. In 1927 its wave properties were proven. Its spin is of major importance for the motion of the electron in the atom. Taking this into account gives the opportunity to explain the periodic system of the elements as well as the chemical bonds. The motion of the electron cannot be described within the frames of the classical mechanics. It obeys the equations of Shrodinger and Dirac for the non-relativistic and the relativistic cases, correspondingly. The Dirac equation is *de facto* a system of four equations in three spatial and one temporal dimension:

$$\sum_{i=0}^3 \gamma_i \frac{\partial \psi(x)}{\partial x_i} + i \frac{mc}{\hbar} \psi(x) = 0 \quad (\text{II.31})$$

Here m is the mass of the particle and γ_i are the matrices of Dirac, which are expressed with the matrices of Pauli $\sigma_1, \sigma_2, \sigma_3$ and the unit matrix I :

$$\gamma_0 = \begin{pmatrix} 1 & 0 \\ 0 & -1 \end{pmatrix}, \quad \gamma_i = \begin{pmatrix} 0 & \sigma_i \\ -\sigma_i & 0 \end{pmatrix}, \quad i = 1 - 3 \quad (\text{II.32})$$

$$I = \begin{pmatrix} 1 & 0 \\ 0 & 1 \end{pmatrix}, \quad \sigma_1 = \begin{pmatrix} 0 & 1 \\ 1 & 0 \end{pmatrix}, \quad \sigma_2 = \begin{pmatrix} 0 & -i \\ i & 0 \end{pmatrix}, \quad \sigma_3 = \begin{pmatrix} 1 & 0 \\ 0 & -1 \end{pmatrix} \quad (\text{II.33})$$

The most significant result from this equation is the obtained relation between the energy, momentum and mass of the free particle (in this case the electron):

$$E_e^2 = m_e^2 c^4 + p^2 c^2 \Rightarrow E = \pm \sqrt{m_e^2 c^4 + p^2 c^2} \quad (\text{II.34})$$

This result suggests the electron can have either positive or negative energy. A forbidden energy interval separates both energetic regions. The negative energy values correspond to the bound states.

3.2. Principles of the scanning electron microscopy

The scanning electron microscopy (SEM) is used for observing bulk samples. It uses an electron beam to probe the specimen. Also since the electrons are charged particles, having magnetic momentum, they can be focused and accelerated in the SEM by means of electrostatic and magnetic fields. When the electron beam reaches the target a number of interactions can take place, thus giving information about the target. The most important processes are schematically shown on **Fig.II.10**.

The electrons, coming from the beam-sample interactions, can be divided into several groups. Rutherford elastic scattering occurs when an incident electron collides with an atom of the sample and deflects without losing energy. The incident electrons reflected backwards by the specimen surface, are called backscattered electrons. Since the scattering angles depend strongly on the atomic numbers of the involved nuclei, the detected backscattered electrons give images with information on the composition of the sample.

When high-energy electrons fly closely by specimen atoms, they can pass on some of their energy to electrons belonging to the outer levels of the atomic shells. As a result secondary electrons are being produced. The amount of energy given to the secondary electrons is so small that only those of them, which are created within a very thin surface layer (less than 10 nm thick), are able to escape from the sample. The detection of these secondary electrons provides high-resolution topographic images.

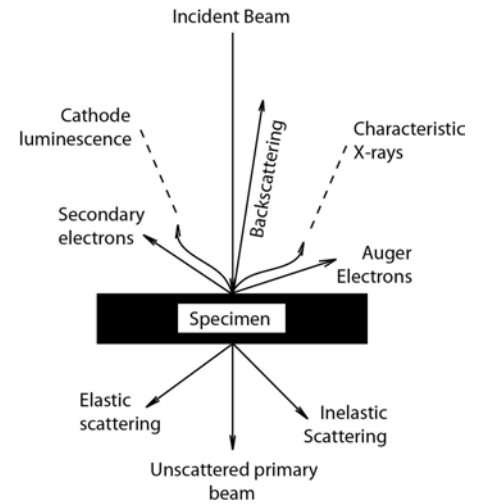


Fig.II.10. Schematic of the interactions between the incident electron beam and the target sample.

When a secondary electron leaves the inner atomic shell a vacancy is produced. A second atomic electron from a higher shell fills it. Some energy must be simultaneously released. A third electron (Auger electron) escapes carrying the excess energy in a radiationless process. The process of excited ion decaying into a doubly charged ion by ejection of an electron is called Auger process. Alternatively, an X-ray photon removes the energy. For low atomic number elements, the most probable transitions occur when a K-level electron is ejected by the primary beam, L-level electron drops into the vacancy, and another L-level electron is ejected. Higher atomic number elements have LMM and MNN transitions that are more probable than KLL. Each auger electron has a characteristic energy, corresponding to the element from which it is emitted and brings information about the specimen composition. The characteristic X-ray radiation corresponds to the electronic transitions involved in the energy release. Since these lines are specific for a given element, the composition of the material can be deduced. This can be used to provide information about the elements present at a given point of the sample, the so-called Energy-dispersive X-ray (EDX) analysis, or alternatively to map the amount of a particular element as a function of the position.

The cathode luminescence (CL) or emission of ultraviolet, visible or infrared radiation is caused by electron bombardment of semiconductors and mineral samples. In combination with the electron-beam-induced-current (EBIC) in semiconductors, CL is used to image lattice defects. This is possible because of the recombination of charge carriers at the lattice defects.

Unscattered primary beam electrons are incident electrons, which fly through the thin specimen without any interaction. Incident electrons, which deflect from their initial path as a result of elastic scattering without energy loss, are elastically scattered electrons. On the contrary, the inelastically scattered electrons are those incident electrons, which lose energy in the interactions with the specimen atoms.

The absorption of incident electrons by the sample can charge it.

The backscattered and secondary electrons carry the most important information for the image production. The backscattered electrons provide a good compositional imaging of the sample, while the secondary electrons produce better topographic images.

3.3. LEO 1530 Gemini – one FE-SEM with cryo stage

The *ex-situ* studies of the CO₂ hydrates for this work were done on a high-resolution cryo field-emission scanning electron microscope (FE-SEM) type LEO 1530 Gemini (**Fig.II.11**). It is equipped with a cryo transfer unit (Oxford instruments). Dry N₂-gas, at -190°C coming from a Dewar full of liquid nitrogen, is used to cool the cryo stage. The gas flow and the level of liquid nitrogen in the Dewar control the temperature of the cryo stage, thus permitting to perform SEM measurements at low temperatures.

A schematic of the FE-SEM is shown on **Fig.II.12**. The primary electrons are emitted from ZrO/W (100) type of hot Schottky field-emission cathode (**Fig.II.13**). They are extracted from it and accelerated by the potential differences between the cathode's tip and the first and the second anode, respectively. ZrO coating lowers the minimum energy required by one electron to leave the surface of the tip from 4.5 eV (in a thermionic tungsten emitter) to 2.8 eV (in a ZrO/W emitter). The electrons are extracted by applying voltage of 5 kV to the extractor anode. Selected (100) crystallographic orientation of the tip concentrates the emission within a cone with a semi-apex angle of about 0.1 rad as a result of the dependence of the potential barrier on the surface orientation of the tip. A second anode accelerates the emitted electrons. The brightness of the field-emission gun is 5×10^8 A/cm²sr that is about 100-1000 times higher than the one of the conventional thermionic gun (10^5 - 10^6 A/cm²sr). The size of the crossover (10-20 nm) (the smallest beam cross-section) of the ZrO/W Schottky type gun is 1000 times smaller than the one of the tungsten thermionic gun (20-50 μ m). A negative biased suppressor electrode, which helps the dispersed electrons with kinetic energies lower than the one of the extracted electrons take the right direction, surrounds the field emission cathode. In order to avoid the destruction of the cathode tip by ion bombardment from the residual gas, ultrahigh vacuum of 10^{-9} mbar (UHV) is created. The vacuum is also necessary to provide free travel of the electron beam from the gun along the column to the target. Also vacuum conditions are necessary for the registration of the secondary electrons. Any foreign atoms along their paths can easily alter their energy, possibly skewing the results. The electrons, coming from the Schottky cathode, are pulled towards the sample surface by the potentials V_0 and V_B and focused on it by the GEMINI column lens system. The beam booster maintains the high beam energy throughout the whole optical column. An electromagnetic multi-hole beam aperture changer is incorporated close to the electron source. This is used to select the optimum beam aperture angle and to tune the probe current in conjunction with the magnetic field lens. The electron beam scans the sample in a mesh controlled by the scan coils. It has a transverse chromatic aberration (enlargement of the focal spot), caused by spreading of electron energy when the beam is redirected by the deflection system. This effect can decrease the resolution of the outer areas of the image. LEO 1530 is equipped with Gemini lenses (magnetic and electrostatic, **Fig.II.12**), specially designed to reduce the chromatic aberration. They are made as an analog of the optic achromatic lenses, consisting of two component lenses, one convergent and the



Fig.II.11 LEO 1530 with cryo stage used for the present studies. Photo by K.Techmer.

other one divergent. The working distance is defined as a distance between the electrostatic lenses and the specimen. With increasing the distance the observed surface area increases together with the spherical aberration, resulting in a blurred and strongly distorted image. With decreasing the working distance the spherical aberration decreases. An optimum distance from the sample, providing optimal observed area and low spherical aberration, has to be found. If the specimen is closer to the front lenses then higher magnification of the observed object can be achieved.

The FE-SEM images are obtained by the secondary electrons. The scintillator – photo-multiplier combination known as a standard Everhart-Thornley detector, detects them. The secondary electrons are collected by a grid at +350V and accelerated to the scintillator. This light produced by the interaction of the secondary electrons with the scintillator enters the photo-multiplier. The current coming out of the photo-multiplier depends on the number of secondary electrons hitting the scintillator. By measuring this current a point of a relevant

gray-scale value is displayed on the graphic container control (GCC – Picture box) of the imaging software. The repetition of this procedure for the whole observed area leads to the complete image build-up. After the scan is finished and the save command is executed the content of the Picture box is saved in a file on the hard disk. Just to cut the long story to a short, I will define the magnification in the SEM as the ratio of the GCC area to the scanned area. Therefore, an increase of the magnification is achieved by scanning over a smaller area. Since the size of the GCC depends on the screen size, the larger the screen is the better. In the old machines, the magnification was the ratio of the effective CRT (cathode-ray-tube) area to the scanned area.

The tiny electron beam and the Gemini lenses permit the images obtained at low accelerating voltage to be with high resolution and good contrast. The improved contrast makes a better gray scale differentiation of the topology of the surface and more details are distinguished. A slow sublimation of the sample surface takes place when the sample stays in the vacuum more than half an hour. A quick sublimation within a defined area of some samples can be obtained with increasing the beam accelerating voltage up to 2.5-3 kV, thus giving clues about the structure development in depth.

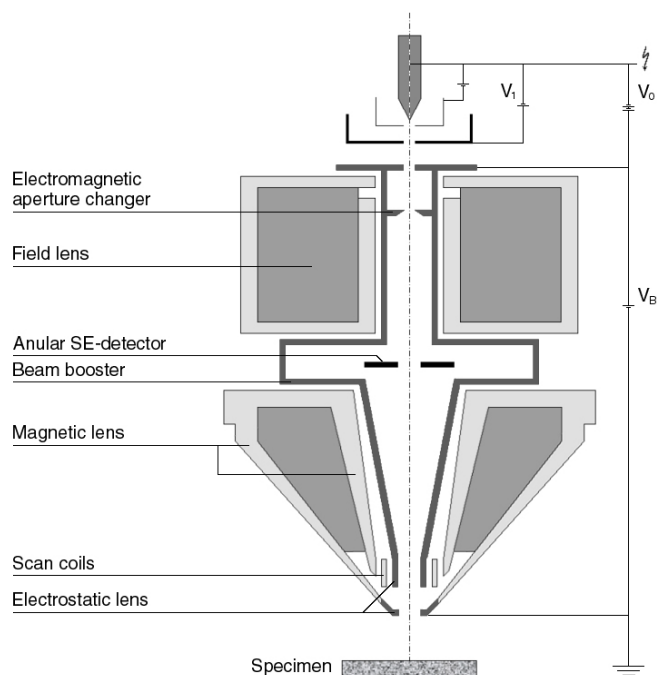


Fig.II.12 Schematic of the optics of LEO 1530 Gemini. The potentials V_1 , V_0 and V_B note the extractor voltage, the accelerator voltage and the booster voltage, respectively. Original by Till Heinrichs. Digitally remastered Georgi Genov.

The surface charging is another effect, which may appear during the scanning. It depends on the sample and scanning resolution (speed). The faster the scanning is, the lower the charging becomes. The sharp edges on the sample surface can also lead to charging.

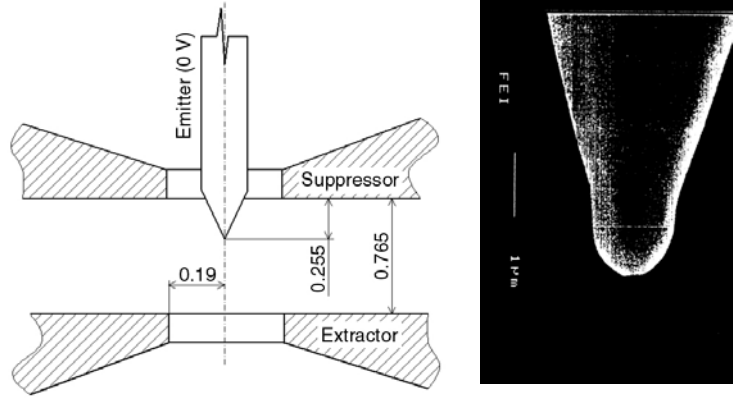


Fig.II.13 Cutaway view of the Schottky gun (left) with an SEM picture of the emitter tip (right). Originals by Till Heinrichs. Digitally remastered Georgi Genov.

§ 4. BET method

Later, when the story comes to the point of the microscopic observations of the CO₂ hydrate, the question of the degree of connectivity of the hydrate foam will arise (see Chapter IV). One very powerful method can be used in the attempts to find the answer – the BET method (surface adsorption). Actually, we started to work on this problem in the methane hydrate case together with Andreas Zeller in 2002. Later on he continued working alone, since this was his master thesis topic. Separate measurements for the CO₂ hydrate case have not been done, but for reasons discussed in Chapter IV, one parallel or extrapolation from the CH₄ to the CO₂ case is justified. Moreover this method was used for estimating the specific surface area of the starting material for the kinetic experiments.

Let the surface of the substrate be an array with N_s identical adsorption sites. No more than one atom can occupy one site and the atoms do not interact between each other. In the grand canonical ensemble, each site's grand partition function is:

$$\Xi_s = 1 + z \exp(\beta(\mu - E_0)) \quad (\text{II.35})$$

E_0 is the surface binding energy; z is the partition function associated with possible internal degrees of freedom at every site (sometimes may be taken as unity); $\beta = 1/k_B T$ is the inversed temperature and μ is the chemical potential of the film. The grand canonical free energy is:

$$\Omega = -\frac{1}{\beta} \ln \Xi = -\frac{N_s}{\beta} \ln \Xi_s \quad (\text{II.36})$$

Since the mean number of particles in the ensemble satisfies:

$$N = -\left(\frac{\partial \Omega}{\partial \mu} \right)_\beta \quad (\text{II.37})$$

the fractional occupation is:

$$\theta = N / N_s = p / (p + p_L) \quad (\text{II.38})$$

The characteristic scale of pressure is:

$$p_L = \frac{g}{z\beta\lambda^3} \exp(\beta E_0) \quad (\text{II.39})$$

Here $\lambda = \sqrt{2\pi\beta\hbar^2/m}$ is the de Broglie thermal wavelength and g is the spin degeneracy of the atom. (II.38) is the Langmuir isotherm. It shows the coverage grows linearly at low p according to Henry's law and saturates at $p \gg p_L$.

Brunauer, Emmett & Teller (1938) (BET) extended this lattice gas model to the case of multi-layer films. Their model allows the particles to occupy a 3D array of sites above the surface. The interactions between the sites are neglected, but the sites closest to the substrate experience additional attraction V_I . The relative probability, exactly N sites above a given surface to be occupied, is proportional to the corresponding term in the grand partition function for this site:

$$\Xi_s = 1 + c \sum_{N=1}^{\infty} z^N \exp(N\beta\mu) \quad (\text{II.40})$$

Here $c = \exp(-\beta V_I)$ and z is the internal partition function per site of the bulk adsorbate. Thus, analogously to the Langmuir isotherm one obtains the BET isotherm:

$$\frac{p}{p_L} \frac{N_s}{\left(1 - \frac{p}{p_L}\right)^N} = \frac{1 + \frac{p}{p_L}(c-1)}{c} \quad (\text{II.41})$$

On the basis of this isotherm, measuring the number of gas molecules adsorbed in the first layer cladding the substrate one can calculate its specific surface area (e.g. Legagneux et al. 2002, Zeller 2004).

The first SSA measurements were performed on the BET machine at LGGE, Grenoble, France, with the group of Florent Dominé. Later on a decision was made to build such machine in our lab in Goettingen in a *consilium* with the group of Dr. Dominé using the French apparatus as a prototype, trying to improve its thermodynamic performance and construction. Zeller (2004) gave a very detailed description of the machine and the experimental procedures.

Chapter III

Modeling approaches

As already mentioned in the beginning (see Chapter I), the processes of gas hydrate formation and decomposition are not well understood. There are two ways to study the problem: 1) molecular dynamics simulations and 2) experimental, and two ways to describe it: 1) phenomenological and 2) theoretical. Unfortunately, up to now, none of them has given the ultimate answers. With a lot of hard work, at some point, both approaches will get closer to each other and finally will merge into a solid theory but this moment is still far in the future. The problem of all previous modelling approaches (phenomenological), briefly mentioned in Chapter I, was firstly - the stand-alone diffusion theory could not describe the initial part of fast transformation and secondly - it was difficult to take account of the shape of the starting material. The latter, for sure also affects the appearance of the diffusion law used for fitting the diffusion controlled part of the reaction. Since the present work is also phenomenological the modelling approaches considered here are also phenomenological.

§ 1. Multistage Model of Gas Hydrate Growth from Ice Powder

1.1 The model

The Multistage Model of Gas Hydrate Growth from Ice Powder (Salamatin & Kuhs 2002) came to fill the gaps, mentioned a few lines earlier, including a description of the initial part. For this purpose, a precise parameterisation of the sample geometry and its evolution with time during the formation is of major importance for the kinetic data interpretation. Even in case of well-defined powders, prepared as a random dense packing of spherical ice particles, the samples are characterized by their size distribution function, typically a lognormal one (Kuhs & Salamatin 2003). A monosize approximation (Salamatin & Kuhs 2002; Staykova et al. (2003)) of the system is applicable only for modelling the starting phase of the process, until the spatial interaction of the hydrate shells growing on the ice spheres becomes a main factor controlling the gas flux towards the ice cores and the formation reaction itself. The theory of the hydrate formation kinetics in long-term experiments has been developed in (Kuhs & Salamatin 2003, Staykova et al. 2003). They distinguish the initial stage (I) of hydrate film spreading over the ice surface and the two subsequent stages, which are limited (II) by the rate of hydrate formation at the ice-hydrate interface and (III) by the gas and water transport (diffusion) through the hydrate shells, surrounding the shrinking ice cores. The second stage is introduced to account for the porous hydrate microstructure, since the pores are considered as pathways for the gas and the water molecules to go to and fro the ice surface covered by the growing

hydrate phase. This means the pores are assumed as tubes or hollows connected in a way that forms tunnels.

The principal concepts of Arzt's monodisperse model (1982) are generalized for the case of the polydisperse structure of growing contacting spheres with special focus on sample consolidation during the porous hydrate layer growth and its expansion beyond the initial ice-grain boundaries into the sample voids. However, in all available experimental runs (e.g. Staykova et al. 2003) with different gases and at different thermodynamic conditions, the model systematically underestimates the rates of the hydrate formation in the very beginning of the initial stage I. Scanning Electron Microscope (SEM) observations of ice powders during the first hours of hydrate formation show that the process of the ice-grain coating is divided in two sub-stages: (a) fast hydrate formation in the cracks of the ice grains and (b) subsequent spreading of the initial hydrate film across the ice-sphere surface (Genov et al. 2004).

A log-normally distributed starting material (ice powder) is assumed:

$$\varphi_0(r_0) = \frac{1}{r_0 \sigma_a \sqrt{2\pi}} \exp\left[-\frac{(\ln r_0 - a)^2}{2\sigma_a^2}\right], \quad (\text{III.1})$$

where r_0 is the initial ice particle radius, and a and σ_a^2 the mathematical expectation and variance of the random value $\ln r_0$, respectively.

Actually in the experiments, one deals with a truncated form of the above distribution, which is non-zero only within a certain finite interval of $\ln r_0$. A 2.5%-accuracy limit of $\ln r_0$ -variation for the lognormal law (III.1) is fixed within the range $a \pm 2.25\sigma_a$. This means that the initial grain-size distribution function is taken as

$$f_0(r_0) = \begin{cases} 1.025\varphi_0(r_0), & r_0 \in [r_{\min}, r_{\max}]; \\ 0, & r_0 \notin [r_{\min}, r_{\max}]. \end{cases}$$

$$r_{\min} = \exp(a - 2.25\sigma_a), \quad r_{\max} = \exp(a + 2.25\sigma_a) \quad (\text{III.2})$$

During the gas hydrate formation, ice spheres of initial radius r_0 transform to ice cores of radius r_i covered by the growing hydrate layers, which are modelled as spherical shells of external radius r_h truncated at the inter-grain contact areas (see **Fig.III. 1**). It should be noted that each ice particle in a polydisperse powder at random dense packing has a specific relative environment of surrounding grains and the initial particle size does not determine uniquely the process of its conversion to hydrate. Consequently, the interaction of a reference ice sphere in the powder with neighbouring spheres can be described only on average. In this context, the above-introduced radii r_i and r_h should be understood as the mean (conditionally averaged) characteristics of all ice-hydrate particles which develop from initial ice grains of the same radius r_0 . The most important consequence of this approach is that the number of ice-hydrate particles in each initial size fraction remains constant

and the statistical ensemble of particles in the sample at any moment t can be represented by the ice-core size distribution function

$$f(r_i, t) = f_0(r_0) \left[\frac{dr_i(t)}{dr_0} \right]^{-1}, \quad r_i > 0. \quad (\text{III.3})$$

Equation (III.3) is the principal ice-particle conservation relation, which describes the evolution of the sample in case of $dr_i/dr_0 > 0$. In general, $f(r_i, t)$ obeys the population balance equation

$$\frac{\partial f}{\partial t} + \frac{\partial}{\partial r_i} \left(\frac{dr_i}{dt} f \right) = 0.$$

In accordance with the recent observations, ice spheres in the starting material may have cracks (see **Fig.III. 2**) most probably caused by thermal strains which arise during ice powder preparation by means of water droplets freezing in liquid nitrogen (Staykova et al. 2003). Correspondingly, let us designate the total crack void fraction of ice grains in a sample as ε_f and the fissure-volume filling degree in ice spheres of initial radius r_0 as χ . Hereinafter ε_f is considered as a small parameter.

By definition, the total number fraction of ice grains, which currently are not completely converted to hydrate, is given by

$$n = \int f(r_i, t) dr_i \quad (\text{III.4})$$

where the ensemble averaged value $\langle \psi \rangle$ of any characteristic $\psi(r_0, t)$, is determined as

$$\langle \psi \rangle = \int \psi(r_0, t) f_0(r_0) dr_0 \quad (\text{III.5})$$

Accordingly, the initial and current mean-volume radii (\bar{r}_0 and \bar{r}_i) of ice cores, average filling degree of their fissures $\bar{\chi}$, and the total reaction degree α are

$$\bar{r}_0 = \langle r_0^3 \rangle^{1/3}, \quad \bar{r}_i = \langle r_i^3 \rangle^{1/3}, \quad \bar{\chi} = \langle r_0^3 \chi \rangle / \bar{r}_0^3, \quad (\text{III.6})$$

$$\alpha = \frac{1}{1 - \varepsilon_f} \left[\left(1 - \frac{\bar{r}_i^3}{\bar{r}_0^3} \right) \left(1 - \varepsilon_f \frac{1 + E}{E} \right) + \bar{\chi} \frac{\varepsilon_f}{E} \right]$$

Here the hydrate-phase expansion coefficient E is the proportion of the hydrate volume excess with respect to the consumed ice volume (Salamatin & Kuhs 2003, Staykova et al. 2003),

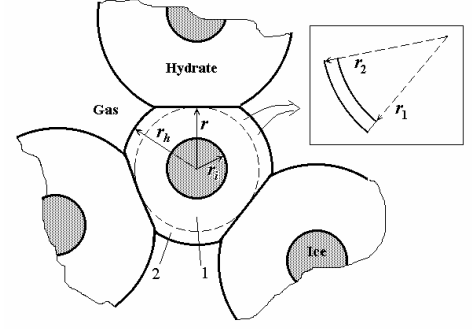


Fig.III.1. Hydrate shell growth around a reference shrinking ice core (Staykova et al. 2003).

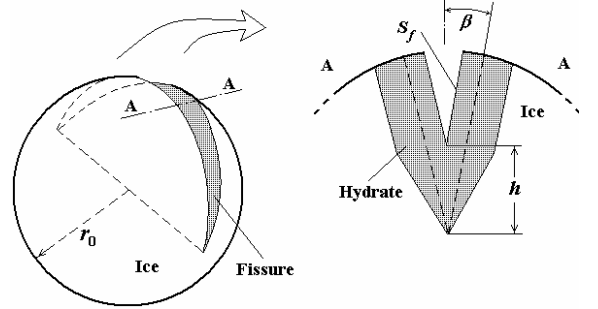


Fig.III.2. Hydrate formation in ice-grain fissure and its A-A profile (Salamatin & Kuhs 2003).

$$E = \frac{\rho_i}{\rho_{hw}(1 - \varepsilon_h)} - 1 ,$$

expressed via the mole density of ice ρ_i , the mole density of water ρ_{hw} in hydrate and meso-porosity ε_h of the clathrate phase.

Finally, the general problem of modelling the gas-hydrate formation from polydisperse powders of randomly packed ice spheres is reduced to mathematical description of the evolution of a single reference grain with a given crack volume fraction (characterized by parameters r_i and χ) plunged into the powder medium with conditionally averaged properties of surrounding ice-hydrate particles.

The formation of the hydrate layer on the spherical surface of a reference ice particle in polydispersed powder has been described in (Kuhs & Salamatin 2003). The conventional assumption of the self-consistent field theory in the statistical physics and mechanics is that the conditionally averaged properties of the system around the reference particle are identical to the corresponding ensemble means. In this framework, as a starting point, one has to consider an ice grain of radius r_0 in the monodisperse powder with random dense packing of ice spheres of the average radius \bar{r}_0 , as shown in **Fig.III.3**. The ice-mass balance equation governing the reduction of the ice core radius r_i due to the hydrate layer growth is written as (Salamatin & Kuhs 2002):

$$\frac{dr_i}{dt} = -\delta_0 \omega_s e^{-\omega_s t} - \frac{\omega_v}{\rho_i} (1 - e^{-\omega_s t}) . \quad (\text{III.7})$$

Here, δ_0 is the thickness of the ice layer converted into initial hydrate film spreading across the ice-grain surface; ω_s and ω_v denote the rates of the surface coating and the ice-to-hydrate transformation, respectively. The former quantity can be defined as the fraction of the ice surface exposed to the ambient gas, which becomes covered by the initial hydrate film during a unit time period, while the latter one is the number of ice moles transformed to hydrate phase per unit of time on a unit area of spherical ice surface after its coating. Depending on the rate-limiting step (stage) of the hydrate formation process, ω_v describes either the rate of the formation reaction (ω_R) or the rate of the gas and water mass transfer (ω_D) through the hydrate shell. Parameter δ_0 is small compared to the initial grain size r_0 , but the formation rate (coating rate) due to the hydrate film formation $\rho_i \delta_0 \omega_s$ is assumed to be much higher than ω_v on the hydrate-coated surface, and the ice-core surface area remains practically constant during the initial stage I.

The driving force of the hydrate formation is the super-saturation of the gas-ice-hydrate system, $\ln(f/f_d)$, expressed via the fugacities f and f_d of the gaseous phase at the imposed and decomposition pressures (p and p_d respectively) at a given temperature T . For each stage, this force determines the formation kinetics and is distributed among different steps of the ice-to-hydrate conversion in proportion to their apparent resistances; namely, k_s^{-1} for the initial hydrate film

spreading over the spherical ice surface, k_R^{-1} and k_D^{-1} for the pure reaction and gas/water diffusion through the hydrate layer, respectively. One can write:

$$\omega_S = k_S \ln \frac{f}{f_d}, \quad \omega_V = \frac{k_R k_D}{k_R + k_D} \ln \frac{f}{f_d}. \quad (\text{III.8}_1)$$

The formation rate constants are assumed to be the Arrhenius-type functions of the temperature:

$$k_J = k_J^* \exp \left[\frac{Q_J}{R_g} \left(\frac{1}{T^*} - \frac{1}{T} \right) \right], \quad J = S, R, D, \quad (\text{III.8}_2)$$

where k_J^* and Q_J are the rate constant at the reference temperature T^* and the activation energy of the J -type step, R_g is the gas constant.

Phenomenological equations (III.7) and (III.8) are considered as a theoretical basis for detailed analysis of the hydrate formation kinetics on ice-grain surface. Actually, each J -th step, explicitly presented in the model may be further divided into a sequence of sub-steps characterised by their own resistances of which sum is k_J^{-1} . Nevertheless, for a fixed temperature k_S and k_R can still be used as tuning parameters. But the sample structure, its permeability, and the permeation rate constant k_D depend on the geometrical characteristics of the hydrate layers growing around shrinking ice cores and must be related to r_i and \bar{r}_i to complete (III.7).

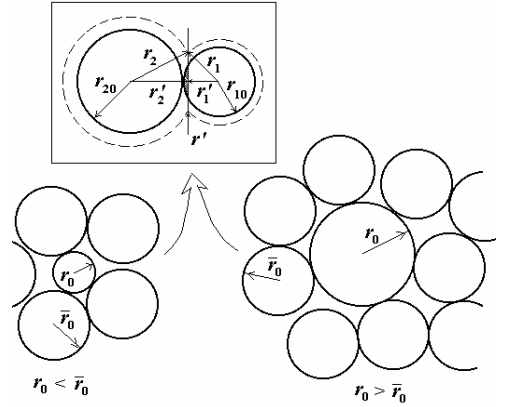


Fig.III.3. Conditionally averaged initial structure of the ice powder around a smaller (left) or larger (right) reference particle. The zoom-in shows the growth geometry of two contacting spheres (Kuks & Salamatov 2003).

Thermal stresses, which occur in freezing water droplets sprayed into liquid nitrogen during the preparation of the ice powder, result in fracturing of some of the ice spheres. The fissures examined in SEM images of the starting material (ice samples), although rather narrow, are open and usually penetrate deep into the powder particles. The observed process of the fast initial hydrate growth in the ice-grain fissure (crack), schematically shown in **Fig.III.2**, is assumed to develop simultaneously with the hydrate film spreading over the spherical surface of the reference grain as an independent counterpart (sub-stage) of the initial stage I (Genov et al. 2004). To calculate the volume filling degree χ in a reference ice grain of initial radius r_0 , one writes analogues of (III.7) and (III.8) for hydrate formation on the crack surface, designating all corresponding characteristics by primes. Thus, for instance, the thickness δ_0' of the ice layer converted to the initial hydrate film spreading over the crack sides is introduced together with the respective rates ω_S' and ω_R' of the crack surface coating and the formation reaction, the latter two being related to the temperature dependent rate constants k'_S and k'_R with activation energies Q'_S and Q'_R . Then, for the mean crack-opening angle β the average

height h of the fissure filling normalised by r_0 can be explicitly expressed (at constant ω_R') versus time t :

$$\xi = h/r_0 = a'(1 - e^{-\omega_s' t}) + b't, \quad h < r_0,$$

$$a' = \frac{E}{\beta r_0} \left(\delta_0' - \frac{\omega_R'}{\rho_i \omega_s'} \right), \quad b' = \frac{E \omega_R'}{\beta \rho_i r_0}, \quad (\text{III.9}_1)$$

until the complete filling is reached at $h = r_0$, i.e. $\xi = 1$.

The area S_f of each crack side exposed to the ambient gas decreases as the hydrate fills the fissure. The volume of hydrate growing in the crack is calculated by integration of the incremental mean hydrate layers with respect to h , which yields the filling degree χ in the following form:

$$\chi = \frac{3}{4} \pi \xi - \frac{3}{2} \xi \arcsin \xi - \frac{3}{2} (1 - \xi^2)^{1/2} + \frac{1}{2} (1 - \xi^2)^{3/2} + 1, \quad \xi < 1, \quad (\text{III.9}_2)$$

and $\chi \equiv 1$ for $\xi > 1$.

Although this relationship is derived for the fissure penetrating to the centre of a reference grain, it has a general structure and after substitution of (III.9₂) can be tuned to any lesser mean initial relative depth of cracks by appropriate correction of a' and b' (e.g. by β).

Hereinafter Kuhs & Salamat (2003) follow the general line of the geometrical description of the powder particle growth developed by Arzt (1982) for a random dense packing of monosize spheres extended by them to a polydisperse powder. In addition, they assume the total crack-void fraction ε_f to be small and neglect a possible minimum influence of fissure openings (grain surface discontinuities) on the spatial (geometric) interaction of hydrate layers growing around ice cores. **Fig.III.1** illustrates that the shape of the hydrate layer formed from the reference ice grain is represented as a truncated sphere of radius r_h . The ice core shrinks due to the inward growth of the hydrate layer. But, because of the lesser density of water in the porous hydrate phase, the excess water molecules must be transported to the outward hydrate surface exposed to the ambient gas, and the hydrate layer simultaneously expands into the macro-pore space of the sample between the original ice grains. To extend Arzt's approach to the polydisperse powder, the above scenario is also assumed for the "average" ice particles surrounding the reference one (see **Fig.III.3**). All of them consist of the inner ice cores of radius \bar{r}_i occluded in the truncated spherical hydrate shells of external radius \bar{r}_h . The existing contact areas between the reference particle and the neighbouring ones increase, and additional contacts form as r_h and \bar{r}_h grow. Obviously, the evolution of a single reference ice grain of initial radius r_0 must be modelled in interaction with the simultaneous ice-to-hydrate conversion in the surrounding "average" monodispersed medium of randomly packed spheres of radius \bar{r}_0 . Correspondingly, the specific surface of original macro-voids S_m and the macro-porosity ε_m of the sample decrease.

In a random dense packing without particle rearrangement, the current number of contacts (coordination number) Z per a reference grain plunged into the monodisperse powder of average

particles can be expressed after Arzt (1982) as a linear function of the respective hydrate shell radii r_h and \bar{r}_h :

$$Z = Z_0 + C \left(\frac{r_h - r_0 + \bar{r}_h - \bar{r}_0}{2\bar{r}_0} \right). \quad (\text{III.10})$$

Here Z_0 is the initial coordination number of the reference ice grain, and $C \sim 15.5$ is the slope of the random density function in the average monosize particle structure. It is well predictable that in a polydispersed system Z_0 monotonically increases with the relative size of the particle, and a plausible parametric approximation can be written as

$$Z_0 = Z_{\min} + (\bar{Z}_0 - Z_{\min}) (r_0 / \bar{r}_0)^\gamma, \quad (\text{III.11})$$

where $\bar{Z}_0 \sim 7$ is the coordination number in the random dense packing of monosize spheres, exponent $\gamma \sim 1-2$ and minimum coordination number $Z_{\min} \sim 2-3$ are the approximation parameters

The principal geometric characteristic of the sample structure which determines the interaction of the reference particle with the surrounding medium is the fraction s of the free surface area of the hydrate shell (in units of $4\pi r_h^2$) exposed to the ambient gas. In the polydisperse powder this quantity is related to development of a contact area between two growing spheres (reference and average ones) of different external radii r_h and \bar{r}_h . The generalised analogue of Arzt's expression (1982) extended to polydisperse systems is

$$s = 1 - \frac{\lambda_0 Z_0}{2r_h} (r_h - r_0 + \bar{r}_h - \bar{r}_0) - \frac{\lambda_0 C}{8r_0 r_h} (r_h - r_0 + \bar{r}_h - \bar{r}_0)^2, \quad (\text{III.12})$$

where $\lambda_0 = \bar{r}_0 / (r_0 + \bar{r}_0)$.

The hydrate layer of the reference particle can grow only on the surface area of $4\pi s r_h^2$ due to the increase in the hydrate volume with respect to the consumed ice volume. The latter proportion is described (Staykova et al. 2003) by the expansion coefficient E determined in (III.6). The initial hydrate film thickness can be simultaneously calculated as $d_0 = \delta_0(1 + E)$.

The mass balance of water molecules directly relates the rate of the ice core radius decrease to the rate of the external hydrate radius increase

$$\frac{dr_h}{dt} = - \frac{E r_i^2}{s r_h^2} \frac{dr_i}{dt}. \quad (\text{III.13})$$

Correspondingly, for the average grain ($r_0 = \bar{r}_0$, $r_h = \bar{r}_h$) from (III.12)-(III.13) comes

$$\frac{d\bar{r}_h}{dt} = - \frac{E \bar{r}_i^2}{s \bar{r}_h^2} \frac{d\bar{r}_i}{dt}, \quad (\text{III.14})$$

where the mean free surface fraction \bar{s} is

$$\bar{s} = 1 - \frac{\bar{Z}_0}{2\bar{r}_h} (\bar{r}_h - \bar{r}_0) - \frac{C}{4\bar{r}_0 \bar{r}_h} (\bar{r}_h - \bar{r}_0)^2.$$

(III.10)-(III.14) determine all important geometrical characteristics of the polydisperse ice powder which are necessary to close the problem (III.7)-(III.9) of the conversion of a single ice grain to hydrate in the powder medium and to model the evolution of the ice core size distribution function (III.3) as well as other mean ensemble characteristics given by (III.4) and (III.5).

First, one has to evaluate the permeation rate constant k_D in (III.8). In accordance with (Staykova et al. 2003; Kuhs & Salamatin, 2003), for a given reference particle they introduce the distance r from the ice core centre to an average contact plane (see **Fig.III.1**) which is calculated in Appendix C

$$r = r_h \left[1 - \frac{2(1-s)}{Z} \right]. \quad (\text{III.15})$$

The spherical boundary of radius r divides the hydrate shell into two sub-layers 1 and 2: from r_i to r and from r to r_h , respectively. The permeation (diffusion) resistance of the spherical sub-layer 1 is known from the diffusion theory (Crank 1975). To estimate the resistance of the truncated sub-layer 2, they assume that locally the mass transfer process in it is similar to diffusion through a concave spherical layer of the same thickness with the same total areas of bounding surfaces (see the insert in **Fig.III.1**). Finally they arrive at the following expression for the permeation rate constant in (III.8):

$$k_D = \frac{\rho_i D}{r_i} \frac{\sqrt{s} r_h r}{\sqrt{s} r_h (r - r_i) + r_i (r_h - r)}, \quad (\text{III.16})$$

where D is the apparent gas/water mass transfer (permeation) coefficient (e.g. see Salamatin et al. 1998). The temperature dependence of the latter characteristic follows (8₂) with k_D^* corresponding to D^* at the reference temperature T^* in (III.16).

The initial macro-porosity of the ice sample ε_{m0} is directly linked to the structural parameters \bar{Z}_0 and C in (III.10) and (III.11), the quantity $(1 - \varepsilon_{m0})^{-1}$ being equal to the maximum relative volume of the average ice-hydrate particle with maximum mean particle radius \bar{r}_h attainable at $\bar{s} = 0$. In accordance with definitions (III.5) and (III.6), the current porosity ε_m , specific surface area S_i of ice cores, and total specific surface area of the original macro-pore space between the particles S_m are

$$\varepsilon_m = \varepsilon_{m0} - E(1 - \varepsilon_{m0}) \left(1 - \frac{\bar{r}_i^3}{\bar{r}_0^3} \right), \quad S_i = \frac{3\langle r_i^2 \rangle}{\rho_i \bar{r}_0^3}, \quad S_m = \frac{3\langle s r_h^2 \rangle}{\rho_i \bar{r}_0^3}. \quad (\text{III.17})$$

Due to the gas-hydrate expansion, the permeability of the pore channels formed by the original ice grains in the sample decreases, and the pores get closed at a certain macro-porosity ε_{mc} , related to a definite value of the free surface fraction \bar{s}_c of average particles. This cuts the ambient gas flow towards the particles and stops the clathration process. In polydisperse powder the close-off porosity is preferentially reached near the bigger grains, which become isolated with time before their complete transformation to the hydrate phase. Here they assume that the gas inflow to a reference grain expires

at $s = \bar{s}_c$, and the ice core is switched out of the reaction. There is indeed evidence in literature (Stern et al. 1996) that a complete transformation is difficult to achieve (except with repeated milling). From this point of view specific surface area of an average grain

$$\bar{S}_m = 3\bar{s}r_h^2 \langle r_0^2 \rangle / (\rho_i \bar{r}_0^5)$$

determined in (Kuks & Salamatin, 2003) overestimates S_m and more closely compares to the specific surface area of open pores.

Thus, they arrive at the complete model (III.1)-(III.17), which describes the detailed evolution of the ice grain ensemble in the ice sample, during its conversion to hydrate.

They use now the basic equations (III.7) and (III.9) to derive the averaged mass balance relation, governing the gas hydrate growth from the powder directly in terms of the reaction degree α . This can be done explicitly only for the initial phase of the clathration process when the number of ice cores does not change i.e. until substantial amount of smaller ice grains has not been completely converted to hydrates and/or many of bigger ice grains have not got isolated, yet.

First, in accordance with (Staykova et al. 2003), they assume that the ice-to-hydrate conversion at the earlier stages is limited by the reaction. Consequently, ω_V is constant ($\omega_V \approx \omega_R$), and the right hand side of (III.7) does not depend on r_0 , that is $dr_i/dr_0 \approx 1$ in (III.3). As a result, the ice-core size distribution function remains similar to the lognormal shape and is simply shifted with time to the left along the r_i -axis. Hence, the multiplication of (III.7) by $r_i^2 f_0(r_0)$ and its integration with respect to r_0 yields the averaged equation for \bar{r}_i of the same structure as the phenomenological one used in the monodisperse approximation (Staykova et al. 2003):

$$\frac{d}{dt} \left(1 - \frac{\bar{r}_i^3}{r_0^3} \right) = S_i \left[\rho_i \delta_0 \omega_s e^{-\omega_s t} + \bar{\omega}_V (1 - e^{-\omega_s t}) \right], \quad (\text{III.18})$$

where S_i is determined by (III.17) and the mean reaction rate $\bar{\omega}_V \approx \omega_R$.

By definition, the relative variance of the initial grain size r_0 in the ice powder is

$$\bar{\sigma}_0^2 = \langle r_0^2 \rangle / \langle r_0 \rangle^2 - 1.$$

Based on the general properties of lognormal distributions, they approximately write

$$\bar{r}_i^2 / \langle r_i^2 \rangle \approx \bar{r}_i / \langle r_i \rangle \approx 1 + \bar{\sigma}_0^2.$$

and express S_i approximately in terms of \bar{r}_i :

$$S_i \approx 3\bar{r}_i^2 / [\rho_i \bar{r}_0^3 (1 + \bar{\sigma}_0^2)].$$

After substitution of this expression, the averaged equation (III.18) can be integrated analytically. This gives the asymptotic solution at $k_D \rightarrow \infty$ in the form derived and discussed by Salamatin & Kuhs (2002) in case of monodisperse powders:

$$\bar{r}_i / \bar{r}_0 = 1 - A(1 - e^{-\omega_s t}) - Bt, \quad (\text{III.19})$$

with the mean-volume ice-grain radius \bar{r}_0 for the initial size of ice particles and with additional factor $(1 + \bar{\sigma}_0^2)^{-1}$ in definitions of coefficients A and B

$$A = \frac{1}{\bar{r}_0(1 + \bar{\sigma}_0^2)} \left(\delta_0 - \frac{\omega_R}{\rho_i \omega_S} \right), \quad B = \frac{\omega_R}{\bar{r}_0 \rho_i (1 + \bar{\sigma}_0^2)}.$$

However, in case of non-zero crack void fraction ε_f the mean relative ice-core radius cannot be directly expressed via the reaction degree α from (III.6). Neglecting terms of $O(\varepsilon_f^2/E^2)$ -order of magnitude, one obtains

$$1 - \frac{\bar{r}_i^3}{\bar{r}_0^3} \approx \left(1 + \frac{\varepsilon_f}{E} \right) \alpha - \frac{\varepsilon_f}{E} \bar{\chi}.$$

In accordance with (III.9), at the start of the reaction, when $h \rightarrow 0$, the degree of fissure filling $\chi \approx (3/4)\pi h/r_0$, and, an approximate relation for $\bar{\chi}$ asymptotically accurate at $t \rightarrow 0$ directly follows from the definition (III.6)

$$\bar{\chi} \approx \chi(\bar{\xi}), \quad \bar{\xi} = A'(1 - e^{-\omega_s t}) + B't,$$

where

$$A' = \frac{E}{\beta \bar{r}_0 (1 + \bar{\sigma}_0^2)} \left(\delta'_0 - \frac{\omega'_R}{\rho_i \omega'_S} \right), \quad B' = \frac{E \omega'_R}{\beta \rho_i \bar{r}_0 (1 + \bar{\sigma}_0^2)}.$$

Substitution of the above equations into (III.19) finally yields a generalized analogue of the basic asymptotic relation (Salamatin & Kuhs, 2002) for the reaction-limited kinetics of the hydrate formation process valid for small α

$$(1 - \alpha)^{1/3} \approx 1 - \frac{\varepsilon_f}{3E} \chi(\bar{\xi}) - A(1 - e^{-\omega_s t}) - Bt. \quad (\text{III.20})$$

As before, (III.20) requires that the plot of $(1 - \alpha)^{1/3}$ against time t in the beginning of the hydrate formation during stage II limited by the clathration reaction for $t \gg \omega_s^{-1}$ should be a straight line with slope B and intercept $1 - A - \varepsilon_f/(3E)$.

In the case of diffusion-limited stage III in the beginning of the gas-hydrate growth, it becomes clear from (III.16) that the rate of the hydrate formation ω_V in (III.7) and (III.8) is inversely proportional to r_i . The averaging procedure applied to the basic equation (III.7) after multiplication by r_i^2 would lead to a term $\langle r_i^2 \omega_V \rangle \sim \langle r_i \rangle$. Again, assuming the ice-core size distribution being approximately a lognormal one, they arrive at (III.18) with $\bar{\omega}_V$ expressed as in (Staykova et al. 2003)

$$\bar{\omega}_V = \omega_R \left(1 - \frac{1}{1 + F\theta} \right), \quad (\text{III.21})$$

$$F = \frac{D\rho_i}{r_0 k_R}, \quad \theta = \frac{\sqrt{s} \bar{R}_h \bar{R}}{\bar{R}_i \left[\sqrt{s} \bar{R}_h (\bar{R} - \bar{R}_i) + \bar{R}_i (\bar{R}_h - \bar{R}) \right]},$$

where $\bar{R}_i = \bar{r}_i / \bar{r}_0$, $\bar{R}_h = \bar{r}_h / \bar{r}_0$, and $\bar{R} = \bar{r} / \bar{r}_0$ are the mean normalised radii with \bar{r} determined by the averaged analogues of (III.10) and (III.15) for a monodisperse powder

$$\bar{r} = \bar{r}_h \left[1 - \frac{2(1-s)}{\bar{Z}} \right], \quad \bar{Z} = \bar{Z}_0 + C(\bar{R}_h - 1)$$

The averaged model (III.18)-(III.21) extends the monosize approximation of the process of the gas-hydrate formation from ice powders to polydispersed systems with non-zero crack void fraction but, as discussed, the model is valid only at the beginning of the clathration reaction for small α until the difference in ice grain size and the volume interaction between the particles does not become crucial. Further on with time, the smaller-size fraction of ice cores disappears while and bigger ice particles become isolated and are excluded from the reaction. This completely changes the size distribution in the ensemble of ice cores involved in the ice-to-hydrate transformation process, and the simplified averaged model breaks down.

At the end let us summarize. A general phenomenological model for the porous gas hydrate formation from polydisperse ice powder is developed to describe the three predictable stages of the process. The first is the initial stage I of the hydrate-film spreading over the ice surface, including a fast sub-stage of hydrate formation in ice-grain cracks and filling the fissures. The two subsequent stages II and III of the porous hydrate layer growth are limited by the clathration reaction (including the gas transport along the pores of the ice-hydrate interface) and by the diffusive gas/water mass transfer through the hydrate shells, respectively. This theory extends the previous results (Staykova et al. 2003) for monodisperse powders to a more general case of ice-grain ensembles characterised by the lognormal distributions. The obtained equations are compared to the monosize description of the hydrate formation from ice powders and show that the latter simplified approach is valid only in the beginning of the clathration process. The difference in size of initial ice particles in the sample results in different rates of their conversion to hydrates with the larger-size fraction getting currently isolated and switched out of the reaction. This additionally slows down the ice-to-hydrate conversion and stops the hydrate growth in the sample before the complete transformation is achieved. At the same time, fast hydrate growth in ice-grain cracks causes a jump-like change in the reaction degree in the very beginning of the reaction clearly distinguished in most of experimental runs.

§ 2. JMAKGB – a combined Avrami-Erofeev and Ginstling-Brounshtein model

2.1. The approach

The search for another approach is provoked on one hand by my belief that the reactions of hydrate formation and decomposition are in general reversible processes and there is no reason to try

to describe them differently (the multistage model was not foreseen to deal with decomposition at this stage). On the other hand, the impression is that the Ockham's razor may have to be applied to the multistage model (see Chapter IV).

The way of data treatment I suggest here assumes that the hydrate formation and decomposition can be treated in similar ways. At first sight it looks like both types of reaction proceed in completely different manners but in fact they both are nucleation-and-growth processes. In the case of hydrate formation, the hydrate is the growing phase and in the decomposition case – the ice is the growing phase. The differences in the formation and decomposition experiments presented in this work are firstly in the geometry of the starting material (ice spheres for formation, and hydrate with unknown geometry for decomposition) and secondly – the mechanisms of water and gas diffusion through ice and gas hydrate (including the porosity and inherent microstructures). All following explanations concern the formation process but can be easily transferred to the one of decomposition.

In the present analyses, I assume that the hydrate formation starts with nucleation on the surface of the starting ice and spreads across it like a point source generated “plane” wave. Thus, a hydrate layer with small thickness compared to its surface extent covers the initial surface (or at least part of it). The thickness will be more or less constant during the hydrate spreading across the surface. The formation at this stage will be limited mainly by the reaction rate. After some time, the available for reacting surface will be transformed into hydrate and to continue the reaction an inward gas (and outward water) transports by means of diffusion through the hydrate layer will come into play and limit the rate of reaction development. At this point it is good to call attention to the fact that there is a clear front of advancing of the hydrate into the ice, which is clearly visible in all our electron microscopic observations. In other words, I suggest a “two-stage interpretation of the results” – stage **A** – nucleation and growth of the nuclei, and stage **B** – diffusion limited bulk growth. Of course one should keep in mind that the diffusion controlled bulk growth takes place during the whole reaction even at the earliest stages. That means the observed reaction profile is a superposition of both processes. To separate both stages and to extract their parameters (ideally), one needs to have sufficiently long reaction data sets in order to find the point when stage **A** switches off completely. Then by analysing the pure diffusion limited part its parameters can be obtained and the data affected mainly by stage **A** can be corrected for the diffusion influence. Thus, the pure stage **A** can be obtained and further analysed. This means a sort of inversed order data analysis is to be performed. For the processing of stage **A** the Avrami-Erofeev theory is used and for stage **B** – the Ginstling-Brounshtein diffusion formula is applied. A detailed discussion on both follows.

2.1.1. Avrami-Erofeev equation

The process of nucleation is always followed by growth of the nuclei, once they reach supercritical size. In many cases the nucleation theory is used for getting better insight in the

nucleation and growth rate laws involved in different processes running in the nature, under laboratory or industrial conditions. The most widely used method to correlate these two is the use of the Avrami equation. Its derivation is fairly straightforward. Assume the nucleation rate, $I(t)$ and the crystal growth rate, $G(t)$, are known functions of the time (e.g. temperature). A crystal, which nucleates at time τ after a while – at time t will have a volume of:

$$V = S \left(\int_{\tau}^t G dt \right)^d \quad (\text{III.22})$$

where S is a shape factor and d depends on the dimensionality of the growth – $d = 1$ for one-dimensional growth (dendrites), to 2 for two-dimensional growth (plates) etc. If the nucleation rate is $I(t)$ at time τ , then the number of crystals nucleated within the time slot from τ to $\tau + d\tau$ is given by $V_{\text{sys}} I(\tau) d\tau$, where V_{sys} is the available volume for nucleation at that time. Therefore, at time t , the total volume of crystals nucleated within the considered time interval is:

$$dV = S V_{\text{sys}} I(\tau) d\tau \left(\int_{\tau}^t G(y) dy \right)^d \quad (\text{III.23})$$

If the shrinkage of the volume available for nucleation is ignored, then V_{sys} can be set equal to the total volume of the material undergoing the transformation, V_{tot} . Let us name the extended volume dV_{ex} instead of dV and also assign the ratio $V/V_{\text{tot}} = \alpha$ and $V_{\text{ex}}/V_{\text{tot}} = \alpha_{\text{ex}}$. To obtain the total volume transformed during the entire nucleation and growth process it is enough simply to integrate (III.23):

$$\alpha_{\text{ex}} = S \int_0^t I(\tau) \left(\int_{\tau}^t G(y) dy \right)^d d\tau \quad (\text{III.24})$$

(III.24) ignores the fact that the available volume for nucleation is shrinking, which leads to reducing the total number of nucleation sites, N_0 . That means the calculated number of nucleation sites will include a number of phantoms, which will never appear. It also neglects the fact that the growing crystals will impinge onto each other. In other words it allows for nucleation on already formed crystals and also crystals to grow into each other. Thus, to correct for these effects, Avrami suggested, the real reaction extent to be related approximately to this gloomy α_{ex} in the following fashion:

$$d\alpha = d\alpha_{\text{ex}} (1 - \alpha) \quad (\text{III.25})$$

In general sense the Avrami correction is nothing but a mean field correction, very similar to those performed in the statistical mechanics, for instance. Integrating both sides of that equation leads to:

$$\alpha_{\text{ex}} = \int \alpha_{\text{ex}} dx = \int (1 - \alpha)^{-1} d\alpha = -\ln(1 - \alpha) \quad (\text{III.26})$$

Let us suppose a first order formation of nuclei takes place. Then the total number of nucleation sites, including the phantoms, N_{ex} is:

$$N_{\text{ex}} = N_0 (1 - \exp(-k_n t)) \quad (\text{III.27})$$

k_n is the nucleation rate coefficient. Then the nucleation rate becomes:

$$I(t) = \frac{dN_{ex}}{dt} = k_n \exp(-k_n t) \quad (\text{III.28})$$

If the growth rate $G(t) = \text{const} = k_g$, i.e. the reaction runs at **isothermal conditions** and also that the growth is in 3D ($d = 3$), the substitution of (III.28) in (III.24) leads to:

$$\alpha_{ex} = Sk_g^3 k_n N_0 \int_0^t (t-y)^3 \exp(-k_n y) dy \quad (\text{III.29})$$

Substituting (III.26) in (III.29) and integrating (III.29) gives:

$$-\ln(1-\alpha) = \frac{6Sk_g^3 N_0}{k_n^3} \left(\exp(-k_n t) - 1 + k_n t - \left(\frac{k_n^2 t^2}{2!} \right) + \left(\frac{k_n^3 t^3}{3!} \right) \right) \quad (\text{III.30})$$

For long times, when the overlapping of the crystals starts to play role, the expression in the brackets can be approximated by its last term:

$$\alpha = 1 - \exp(-Sk_g^3 N_0 t^3) \quad (\text{III.31})$$

The widely used general form of this equation is:

$$\alpha = 1 - \exp(-Kt^3) \quad (\text{III.32})$$

This equation is referred in many different ways as for example: JMA (Johnson-Mehl-Avrami), JMAK (JMA with added Kolmogorov), Avrami, Avrami-Erofeev and what so ever.

Let us analyze equation (III.32). I particularly like to do that because in the literature one can find a number of wrong uses and interpretations of this formula (see Lasaga 1998). Some authors derive activation energies from the term K in (III.32), for instance. This cannot be done since in this coefficient are mixed both – nucleation and growth, i.e. no activation energy can be extracted out of it. What one can try to do is once obtaining K to go back to I and G and by treating them individually to obtain some meaningful activation energies. Unfortunately, presently this is not possible (there are some ideas how to overcome these problems in future) but still one can test whether it describes the experimental results. Let us rewrite (III.32) in the following shape:

$$\alpha = 1 - \exp(-Kt^d) \quad (\text{III.33})$$

The check is done by plotting the experimental data in the shape $\ln(\ln(1/(1-\alpha)))$ vs. $\ln t$. This is the well-known (triple) logarithmic plot¹, which should result in a straight line. Its slope gives d because if one takes the logarithm of (III.33) obtains:

$$\ln \left(\ln \frac{1}{1-\alpha} \right) = \ln K + d \ln t \quad (\text{III.34})$$

Usually the power d is attributed to the number of the dimensions of growth of the investigated matter. According to the pure Avrami theory, it can have only integer values from 1 to 3, as mentioned above. But Erofeev considered the possibility that a nucleus may require β successive events to form it, before it starts to grow. This leads to the more general form of (III.33):

¹ One should always keep in mind that such type of plots can smear to a grate extend some reaction features.

$$\alpha = 1 - \exp(-Kt^{\beta+d}) \quad (\text{III.35})$$

It means that the power may get integer values equal or greater than 1. If it is equal to 1 only nucleation takes place.

Since the growth never proceeds in only 1, 2 or 3D, a requirement the power to take not only integer values, but values bigger than 1 appears. In fact this is the case found most often in the literature and rarely somebody obtains an integer d .

In general the Avrami-like reaction is a partial case of a sigmoid growth function. Such functions are used in many different fields of the science to investigate processes from population growth to crystal growth. As seen from **Fig.III.4**, for values of d bigger than 1, the function has the traditional S-shape of the sigmoid growth functions. For $d = 1$, the Avrami formula describes the case of a classical first order growth. The question is: is it possible for d to obtain values smaller than 1 and if yes, what this means. As it will be shown in the next Chapter IV, this is the case observed in most of the CO₂ hydrate formation reactions. The first thought, which comes forward when finding such case is that, the considered events are in direct contradiction with the Avrami theory (in the face of equation (III.35)) and it cannot be applied for their analyses. But *de facto*, in some of the formation runs a sigmoid reaction shape appears and actually this is the way in which the reaction should develop. The abnormal thing is when it does not show this S-shape. I will come back to this problem in the next Chapter IV.

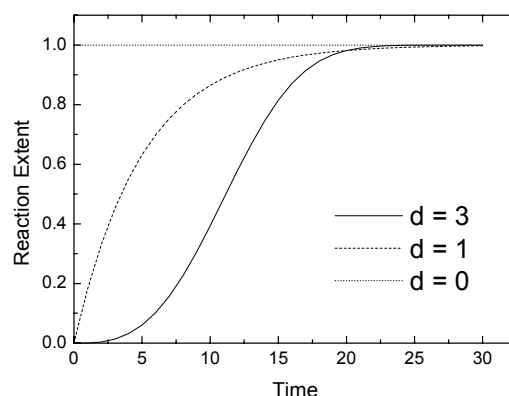


Fig.III.4 Sample Avrami curves with different values of the exponent, d .

2.1.2. Ginstling-Brounshtein – reaction of spherical particles

Let us consider a problem in which diffusion occurs in two different regions separated by a moving interface. Examples of such problems are: (1) tarnishing reactions in which a film of tarnish is formed at the surface of a metal by reaction with gas, where the diffusion of the gas through the layer is the rate controlling process; (2) the progressive freezing of a liquid etc. The moving boundary may be defined by a discontinuous change in the concentration as in (1) or by a discontinuity in the gradient of the concentration as in (2). Nevertheless, these are the different faces of one mathematical problem, which has been treated generally by Danckwerts (1950).

The formation, controlled by bulk hydrate diffusion, after the creation of the thin clathrate surface crust can be considered as a typical case of a tarnishing reaction. A detailed description of this and many other diffusion problems can be found in the book of Crank (1956).

Let us assume having a plane surface separating the two regions and let the diffusion take place only in the direction perpendicular to this surface (x -axis). The concentration is initially uniform in every region. The diffusion may cause changes, which result in appearance or disappearance of matter at the interface in one or both regions, causing bodily movement of the matter in one or both regions relative to the interface. The rates of bodily motion of the stuff in both regions with respect to the interface are directly proportional to each other. Positions in medium 1 are defined by a coordinate in x_1 system, which is stationary with respect to medium 1. For medium 2 the positions are specified in x_2 system, stationary with respect to medium 2. At time t the media are separated by a plane with coordinates in both systems $x_1 = X_1$ and $x_2 = X_2$, which is initially at $x_1 = x_2 = 0$. Medium 1 occupies the space between $X_1 < x_1 < \infty$ and medium 2 between $-\infty < x_2 < X_2$. In both media there is a substance moving by diffusion from one to another medium, relative to x_1 and x_2 . The concentration of the diffusing substance at time t is c_1 at x_1 and c_2 at x_2 . One can write the following equations:

$$\frac{\partial c_1}{\partial t} = D_1 \frac{\partial^2 c_1}{\partial x_1^2} \quad (\text{III.36})$$

$$\frac{\partial c_2}{\partial t} = D_2 \frac{\partial^2 c_2}{\partial x_2^2} \quad (\text{III.37})$$

where the diffusion coefficients D_1 and D_2 do not depend on c_1 and c_2 .

At any time the concentrations c_1 and c_2 obey an equilibrium expression:

$$c_2(X_2) = Qc_1(X_1) + R \quad (\text{III.38})$$

where Q and R are constants. The diffusing substance is conserved at the interface so that

$$D_1 \left(\frac{\partial c_1}{\partial x_1} \right)_{x_1=X_1} - D_2 \left(\frac{\partial c_2}{\partial x_2} \right)_{x_2=X_2} + c_1(X_1) \frac{dX_1}{dt} - c_2(X_2) \frac{dX_2}{dt} = 0 \quad (\text{III.39})$$

As mentioned above, the rates of bodily motion of the stuff in both regions with respect to the interface are directly proportional to each other, i.e.:

$$X_2 = PX_1 \quad (\text{III.40})$$

where P is a constant, depending on the conditions of the problem and sometimes may be zero².

Consider an infinite media where equations (III.36) and (III.37) hold. Then the solutions are:

$$\frac{c_1(\infty) - c_1}{c_1(\infty) - c_1(0)} = 1 - \operatorname{erf} \left(\frac{x_1}{2\sqrt{D_1 t}} \right) \quad (\text{III.41})$$

$$\frac{c_2(\infty) - c_2}{c_2(\infty) - c_2(0)} = 1 - \operatorname{erf} \left(\frac{x_2}{2\sqrt{D_2 t}} \right) \quad (\text{III.42})$$

with initial and boundary conditions as follows:

$$\begin{array}{lll} c_1 = c_1(\infty), & x_1 > 0, & t = 0 \\ c_1 = c_1(0), & x_1 = 0, & t > 0 \end{array}$$

² $P = 0$ in case of absorption of a single component of a gas mixture by a liquid, for instance. Then the x_2 coordinate of the liquid surface does not change and therefore $X_2 = 0$, $c_2(X_2) = c_2(0)$ for all t .

$$\begin{aligned} c_2 &= c_2(-\infty), & x_2 < 0, & & t = 0 \\ c_2 &= c_2(0), & x_2 = 0, & & t > 0 \end{aligned}$$

For the same conditions, the total amounts of diffusing substance V_1 and V_2 crossing the planes $x_1 = x_2 = 0$ in time t in the direction of decreasing x are:

$$V_1 = 2(c_1(\infty) - c_1(0))\sqrt{\frac{D_1 t}{\pi}} \quad (\text{III.43})$$

$$V_2 = 2(c_2(0) - c_2(-\infty))\sqrt{\frac{D_2 t}{\pi}} \quad (\text{III.44})$$

Now let us show that the solutions (III.41) and (III.42) are compatible with expressions (III.38), (III.39) and (III.40) and the conditions determined by the character of the problem. There can be two types of problems – problems of class A³ and class B⁴. The gas hydrate formation (as described above) being a classical example of a problem of class A allows us to limit ourselves to consideration only of the class A problems. Here should be mentioned that values of c_1 outside medium 1 and of c_2 outside medium 2 are considered without physical significance.

The motion of one or both media relative to the interface is caused by diffusion of substance across the layer. Here two of the quantities $c_1(\infty)$, $c_1(0)$, $c_1(X_1)$, $c_2(-\infty)$ or $c_2(0)$ are known and X_1 and X_2 are all the time proportional to the amount of diffusing substance crossing the layer ($x_1 = X_1$ and $x_2 = X_2$). Thus one can write:

$$\frac{dX_1}{dt} = S \left(D_1 \left(\frac{\partial c_1}{\partial x_1} \right)_{x_1=X_1} + c_1(X_1) \frac{dX_1}{dt} \right) \quad (\text{III.45})$$

Here S is the ratio of the magnitude of X_1 to the amount of diffusing substance crossing the interface in the direction of decreasing x . Combining this with (III.39) and (III.40) one gets:

$$\frac{dX_2}{dt} = PS \left(D_2 \left(\frac{\partial c_2}{\partial x_2} \right)_{x_2=X_2} + c_2(X_2) \frac{dX_2}{dt} \right) \quad (\text{III.46})$$

Substituting (III.38), (III.40), (III.41), (III.42) in (III.45) and (III.46) leads to

$$\frac{dX_1}{dt} \left(\frac{1}{S} - c_1(X_1) \right) = (c_1(\infty) - c_1(0)) \sqrt{\frac{D_1}{\pi t}} e^{-X_1^2/4D_1 t} \quad (\text{III.47})$$

$$\frac{dX_1}{dt} \left(\frac{1}{S} - PR - PQc_1(X_1) \right) = (c_2(0) - c_2(-\infty)) \sqrt{\frac{D_2}{\pi t}} e^{-P^2 X_1^2/4D_2 t} \quad (\text{III.48})$$

Putting $x_1 = X_1$ and $c_1 = c_1(X_1)$ in (III.41) gives

$$c_1(X_1) = c_1(0) + (c_1(\infty) - c_1(0)) \operatorname{erf} \left(\frac{X_1}{2\sqrt{D_1 t}} \right) \quad (\text{III.49})$$

Equations (III.47), (III.48), (III.49) can be simultaneously satisfied only if $X_1/t^{1/2} = \text{const}$. Assuming

³ Class A problems – the movement of one or both media relative to the boundary is caused by the transfer of diffusing substance across the layer.

⁴ Class B problems – the movements of the media on either side of the interface are not related to the amount of diffusing substance, which has crossed the interface.

$$X_1 = 2\alpha\sqrt{D_1 t} \quad (\text{III.50})$$

and (III.47), (III.48), (III.49) become respectively

$$c_1(\infty) - c_1(0) = \alpha\sqrt{\pi}\left(\frac{1}{S} - c_1(X_1)\right)\exp(\alpha^2) \quad (\text{III.51})$$

$$c_2(0) - c_2(-\infty) = \alpha\sqrt{\pi\frac{D_1}{D_2}}\left(\frac{1}{S} - PR - PQc_1(X_1)\right)\exp\left(\alpha^2 P^2 \frac{D_1}{D_2}\right) \quad (\text{III.52})$$

$$c_1(X_1) = c_1(0) + (c_1(\infty) - c_1(0))\text{erf}(\alpha) \quad (\text{III.53})$$

putting in (III.42) $x_2 = X_2$ and using (III.50) and (III.40) gives

$$\frac{Qc_1(X_1) + R - c_2(-\infty)}{c_2(0) - c_2(-\infty)} = 1 + \text{erf}\left(P\alpha\sqrt{\frac{D_1}{D_2}}\right) \quad (\text{III.54})$$

Equations (III.51) and (III.54) are independent and contain the quantities $c_1(\infty)$, $c_1(0)$, $c_1(X_1)$, $c_2(-\infty)$, $c_2(0)$, R , S and α . Thus, if two of the concentrations are given, the four equations can be solved for α and the other three and c_1 and c_2 come as functions of x and t from (III.41) and (III.42). The so obtained expressions for c_1 and c_2 satisfying the initial and the boundary conditions give the solution. Substitution for α in (III.50) gives X_1 in terms of t and then X_2 comes from (III.40). At the end one should point out that $c_1(X_1)$ and $c_2(X_2)$ at the interface are constant from (III.38) and (III.53).

Let us now go to the particular case of the tarnishing reactions. A film of tarnish (gas hydrate) is formed on the ice surface. The reaction proceeds by diffusion of gas/water through the film to/from the ice surface where its concentration $c_1(X_1)$ is assumed to be zero (the film is assigned as medium 1). That means that the rate of the reaction is entirely controlled by the diffusion. The outer surface of the film is constantly saturated with gas.

Since $c_1(X_1)$ is not determined by diffusion through another medium, expressions (III.52) and (III.54) are not necessary. Let V_M be the volume of tarnish containing one mole of gas and c_1 – the concentration of dissolved gas expressed in moles per unit volume at a distance x_1 underneath the film surface. The outer film surface is at $x_1 = 0$ and the ice surface is at $x_1 = X_1$. From (III.45)

$$S = -V_M \quad (\text{III.55})$$

Moreover, since $c_1(X_1) = 0$ and from equations (III.51) and (III.53), the saturated concentration of gas at the outer film surface $c_1(0)$ is:

$$V_M c_1(0) = \alpha\sqrt{\pi}\exp(\alpha^2)\text{erf}(\alpha) = g(\alpha) \quad (\text{III.56})$$

and we also know that

$$X_1 = 2\alpha\sqrt{D_1 t} \quad (\text{III.57})$$

where D_1 is the diffusion coefficient of the dissolved gas in the film. If $c_1(0) \ll 1/V_M$ the expansion of $\exp(\alpha^2)$ and $\text{erf}(\alpha)$ shows that $g \approx 2\alpha^2$ and

$$X_1 = \sqrt{2D_1 c_1(0)V_M t} \quad (\text{III.58})$$

This is the well-known parabolic law for tarnishing reactions, which were first studied in detail by Wagner in the middle of the 1930-ties.

The above treatment involves an approximation of quite obscure nature without a more detailed treatment. Practically it gives a good approximation if the concentration of the diffusing gas is much less than the concentration of the gas immobilized in the solid product. This means that large fractional readjustments of concentration in the diffusion region can take place, while the interface is moving very little.

As mentioned in the beginning of this paragraph, the above derivations deal with semi-infinite geometry. In my formation experiments this is not the case because the starting material consists of spherical ice grains. The question is how I can modify the above results to match my case. There is some gloom in the literature on this. Usually three equations are used – the ones of Jander (1927), of Ginstling-Brounshtein (1950) and of Dünwald-Wagner-Serin-Ellickson (Dünwald & Wagner (1934); Serin & Ellickson (1941)). In the references to these equations clear indications of the approximations involved are missing. Also it does not become clear that *de facto* they do not refer to one and the same situation.

The equation of Dünwald-Wagner-Serin-Ellickson describes the total amount of material entering or leaving a sphere as a fraction of the final amount, $\alpha = M_t/M_\infty$:

$$\frac{M_t}{M_\infty} = 1 - \frac{6}{\pi^2} \sum_{n=1}^{\infty} \frac{1}{n^2} \exp(-Dn^2\pi^2 t / a^2) \quad (\text{III.59})$$

It comes from

$$\frac{C - C_1}{C_0 - C_1} = 1 + 2 \sum_{n=1}^{\infty} (-1)^n \exp(-Dn^2\pi^2 t / a^2) \quad (\text{III.60})$$

Here C_0 is the constant concentration at the sphere surface, C_1 – the concentration in the sphere, a – radius of the sphere, D – diffusion coefficient. A curve of α vs. the dimensionless parameter Dt/a^2 can be computed and used to convert values between both of them. A graph of α vs. time would be a straight line with slope D/a^2 . In any case this equation is applicable to diffusion with constant D into or out of a system of spheres of uniform radius with constant surface concentration of the diffusing species. And here comes the important point – it is not appropriate to the case of a sharp reaction interface advancing into the sphere. It works in cases in which the original interface becomes blurred with the development of the reaction and disappears at the end as such. This expression cannot be used here being in controversy with the always-observed (SEM) phenomenon of sharp borders between hydrate and ice.

The equations of Jander and Ginstling-Brounshtein are both attempts to treat the advancing reaction interface case in spherical geometry. The expression of Jander, being a very rough

approximation should be used only for small extents of the reaction α . The one of Ginstling-Brounshtein is the proper analogue of the parabolic law in spherical geometry.

Now let us consider a sphere with initial radius b at which the concentration of the diffusing species is $c_1(b) = \text{const}$ all the time. At time t the reaction front has penetrated to radius a at which the reaction removes the diffusing species so that the concentration $c_1(a)$ becomes zero. The extent of the reaction will be:

$$\alpha = 1 - \frac{a^3}{b^3} \quad (\text{III.61})$$

Jander assumed that the thickness of the reacted layer $X = (b - a)$ is given by the parabolic law applicable to the semi-infinite geometry (III.58) with the following assumption:

$$(b - a)^2 = 2D_1c_1(b)V_Mt \quad (\text{III.62})$$

Equations (III.61) and (III.62) lead to

$$\left(1 - (1 - \alpha)^{1/3}\right)^2 = \frac{2D_1c_1(b)V_Mt}{b^2} \quad (\text{III.63})$$

This is the Jander equation, which obviously does not take into account the convergence of the diffusion paths at the center of the sphere. It has been shown it cannot be trusted for $\alpha > 0.15$ (Giess 1963).

The steady-state solution of the diffusion equation for a spherical shell of radii a and b is

$$C = bc_1(b) \frac{(r - a)}{r(b - a)} \quad (\text{III.64})$$

from this the flow rate of matter through the shell is

$$\frac{dM_t}{dt} = -4\pi a^2 D_1 \left(\frac{\partial C}{\partial r} \right)_{r=a} = 4\pi D_1 c_1(b) \frac{ab}{b - a} \quad (\text{III.65})$$

In the usual manner of the quasi-stationary state approach, having derived the above expression on the basis of constant a , let us allow a to vary with t :

$$\frac{dM_t}{da} = -\frac{4\pi a^2}{V_M} \quad (\text{III.66})$$

$$\frac{da}{dt} = -\frac{D_1c_1(b)V_Mb}{a(b - a)} \quad (\text{III.67})$$

$$D_1c_1(b)V_Mt = \int_b^a \left(\frac{a^2}{b} - a \right) da \quad (\text{III.68})$$

Integrating and using (III.61) to convert from a to α leads to the Ginstling-Brounshtein equation:

$$1 - \frac{2}{3}\alpha - (1 - \alpha)^{2/3} = \frac{2D_1c_1(b)V_Mt}{b^2} \quad (\text{III.69})$$

The plot of the left-hand side of this equation vs. t should be linear with a slope $2D_1c_1(b)V_M/b^2$. It should be practically applicable up to high values of α . Its validity of course depends on the constancy of D and on how well the system can be approximated with spherical geometry.

In the gas hydrate formation case the best variant, which seems to satisfy the observations, is to use the Ginstling-Brounshtein equation. To apply it directly and to extract D , on the first place a value for b is needed. Measuring spheres of the starting material gives it. Secondly – knowing the thermodynamic conditions at which the gas is imposed one can calculate $c_1(b)$, using the van der Waals real gas approximation. In the present interpretation I do not use $c_1(b)$, but the difference between $c_1(b)$ and the hypothetical concentration at p-T conditions corresponding to the hydrate formation/decomposition boundary, $c_d(b)$, i.e. $C_1(b) = c_1(b) - c_d(b)$. This plays the role of the driving force for the reaction development.

V_M can be calculated from:

$$V_M = \frac{m_h}{\rho_h} \quad (\text{III.70})$$

where m_h is the mass of the hydrate and ρ_h is its density. The mass of the hydrate should be given as a sum of the masses of the CO_2 molecules, m_{CO_2} (or those of the gas involved) and that of the water molecules, $m_{\text{H}_2\text{O}}$:

$$m_h = m_{\text{CO}_2} + m_{\text{H}_2\text{O}} \quad (\text{III.71})$$

The number of water molecules building a clathrate structure containing 1 mol of CO_2 if the hydrate is ideally stoichiometric, i.e. the occupancy $\chi = 1$, is approximately six water molecules per one gas molecule. But this is often not the case and $\chi \leq 1$ and varies with temperature. Then the expression for V_M becomes:

$$V_M = \frac{m_{\text{CO}_2} + \frac{m_{\text{H}_2\text{O}}}{\chi}}{\rho_h} \quad (\text{III.72})$$

Thus the modification of the Ginstling-Brounshtein equation I implement is:

$$1 - \frac{2}{3}\alpha - (1 - \alpha)^{2/3} = \frac{2D_1C_1(b) \left(m_{\text{CO}_2} + \frac{m_{\text{H}_2\text{O}}}{\chi} \right)}{\rho_h b^2} t \quad (\text{III.73})$$

Chapter IV

Experiments, results and conclusions

In this chapter will be presented the results from the CO₂ formation and decomposition experiments as well as the observations of the microstructure. In the first paragraph, dealing with the clathrate formation, a comparison and critical discussion of the results arising from the two methods of data analysis, described in detail in Chapter III, will be given. In the second paragraph will be presented the data on CO₂ hydrate decomposition. There, the first ideas of approaching the physics of the decomposition process will be discussed and a first attempt of data analysis will be shown. At the end the reader will be introduced to the micro-structural issues accompanying the CO₂ hydrate kinetic problems.

§ 1. Experiments on CO₂ hydrate formation

1.1. The starting material

As a starting material for the *in situ* formation experiments of CO₂ hydrate, for both neutron diffraction and pVT studies, an ice Ih powder was used. Since hydrogen has an enormous incoherent scattering cross section for neutrons (40 times larger than for deuterium), the initial ice powder was prepared out of heavy water. It was used for the neutron diffraction as well as for the in house experiments. The isotope influence on the gas hydrate formation was discussed in Staykova et al. (2003) and Staykova (2004). The authors concluded that there was no significant difference between the hydrate formation kinetics in the deuterated and the hydrogenated cases, at least for temperatures well below the ice melting.

Two methods of preparation of the starting material were implemented. The goals were to obtain a powder with well-defined, reproducible geometry and at the same time with sufficiently high SSA. The first method was the one used by Staykova (2004) where heavy water is sprayed in liquid nitrogen. After the production the material is annealed at –30 °C for 3 hours to anneal the stacking faults in the ice Ih (see e.g. Kuhs et al. 2004). The resulting starting material consists of log-normally distributed spheres (**Fig. IV.1** left) with a mean diameter of 54 µm. Its SSA was measured using the BET method, described in Chapter III and was found to be $\approx 0.1 \text{ m}^2/\text{g}$ (Zeller, 2004). This diameter is still too big compared to the one of the expected Martian diamond dust (see Chapter I). For this reason further attempts were made to reduce the sphere size and thus to increase the SSA. Moreover, as it will become clear later on in this paragraph, the low SSA affects the growth kinetics. The way out was searched in the construction of an electro-spraying device (Grigoriev & Edirisinghe 2002) but the idea

was abandoned, since the production rate of such device was calculated unacceptably low. Therefore, a new technology of controlled D₂O frost formation in inert gas environment was developed. With the help of the technical staff, a frost generator was built and the produced material showed an SSA of 14 m²/g (A. Zeller 2004, private communication). Unfortunately the price for the large SSA was a poorly defined geometry (**Fig. IV.1** right). That made the treatment of the reaction data obtained using this starting material with the multistage model (see Chapter III) questionable, since it requires spherical ice powder with a lognormal distribution. This is also true for the GMAKJB approach, as seen in Chapter III. Another point here is that the samples produced this way are not annealed due to the fact that at present there is no technical possibility in our labs to precisely control the annealing regime. Any improper annealing technology may lead to a loss of SSA.

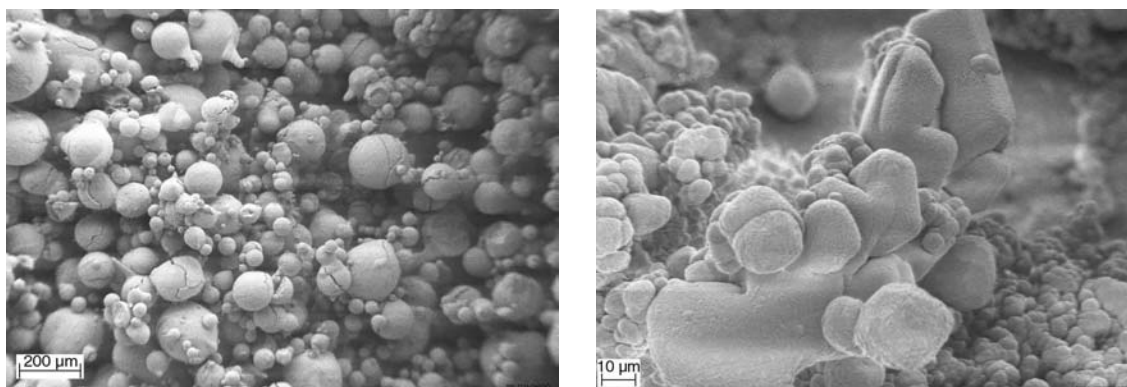


Fig.IV.1. Starting ice Ih material produced by spraying (left) and frost deposition (right).

The starting material (without accounting for the way of production) was filled in the same type Al cans as described in Staykova (2004).

1.2. The Experiments

For the neutron diffraction experiments, the Al-cans with the ice samples, prepared after the procedures described above, are transported in a dry-N₂ mover dewar to ILL/Grenoble. The sample cell, already fixed to the sample stick (**Fig. II.6**), is cooled in dry ice. The Al cans are loaded into the cell.

For the reactions above 1 bar, a weak gas flow during the sample loading ensures the full replacement of the air in the system with CO₂. Then the Bridgman seal is closed and the stick goes into the “Orange cryostat”, which is set to the required temperature. After achieving temperature equilibrium, a high gas pressure, providing the hydrate formation conditions at the given temperature, is applied within a few seconds and the data collection begins. According to the security rules at the instrument the high-pressure gas bottle should be closed if left unattended. This is not a problem because of the large volume of the gas lines, providing almost constant pressure at the sample during the run. If necessary, the pressure is readjusted manually.

For the reactions below 1 bar, the air is evacuated after closing the Bridgman seal and putting the stick into the cryostat. This is done by pumping the system, flashing it with CO₂ and then again pumping, this time for 10 to 30 min or pressure values of 10⁻³ mbar. Until achieving the temperature equilibration, the pressure is kept below the hydrate formation limit via pumping. Then the required gas pressure for the hydrate formation at the given temperature is applied within seconds and the data collection begins.

A series of *in situ* neutron diffraction experiments

were performed to study the kinetics of gas hydrate formation from deuterated ice prepared following the already described procedures (Table IV.1). Most of the runs lasted 8 – 23 h, using D₂O at its highest intensity setting, at $\lambda = 2.414 \text{ \AA}$.

For the in-house pVT experiments the same spherical ice powder as the one used in the neutron runs is used. Before starting the reaction, the sample cell is cooled down to almost dry ice temperature. The evacuation of the system is done in the way described above for the neutron experiments. The sample cell is inserted in the low temperature bath, already adjusted at the chosen temperature. Then the desired gas pressure is applied and the acquisition of the pressure drop in the closed ice-gas system begins. The time steps of the data collection are from 30 s to 30 min, depending on the reaction. The pressure in the system is adjusted manually to maintain it within a few percent of the desired value. The recorded pressure drop is then converted to gas consumed per unit time (see Chapter II, § 2). At

Table IV.1 Summary of the successful reactions used in the present study. It shows the reaction temperature and pressure, p; the decomposition pressure for the given temperature, p_d, and the corresponding gas concentrations, calculated from the van der Waals real gas law. The decomposition pressures are calculated from the formula found by Staykova (2004):

$$p_d = \exp(A - B/T)$$

In the CO₂ case:

$$A = 11.74 \pm 0.07$$

$$B = -2559 \pm 13$$

The duration of each run is also shown.

Temperature [K]	p [bar] Concentrat. [mol/m ³]	p _d [bar] Dec. Conc. [mol/m ³]	Durat [h]
185 ¹	0.365 23.71764	0.124 8.06024	21
185 ²	0.266 17.28706	0.124 8.06024	25
190 ²	0.36 22.77758	0.178 11.26508	22
195 ²	0.505 31.12688	0.252 15.53792	15
193 ³	0.5 (0.5) 31.33821	0.22 (0.22) 13.70597	126
203 ³ E1 (Ch. II)	0.89 (0.88) 53.21975	0.433 (0.43) 25.64022	48
203 ³ E2 (Ch. II)	0.89 (0.88) 53.21975	0.433 (0.43) 25.64022	185
203 ³ E2	0.89 (0.88) 53.21975	0.433 (0.43) 25.64022	2255
213 ³ E2	1.5 (1.47) 85.91072	0.763 (0.75) 43.04345	185
218 ³ E2	1.95 (1.88) 109.52907	1.005 (0.99) 55.37993	288
223 ³ E2	1.95 (1.9) 106.95191	1.3 (1.28) 70.00667	240
230 ¹	3 (2.9) 160.77174	1.86 (1.86) 97.05614	26
253 ¹	10 (9.1) 510.20337	5.1 (4.9) 241.14299	23
263 ¹	10 (9.3) 485.43633	7.5 (7.1) 340.36857	18
272 ⁴	20 (19.7) 884.96178	11.4 (11.3) 498.43705	18

¹ A neutron reaction with spherical (sprayed) starting material (d = 54 μm)

² A neutron reaction with the large SSA starting material (frost deposition)

³ In house reaction

⁴ Staykova et al. (2003)

the same time the temperature in the room is recorded. It is sometimes needed for the HSC (see Chapter II, § 2).

1.3. Data analyses and discussion

1.3.1. With the multistage model (Genov et al. 2004)

In most of the neutron-diffraction measurements, the gas hydrate growth reveals itself by immediate increase of the gas hydrates' Bragg intensities after the application of the gas pressure, followed by a slow-down while the amount of ice Ih decreases. The repeatedly reported induction period (Sloan 1998) was observed as a sigmoid growth only at temperatures below 200 K (Grenoble set up) and is not discussed within the frames of this model, in which this effect is not considered explicitly. A series of three experiments at 263, 253, and 230 K was performed with deuterated samples (see **Fig. IV.2a**). The reactions lasted between 17 and 26 h resulting in 13 – 37 % ice-to-hydrate conversion. An experiment performed with larger ice grains at 272 K (**Fig. IV.2b**), reported by Staykova et al. (2003) with a total degree of transformation (reaction degree) – about 56 % was also used and re-analyzed here.

Another series of in house experiments at 193, 203, 213, 218 and 223 K were processed. As mentioned before these experiments were done using the gas consumption technique (see Chapter II), also starting with deuterated ice. Practically no induction period was observed. All these experiments covering the temperature range from 193 to 272 K were used to obtain the tuned model parameters listed in Table IV.2; examples are shown on **Figures IV.2c**.

During the first 6 – 7 hours both reactions, at 253 and 263 K run closely together; only at a later stage the reaction at 253 K significantly exceeds the one at 263 K. The explanation within this model is the counterbalancing of the influences of the temperature and the excess fugacity, $(f - f_d) / f_d$ (see **Fig. IV.2a** and Table IV.2). To reach the same transformation degree of 10 %, a time of about 1 h is needed at 253 K; this is approximately 15 h at 230 K and exceeds 24 h at 193 K (compare **Figs. IV.2a** and **IV.2c**). In all experiments (except the ones revealing a sigmoid growth) the kinetic curve for the initial stage shows a strongly non-linear development with time and flattens at later stages while keeping a smooth overall shape without inflection points (more like a first order kinetics). The electron microscopic observations of the porous hydrate layer during stage I show that the coating process preferentially starts in cracks (see **Fig. IV.3**) with a subsequent spreading over the spherical grain surface. As explained in Chapter II, the model copes with this by dividing stage I into two sub-stages: stage Ia (crack-filling) and stage Ib (surface-coating). The formation and spreading of hydrate patches is much slower than the filling of the cracks. Even at high temperatures, the ice surface is **not** fully covered with a hydrate shell after several hours, although in almost all cracks in the grains traces of hydrate can be found.

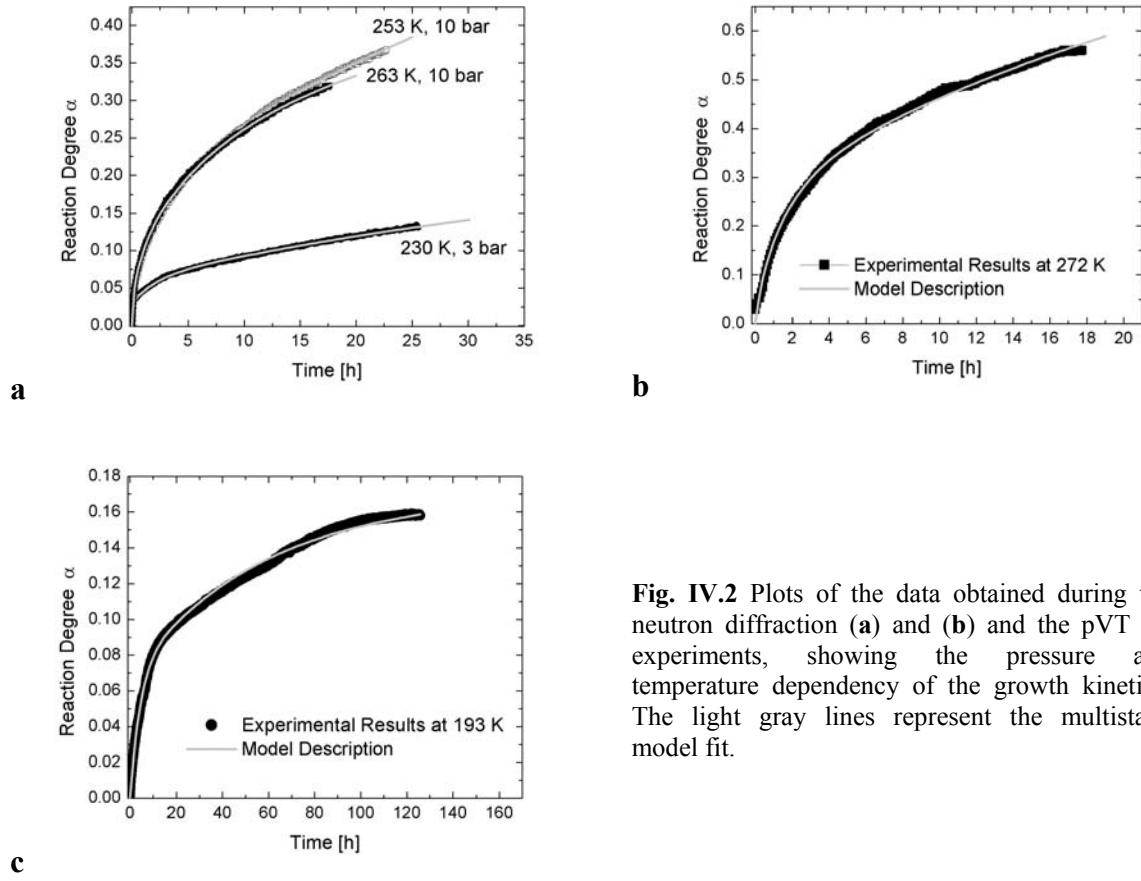


Fig. IV.2 Plots of the data obtained during the neutron diffraction (a) and (b) and the pVT (c) experiments, showing the pressure and temperature dependency of the growth kinetics. The light gray lines represent the multistage model fit.

The multistage model was used to interpret the gas-consumption and diffraction data. A computer program was implemented to perform all necessary simulations. An intuitive manual iterative procedure was used to fit the model to the data. The same approach was employed previously in Staykova et al. (2003). Experimental constraints on the coating rate constants k_s and k_s' in (IV.8₁) and (IV.9) derived from the SEM images in experiments interrupted after different time elapsed were also taken into account, together with the SEM based estimates of the average crack opening angle $\beta \sim 0.06$.

Unfortunately, I could not derive such constraints up to now. Here are mentioned some of the reasons for that: the electron microscopy is a local method (square microns can be investigated) and (a) cannot give statistically reliable information about a sample with square meters available surface, within a reasonable time period. Consequently, no serious constraints on the coating rate constants can be derived; (b) since far not all spheres are cracked and many of the cracked spheres are split into 2 or more pieces, any estimate of the crack opening angle β becomes gloomy; (c) since the SEM is a method used for surface observations (in my case) no estimate for the thickness δ_0 or δ_0' can be obtained. Looking at (IV.7) one can immediately see the extremely strong correlation between $\delta_0'(\delta_0)$ and $k_s' (k_s)$. If there are no constrains for them, they can vary freely. This will be shown a few lines later; (d) here comes the purely statistical problem of deriving the parameters of the lognormal distribution of the quite irregular spheres and the following calculation of the SSA. I performed a

number of Monte Carlo-like simulations of real lognormal samples and the idealized SSA I got, underestimates the real SSA (measured by A. Zeller 2004) by a factor of two. One should keep in mind that the multistage model described in Chapter III uses more idealized (simple) approach for the sample geometry definition and sample packing. The conclusion is that the attempt to better describe the sample is not entirely successful, but this is not only a problem of the model but also of the sample preparation; (e) as a sequence of this comes the limited application of the model, since it is not likely that a spherical log normally distributed starting material will be always used. Still this approach can be implemented in attempt to deduce values of the pure reaction parameters from well-defined samples and later on to use these values for further analyses.

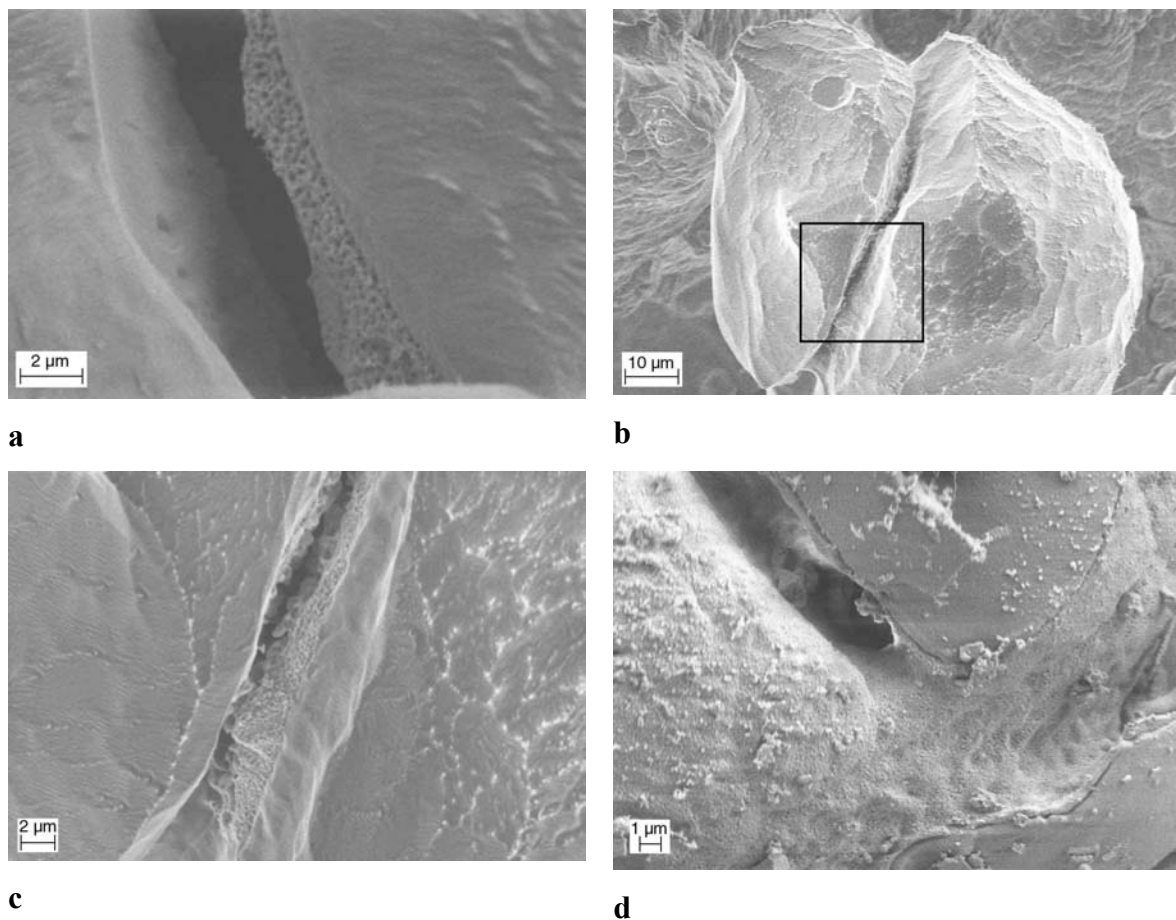
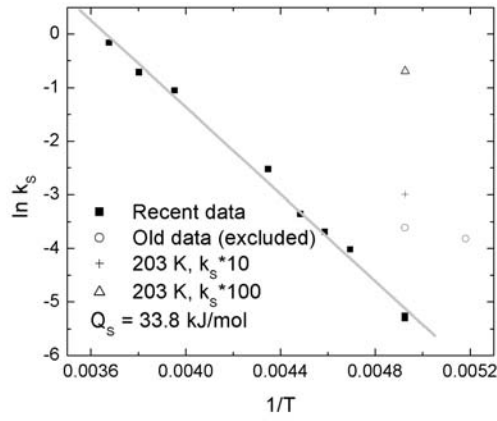


Fig.IV.3 FE-SEM images of samples quenched at various stages of the CO₂ hydrate formation process: (a) CO₂ hydrate formation on a crack surface after 3 h of reaction at 193 K, 0.5 bar; view of a crack (b) and a zoom-in of the area of the black rectangle (c) under the same conditions after 8 h; (d) reaction, which had started in the crack and possibly spread across the grain surface (185 K, 0.36 bar, 21 h).

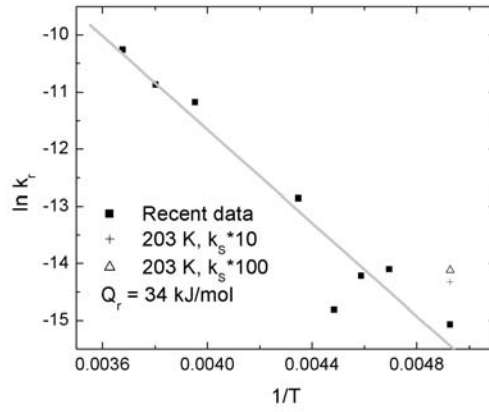
Nevertheless, assuming that the constraints, described above, can be applied, as they were previously, one may say that the typical time scale ($1/\omega_s$) of stage Ib is proportional (see (IV.8₁)) to the reciprocal value of the ice grain coating rate constant $1/k_s$ which increases from about 1 to approximately 12 h as the temperature decreases from 272 to 230 K (see Table IV.2). At 193 K it takes about 45 h. In these terms, for the thermodynamic driving force $\ln(f/f_a) \sim 1$, the reaction at 193 K can be interpreted as pure crack-filling during the first 5 – 7 h, followed by a transition period and surface coating until approximately 150 h.

Assuming that in all CO₂ experiments presented here the surface-coating stage is sufficiently well developed allows obtaining values for the coating rate constant k_s . Thus, the activation energy Q_s of this process may be extracted (see **Fig. IV.4a**). Previously, two different regions were considered, above and below around 225 K. For the high temperature region, the value of the activation energy was 31.5 kJ/mol while it was 5.5 kJ/mol for the lower range (Genov et al. 2004). The newer observations reject this separation into two regimes (which was apparently due to the insufficient time/transformation extent of the runs at low temperatures as well as insufficient number of experiments) and give $Q_s = 33.8 \text{ kJ/mol}$. Nevertheless, at higher temperatures the reactions go far enough in time and transformation degree allowing for a model interpretation. The values of the reaction rate constant k_R and diffusion coefficient D deduced under the assumption that the hydrate formation is either limited by reaction or diffusion are given in Table IV.2. The only exception is the 3-months reaction at 203 K where the balance between reaction and diffusion could be found. The activation energy of the diffusion-limited process obtained for the 203 to 272 K range is $Q_D = 36 \text{ kJ/mol}$ (**Fig. IV.4b**), while for the reaction-limited process energy of $Q_r = 34 \text{ kJ/mol}$ results from the analysis (**Fig. IV.4c**). This result suggests that the diffusion and the reaction-controlled stages should develop with the same speed, i.e. there is either no diffusion or no reaction limitation. The second is more likely, i.e. there is no reaction-limited stage. It was initially introduced because the pores in the hydrate structure were interpreted like pathways for the gas and water to and from the interior of the reacting matter after the pure surface coating. BET SSA measurements suggested that the porosity was predominantly closed (Zeller 2004) and further image analyzes showed it could be described as solid foam (see §3). In the light of these facts it becomes clear that the reaction-limited stage needs some revision and possibly unification with the surface coating stage. This will certainly affect the values for the activation energies for both – surface coating and diffusion limited stages.

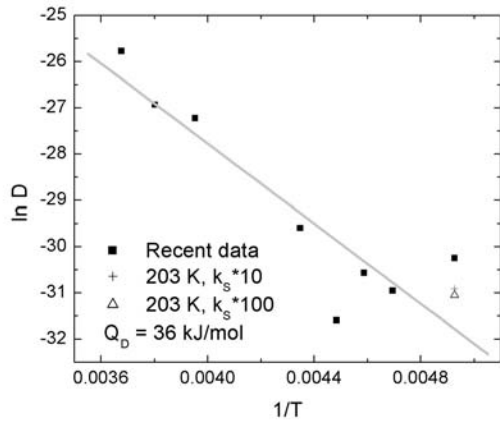
Concerning the initial crack-filling sub-stage and once again assuming all previous constraints hold true, one can deduce from k_s' and k_R' listed in Table IV.2 that, in general, this process is more rapid at high temperatures, but the surface coverage, being several orders of magnitude slower at low temperatures, accelerates to a much higher degree and becomes hardly distinguishable from the crack-filling coverage (compare k_R' and k_R) at the melting point. This is in agreement with the SEM observations. As a consequence, at lower temperatures the crack-filling stage is much more easily separated from a subsequent surface-coating sub-stage. From the model fits typically several μm are obtained for the thickness δ_0' of the ice layer converted to the initial hydrate film on the crack walls, which compares well with the thickness δ_0 of the coating layer on the ice grain surface (obtained again from these model fits).



a



b



c

Fig.IV.4 Arrhenius plots of the various stages of the CO₂ hydrate formation process at temperatures above 203 K: **(a)** the surface coating stage; **(b)** the reaction limited stage; **(c)** the diffusion limited stage. The open circles represent old data excluded as “short and not reliable”. The open triangles and the crosses stay for data points resulting from the alternative fits of the long 203 K reaction with varying k_s (not included for the activation energy). The latter will be explained later in the text.

In any case, in the results for k_s' and k_r' listed in Table IV.2 a systematic behavior cannot be found. This suggests for some difference in the initial part of the reaction that does not seem to come from one temperature to another but from one sample to another. The reason can be that the different samples have a different number and geometry of the cracks, for instance. Or more realistically and more importantly, it can be caused by some frost collected in the sample during the preparation, thus changing the initial sample geometry. This may happen despite the “antifrost” measures taken (spraying in inert gas environment). The frost has a very large SSA and reacts faster, i.e. the different initial quantity of frost will lead to a different set of crack-filling-stage parameters. The amount of frost certainly depends on the weather (i.e. on the prevailing humidity in the air) and since the different samples are produced at different time of the year, they will contain different quantities of frost.

Let us go back to the discussion on the robustness of the results of this model, already started a few lines above and first concentrate on the crack filling. The formulae describing it (IV.9) are absolutely independent from the others, describing the surface coating and reaction and diffusion limited stages. In other words the full reaction is considered as a superposition of crack filling and everything else. There is nothing wrong in this except that having all these unconstrained free parameters only in the fissure filling stage makes it easier to play with them in very broad ranges (3

orders of magnitude and possibly more) without changing the overall fit and still pretending they are full of sense (Table IV.3 and **Fig. IV.5**). For the examples from here on, I will take the reaction at 203

React.	k_s' [1/h]	k_R' [kmol/m ² h]	δ_0' [μm]	k_s [1/h]	k_R [kmol/m ² h]	D [m ² /h]	δ_0 [μm]	ε_f
193	0.7	$7 \cdot 10^{-5}$	2.3	$2.2 \cdot 10^{-2}$	—	—	1.9	$1.8 \cdot 10^{-2}$
203 E1	5	$2.3 \cdot 10^{-4}$	2.3	$2.7 \cdot 10^{-2}$	—	—	1.9	$1.8 \cdot 10^{-2}$
203 E2	0.37	$4 \cdot 10^{-5}$	3.5	$5.2 \cdot 10^{-3}$	—	—	2.45	$1.9 \cdot 10^{-2}$
203 long	0.32	$2.1 \cdot 10^{-4}$	2.45	$5 \cdot 10^{-3}$	$2.85 \cdot 10^{-7}$	$7.3 \cdot 10^{-14}$	2.45	$2.5 \cdot 10^{-2}$
213	1.5	$6.7 \cdot 10^{-5}$	3.5	0.018	$7.5 \cdot 10^{-7}$	$3.6 \cdot 10^{-14}$	1.5	$1.7 \cdot 10^{-2}$
218	3	$4 \cdot 10^{-5}$	3.5	$2.5 \cdot 10^{-2}$	$6.7 \cdot 10^{-7}$	$5.3 \cdot 10^{-14}$	1.8	$4 \cdot 10^{-2}$
223	1.8	$1.18 \cdot 10^{-4}$	2.3	$3.5 \cdot 10^{-2}$	$3.7 \cdot 10^{-7}$	$1.9 \cdot 10^{-14}$	1.4	$1.8 \cdot 10^{-2}$
230	20	$2 \cdot 10^{-4}$	3.7	$8 \cdot 10^{-2}$	$2.6 \cdot 10^{-6}$	$1.4 \cdot 10^{-13}$	1.4	$1.5 \cdot 10^{-2}$
253	20	$4 \cdot 10^{-4}$	3.3	0.35	$1.4 \cdot 10^{-5}$	$1.5 \cdot 10^{-12}$	2.8	$1.6 \cdot 10^{-2}$
263	30	$8 \cdot 10^{-4}$	3.3	0.49	$1.9 \cdot 10^{-5}$	$2 \cdot 10^{-12}$	3.5-4.2	$2.2 \cdot 10^{-2}$
272	5	$4 \cdot 10^{-5}$	3.3	0.85	$3.5 \cdot 10^{-5}$	$6.4 \cdot 10^{-12}$	4-5.6	$1.7 \cdot 10^{-2}$

Table IV.2 Summary of the parameters obtained after implementing the multistage model

K, which had been running for 3 months. In that reaction, according to the model, all stages are present and in accordance with our previous assumptions all parameters could be derived with a fair degree of reliability. These master parameters are shown on **Fig. IV.5** and in Table IV.3 as “Fit Number 1”. All other parameters are kept fixed as in Table IV.2. The fits with parameters different by 1, 2 or 3 orders of magnitude show even better match to the experimental data (on the basis of STD).

Looking at the graph (**Fig. IV.5**) one can see that all four fits are practically indistinguishable. To examine the situation with the second part of the reaction – the surface coating plus the reaction and the diffusion parts (Table IV.4 and **Fig. IV.6**) – the parameters describing the crack filling are kept as the ones obtained from “Fit Number 1”, Table IV.3. This is justified because the variation in the crack filling parameters keeping the same initial fit does not affect the values of all the rest, since this part can be considered as a constant

background, shortly after the reaction beginning. As seen from Table IV.4 and **Fig. IV.6**, the coating rate constant k_s , and the thickness of the hydrate layer, δ_0 can vary with 3 orders of magnitude resulting in variations in the reaction rate constant, k_r and the diffusion coefficient D up to 56 %, without changing the STD and visibly to influence the overall reaction fit (see also **Fig. IV.4**). The case when the crack filling background additive is changed and compensated by variations in the

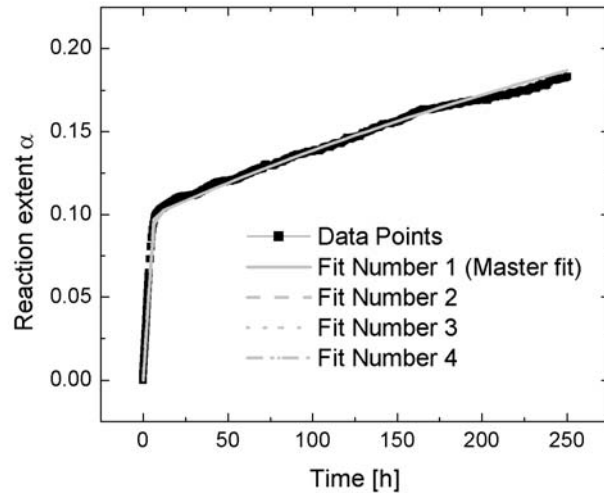


Fig. IV.5 Demo fits with different values for the crack filling parameters as shown in Table IV.3 of the first 250 h of the 3 months reaction at 203 K. The plot displays a fair part of the surface coating and the reaction limited stages. The rest of the reaction is not shown for better visual resolution of the initial part; moreover there is no difference at all between the four fits later.

parameters of the rest of the reaction I will not consider here because the story is already quite confusing. In any case it is clear; this will add degrees of freedom to vary all parameters. Moreover, as mentioned before, this reaction was going for 3 months, thus giving enough room for the model to deploy all its tools for reaction stage treatment.

The conclusion is: with so many free parameters (Table IV.5) and no means to constrain them, there is probably infinite number of “ultimate” fits. Consequently, no reliable values for the activation energies can be obtained (see **Fig.IV.4**). This is not so extremely dramatic for the reaction and the diffusion limited stages, since their coefficients differ only within 55-60 % but for the crack filling and the surface coating the variations are of orders of magnitude. Some other experiments of mine and also of D. Staykova (2003 – 2004 private communications) with the geometry of the model (varying the

Fit Number	δ_0' [μm]	k_s' [h^{-1}]	k_r' [kmol/h.m^2]	STD
1	3.5	0.32	0.00021	0.00204
2	0.35	0.032	0.0021	0.00188
3	0.035	0.0032	0.021	0.00183
4	0.0035	0.00032	0.21	0.00183

Table IV.3 Shows the crack filling parameters’ values used to demonstrate the correlation between them. A little bit of extra tuning can lead even to obtaining the same STD for all 4 runs. All other reaction parameters were kept fixed as they were obtained from Fit Number 1.

Fit Number	δ_0 [μm]	k_s [h^{-1}]	k_r [kmol/h.m^2]	D [m^2/h]	STD
5	2.45	0.005	2.85E-7	7.3E-14	0.00336
6 ($k_s.10$)	0.245	0.05	6E-7	3.75E-14	0.00336
7 ($k_s.100$)	0.0245	0.5	7.35E-7	3.25E-14	0.00336

Table IV.4 Shows the reaction parameters’ values used to demonstrate the correlation between them. The fissure filling parameters were kept fixed as they were obtained from Fit Number 1, Table IV.3. Fit Number 5, Table IV.4. corresponds to the master fit.

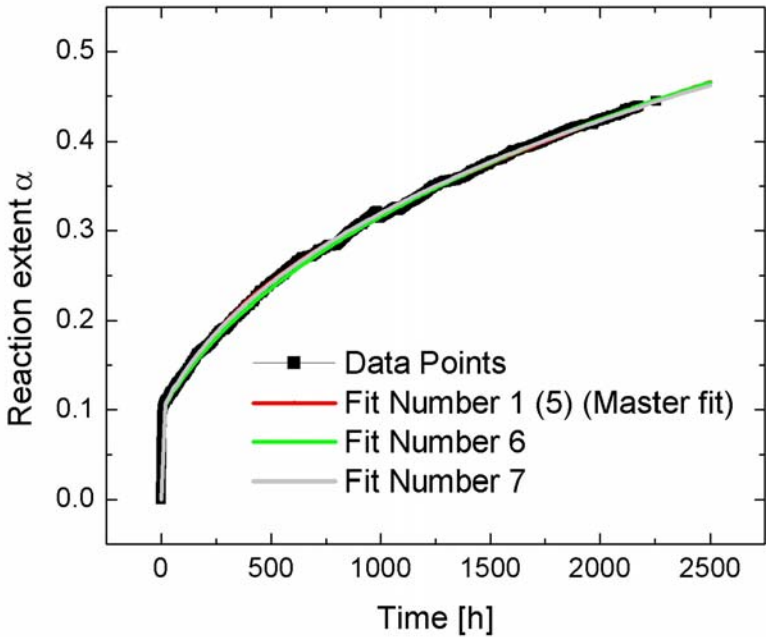


Fig. IV.6 Demo fits with different values for the surface coating, reaction and diffusion parameters as shown in Table IV.4 of the 3 months reaction at 203 K.

distribution's mean and standard deviation, porosities, crack geometry parameters within reasonable limits) also showed significant influence on the simulated reaction development.

At the end let us summarize the parameters required for the model initialization. For clarity I will divide them into three groups (Table IV.5): (1) well-defined parameters, (2) not-very-well-defined parameters and (3) free parameters. To the first group belong the measured parameters. To the second group belong the parameters derived on the basis of some measurements and assumptions. For instance the mean radius and the STD were extracted on the basis of measuring the sizes of the starting ice spheres from SEM images (Klapp 2003, private communication). From several different samples, around 1000 spheres per sample were measured, from that their distribution was built and its parameters derived. The results differed to some extent from set to set. It is clear that far not every sample can be investigated that way, which means some average value for these quantities should be assumed. Moreover, variations of the STD lead to variations in the calculated specific surface area (SSA). Obviously this will affect, for example, the calculated coordination number Z per reference grain (III.10). In any case the negative effects coming as results of the uncertainties carried by the not-well-defined parameters are negligible compared to the possible ones due to the free parameters. To reduce these uncertainties one needs to find ways to constrain all possible parameters. Let us start with the micro-porosity of the hydrate. It was taken to be around what Suess et al. (2002) measured for the natural methane hydrate case. Again the lack of representativity appears here, hand in hand with some purely experimental problems, like the one of the hydrate decomposition, which had taken place upon the hydrate recovery from the ocean floor. It is also uncertain if this parameter stays the same for the different sorts of gas hydrate. Concerning the crack opening angle and the crack void fraction – these are two correlating parameters. Initially the

opening angle was defined from the SEM pictures mentioned above. For a number of reasons the statistics was very poor and the obtained values not fully reliable. The most important thing is that none of the coating rate constants as reaction rate constants and initial film thickness can be constrained. Neither the diffraction nor the SEM observations can be used for this purpose. Concerning the diffusion coefficient, it is traditionally a fitting parameter.

Well-defined parameters	Ice density	1
	Water density in hydrate	2
	Excess fugacity	3
Not-very-well-defined parameters	Initial coordination number, Z_0	1
	Min coordination number, Z_{min}	2
	Slope of the random density function, C	3
	Mean radius	4
	STD	5
Free parameters	Micro porosity of hydrate, ε_h	1
	Crack opening angle, β	2
	Crack void fraction, ε_f	3
	Initial film thickness on grain, δ_0	4
	Initial film thickness in crack, δ_0'	5
	Coating rate constant on grain, k_S	6
	Reaction rate constant on grain, k_r	7
	Coating rate constant in crack, k_S'	8
	Reaction rate constant in crack, k_r'	9
	Permeation (diffusion) coefficient, D	10

And to conclude, the model itself

Table IV.5

has a value of a model, which tries to take into account all possible geometric effects and this way to extract the ultimate values of the transformation parameters for implementation in other types of analyses. Unfortunately it needs constraints, which cannot be applied at present.

1.3.2. With the JMAKGB

To overcome all the problems described above, a new approach needs to be implemented. It should be more robust and lead to a single ultimate solution for every reaction. The way to achieve the goal is to find an interpretation with less free parameters, as well as to rethink the way of data analyses. The main idea of the approach I had chosen was described in Chapter III JMAKGB. The only user-controlled parameter in this treatment is the switch point – or the moment from which on only the diffusion controls the reaction. All other parameters are obtained automatically by least squares fitting, which is not the case with the multistage model, where the fitting is done by certain prescriptions, which are not necessarily based on physical and mathematical arguments. The reason for that was demonstrated a few lines before.

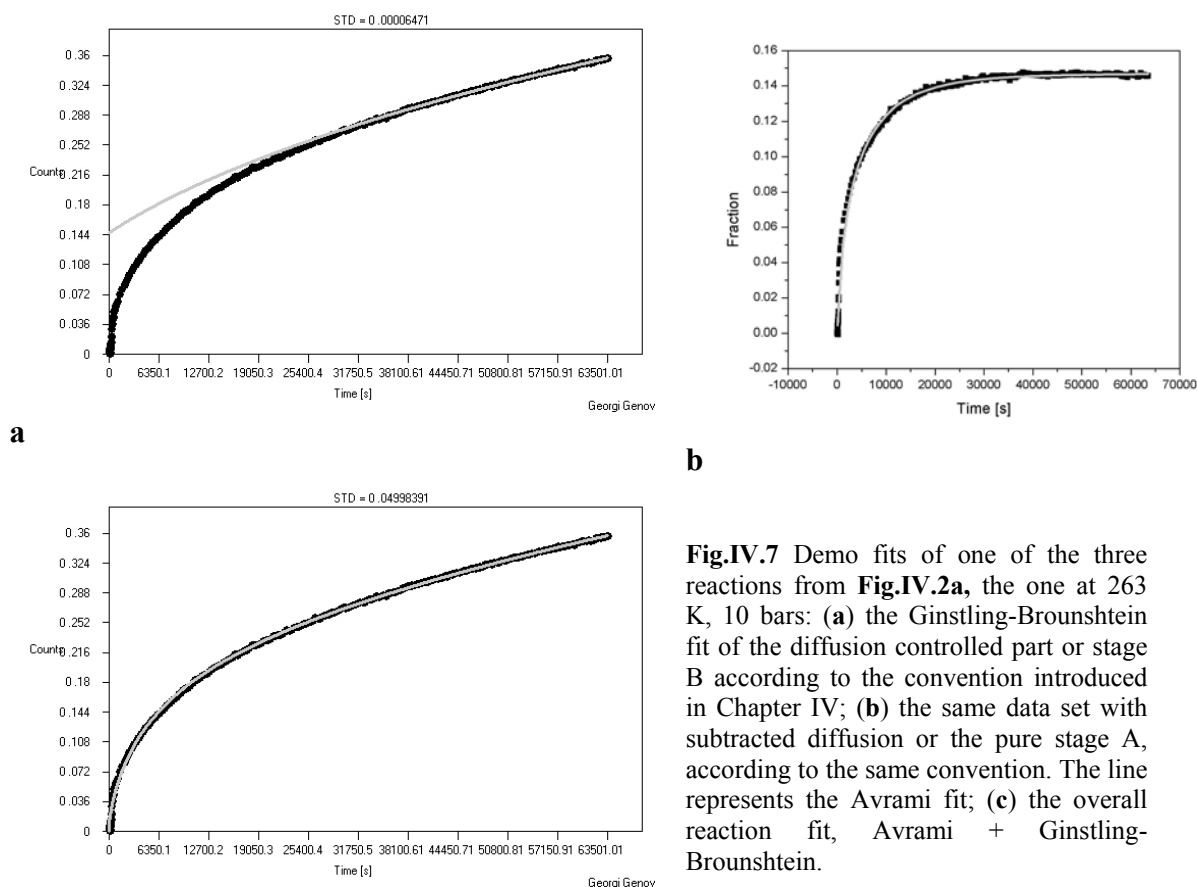


Fig.IV.7 Demo fits of one of the three reactions from **Fig.IV.2a**, the one at 263 K, 10 bars: **(a)** the Ginstling-Brounshtein fit of the diffusion controlled part or stage B according to the convention introduced in Chapter IV; **(b)** the same data set with subtracted diffusion or the pure stage A, according to the same convention. The line represents the Avrami fit; **(c)** the overall reaction fit, Avrami + Ginstling-Brounshtein.

On **Fig.IV.7** one of the neutron diffraction runs at 263 K, 10 bars is shown. The line on **Fig.IV.7a** represents the Ginstling-Brounshtein diffusion fit. The switch point is 9.79 h. Then the data set is corrected for this diffusion and the result is fitted with the Avrami formula (**Fig.IV.7b**). On this basis an overall fit of the data can be obtained and it will be the superposition between both Avrami and diffusion (**Fig.IV.7c**). The criterion of selecting the switch point is that after the correction for the

diffusion the data should flatten as shown on **Fig.IV.7b**. If there is a trend of the corrected reaction to continue to increase or to start to decrease from some point on, one should choose another switch point. Obviously this is an easily defined free parameter. Of course, one should keep in mind that some reactions may not reach far enough in time/reaction extent to define well the diffusion limited stage B. This is the case with the 193 K in-house experiment, for instance.

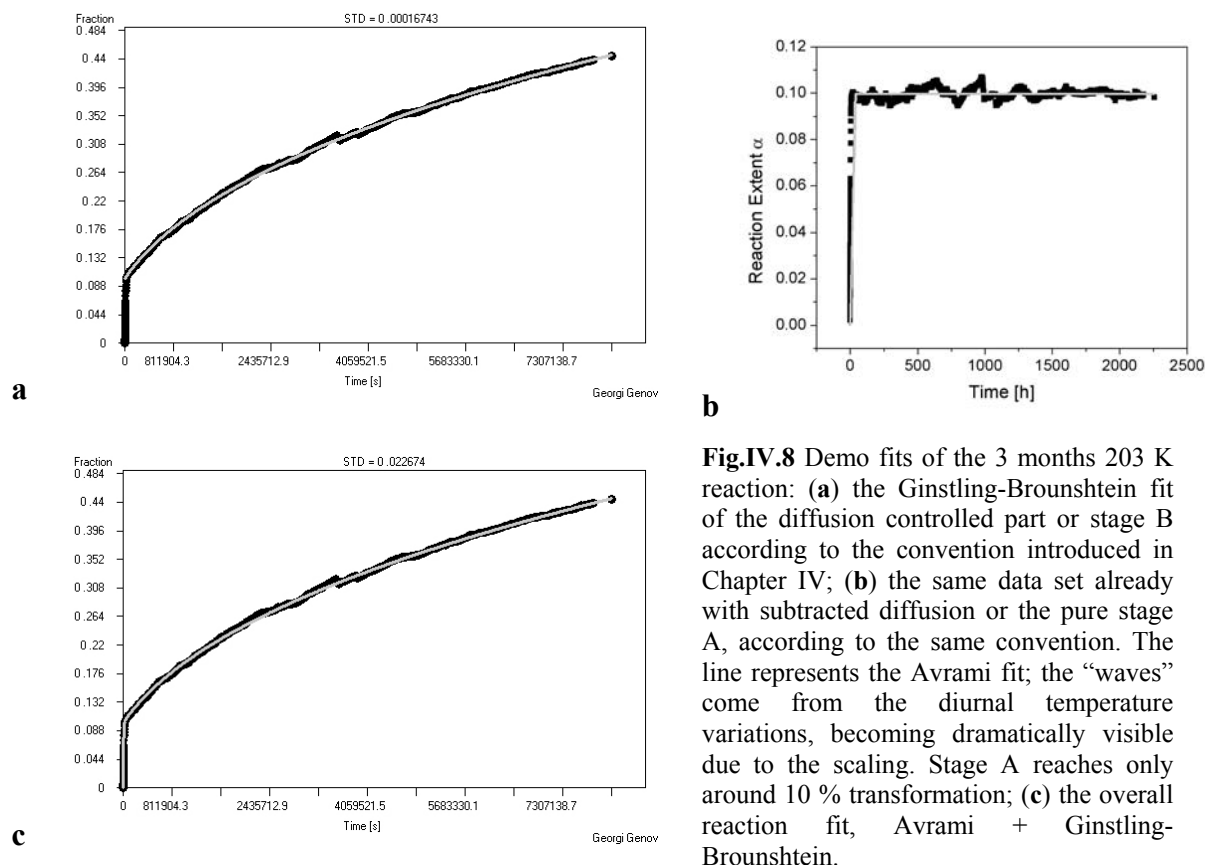


Fig.IV.8 Demo fits of the 3 months 203 K reaction: (a) the Ginstling-Brounshtein fit of the diffusion controlled part or stage B according to the convention introduced in Chapter IV; (b) the same data set already with subtracted diffusion or the pure stage A, according to the same convention. The line represents the Avrami fit; the “waves” come from the diurnal temperature variations, becoming dramatically visible due to the scaling. Stage A reaches only around 10 % transformation; (c) the overall reaction fit, Avrami + Ginstling-Brounshtein.

Following the described procedure I processed all other non-sigmoid reactions. From the Ginstling-Brounshtein fits came the diffusion coefficients for the different temperatures. As mentioned in Chapter III, for deriving the concentrations of the gas at the different pT conditions, I used the van der Waals real gas law. **Fig.IV.9** shows the Arrhenius plot of the diffusion coefficients ($Q_D = 20$ kJ/mol). The error bars are derived on the basis of the difference in the switch point selection, resulting in the best and the worst possible fits taken in “+” and in “-”, i.e. the worst achievable case. If the reaction is long enough, the switch point selection plays a very little role, close to nothing (the three months reaction at 203 K). At 203 K there are three reactions with three different error bars. The analyses of the longest one – 3 months – shown on **Fig.IV.8** gave $D = (2.431 \pm 0.001)^{-16}$ where the uncertainty given is the statistical one. The maximal estimated error value, obtained as described above and also shown on **Fig.IV.9** is around 2 %, compared with the 56 % gotten from the multistage model for the same reaction (see § 1 of this chapter).

The reaction at 223 K comes from the in-house system E1 (see Chapter II) as well as the reaction with the biggest error bar from the 203 K reaction set and the one at 193 K. The runs at 230 K

253 K, 263 K and 272 K are neutron ones.

The two other reactions at 203 K, together with the 213 K and 218 K ones come from the in-house E2b system. The only reaction, which was corrected with the HSC (see Chapter II) was the one at 223 K. For the others it was either unnecessary or it had not been invented yet. Unfortunately, for the present reactions showing sigmoid shape this approach is not applicable since none of them really reaches the stage where only the diffusion governs it. All the parameters from the

Avrami and Ginstling-Brounshtein fits are summarized in Table IV.6.

The Avrami fitting was done with the help of one of the built-in functions of Origin 6.0 – Weibull2 – after a slight modification, leading to the Avrami formula. The Levenberg-Marquardt chi-square minimization was implemented. On **Fig.IV.10** one can see how the pure Avrami formula fits the sigmoid reactions and also the Avrami triple logarithmic plots of the data. The parameters obtained this way are included in Table IV.5.

The first of the Avrami parameters considered here is the one describing the dimensions of the hydrate crystals growth – d . As mentioned in Chapter III, this parameter should stay above 1, since any growth in lower dimensions cannot proceed. Still the values of d between 1 and 0 exist. The diffusion correction brings them above 1 for the low temperature runs but does not do the job at higher temperatures. To shed light upon this problem I will spend the next few lines to discuss the physics behind the Avrami exponent. A more detailed discussion on this and especially on the diffusion controlled grain growth in relation to the Avrami exponent can be found in Pradell et al. (1998) and the references reviewed there. I will allow myself to recall the reader's attention once again at the derivations shown in Chapter IV, namely at the formulae (IV.22) – (IV.35). Lets now rewrite (IV.29) in the shape:

$$\alpha_{ex} = \int_0^t I(T, y) V(T, y, t) dy = \int_0^t I(T, y) S[r(T, y, t)]^d dy \quad (IV.1)$$

where T stays for the temperature, as well as for any other external variables affecting the process; $V(T, y, t)$ is the d -dimensional volume at time t , born at time y with a radius of $r(T, y, t)$ the rest of the assignments are as in Chapter IV. The value of the Avrami exponent comes from (IV.34) assuming an isothermal crystallization, i.e. T is fixed. The radius $r(T, y, t)$ comes from the integration of the

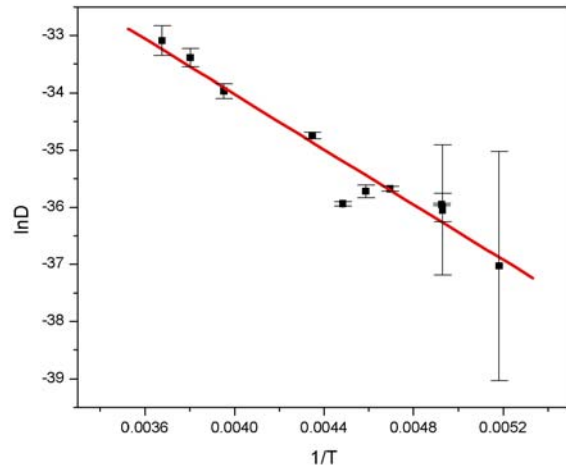


Fig.IV.9 Arrhenius plot of the diffusion-controlled stage B of the CO₂ hydrate formation process at temperatures above 193 K. The obtained value for the activation energy is $Q_D = 20 \text{ kJ/mol}$

growth rate $G(T, y)$. Thus for a constant nucleation and a radius dependent grain growth $G(T, r(y, t))$ the radius is $r(T, y, t) = G_0(T)(t - y)^q$ then (IV.1) becomes:

$$\alpha_{ex} = \frac{I_0 S G_0^d t^{qd+1}}{qd + 1} \quad (IV.2)$$

Temperat. ⁵ [K]	p [bar] Concentr. [mol/m ³]	p _d Dec. Conc. [mol/m ³]	Switch point [h]	D [m ² /s]	A	K	d
185 First Gren.	0.365 23.718	0.124 8.060			0.03976	2E-5	1.78043
185 Gren.	0.266 17.287	0.124 8.060			0.33058 0.84 1	1E-5 5.8649E-6 5.2827E-6	2.35236 2.0453 2.02089
190 Gren.	0.36 22.778	0.178 11.265			0.49434 0.84 1	1E-5 9.8715E-6 8.8247E-6	2.48579 2.16036 2.10464
195 Gren.	0.505 31.127	0.252 15.538			0.81176 0.84	4E-5 3E-5	1.96926 1.87708
193 Home	0.5 31.338	0.22 13.706	116.1 0	(8.3±0.6)E-17 (7.04±0.02)E-16	0.18607 0.07582	6.6345E-6 6E-5	0.49017 1.00626
203 old Home	0.89 53.22	0.433 25.640	3.71	(2.20±0.01)E-16	0.07134	2.9 E-4	0.81574
203 calibr. Home	0.89 53.22	0.433 25.640	21.83	(2.299±0.004)E-16	0.07096	5E-5	1.00726
203 long Home	0.89 53.22	0.433 25.640	13.81	(2.431±0.001)E-16	0.09906	8E-5	1.24679
213 Home	1.5 85.911	0.763 43.044	9.03	(3.19±0.02)E-16	0.05727	1.5E-4	0.9015
218 Home	1.95 109.53	1.005 55.38	42.3	(3.06±0.01)E-16	0.1039	5E-5	0.54825
223 Home	1.95 106.952	1.300 70.007	100.1	(2.46±0.01)E-16	0.13149	4E-5	0.43631
230 Gren.	3 160.772	1.86 97.056	3.08	(8.12±0.01)E-16	0.06099	7.6E-5	0.57066
253 Gren.	10 510.203	5.1 241.143	11.18	(1.77±0.01)E-15	0.15433	2E-4	0.56945
263 Gren.	10 485.436	7.5 340.369	9.79	(3.16±0.01)E-15	0.14693	2.5E-4	0.6733
272 Gren.	20 884.962	11.4 498.437	10.63	(4.25±0.03)E-15	0.39763	2.3E-4	0.66661

Table IV.6 Summary of all parameters derived on the basis of JMAKGB

and the Avrami exponent is equal to $qd + 1$. If there is no change in the transformation mechanism it should be constant through the whole reaction. Considering increasing ($I(T, y) = I_0(T) y^p$) or decreasing ($I(T, y) = I_0(T) (a + y)^{-p}$) nucleation rates gives increasing or decreasing Avrami exponents, which at the end become equal to $p + qd + 1$ and qd respectively. Usually increasing or decreasing nucleation rate is responsible for non-constant Avrami exponents. In the case of interface controlled growth, the growth rate is constant and the Avrami exponent becomes equal to $d + 1$, or 4

⁵ Light gray stays for a sigmoid reaction.

for 3D growth (with constant nucleation rate), 3 for 2D growth etc. For diffusion controlled growth rate, when steady state is reached holds:

$$G(T, r) = \frac{dr}{dt} = \frac{D_0(T)}{r} \Rightarrow r(t, y) = 2\sqrt{D_0(T)(t - y)} \quad (\text{IV.3})$$

which leads to a value of the Avrami exponent of $1 + d/2$, for a constant nucleation rate (5/2 for the 3D growth). For primary transformations where a 3D diffusion controlled growth rate is expected, the minimum value even for decreasing nucleation rates is $qd = 3/2$. For a decreasing growth rate with constant nucleation rate, the minimal expected value for the Avrami exponent is 1. Values of the Avrami exponent below 1 are normally attributed to **decreasing nucleation and growth rates**. This can be a result of the mixing of the lognormal starting material (relatively low SSA) with frost (large SSA), as discussed in the previous paragraph. On one hand the frost contains many more surface nucleation sites and on the other hand it is consumed much faster than the rest. This may lead to decreasing nucleation and growth rates. Pradell et al. (1998) also demonstrated that the consideration of a diffusion-controlled growth with soft impingement⁶ would explain such anomalous behavior of the Avrami exponents without introducing a decreasing nucleation rate. Then the Ginstling-Brounshtein model does not succeed to correct for it completely because it is also a shrinking core approach exactly as the multistage model. I assume that works as a mean-field approximation but it may also fail completely due to a strongly inhomogeneous reaction development across the sample. Another explanation may be that in the beginning the diffusion coefficient is different from the following one, obtained from the Ginstling-Brounshtein treatment, since for the second only a hard impingement is assumed. The mathematics of processes with changing diffusion coefficients differs significantly from the one used here. Evidence supporting the diffusion idea is that the sigmoid reactions at 185, 190 and 195 K do not show any anomalies in the Avrami exponent. The starting

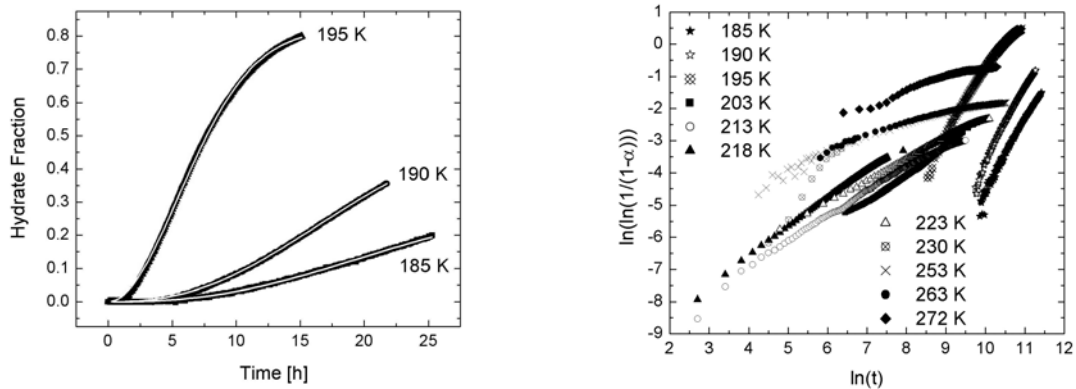


Fig.IV.10 (a) Sigmoid runs fitted with the Avrami formula; (b) the Avrami triple logarithmic plot of most of the data sets, which should lead to a linear data representation.

⁶ As crystallization proceeds the diffusion profiles of neighboring grains begin to overlap appreciably (soft impingement), leading to a further decrease in the growth rate due to the reduction in the concentration gradient

material for these runs was the one with the very large SSA of $14 \text{ m}^2/\text{g}$. This gives an equivalent ice sheet with an area of 14 m^2 and a thickness of 77 nm . Obviously this is a thin layer for the gas to penetrate, compared to the ice spheres with $54 \text{ }\mu\text{m}$ radii. The Avrami exponents there are around 2, which is reasonable since the hydrate formed consists of 3D crystals of the order of a μm as well as of some fluffy material looking like something between dendrites and scales (**Fig. IV.11**).

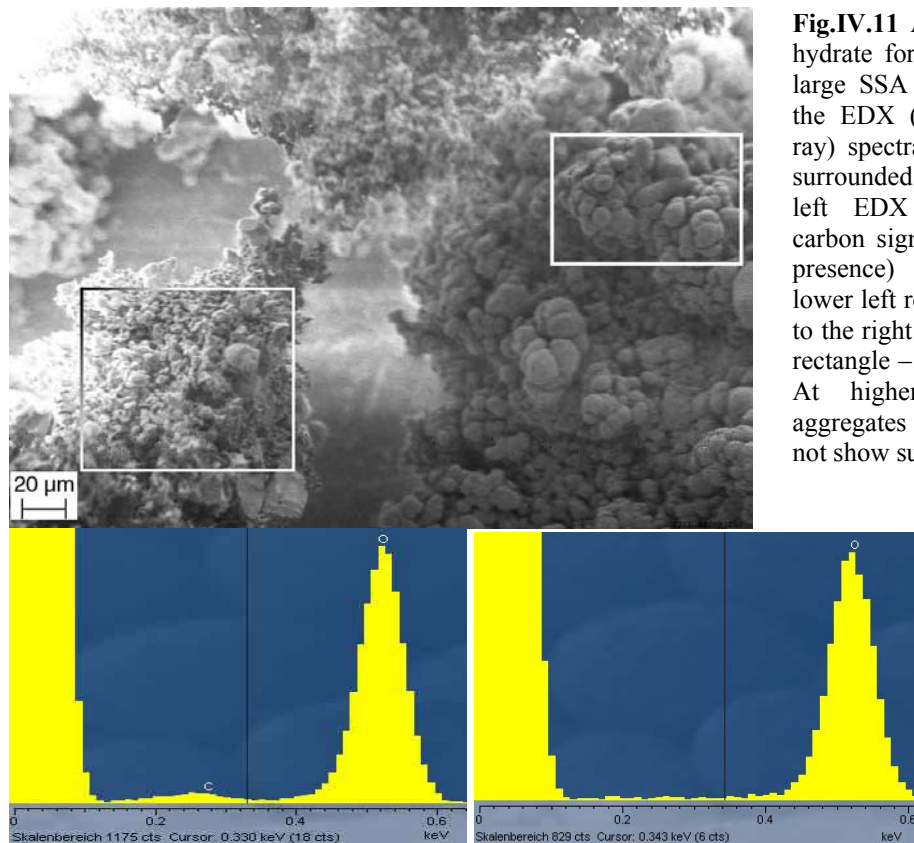


Fig.IV.11 Appearance of the gas hydrate formed at 185 K from a large SSA starting material with the EDX (Energy dispersive X-ray) spectra taken in the regions surrounded with rectangles. The left EDX spectrum with the carbon signal (a sign for hydrate presence) corresponds to the lower left rectangle. The spectrum to the right is taken from the right rectangle – remaining starting ice. At higher magnification the aggregates of hydrate crystals do not show submicron porosity.

To summarize: in this treatment there are practically 5 free parameters: diffusion coefficient D , switch point, and the three Avrami parameters. D depends insignificantly on the switch point. But A depends on it and, from there on so do d and K . Unfortunately, no reliable numbers for the first part of the reaction can be obtained due to possible effects like decreasing nucleation and/or growth rates or changing diffusion coefficients. One can see that this treatment provokes more questions than gives answers but nevertheless, I consider it as giving better physical insights to the processes involved in the hydrate formation on a “macroscopic” level. As a disadvantage one can consider the dependence of the results on the geometry of the starting material, but in any case this is unavoidable.

Unfortunately, a comparison between the results of both approaches cannot be done directly, since the multistage model presently contains three stages but the JMAKGB has only two. Eventually, after removing the reaction-limited stage from the multistage model, which in a way “consumes” from the surface coating and the diffusion-limited stages, such comparison may become possible.

§ 2. Experiments on CO_2 hydrate decomposition

2.1. Starting material and experiments

As a starting material for the CO₂ hydrate decomposition *in situ* neutron diffraction experiments were used CO₂ clathrate samples (~ 97 %). They were prepared as follows: deuterated ice was crushed into a very fine powder under a nitrogen atmosphere. This ice was then filled in the aluminum cans already mentioned in §1 of this chapter. These cans with the crushed ice were loaded into a big pressure cell and were reacted at –10°C and 25 bars CO₂ pressure for nearly three weeks. The hydrate formed this way was stored in liquid N₂ and transported to ILL. The hardware employed for these experiments was the vacuum setup used in the low-pressure formation runs.

The sample cell, already fixed to the sample stick (**Fig. II.6**) was cooled in dry ice while the air was evacuated from the system. Afterwards, around 1 bar of CO₂ was introduced into the system to avoid inflation with normal air upon opening the Bridgman seal for the sample loading. The Al can was put into the cell and a pressure providing conditions of stability for the clathrate sample was applied. The sample stick was introduced into the “Orange cryostat”. The pressure in the sample environment was manually kept in the narrow region of hydrate and gaseous CO₂ coexistence all the way down to the requested reaction temperature. Otherwise, dry ice would have been formed (see **Fig.I.7**).

After achieving temperature equilibrium, the reaction was ready to go, the pressure in the system was reduced to 6 mbar – Martian conditions – and the data acquisition began. The only exception was the reaction at 260 K, 1 bar. Five decomposition reactions were followed: 170 K, 200 K, 220 K and 260 K at 6 mbar and 260 K 1 bar. The runs lasted 3 – 12 h, again using D20 at its highest intensity setting, at $\lambda = 2.414 \text{ \AA}$.

Table IV.6 Summary of the decomposition reactions used in the present study. It shows the reaction temperature and pressure, p ; the decomposition pressure for the given temperature, p_d , and the corresponding gas concentrations, calculated from the van der Waals real gas law. The decomposition pressures calculated as in Table IV.1. The duration of each run is also shown.

Temperature [K]	p [bar] Concentration [mol/m ³]	p_d [bar] Dec. Conc. [mol/m ³]	Duration [h]
170	0.006 0.4245	0.037 2.6176	12
200	0.006 0.3608	0.349 20.9783	9
220	0.006 0.328	1.118 61.039	5
260	0.006 0.2776	6.69 307.3433	3.5
260	1 46.2116	6.69 307.3433	5

A summary of the decomposition reactions with their thermodynamic conditions and durations are given in Table IV.6.

2.2. Data analyses and discussion

The results from all performed neutron diffraction experiments on CO₂ hydrate decomposition are shown on **Fig.IV.12**. The 170 K reaction (1) is extremely slow but plotted on a larger scale it is visible that it starts to develop an inverted S-shape curve similar to the one at 200 K (3). Interestingly,

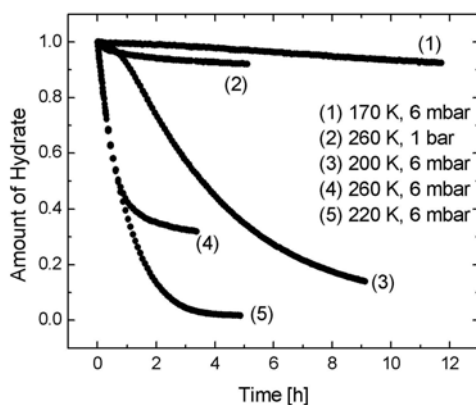


Fig.IV.12 All CO₂ hydrate decomposition runs. Self-preservation is observed in the 260 K reactions.

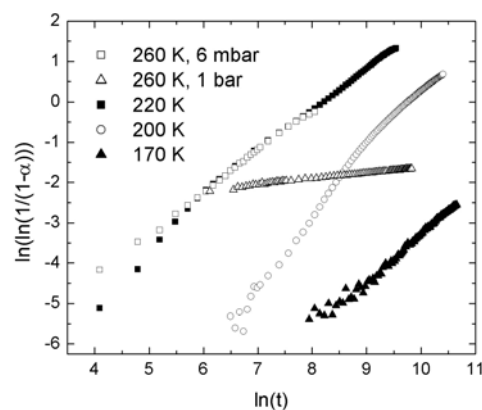


Fig.IV.13 Avrami plot of all decomposition reactions.

run (2) at 260 K, 1 bar decomposes also very slowly and looking at **Fig.I.10** it becomes clear that its pT conditions are deeply in the anomalous preservation region established by Stern et al. (2001) for the CH₄ hydrate case. This observation confirms the appearance of anomalous preservation in the CO₂ hydrate case reported by Stern et al. (2003). Reactions (1), (3) and (5) should be out of this peculiar region, according to the nomenclature of Stern et al. and they really behave as if the temperature regulates the decomposition rate till completion (at least for (3) and (5)). Despite the fact that the reaction at 260 K, 6 mbar is in the preservation temperature region the decomposition starts very fast (as in (5)), passing the 50 % limit in less than 1 hour, but suddenly slows down and almost stops at about 30 % hydrate left. Following the Stern et al. nomenclature, this is not anomalous preservation since they build the preservation picture on the basis of “Time to 50 % dissociation” (see **Fig.I.10**). But as long as there is 30 % hydrate preserved, it is anomalous preservation (or perhaps more accurately “anomalous slowing down of the reaction”). Still one can argue if this is a real self-preservation or an artifact caused by a blockage of the stick leading to a pressure build-up in the sample volume, stabilizing the remaining hydrate. This is very unlikely for the system used in this run since, on one hand, it is kept out of the dry ice formation conditions with the help of the stick capillary heating and on the other hand, the stick tube inner diameter is 5 mm at the narrowest point. It is very unlikely at the present conditions to build a *bouchon* of dry ice capable to stand almost 7 bar decomposition pressure.

Table IV.7 Summary of the parameters of the Avrami treatment of the CO₂ hydrate decomposition neutron diffraction runs.

T [K]	<i>A</i>	<i>K</i>	<i>d</i>
170	1	2.74E-6	1.166
200	0.91	6E-5	1.4285
220	1	2.8E-4	1.0109
260 (6 mbar)	0.68	4.8E-4	1.0733
260 (1 bar)	--	--	0.14

Since the data sets are by far not enough in number to develop any serious theory about the kinetics of the CO₂ hydrate dissociation, here I can only try to give some hints about a possible way of

analysis⁷. The hydrate decomposition can also be considered as a growth of ice. Then all these descending clathrate dissociation curves from **Fig.IV.12** can be considered as sigmoid ice growth functions. As soon as the ice growth out of hydrate is again a nucleation and growth process, as discussed in Chapter IV, an attempt for treating it with the Avrami theory is justified. Concerning the Ginstling-Brounshtein part of the treatment it may appear necessary for the self-preservation cases. In any case none of the datasets allows for trying diffusion approaches, since they are all too short. Therefore, at this stage I will limit myself to considering the reactions as pure nucleation-and-growth ones. The first thing to do in such case is to have a look at the Avrami triple logarithmic plot (**Fig.IV.13**). All reactions show more or less linear behavior, which is in favor of the theory. The only run with a peculiar slope is the one at 260 K, 1 bar. This is the preservation run at the conditions for which Stern et al. observed the methane hydrate anomalous preservation. Nothing can be said about this run since the transformation extent is very limited and the kinetics itself does not show any clear S-shape. But all the rest, including the reaction at 260 K, 6 mbar, show similar slopes, i.e. very similar transformation behavior. The results of the fitting can be found in Table IV.7.

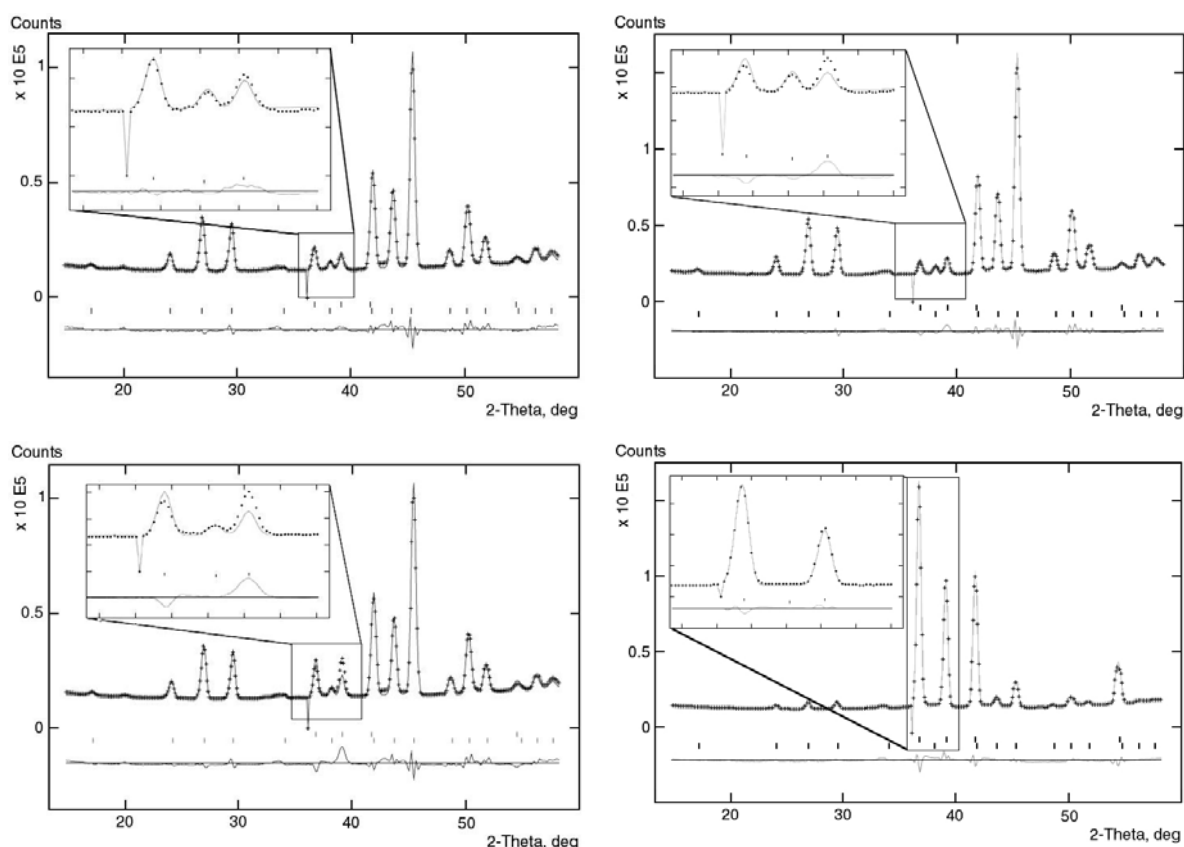


Fig.IV.14 Diffraction patterns and Rietveld-fits for various stages of the decomposition at 170 K (left column) and 200 K (right column). A model fit assuming perfect ice Ih was used and the differences between observed and calculated profiles as well as tick-marks indicating the reflection positions are shown (top phase ice Ih, bottom phase hydrate). The inserts show zoom-ins of the 100 and 002 reflections of ice (at approximately 39° in 2-Theta). The beginning of the reactions – figures on top and the ends – bottom figures; after 12 and 9.5 h for 170 and 200 K respectively.

⁷ Takeya et al. (2001, 2002) treated their data on decomposition of CH₄ hydrate using the diffusion formula of Dünwald-Wagner-Serin-Ellickson (III.59).

An inspection of the diffraction features of the ice obtained upon gas hydrate decomposition clearly shows that imperfect ice Ih is formed at 170 K (see **Fig.IV.14**). It is worth noting that the starting ice in this case is almost perfect, suggesting that some annealing of most of the stacking faults (clearly visible as shoulders of the main hexagonal diffraction peaks after the decomposition) has taken place (most likely, during loading the sample into the sample stick and waiting for the temperature establishment). In contrary, the starting material for the 200 K decomposition is very defective initially. At the end of the run, the produced ice does not show any appreciable degree of defectivity. Obviously the higher the temperature goes, the higher the cooperative mobility of water molecules becomes, thus leading to annealing of defective crystallites with a resulting closing of existing pathways for gas diffusion. This in turn leads to the on-set of anomalous preservation (Kuhs et al. 2004). At this point, the gas molecules can only escape by solid-state diffusion, which slows down the decomposition reaction by orders of magnitude. It should be noted here that high gas pressures are not obligatory to stabilize the gas hydrate. What is needed is a chemical activity of the gas at the hydrate surface, which corresponds to conditions inside the stability field. Continuing in this direction leads to the impression that the self-preservation should not be a “threshold-like” effect as suggested by **Fig.I.10**, since the speed and degree of annealing depend on the temperature and may even compete with the hydrate-to-ice transformation rate. Subsequently the diffusion will become involved in the process to a different extend at different temperatures. The 200 K run supports this deduction with its highly asymmetric S-shape (see **Fig.IV.12**) and the ice produced at the end with a high degree of perfection.

§ 3. Topological observations – hydrate foam structure

In the year 2000 the porous microstructure of the gas hydrates was found (Kuhs et al. 2000). It was observed even in the CO₂ hydrate case, though the pore size was much smaller. This raised first questions about the possible influence of the pores on the further transformation of ice, remaining underneath the porous hydrate, as well as on the hydrate decomposition. The first assumption was that the pores, having some connectedness, were pathways for the gas to reach the buried ice and for the excess water to get out. On this basis the reaction limited stage was introduced in the multi-stage model. In any case, there were evidences neither for the connectedness nor against it. To clarify this situation I decided to have a careful look at some selected FE-SEM images. For this purpose, I got pictures of the CH₄ hydrate sample produced together with A. Zeller at –8.8 °C and 60 bars in 2002. This sample was interesting because after the recovery it was crushed and by sieving through sieves with different sizes, it was separated in different fractions. The only fact of crushing the sample already made clear that some inner surface would be discovered. The picture looked always the same (e.g. see **Fig.IV.15**), regardless of the orientation, i.e. the structure was homogeneous in every direction. It resembled a sponge for washing dishes, which meant it was foam.

To put an end of an argument, which has not yet begun, let me define what foam is: it is a solution, which consists of interconnected network of struts or plates, which form the edges and faces of cells (**Fig.IV.16**). Most commonly the cells are polyhedra, packed in 3D, forming the foam. If all the material forming the foam is concentrated along the Plateau borders (i.e. there are no lamellae), the foam is open-celled. If the lamellae exist, i.e. the neighboring cells are sealed off from each other, then the foam is closed-celled. Of course, some kinds of foam are partly open and partly closed. Obviously, the definition is very broad. For instance, the polyurethane forms open-cell foam, the polyethylene – closed-cell, the polyether – both closed- and open-cell. Foams form metals like nickel, copper, zirconium, titanium also the glass. There are many examples of naturally formed foam as for instance cork, natural sponge, cancellous bone, coral etc. The bread and the aero chocolate are foams too. Clearly the foams do not finish with the soap and the beer froth, which is what the people usually think for when they are told about foam, as my experience has shown.

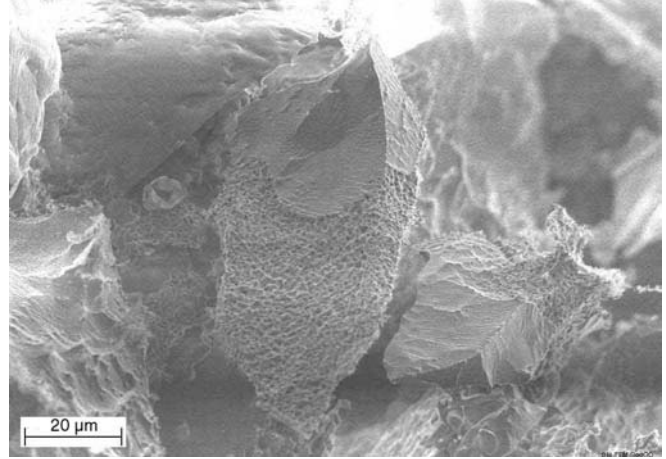


Fig.IV.15 Example of a crushed piece of CH₄ hydrate. In both dimensions it looks the same. Still untransformed ice is visible.

The attempts to qualify and quantify the foam structures date back to Leonhard Euler, Josef Plateau and William Thomson. They have discussed the possible ways of space filling, coordination numbers, equilibrium rules etc. One of the most important parameters of the foam is the degree of “wetness”. It is expressed by its volume liquid/solid fraction Φ_s or gas fraction Φ_g :

$$\Phi_s = 1 - \Phi_g \quad (\text{IV.4})$$

The volume (average volume) of a cell or bubble is:

$$V_b = \frac{4\pi}{3} \left(\frac{d}{2} \right)^3 \quad \bar{V}_b = \frac{4\pi}{3} \left(\frac{\bar{d}}{2} \right)^3 \quad (\text{IV.5})$$

Then obviously:

$$N_b \bar{V}_b = \Phi_g \quad (\text{IV.6})$$

where N_b is the number of bubbles.

Another interesting parameter, which is *de facto* the most important for the kinetic investigations, is the connectivity of the foam or in other words how much it is open-celled or closed-celled. An attempt to clarify this follows.

The results shown next, are obtained by taking electron micrographs of gas hydrate samples with the proper magnification and measuring the diameter of every single bubble in an attempt to

achieve good counting statistics (counting). In general it takes from one to three days to count one thousand bubbles.

As mentioned before, the CO₂ hydrate forms bubbles much smaller than the other hydrates and often they are beyond the resolution of the microscope. Only at high temperatures they allow for counting. For that reason the results I show here are based exclusively on counting CH₄ hydrate and only one result from CO₂ hydrate is given. On **Fig.IV.17 left column** is shown one of the pictures used in the counting. Totally three distributions were created for three different bubble “plantations” – two of them from one sample and one from a different run. On this basis their foam parameters were derived, as described above. The results are shown in TableV.8 together with the one for the CO₂ case (**Fig.IV.18 right column**). The bubble size distribution appeared to be lognormal in both cases – CO₂ and CH₄ hydrate.

One should mention here the problems of this counting. It is not only the time and the pain stacking labor for obtaining these results. There are purely technical problems. First of all it is necessary that the picture that is used for the counting is perpendicular to the incident electron beam, since there is no way to estimate any tilt and to correct for it the measured bubble diameter. Secondly, the resolution – one needs to compromise between the best resolution and the possible charging effect. This often leads to the wicked situation of finding a wonderful surface but with a bad achievable resolution. Thirdly, the locality of the electron microscopy, already discussed before – 1000 bubbles counted at this place does not make the picture representative for the whole sample. Most probably the distribution will be always lognormal throughout the whole sample but it will differ in mean and standard geometric deviation. All these things lead to the conclusion that an automatic image processing procedure needs to be implemented (one attempt of mine in this direction can be found in **Appendix IV**).

Counting the bubbles whose bottoms are not visible can give an estimate for the connectivity of the foam. The number of the bottomless bubbles obtained from the CH₄ hydrate pictures is around 30 %. This should be considered as the highest bound since the electron beam and the high vacuum conditions lead to sample etching. The first parts of the hydrate surface, which will sublime are the thinnest ones or the lamellae. This will lead to opening new and new holes and create an artificial connectivity. This effect, which appeared to be dramatic initially, was investigated in detail and even a film of the development of the artifacts was made. Unfortunately, for technical reasons I cannot show it on the pages of this thesis. But if one takes an overestimated number of, let us say, 40 % connectivity that means a surface covered with 1000 bubbles, of 465 nm diameter on average (CH₄

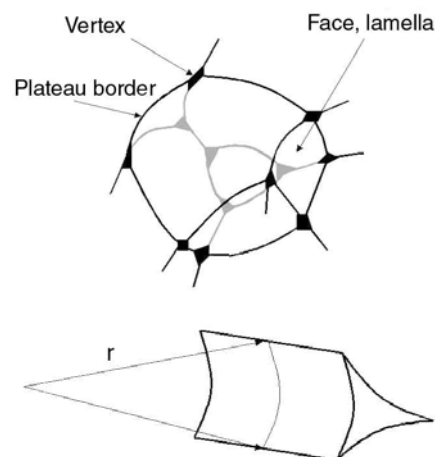


Fig.IV.16 polyhedral foam cell (left) and a zoom-in with the cross-section of a Plateau border (right). The cross-section of a Plateau border is a concave triangle.

case), will have contact with only one bubble belonging to the sixth bubble level, which is less than 3 μm depth. This leads to the conclusion that in this particular case the CH_4 hydrate foam structure is poorly connected and cannot serve as an appreciable pathway for gas and water transport to

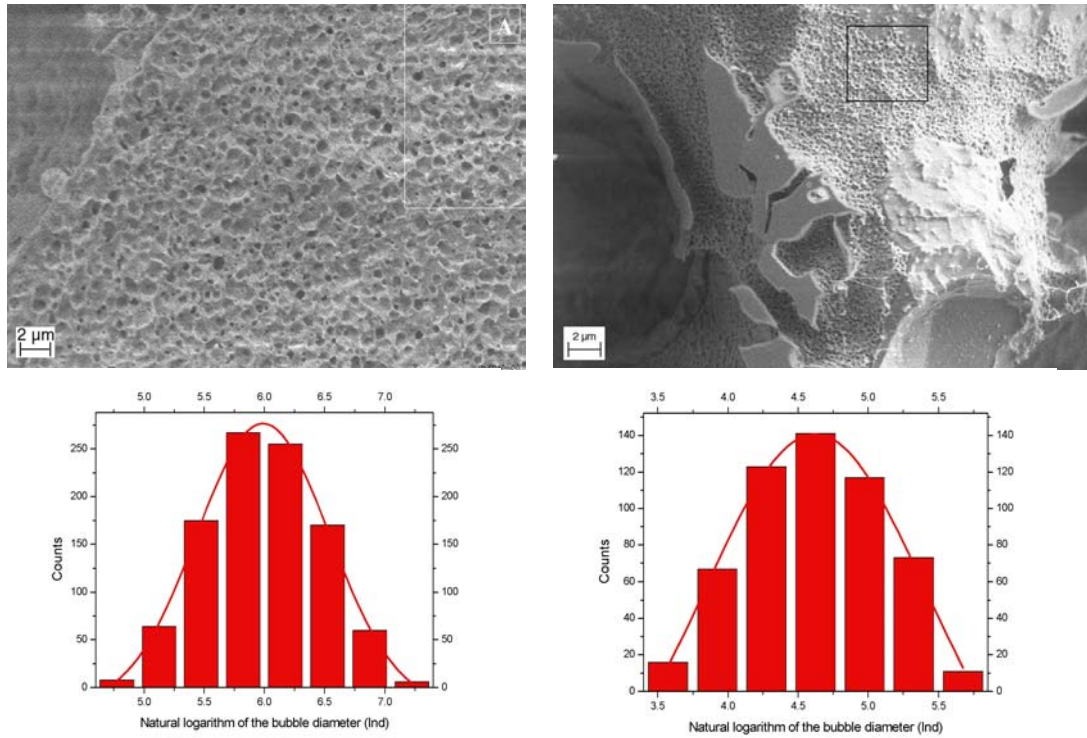


Fig.IV.17 (left column) CH_4 hydrate formed at -8.8°C , 60 bar and its bubble size distribution: mean 5.99, STD = 0.56, average bubble diameter of 465 nm, based on 1005 bubbles; (right column) CO_2 hydrate formed at -10°C , 10 bar and its bubble size distribution: mean 4.62, STD = 0.78, average bubble diameter of 137 nm, based on 548 bubbles.

and from the ice underneath. This estimate was confirmed for the whole sample by the BET measurements (Zeller 2004) for the CH_4 case. The measured samples quenched after different times of reaction at the same conditions (different transformation extents) showed almost the same SSA within the uncertainty. Whether or not it can be extrapolated to the CO_2 hydrate case is not sure. But since the counting suggests that the CO_2

and CH_4 hydrate foams appear to differ only in mean and standard geometric deviation keeping the same distribution shape (CO_2 hydrate foam is a scaled down version of the CH_4 hydrate foam), such

Gas	Conditions of preparation		Average Bubble Diameter [nm]	Average Bubble Volume [μm^3]	Gas Fract. Φ_g [%]	Solid Fract. Φ_s [%]
	Temperat. [$^\circ\text{C}$]	Press. [bar]				
CH_4	-8,8	60	465 ± 3	$0,053 \pm 0,001$	38 ± 1	62 ± 1
CH_4	-8,8	60	319 ± 7	$0,017 \pm 0,001$	60 ± 3	40 ± 3
CH_4	0	600	627 ± 25	$0,13 \pm 0,02$	32 ± 4	68 ± 4
CO_2	-10	10	137 ± 12	$(1,3 \pm 0,4) \cdot 10^{-3}$	39 ± 5	62 ± 5

TableV.8 Summary of the results of the counting of the different SEM images.

extrapolation seems justified. This result also confirms that the multi-stage model described and demonstrated previously needs a revision for the reaction-limited stage.

CO₂ clathrate hydrates on Mars – yes or no?

(Conclusions and outlook)

The reader already became acquainted (in Chapter I) with the most important effects of the possible CO₂ hydrate existence on Mars. Now, let me try to summarize the results of this work in the light of the Martian near-surface atmospheric and subsurface pressure-temperature conditions. All CO₂ hydrate formation experiments performed and represented here, were at temperatures between 185 K and 272 K and at pressures from 0.27 to 20 bars. This roughly corresponds to a region, which extends approximately between 60°N and 60°S or in somewhat more Martian terms, from the crater of Lomonosov, to the north, to the south most parts of *Argyre planitia*, and to depths from 1 m to 200 m, depending on the latitude. This covers at about 87 % of the Martian surface, but the remaining 13 % include the polar caps. Clearly, these 13 % are of major importance, since these are the places where the most significant water deposits exist and therefore, CO₂ hydrate can be searched on the surface of Mars. Unfortunately, going down to temperatures as low as 150 K for a long time is a technical challenge, which is on its way to find its solution in our labs in the second and the third period of this project.

In the first chapter I put forward a number of questions, which needed to be answered. Here I will repeat and try to clarify them in the light of the present results.

1. How fast do CO₂ hydrates form?
2. What limits their growth?
3. What controls the hydrate decomposition? Is a catastrophic decomposition likely?
4. Are the physics behind hydrate formation and decomposition similar? In particular, for accumulation in diurnal or seasonal cycles, it is important which of the processes is faster.
5. Can we describe better the hydrate microstructure, which certainly affects its physical and mechanical properties?

Apparently, the first two questions go hand in hand and once realizing what limits the hydrate growth, this will give a clue about the rates of reaction development. The experimental results and their analyses in Chapter IV demonstrated the tremendous **influence of the ice surface available for reaction**. But on one hand the large specific surface area provides many more nucleation sites; on the other hand this reduces the potential diffusion problems. These problems are in fact very serious, since firstly the diffusion law depends strongly on the geometry and secondly there are not too many geometries, for which the diffusion equation has practically applicable analytical solutions. The logic conclusion is that the larger the SSA is, the closer to the purely reaction limited transformation we come. Of course, one should always keep in mind possible transformations undergone by ice at

temperatures above 195 K, which may lead to annealing or even to a surface loss due to consolidation (at higher temperatures). In Martian terms, the compression caused by the weight of overlaying deposits may also lead to consolidation and loss of SSA, if the transformation goes in depth. It is clear one has to compromise with the diffusion through the hydrate layer by trying to quantify it as well as possible. Obtaining its activation energy will help calculating the diffusion coefficient for any temperature. Thus, using the results listed in Chapter IV, for a temperature of 150 K, the extrapolated diffusion rate coefficients are 2.68×10^{-18} m²/s and 8.45×10^{-18} m²/s after the JMAKGB and the multistage model, respectively. Still it is not clear if such extrapolation is justified. As seen from Chapter II, § 2, the low-temperature bath used for the long-term in-house experiments could not go below 193 K. On the other hand, the limited beam time on D20 did not allow for sufficiently long runs below 185 K. For these reasons, the temperature region between 140 K and 185 K (roughly corresponding to the Polar Regions) was not covered. Moreover, the nucleation behavior at these temperatures is not clear. It may be that below some temperature the nucleation proceeds on a geological time scale. Fortunately, the technical problems seem to have found their solution, given that a new cryostat arrived in our labs and this temperature interval will be investigated during the next period of this project. Nevertheless, assuming such an extrapolation can be done, one can estimate the timescales for hydrate formation on Mars, using the apparatus already discussed in Chapter III, §2. Supposing typical Martian Polar Region surface conditions, i.e. temperatures of about 150 K and pressures around 6 mbar, it can be calculated that a given volume of ice with a specific surface area of around 0.1 m²/g, will be half transformed into CO₂ hydrate in approximately 10 000 yr and fully transformed – in approximately 90 000 yr, disregarding the initial reaction-controlled part and allowing only the diffusion to control the transformation. If this holds it would be unlikely to find much hydrate on the surface due to seasonal variations. A similar calculation can be made to see if there are places on Mars where CO₂ hydrate can be formed in shorter period, e.g. 1 earth year (approximately ½ Martian years). This appears possible in regions where the temperature is above 200 K. Such surface temperatures are relatively common for the areas locked between approximately 27°N and 27°S, i.e. south of Curie crater and north of *Nirgal Vallis*. But according to the remote sensing observations, there is almost no water there down to 1 m depth to form the hydrate. Going north (or south) from the 27th parallel, to keep the temperature above 200 K, one needs to go deeper in the regolith. At about 70° north or south this temperature is reached as deep as 500 m under the surface. These are by far not very optimistic conclusions but nevertheless, it is worth mentioning that they should be considered as low estimates, since the starting ice there is expected to have much larger SSA (at least on the surface in the Polar Regions). Moreover, the first part of fast transformation, resulting in around 10 % formed hydrate, is totally neglected and including it may earn several thousand years. The reason not to include the initial fast reaction part was illustrated in Chapter IV. Since at some conditions the formation reaction reveals a sigmoid shape and in other cases it does not, this leads to,

sometimes peculiar parameters, describing the nucleation-and-growth stage, most likely because of frost collection problems in the starting material (see Chapter IV, §1, 1.3.1). The calculations demonstrated here are based entirely on the JMAKGB, since, as discussed in Chapter IV, the multistage model needs some modifications suggested by the experimental observations, namely cutting off the reaction limited stage.

Concerning the CO₂ hydrate decomposition – it seems that at temperatures below 220 K diffusion plays a small role. Its influence grows with increasing the temperature, since the mobility of the water molecules in the ice becomes high enough to cause the closing of a great deal of the paths for easy out gassing, by forming a contiguous shell of ice crystallites, encapsulating the remaining hydrate. Thus the diffusion comes to the fore. This appears to lead to the onset of the anomalous preservation, which may appear to be of significant importance for the Martian terra-formation processes. For instance, if the achieved temperature at a certain depth in the regolith becomes higher (see Chapter I) then the one of the ice melting, one would expect catastrophic outflows (if there is ice present). If there is CO₂ hydrate instead of ice, it may still be stable, thus preventing a catastrophic event. Another possibility is that at some place in the regolith, the temperature goes out of the hydrate stability field but still stays well below the ice melting point. This will lead to hydrate decomposition into ice and gas. The gas will tend to move to the surface, forming some kind of out-gassing feature (e.g. Martian spiders in the South Polar Region). Since the ice formed this way has a smaller volume than the hydrate, this may lead to the formation of grooves alongside the out-gassing features. Obviously, the anomalous preservation effect would be of major importance in such cases. Unfortunately, there is no detailed investigation of the anomalous preservation region for the CO₂ hydrate and the results presented here are very intriguing but still preliminary. Long term dissociation experiments in the whole temperature region from 140 K to 272 K need to be performed and they are also foreseen for the next period of this project.

The question about the similarity between the physics of the hydrate formation and decomposition processes was already addressed several times in the text (see Chapters III and IV). Since, both types of reactions are nucleation-and-growth with diffusion involved, the mathematical apparatus used in both cases will be, if not the same, at least very similar. A difference due to the sample geometry is expected in the implemented diffusion laws.

The physical properties of the materials are connected to their composition and structure at all scales. The CO₂ hydrate, with its porous microstructure, is particularly interesting in this context. The knowledge of its thermal conductivity may play a major role for a better understanding of the basal melting of the Martian polar caps and their rheology. Of course, the microstructure can influence significantly the hydrate decomposition kinetics. This may also affect the remote infrared clathrate detection, since the different microstructures lead to different reflectivity. Clearly, the porous hydrate will have much smaller albedo than a dense one. Image processing software is being developed for

fast quantification of the hydrate foam structure. Information on its present status can be found in **Appendix III**. A series of BET measurements of the specific surface area of the CO₂ hydrate are to be performed in future on the system existing in our labs for such observations to help to estimate its connectivity.

Recently in our department a DTA/TG-DSC analyser with a coupled quadrupol mass spectrometer (Netzsch STA 449 Jupiter) was installed. During the second and the third period of the project, experiments on CO₂ hydrate decomposition with this instrument are to be performed, in order to shed further light on the energetics of the reaction. From these experiments are expected **detailed prescriptions for the detection of CO₂ hydrates (possibly occurring in intimate mixtures with solid CO₂ and water ice) by *in-situ* analysers of future Mars missions.**

Unfortunately, a definite answer of the question about the existence of CO₂ hydrate on Mars has not been found yet. The presented experimental results give new clues but also pose new problems that need more work to be solved. In any case to achieve this was initially foreseen to be done within a six-year-long project and in these terms, this thesis comes as a mile-stone somewhere in the middle of the road to a final answer.

References:

- Aya, K., Yamane, K. & Yamada, N. (1992) Stability of clathrate hydrate of carbon dioxide in highly pressurized water. In *Fundamentals of Phase Change: Freezing, Melting, and Sublimation - 1992 HTD 215* (P.E. Kroeger & Y. Bayazitoglu, eds.), The American Society of Mechanical Engineers, New York, 17-22.
- Arnold, G.P., Finch, E.D., Rabideau S.W. & Wenzel, R.G. (1968) Neutron-diffraction study of ice polymorphs. III. Ice Ic. *J. Chem. Phys.*, 49, pp. 4365-4369.
- Arzt, E. (1982). The influence of an increasing particle coordination on the densification of spherical powders. *Acta Metallurgica* 30, pp. 1883-1890.
- Baker, V. R., Strom, R. G., Gulicvk, V. C., Kargel, J. S., Komatsu, G. & Kale, V. S. (1991) Ancient oceans, ice sheets and the hydrological cycle on Mars. *Nature* 352, pp. 589-599
- Balabanov, N. (1998) Nuclear physics. *Jusautor*, Sofia (Original language Bulgarian).
- Barlow, M.J., In the proceedings of 'ISO's view on stellar evolution', Noordwijkerhout July, 1-4, 1997
- Barrer, R.M. & Edge, A.V.J. (1967) Gas hydrates containing argon, krypton and xenon: kinetics and energetics of formation and equilibria. *Proceedings of the Royal Society London A* 300, 1-24.
- Beckwith, S. V. W., Henning, T., & Nakagawa, Y. (2000) Dust properties and assembly of large particles in protoplanetary disks. *Protostars and Planets IV*, p. 533
- Berliner, R., Popovici, M., Herwig, K.W., Berliner, M., Jennings, H.M. & Thomas, J.J. (1998) Quasielastic neutron scattering study of the effect of water-to-cement ratio on the hydration kinetics of tricalcium silicate. *Cement and Concrete Research*, 28(2), pp. 231-243.
- Bertie, J.E., Calvert L.D. & Whalley, E. (1963) Transformation of ice II, ice III and ice V at atmospheric pressure. *J. Chem. Phys.*, 38, pp. 840-846.
- Bluhm, H., Ogletree, D. F., Fadley, Ch. S., Hussain, Z. & Salmeron, M. (2002). The premelting of ice studied with photoelectron spectroscopy. *J. Phys.: Condens. Matter*, 14, pp. L227-L233.
- Brunauer, S., Emmett, P. H. & Teller, E. (1938) Adsorption of gases in multimolecular layers. *J. Am. Chem. Soc.* 60, pp. 309-319
- Cabrol, N.A., Grin, E.A., Landheim, R. & McKay, C.P. (1998) Cryovolcanism as a possible origin for pancake-domes in the Mars 98 landing site area: relevance for climate reconstruction and exobiology exploration. In *Lunar and Planetary Science XXIX*, Lunar and Planetary Institute, Houston, Texas, abstract No. 1249.
- Chadwick, J. (1932) Possible existence of a neutron, *Nature*, p. 312
- Circone, S., Stern, L.A. & Kirby, S.H. (2004) The role of water in gas hydrate dissociation. *J. Phys. Chem. B*, 108, pp. 5747-5755.
- Circone, S., Stern, L.A, Kirby, S.H., Durham, W.B., Chakoumakos, B.C., Rawn, C.J., Rondinone A.J. & Ishii, Y. (2003) CO₂ hydrate: synthesis, composition, structure, dissociation behaviour and comparison to Structure I CH₄ hydrate. *J. Phys. Chem. B*, 107, p. 5529.

- Clampin, M. et al. (2003) Hubble Space Telescope ACS Coronagraphic Imaging of the Circumstellar Disk around HD 141569A. *Astron. J.* 126, pp. 385-392
- Clifford, S. (1980a) Mars: Polar cap basal melting as a recharge mechanism for a global groundwater system, *Lunar Planet. Sci.*, XI, pp. 165– 167
- Clifford, S. (1980b) Chasma Boreale (85_N, 0_W): Remnant of a Martian jökulhlaup? *Bull. Am. Astron. Soc.*, 12, p. 678
- Clifford, S. (1993) A model for the hydrologic and climatic behavior of water on Mars, *J. Geophys. Res.*, 98, pp. 10973 – 11016
- Clifford, S., et al. (2000) The state and future of Mars polar science and exploration. *Icarus* 144, pp. 210–242.
- Crank, J. (1956), The mathematics of diffusion. *Oxford University Press, Amen House*, London
- Danckwerts, P. V. (1950), Absorption by Simultaneous Diffusion and Chemical Reaction. *Trans. Faraday Soc.*, vol. 46
- Dash, J. G., Fu, Haiying & Wettlaufer, J. S. (1995). The premelting of ice and its environmental consequences. *Rep. Prog. Phys.*, 58, pp. 115-167.
- Davidson, D.W., Garg, S.K., Gough, S.R., Handa, Y.P., Ratcliffe, C.I., Ripmeester, J.A., Tse, J.S. & Lawson, W.F. (1986) Laboratory analysis of a naturally occurring gas hydrate from the sediment of the gulf of Mexico. *Geochim. Cosmochim. Acta*, 50, pp. 619-623.
- Dominé, F., Lauzier, T., Cabanes, A., Legagneux, L., Kuhs, W.F., Techmer, K. & Heinrichs, T. (2003) Snow metamorphism as revealed by scanning electron microscopy. *Microscopy. Microscopy Research and Technique*, 62, pp. 33-48.
- Dowell, L.G. & Rinfret, A.P. (1960) Low-temperature forms of ice as studied by X-ray diffraction. *Nature*, 188, pp. 1144-1148.
- Dünwald, H. & C. Wagner (1934), *Z. Physik. Chem.*, B24, p. 53
- Durham W. B. (1998) Factors affecting the rheologic properties of Martian polar ice. In *First International Conference on Mars Polar Science ICMPS, Houston, Texas*, abstract No. 3024
- Faugeras, O. (1993) Three-Dimensional Computer Vision: A Geometric Viewpoint. *M.I.T. Press*
- Fishbaugh, K. E. & Head III, J. W. (2002) Chasma Boreale, Mars: Topographic characterization from Mars Orbiter Laser Altimeter data and implications for mechanisms of formation. *J.G.R.* 107, E3, pp. 2-1 – 2-23
- Froment, G.F. & Bischoff, K.B. (1990) Chemical Reactor Analysis and Design. Wiley & Sons, New York.
- Frost, E. M. & Deaton, W. M. (1946) Gas hydrate composition and equilibrium data. *Oil and Gas Journal*, 45, pp. 170-178

- Fujii, K., & Kondo, W. (1974) Kinetics of hydration of tricalcium silicate. *Journal of the American Ceramic Society*, 57, pp. 492-497.
- Fukazawa, H., Suzuki, D., Ikeda, T., Mae, S. & Hondoh, T. (1997) Raman spectra of transitional lattice vibrations in polar ice. *J. Phys. Chem .B*, 101, pp. 6184-6187.
- Genov, G., Kuhs, W. F., Staykova, D. K., Goreshnik, E. & Salamatina, A. N. (2004) Experimental studies on the formation of porous gas hydrates. *Am. Mineral.* 89, pp. 1228-1239
- Giess, E. A. (1963) *J. Am. Ceram. Soc.*, 46, p. 374
- Ginstling, A. M. & Brounshtein, B. I. (1950) Concerning the Diffusion Kinetics of Reactions in Spherical Particles. *J. Appl. Chem. U.S.S.R.*, 23, pp. 1327-1338
- Glen, J.W. (1968) The effect of hydrogen disorder on dislocation movement and plastic deformation on ice. *Phys. kondens. Materie*, 7, pp. 43-51.
- Gotthardt, F. (2001) Structure and transformations of ice phases in presence of helium, neon and argon. Ph.D. Thesis, University of Göttingen (Original language German).
- Grigoriev, D. A. & Edirisinghe, M. J. (2002) Evaporation of liquid during cone-jet mode electrospraying. *J. Appl. Phys.* 91(1), pp. 437-439
- Handa, Y.P., Klug, D.D. & Whalley, E. (1986) Difference in energy between cubic and hexagonal ice. *J. Chem. Phys.*, 84, pp. 7009-7010.
- Heisenberg, W. (1932) On the building of the atomic nuclei. *Z. Phys.* 77, p. 1 (Original language German).
- Henning, R.W., Schultz, A.J., Thien, Vu & Halpern, Y. (2000) Neutron diffraction studies of CO₂ clathrate hydrate: formation from deuterated ice. *Journal of Physical Chemistry A*, 104, pp. 5066-5071.
- Hersant, F., Gautier, D., Lunine, J. I. (2004) Enrichment in volatiles in the giant planets of the Solar System. *Planetary and Space Science* ,52 , p. 623
- Higashi, A. (ed.) *Lattice defects in ice crystals* (1988), Hokkaido University Press, Sapporo.
- Hobbs, P.V. (1974) *Ice Physics*, Clarendon Press, Oxford.
- Hoffman, N. (2000) White Mars: A new model for Mars' surface and atmosphere based on CO₂. *Icarus*, 146, pp. 326–342.
- Hondoh, T. & Uchida, T. (1992) Formation process of clathrate air-hydrate crystals in polar ice sheets. *Teion Kagaku [Low Temperature Science]*, A(51), pp. 197-212.
- Hwang, M.J., Wright, D.A., Kapur, A. & Holder, G.D. (1990) An experimental study of crystallization and crystal growth of methane hydrates from melting ice. *Journal of Inclusion Phenomena*, 8, pp. 103-116.
- International thermodynamic tables of the fluid state 3: Carbon Dioxide (1976). *International Union of Pure and Applied Chemistry*, Pergamon Press.

- Iro, N., Gautier, D., Hersant, F., Bockelée-Morvan, D. & Lunine, J. I. (2003) An interpretation of the Nitrogen deficiency in comets. *Icarus*, 161, p. 513
- Ivanenko, D. (1932) The neutron hypothesis. *Nature* 129, p. 798
- Jakosky, B., B. Henderson, & M. Mellon (1995) Chaotic obliquity and the nature of the Martian climate. *J. Geophys. Res.*, 100, pp. 1579 – 1584
- Jander, W. (1927), *Z. Anorg. Allgem. Chem.*, 163, 1
- Jaschek, C. & Jaschek, M. (1992) *Astron. Astrophys*, 95, p. 535
- Kargel, J.S., Tanaka, K.L., Baker, V.R., Komatsu, G. & MacAyeal, D.R., 2000, Formation and dissociation of clathrate hydrates on Mars: Polar caps, northern plains, and highlands. In *Lunar and Planetary Science XXX*, Lunar and Planetary Institute, Houston, Texas, abstract No. 1891
- Kashchiev D. & Firoozabadi, A. (2002) Driving force for crystallization of gas hydrates. *Journal of Crystal Growth*, 241, pp. 220-230.
- Kashchiev D. & Firoozabadi, A. (2002) Nucleation of gas hydrates. *Journal of Crystal Growth*, 243, pp. 476-489.
- Kashchiev D. & Firoozabadi, A. (2003) Induction time in crystallization of gas hydrates. *Journal of Crystal Growth*, 250, pp. 499-515.
- Keepin, G. R. (1965) Physics of Nuclear Reactors. Addison-Wesley Publishing Co., Massachusetts
- Kieffer, H. H. (2000) Clathrates Are Not the Culprit. *Science*, 287, 5459, pp. 1753-1754
- Klapproth, A. (2002) Structural investigations of methane- and carbon dioxide clathrate hydrates. Ph.D. Thesis, University of Göttingen (Original language German).
- Klapproth, A., Goreshnik, E., Staykova, D., Klein H. & Kuhs W.F. (2003) Structural Studies of Gas Hydrates. *Canadian Journal of Physics*, 81, 503-518.
- Kohl, I., Mayer E. & Hallbrucker, A. (2000) The glassy water-cubic ice system: a comparative study by X-ray diffraction and differential scanning calorimetry. *Phys. Chem. Chem. Phys.*, 2, pp. 1579-1586.
- Komatsu, G., Kargel, J.S., Baker, V.R., Strom, R.G., Ori, G.G., Mosangini, C. & Tanaka, K.L. (2000) A chaotic terrain formation hypothesis: explosive outgas and outflow by dissociation of clathrate on Mars. In *Lunar and Planetary Science XXXI*, Lunar and Planetary Institute, Houston, Texas, abstract No. 1434.
- König, H. (1943) A cubic modification of ice. *Z. Kristallogr.*, 105, p. 279 (Original language German).
- Kuhs, W.F., Bliss D.V. & Finney, J.L. (1987) High-resolution neutron powder diffraction study of ice Ic. *J. Physique (Colloque C1)*, 48, pp. 631-636.
- Kuhs, W. F., Genov, G., Staykova, D. K. & Hansen, T. (2004) Ice perfection and onset of anomalous preservation of gas hydrates. *Phys. Chem. Chem. Phys.*, 6, (Advance Article), pp. 4917 – 4920

- Kuhs W.F., Klapproth, A., Gotthardt, F., Techmer, K. & Heinrichs, T. (2000) The formation of meso- and macroporous gas hydrates. *Geophysical Research Letters* 27(18), 2929-2932.
- Kuhs, W. F. & Lehmann, M. S. (1986). The structure of ice-Ih. In *Water Science Reviews* 2, F. Franks, ed., Cambridge University Press, pp. 1-65.
- Kuhs, W.F. & Salamatina, A.N. (2003) Formation of porous gas hydrates from polydispersed powders: Model concepts. *Project "Modelling gas-hydrate formation on ice and transport properties of porous hydrates" subject to the BMBF Project "Gas-Hydrate im Geosystem", Res. Rep. No4 (January, 2003).*
- Kumai, M. (1968) Hexagonal and cubic ice at low temperatures. *J. Glaciology*, 7, pp. 95-109.
- Kume, J K. (1960) Proton magnetic resonance in pure and doped ice. *Phys. Soc. Japan*, 15, pp. 1493-1501.
- Lambert, R.S. & Chamberlain, V.E. (1978) CO₂ permafrost and Martian topography. *Icarus*, 34, p. 568-580.
- Larson, A.C. & van Dreele, B. (1994) GSAS – General Structure Analysis system. Los Alamos National Laboratory, Report LAUR 86-748.
- Lasaga, A. C. (1998) Kinetic theory in the Earth sciences. *Princeton University Press*, Chichester, West Sussex, UK
- Legagneux, L., Cabanes, A. & Dominé, F. (2002) Measurement of 176 snow samples using methane adsorption at 77 K. *J. G. R. 107, D17*, p. 4335
- Levenspiel, O. (1999) Chemical Reaction Engineering. Wiley & Sons, New York.
- Li, A. & Lunine, J. I. (2003) Modeling the infrared emission from the HD 141569A disk. *Astrophys. J.* 594, pp. 987-1010
- Li, A., Lunine, J. I. & Bendo, G. J. (2003) Modeling the infrared emission from the Eridani disk. *Astrophys. J.* 598, pp. L51-L54
- Lobban C. (1998) Neutron diffraction studies of ices. *Ph.D. Thesis*, University College London.
- Lobban, C, Finney, J. L. & Kuhs, W.F. (1998). The structure of a new phase of ice. *Nature* 391, pp. 268-270.
- Lobban, C., Finney, J.L. & Kuhs, W.F. (2000) The structure and ordering of ices III and V. *J. Chem. Phys.*, 112, p. 7169-7180.
- Lu, T. J. & Chen, C. (1999) Thermal transport and fire retardance properties of cellular aluminium alloys. *Acta mater.* 47 (5), pp. 1469-1485.
- Malfait, K., Waelkens, C., Bouwman, J., de Koter, A. & Waters, L. B. F. M. (1999) The ISO spectrum of the young star HD 142527. *Astron. Astrophys.* 345, p. 181

- Malfait, K., Waelkens, C., Waters, L. B. F. M., Vandenbussche, B., Huygen, E. & de Graauw, M. S. (1998) The spectrum of the young star HD 100546 observed with the Infrared Space Observatory. *Letter to the Editor Astron. Astrophys.* 332, p. L25-L28
- Matsuoka, T., Mae, S., Fukazawa, H., Fujita, S. & Watanabe, O. (1998) Microwave dielectric properties of the ice core from Dome Fuji, Antarctica. *Geophys. Res. Lett.*, 25, pp. 1573-1576.
- Max, M. D. & Clifford, S. M. (2001) Initiation of Martian outflow channels: Related to the dissociation of gas hydrate? *G. Res. Lett.* 28, 9, pp. 1787-1790
- Mayer, E. & Hallbrucker, A. (1987) Cubic ice from liquid water. *Nature*, 325, pp. 601-602.
- Mckenzie, D. & Nimmo, F. (1999) The generation of Martian floods by the melting of ground ice above dykes. *Nature*, 397, pp. 231-233.
- Mellon, M. (1996) Limits on the CO₂ content of the Martian polar deposits. *Icarus*, 124, pp. 268– 279
- Miller S. L. & Smythe W. D. (1970) Carbon Dioxide Clathrate in the Martian Ice Cap, *Science* 170, pp 531-533
- Milton, D.J. (1974) Carbon Dioxide Hydrate and Floods on Mars. *Science*, 183, pp. 654-656.
- Mizuno, Y. & Hanafusa, N. (1987) Studies of surface properties of ice using nuclear magnetic resonance. *Journal de Physique*, Colloque C1, Supplement au N3, 48, C1-511 -- C1-517.
- Mori, Y.H. (1998) Clathrate hydrate formation at the interface between liquid CO₂ and water phases: a review of rival models characterizing "hydrate films". *Energy Conversion and Management* 39(15), 1537-1257.
- Mori, Y.H. & Mochizuki, T. (1997) Mass transport across clathrate hydrate films – a capillary permeation model. *Chemical Engineering Science* 52(20), 3613-3616.
- Musselwhite D. S., Swindle T. D. & Lunine J. I. (2001) Liquid CO₂ breakout and the formation of recent small gullies on Mars. . In *Lunar and Planetary Science XXX, Lunar and Planetary Institute, Houston, Texas, abstract No. 1030*
- Natta, A., Grinin, V. & Mannings, V. (2000) Properties and Evolution of Disks around Pre-Main-Sequence Stars of Intermediate Mass. *Protostars and Planets IV*, p. 559
- Ness, P. K. & Orme, G. M. (2002) Spider-ravine models and plant-like features on Mars - possible geophysical and biogeophysical modes of origin. *Journal of the British Interplanetary Society* 55, 3/4, pp. 85-108
- Nye, J., Durham, W., Schenk, P. & Moore J. (2000) The instability of a south polar cap on Mars composed of carbon dioxide. *Icarus* 144, pp. 449–455.
- Ori, G. & Mosangini, C. (1997) Fluidization and water production in Chaos on Mars. *Proc. LPSC XXVIII*, pp. 1045-1046.
- Ori, G. & Mosangini, C. (1998) Complex depositional systems in Hydraotes Chaos, Mars: An example of sedimentary process interactions in the Martian hydrological cycle. *J. G. R. - planet*, 103, E10, pp. 22713-22723.

- Parmentier, E.M., Sotin C. & Travis B.J. (1994) Turbulent 3D thermal convection in an infinite Prandtl number fluid: Implications for mantle dynamics. *Geophys. J. Int.* 116, pp. 241-251
- Pellenbarg, R. E., Max, M. D. & Clifford, S. M. (2003) Methane and carbon dioxide hydrates on Mars: Potential origins, distribution, detection, and implications for future in situ resource utilization. *J. G. R. - planet*, 108, E4, pp. 23-1 – 23-5.
- Petrenko, V. F. & Whitworth, R. V. (1999). Physics of ice. *Oxford University Press*.
- Pradell, T., Crespo, D., Clavaguera, N. & Clavaguera-Mora, M. T. (1998) Diffusion controlled grain growth in primary crystallization: Avrami exponents revisited. *J. Phys.: Condens. Matter* 10, pp. 3833-3844
- Pratt, William K. (1991) Digital Image Processing –2-nd Edition, John Wiley and Sons
- Pynn, R. (1990) Neutron Scattering – A Primer. *Los Alamos Science No. 19*
- Read, P. L. & Lewis, S. R. (2004) The Martian climate revisited – atmosphere and environment of a desert planet. *Praxis Publishing Ltd, Chichester, UK*
- Ross, R.G. & Kargel, J.S. (1998) Thermal conductivity of solar system ices, with special reference to Martian polar caps. in Schmitt, B., et al., eds., Solar system ices: *Dordrecht, Netherlands, Kluwer Academic Publishers*, p. 33–62.
- Salamatin, A.N., Hondoh, T., Uchida, T. & Lipenkov, V.Y. (1998) Post-nucleation conversion of an air bubble to clathrate air-hydrate crystal in ice. *Journal of Crystal Growth*, 193, pp. 197-218.
- Salamatin, A. N. & Kuhs W.F. (2002) Formation of porous gas hydrates. *Proceedings of the Fourth International Conference on Gas Hydrates, Yokohama, May 19-23, 2002*, pp. 766- 770.
- Salamatin, A.N. & Kuhs W.F. (2003) Modelling formation of porous gas hydrates from polydispersed ice powders, taking account of crack filling. *Report No 5 to the BMBF Project – “Gas-Hydrate im Geosystem”, August, 2003*.
- Schlei, B. R., Prasad, L. & Skourikhine, A. N. (2001) Geometric Morphology of Granular Materials *Proc. SPIE 4476*, pp. 73-79.
- Schmitt, B. (1986) The surface of ice: structure, dynamics and interactions – astrophysical implications. Ph.D. thesis, USTM Grenoble, France. (Original language French).
- Schubert G. & Spohn T. (1990) Thermal history of Mars and the sulfur content of its core. *J. Geophys. Res.*, v. 95, pp. 14,095-14,104
- Serin, B. & R. T. Ellickson (1941), *J. Physik. Chem.*, 9, p. 742
- Sleep, N.H. (1994) Martian plate tectonics. *J. Geophys. Res.*, v. 99, pp. 5639-5655.
- Sloan E. D., Jr. (1998) Clathrate hydrates of natural gases. Second edition, Marcel Dekker Inc.:New York.
- Sloan, E.D., Jr. & Fleyfel, F. (1991) A molecular mechanism for gas hydrate nucleation from ice. *American Institute of Chemical Engineering Journal* 37, 1281-1292.

- Sotin C. & Labrosse S. (1999) Thermal convection in an isoviscous, infinite Prandtl number fluid heated from within and from below: applications to the transfer of heat through planetary mantles. *Phys. Earth Planet. Int.*, 112, pp. 171-190
- Sotin, C. & Lognonné, Ph. (1999) Revisited models of mars internal structure and thermal evolution. *The V-th International Conference On Mars*, # 6091
- Squires, G. L. (1997) Introduction to the Theory of Thermal Neutron Scattering. *Dover Publications Inc. Mineola, NY 11501-3852*
- Staykova, D.K., Hansen, T., Salamatin, A.N. & Kuhs, W.F. (2002) Kinetic diffraction experiments on the formation of porous gas hydrates. *Proc. 4th Int. Conf. Gas Hydrates*, 537-542.
- Staykova, D.K., Kuhs, W.F., Salamatin, A.N. & Hansen, Th. (2003) Formation of porous gas hydrates from ice powders: Diffraction experiments and multistage model. *J. Phys. Chem. B*, 107, 10299-10311.
- Stern, L.A., Circone, S. & Kirby, S.H. (2001) Anomalous preservation of pure methane hydrate at 1 atm. *J. Phys. Chem. B*, 105, pp. 1756-1762.
- Stern, L.A., Circone, S., Kirby S.H. & Durham, W.B. (2002) Reply to “Comments on “Anomalous preservation of pure methane hydrate at 1 atm”” *J. Phys. Chem. B*, 106, p. 228.
- Stern, L.A., Hogenboom, D.L., Durham, W.B., Kirby, S.H. & Chou, I-M. (1998) Optical-cell evidence for superheated ice under gas-hydrate-forming conditions. *J. Phys. Chem. B* 102, 2627-2632.
- Stern, L.A., Kirby, S.H., Durham, W.B. (1996) Peculiarities of Methane Clathrate Hydrate Formation and Solid-State Deformation, Including Possible Superheating of Water Ice. *Science*, 273, 5283, pp. 1843-1848
- Stevenson D. J. (2004) Mars' core and magnetism. *Nature Insight* 412, 6843, pp. 214-219
- Suess, E., Bohrmann, G., Rickert, D., Kuhs, W.F., Torres, M.E., Trehu, A. & Linke, P. (2002) Properties and fabric of near-surface methane hydrates at Hydrate Ridge, Cascadia Margin. *Proc. 4th Int. Conf. Gas Hydrates*, 740-744.
- Sugaya, M. & Mori, Y.H. (1996) Behavior of clathrate hydrate formation at the boundary of liquid water and fluorocarbon in liquid or vapor state. *Chemical Engineering Science* 51(13), 3505-3517.
- Sugisaki, M., Suga, H. & Seki, S. (1968) Calorimetric study of the glassy state. IV. Heat capacities of glassy water and cubic ice. *Bull. Chem. Soc. Japan*, 41, pp. 2591-2599.
- Takenouchi, S. & Kennedy, G. C. (1965) Dissociation pressures of the phase $\text{CO}_2 \cdot 5 \frac{3}{4} \text{H}_2\text{O}$. *J. Geology*, 73, pp. 383-390
- Takeya, S., Ebunima, T., Uchida, T., Nagao, J. & Narita, H. (2002) Self-preservation effect and dissociation rates of CH_4 hydrate. *J. Cryst. Growth*, 237-239, pp. 379-382.
- Takeya, S., Shimada, W., Kamata, Y., Ebunima, T., Uchida, T., Nagao J. & Narita, H. (2001) In situ X-ray diffraction measurements of self-preservation effect of CH_4 hydrate. *J. Phys. Chem. A*, 105, pp. 9756-9759.

- Takeya, S., Hondoh, T. & Uchida, T. (2000) In-situ observations of CO₂ hydrate by X-ray diffraction. *Annals of the New York Academy of Sciences*, 912, 973-982.
- Tamman, G. & Krige, G. J. (1925) Equilibrium pressures of gas hydrates. *Zeit. Anorg. Und Algem. Chem.*, 146, pp. 179-195 (Original language German)
- Thomas, P., K. Herkenhoff, A. Howard, B. Murray & S. Squyres (1992) Polar deposits on Mars. In *Mars*, pp. 767-795. Univ. of Arizona Press, Tucson.
- Tillman, J. E., Henry R. M. & Hess S. L. (1979) Frontal Systems During Passage of the Martian North Polar Hood Over the Viking Lander 2 Site Prior to the First 1977 Dust Storm. *J. Geophys. Res.*, v. 84, B6, pp 2947-2955.
- “Towards Mars!” – Edited by R. Pellinen & P. Raudsepp (2000) – *Oy Raud Publishing Ltd. Helsinki*
- Uchida, T., Hondoh, T., Mae, S., Duval, P. & Lipenkov V.Ya. (1992) In-situ observations of growth process of clathrate air-hydrate under hydrostatic pressure. In *Physics and Chemistry of Ice* (N. Maeno & T. Hondoh, eds.), Hokkaido University Press, Sapporo, Japan. 121-125.
- Uchida, T., Hondoh, T., Mae, S., Duval, P. & Lipenkov V.Ya. (1994). Effects of temperature and pressure on transformation rate from air bubbles to air-hydrate crystals in ice sheets. *Annals of Glaciology* 20, 143-147.
- Uchida, T. & Kawabata, J. (1995) Observations of water droplets in liquid carbon dioxide. *Proceedings of the MARIENV'95 Conference*, 906-910.
- Van der Waals, J. H. & Platteeuw, J. C. (1959) Clathrate solutions. *Adv. Chem. Phys.* 2, 1-57.
- Villard, M., P. (1894) On the carbonic hydrate and the composition of gas hydrates. *Acad. Sci. Paris, Comptes rendus*, 119, pp. 368-371 (Original language French)
- Villard, M., P. (1894) Experimental study of gas hydrates. *Ann. Chim. Phys. (7)*, 11, pp. 353-360 (Original language French)
- Von Stackelberg, M. & Müller, H. R. (1954) Feste Gashydrate II. Struktur und Raumchemie. *Z. Electrochem.* 58, 25-39.
- Wang, X., Schultz, A.J. & Halpern, Y. (2002) Kinetics of ice particle conversion to methane hydrate. *Proc. 4th Int. Conf. Gas Hydrates*, 455-460.
- Wettlaufer, J. S., Worster, M. G. & Wilen, L. A. (1997). Premelting dynamics: geometry and interactions. *J. Phys. Chem. B*, 101, pp. 6137-6141.
- Wilder, J.W. & Smith, D.H. (2002) Comments on “Anomalous preservation of pure methane hydrate at 1 atm”. *J. Phys. Chem. B*, 106, p. 226.
- Wooldridge, P.J., Richardson H.H. & Devlin, J.P. (1987) Mobile Bjerrum defects: A criterion for ice-like crystal growth. *J. Chem. Phys.*, 87, pp. 4126-4131.
- Wroblewski, S. (1882a) On the combination of carbonic acid and water. *Acad. Sci. Paris, Comptes rendus*, 94, pp. 212-213 (Original language French)

Wroblewski, S. (1882b) On the composition of the hydrate of the carbonic acid. *Acad. Sci. Paris, ibid.*, pp. 954-958 (Original language French)

Wroblewski, S. (1882c) On the laws of solubility of the carbonic acid in water at high pressures. *Acad. Sci. Paris, ibid.*, pp. 1355-1357 (Original language French)

Wulfsohn, D. (2000) Quantifying the morphology of microcellular foams. *Proc. 3rd Biannual Nordic Meeting on Materials and Mechanics*, Rebild Bakker, Denmark, May 8-11, pp. 361-374.

Yakushev, V.S. & Istomin, V.A. (1992) Gas-Hydrates Self-Preservation Effect. In *Physics and Chemistry of Ice*, ed. N. Maeno and T. Hondoh, Hokkaido University Press, Sapporo, pp. 136-139.

Zeller, A. (2004) Measuring the specific surface area of gas hydrates. Master Thesis, University of Göttingen (Original language German).

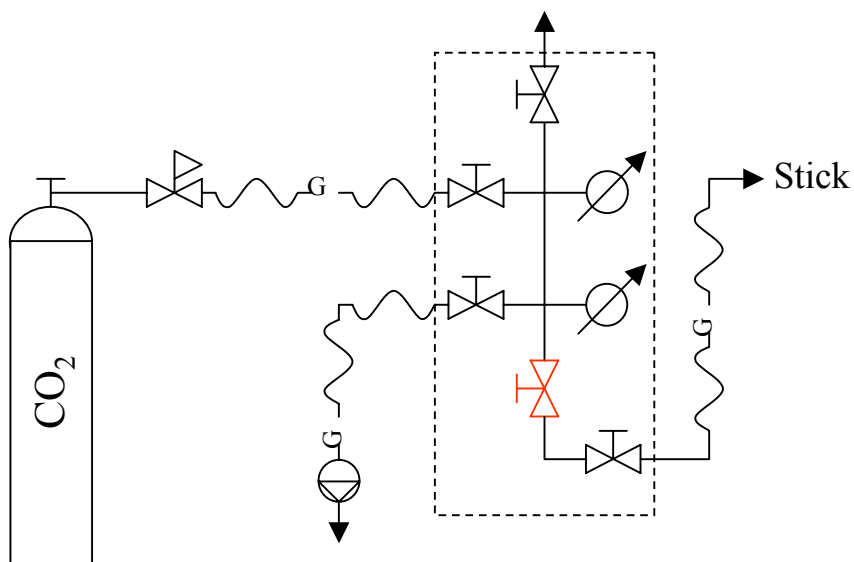
Appendix I

Basic Facts About The Planet Mars

Mass	6,42.10 ²³ kg	
Density	3.933 g/cm ³	
Composition of the atmosphere (by volume)	95.32% carbon dioxide 2.7% nitrogen 1.6% argon 0.13% oxygen 0.07% Carbon monoxide 0.0 – 0.03% Water vapour	0.0 – 0.03% Water vapour 2.5 ppm ¹ neon 0.3 ppm krypton 0.08 ppm xenon 0.04 – 0.2 ozone
Average air pressure at the surface	6 millibars (compared to 1013 millibars on Earth)	
Average diameter of Mars	6 794 km (about half that of the Earth)	
Average distance from the Sun	227 940 000 km (or 1.52 Astronomical Units, i.e. 1.52 times as far as Earth)	
Maximum distance from the Sun	249.10 ⁶ km	
Minimum distance from the Sun	207.10 ⁶ km	
Maximum distance from Earth	2.67 a.u.	
Minimum distance from Earth	0.37 a.u.	
Orbital Parameters	(a) Semimajor axis: 227940000 kms (i) Inclination: 1.85 ° (e) Eccentricity: 0.093	(N) Longitudinal Node: 49.56 ° (W) Ascending Node: 286.50 °
Albedo	0.15	
Visual Magnitude	-2	
Martian sidereal day (i.e., rotation time)	24 h 37 min 23 s	
Martian solar day (i.e., time between two successive noons)	24 h, 39 min 35 s	
Martian year (i.e., time to orbit the Sun)	669.6 Martian solar days or 686.98 Earth days (i.e., about 1.9 Earth years)	
Length of seasons in northern hemisphere	Spring 199 days = 194 sols Summer 182 days = 177 sols	Autumn 146 days = 142 sols Winter 160 days = 156 sols
Length of seasons in southern hemisphere	Spring 146 days = 142 sols Summer 160 days = 156 sols	Autumn 199 days = 194 sols Winter 182 days = 177 sols

¹ ppm – parts per million by volume

Axis inclination	25.2 °
Speed on heliocentric orbit	24.13 km/s
Compression	1:192
Gravity on surface	3.73 m/s ²
Magnetic field	A planet-wide magnetic field has not been detected; however, ancient remnant fields have been located in certain regions
Global average temperature	218 K (-55 °C)
Minimum surface temperature:	140 K (-133 °C) (temperature of frozen carbon dioxide on high elevations at the winter pole)
Maximum surface temperature:	300 K (27 °C) (dark tropical regions in summer)
Surface area	about the same as the land area on Earth
Highest mountain	Olympus Mons - the largest mountain in the Solar System rising 24 km above the surrounding plain (21.2 km above the reference level**). Its base is more than 500 km in diameter and is rimmed by a cliff 6 km high
Largest canyon	Valles Marineris - a canyon 4 000 km long, up to 5.3 km deep, and up to 20 km wide.
Largest impact crater and deepest point on Mars	Hellas Planitia - an impact crater in the southern hemisphere up to 7.8 km deep and 2 000 km in diameter
Surface bulge:	Tharsis - a huge bulge on the Martian surface that is about 4 000 km across and 10 km high

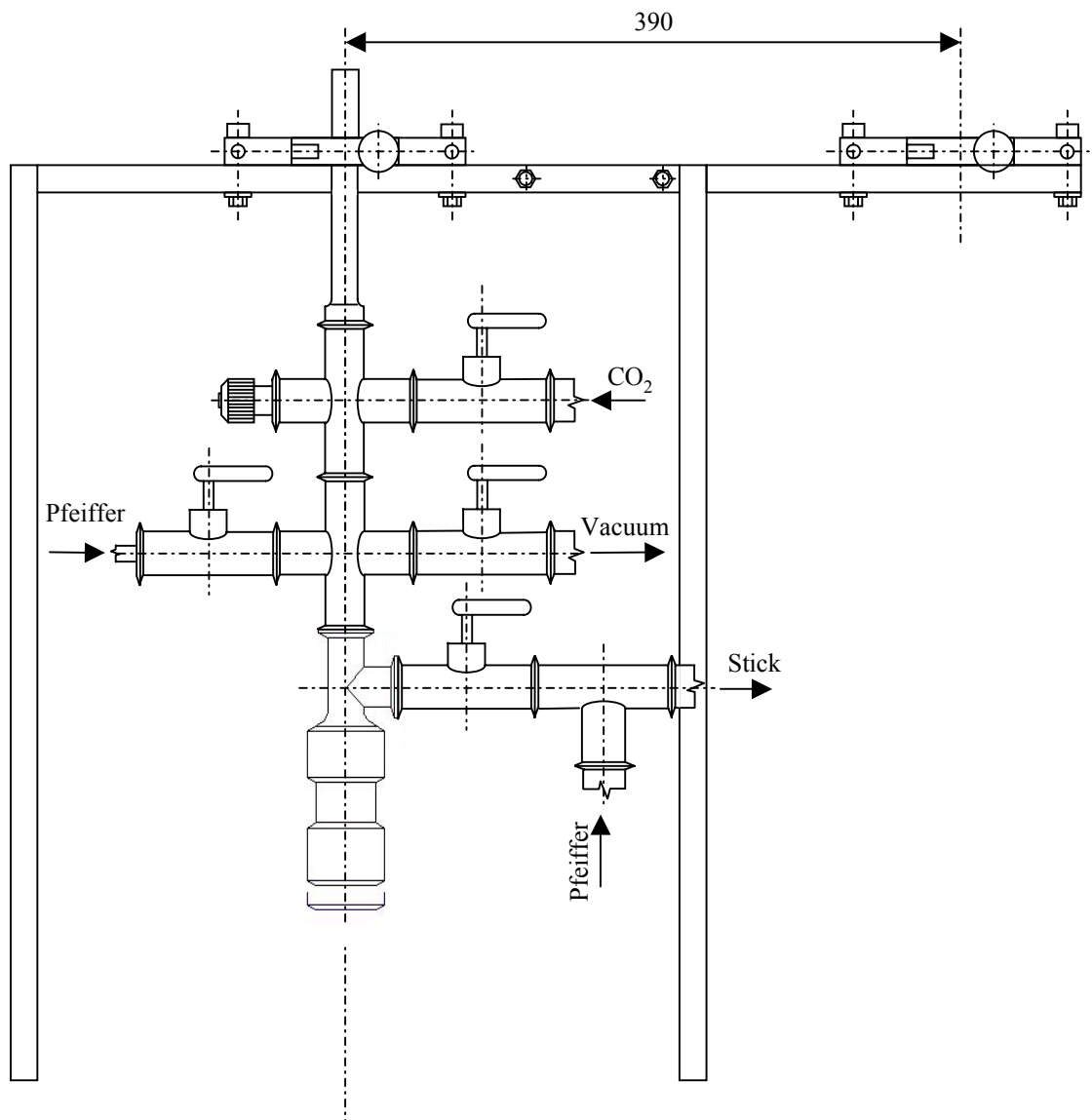


Appendix II

Schematic of the hardware used at D20 and in the lab

Sheet 1 | All sheets 7

GZG Goettingen



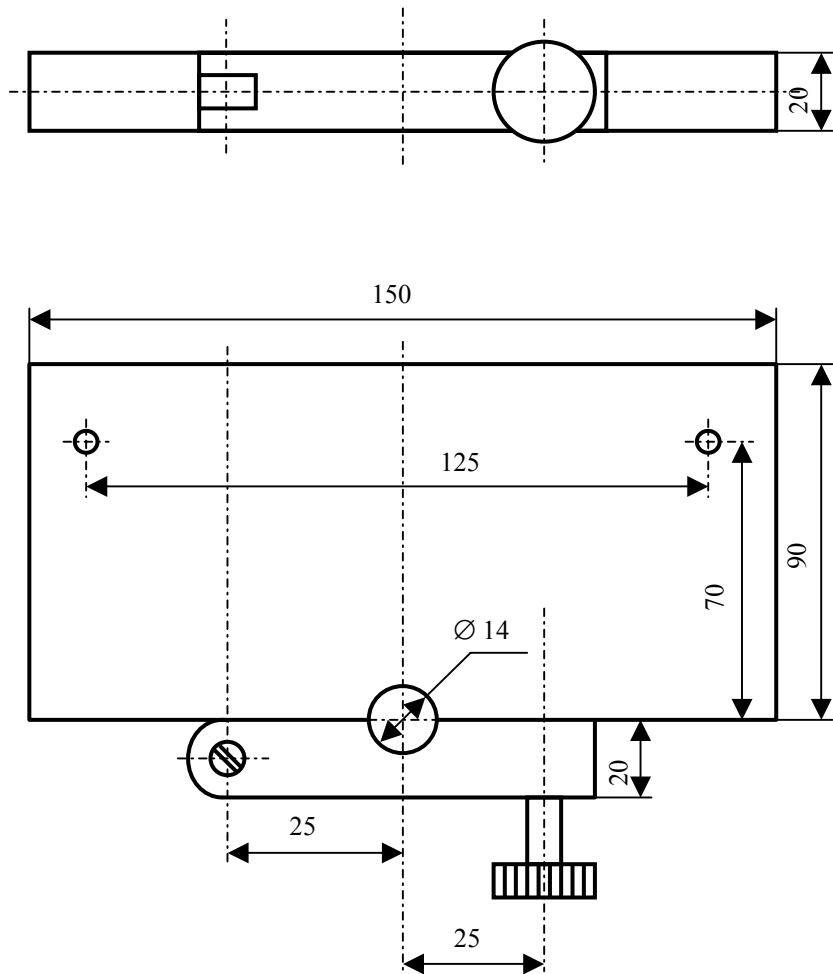
Appendix II

The gas handling -
D2O Realization

Draft G. Genov

Sheet 3 All sheets 7

GZG Goettingen



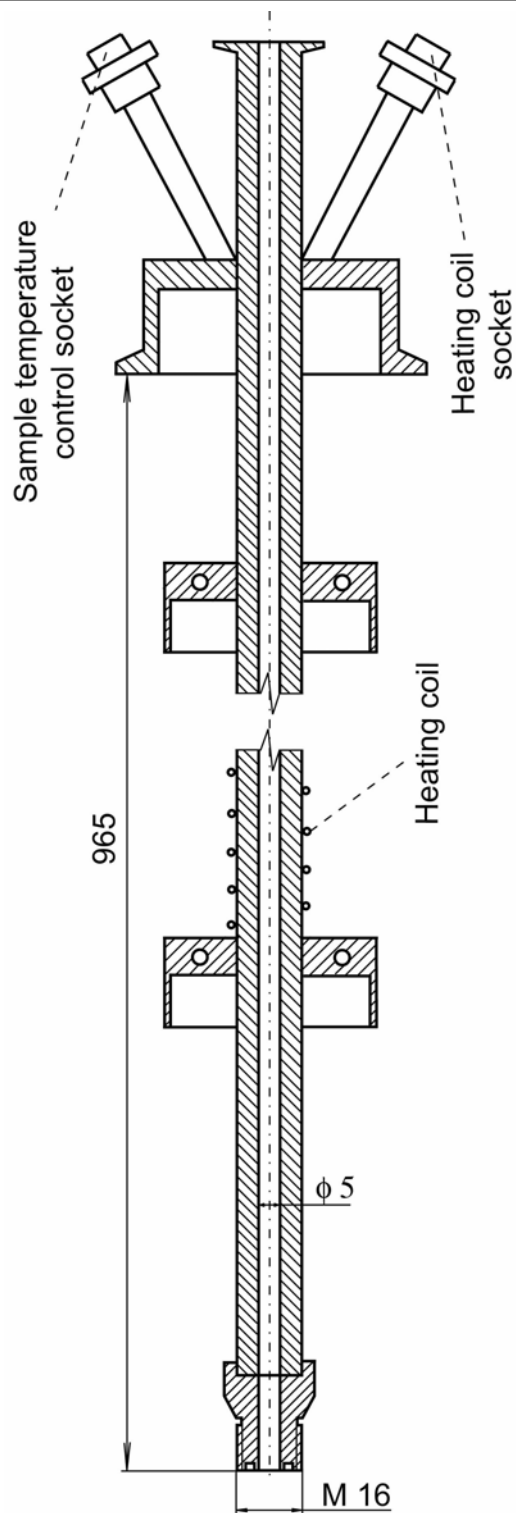
Appendix II

The auxiliary supporting
plank for the stick
(D20 Realization)

Draft G. Genov

Sheet 4 All sheets 7

GZG Goettingen



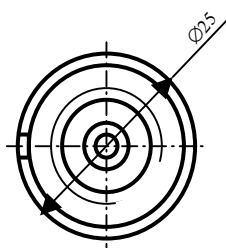
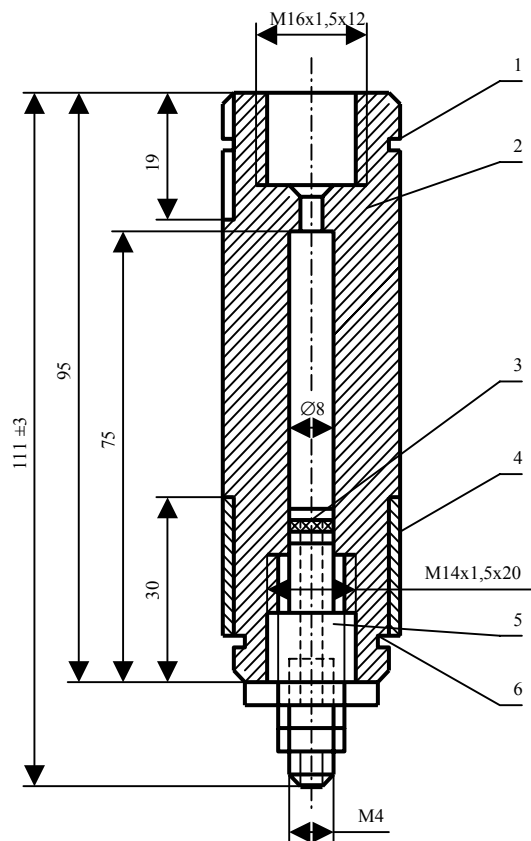
Appendix II

D20 Stick

Draft G. Genov

Sheet 5 All sheets 7

GZG Goettingen



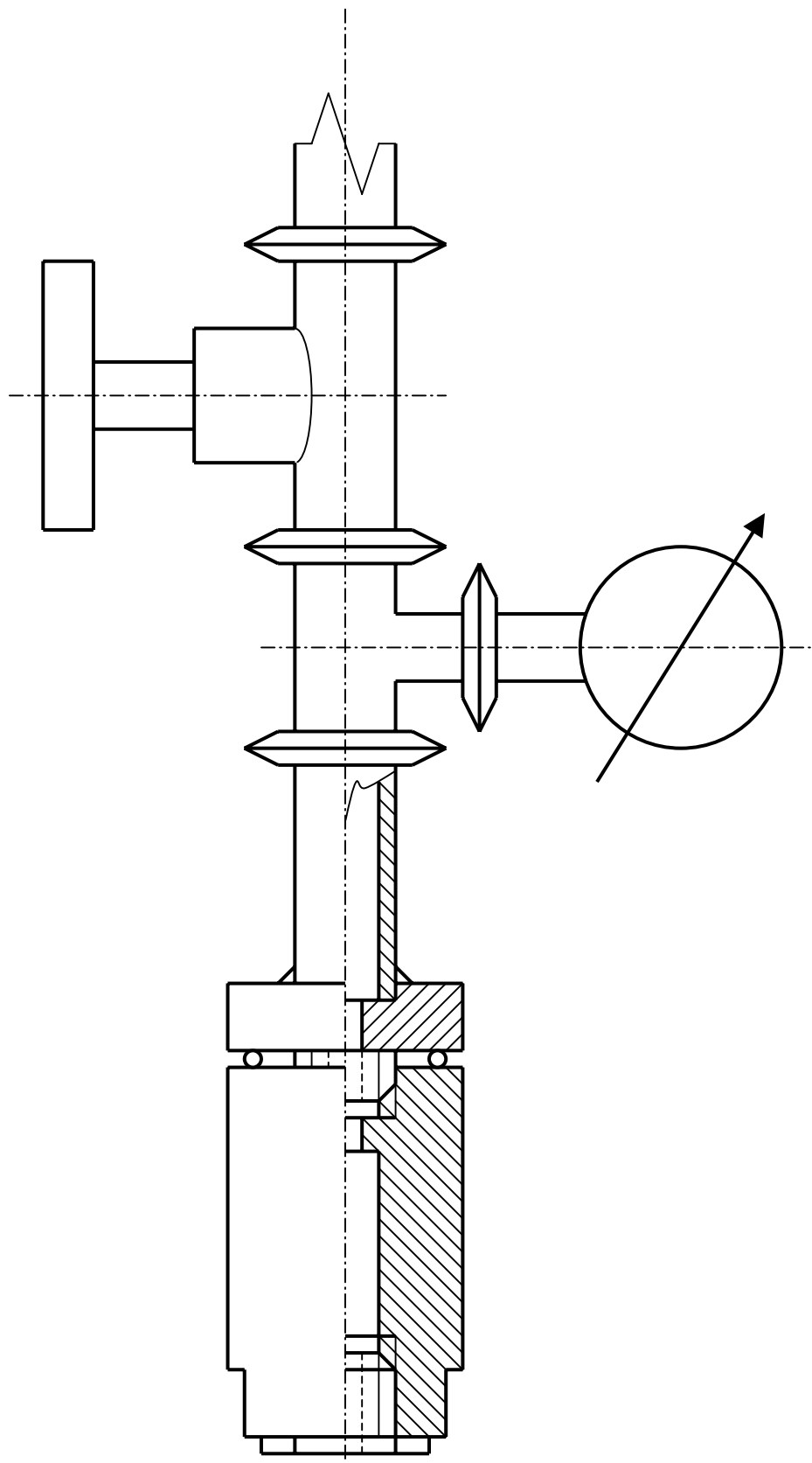
Appendix II

Sample Cell

Draft G. Genov

Sheet 6 All sheets 7

GZG Goettingen



					<div>Appendix II</div>				
					Schematic of the stick replacement for the in-house pVT rig (no scale)				
Draft	G. Genov								
								Sheet 7	All sheets 7
								GZG Goettingen	

Appendix III

Data processing apparatus

In this Appendix are briefly described the methods used for the analyses of the experimental results. In the first paragraph is given a description of the full-pattern Rietveld refinement software GSAS, including the automatic procedure for processing large numbers of files. At the end, will be described the approach for image processing of the SEM pictures I tried to implement. It is far from being finished but at least gives one of the two possible directions to go ahead.

§ 1. GSAS

1.1. Rietveld refinement – general information

In the late 1960s the necessity of algorithm for extracting the structural information for powder samples led to the popularization of the Rietveld method (Rietveld 1967, 1969). The analysis is based on a curve-fitting procedure. The input structural model is modified by least squares refinement in a way to minimize the differences between the observed and calculated profiles. In this sense the Rietveld method is a structure refinement method. It needs a good starting model to calculate the needed diffraction pattern (**Fig. 1**) using: (a) lattice parameters to calculate the positions of the reflections, (b) coordinates and temperature factors of the atoms to determine the intensities of the reflections in an asymmetric unit, (c) peak profile functions to model the reflections' profiles and (d) background functions to model the background.

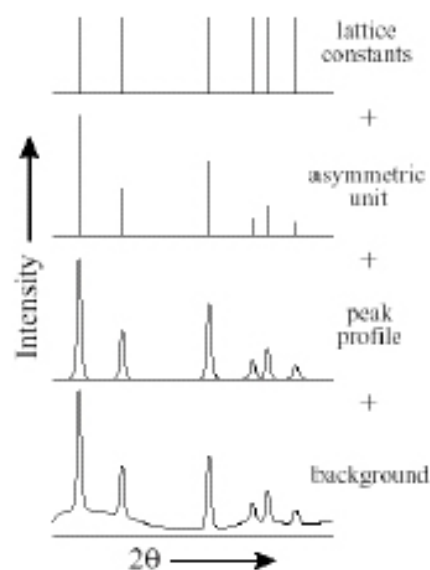


Fig 1 Constructing the diffraction pattern out of the input model information (taken from Staykova 2004).

One diffraction pattern can be described numerically by a number of intensity values y_i , related to a consequence of equal steps i , which can be the scattering angles 2θ , for instance. The least-squares refinement minimizes the residual Φ_y , calculated as follows:

$$\Phi_y = \sum_{i=1}^n w_i (y_i - y_{ci})^2 \quad (\text{AppV.1})$$

where $w_i = 1/y_i$, y_i and y_{ci} are the measured and the calculated intensities at the i -th point, respectively; n is the number of data points.

The result of a successful refinement of the model parameters is that a minimum of the residual (IV.1) is reached and the entire calculated pattern is fitted to the measured pattern. There is a number

of criteria of a good fit, which help checking its quality. For example $R_p = \frac{\sum_{i=1}^n |y_{io} - y_{ic}|}{y_{io}}$ is the profile

R -factor and $R_{wp} = \left(\frac{\sum_{i=1}^n w_i (y_{io} - y_{ic})^2}{\sum_{i=1}^n w_i y_{io}^2} \right)^{1/2}$ is a weighted profile R -factor, where y_i is the intensity at a

step i , and w_i is the related weight factor. The subscripts “ o ” and “ c ” denote the observed and the calculated values, respectively. The progress of the refinement is shown by the weighted profile R -factor, R_{wp} being minimized during the refinement. It is proportional to the residual (IV.1). However, the quality of the fit, estimated by R -factors, has to be checked always by plotting the data and the fit.

The refinement procedure is controlled by criteria of convergence and it continues until the changes, made in each refined parameter, become smaller than the uncertainty given by an estimated standard deviation, i.e. each parameter stays within its interval of uncertainty. This can be written as:

$$\sum_j \left(\frac{\Delta x_j}{\sigma_j} \right)^2 < \varepsilon \quad (\text{AppV.2})$$

where Δx_j is the change in the parameter x_j ; σ_j is the estimated standard deviation of x_j ; and ε is the value determining when the refinement will reach convergence. When the convergence is achieved a minimum of the residual (AppV.1) is obtained. Starting from different values of x the refinement would lead to different minima of the residual. It is essential to start the refinement at such values of the parameters that would make it reach the global minimum. It means the initial model has to describe reasonably well the real crystal structure.

1.2. GSAS

Larson and von Dreele (1990) developed the program package GSAS (Generalized Structure Analysis System) to perform the Rietveld least-squares refinement of diffraction data. GSAS is a multitask software, which has versions running under UNIX/LINUX and Windows. It is widely used for analyzing powder diffraction data. The kinetic diffraction data of gas hydrate formation and decompositions in this work were processed using GSAS, to model the (hkl) reflections, which belong to all crystalline phases in the diffracting sample.

The intensity at every point in a powder diffraction pattern has contributions from nearby reflections and background scattering. The reflection contributions are calculated from the structure factors and the background is modeled by empirical functions (Larson and von Dreele, 1990). Thus, the calculated intensity y_c is determined as:

$$y_c = s_h \sum_p s_{ph} Y_{ph} + y_b \quad (\text{AppV.3})$$

where s_h is a histogram scale factor, applied to the reflections from all phases in the sample; s_{ph} is an individual phase scale factor, applied only to the reflections from the p^{th} phase; Y_{ph} is the contributed intensity from h^{th} Bragg reflection of the p^{th} phase; y_b is the background value.

The contributed intensity Y_{ph} from a Bragg peak to particular profile intensity is determined as:

$$Y_{ph} = F_{ph}^2 \phi(\theta - \theta_{ph}) K_{ph} \quad (\text{AppV.4})$$

where F_{ph} is the structure factor for this reflection; $\phi(\theta - \theta_{ph})$ is the value of its profile peak shape function at position θ , displaced from its expected position θ_{ph} ; K_{ph} is the intensity correction factor for that reflection. Each scale factor s_{ph} is proportional to the number of unit cells of the related phase that is presented in the sample. The scale factor can be converted to a weight fraction W_p of a phase in a multiphase composition:

$$W_p = \frac{s_{ph} m_p}{\sum_{p=1}^{n_p} s_{ph} m_p} \quad (\text{AppV.5})$$

where m_p is the unit cell mass for the phase p , computed from the atom site multiplicities and fractions, which are presented in that phase. The weight fractions for multiphase mixtures are automatically computed during the least-squares refinement in GSAS (routine GENLES) and are given together with their estimated standard deviations in the output ASCII file.

The input powder data file used in the GSAS program has a header depending on the type of the data in it. For standard data types the header is: (**'BANK'**, 3I, A, 4F, A) **IBANK**, **NCHAN**, **NREC**, **BINTYPE**, (**BCOEF (I)**, I=1, 4), **TYPE** where **IBANK** is a bank number; **NCHAN** is the number of data points in the block of data; **NREC** is the number of records. The form of header with a **TYPE** of **'ALT'** shows that the data records include the position of each point in rather unusual units. A **BINTYPE** of **'RALF'** makes GSAS to use a **BCOEF (2)** to control the steps between the data points within the data block. When Staykova (2004) used for the first time GSAS for her neutron diffraction data analysis, she found that some of the GSAS data files had an error in **BCOEF (2)**. It had occurred while they had been produced by LAMP out of the raw experimental data. This error did not allow the data processing before being corrected. When the value of **BCOEF (2)** was changed the processing of the neutron diffraction data was possible. As it was mentioned before each obtained neutron diffraction pattern was analyzed using GSAS. The structural model of the D₂O-CO₂ hydrate phase used in the Rietveld refinement of all neutron diffraction data has been already discussed in detail by Klapproth (2002) and Staykova (2004). The atomic positions and the displacement parameters of the input models were kept fixed during the refinement of the gas hydrate kinetic data. For each data set the lattice constants of the ice and the gas hydrate were kept fixed at values, refined from the last recorded diffraction pattern. The background, coming from the incoherent scattering, air

scattering, and thermal diffuse scattering was modeled using cosine Fourier series (Larson and Von Dreele, 1990)

$$y_b(Q) = B_1 + \sum_{j=2}^n B_j \cos(Q(j-1)) \quad (\text{AppV.6})$$

where B_j were determined by the Rietveld refinement background parameters and Q was the position, in degrees 2θ , along the diffraction profile. This background description can be applied in case of a slowly changing generally flat background. Cosine Fourier series with five parameters were used to describe it in the present experiments. GSAS modeled the reflection profiles, using a profile peak shape function, developed by Howard (1982) and Thompson et al. (1987) for angle-dispersive data.

An experimental (EXP) file containing two phases (ice Ih + CO₂ hydrate) was prepared using one reference histogram from the data set. There the lattice constants, profile parameters and phase fractions of the ice Ih, background parameters and the gas hydrate were refined on the basis of this reference histogram. Once the successful refinement was achieved, the lattice constants and the profile parameters were fixed in the EXP file. This file was copied to a backup file (BAC) and used as ‘initial’ EXP file (see below).

1.3. Automatic procedure for processing large numbers of data sets

All collected data sets were analyzed in an automated way with GSAS and the tools available in the Linux shell. The flowchart of the algorithm for automatic data processing (script **dory.csh**) is shown on **Fig. 2**. First the data file header was corrected (script **doro.awk**) and copied into a buffer. Then the EXP file called the buffer for processing. A GSAS refinement of each diffraction pattern by the same ‘initial’ EXP file (script **expCO2**) was performed. The use of the same EXP file was necessary to avoid a crash of the automatic procedure if some of the data files created problems in the refinement. After the “GSASing” (by POWPREF and GENLES routines) an output file (LST) of the

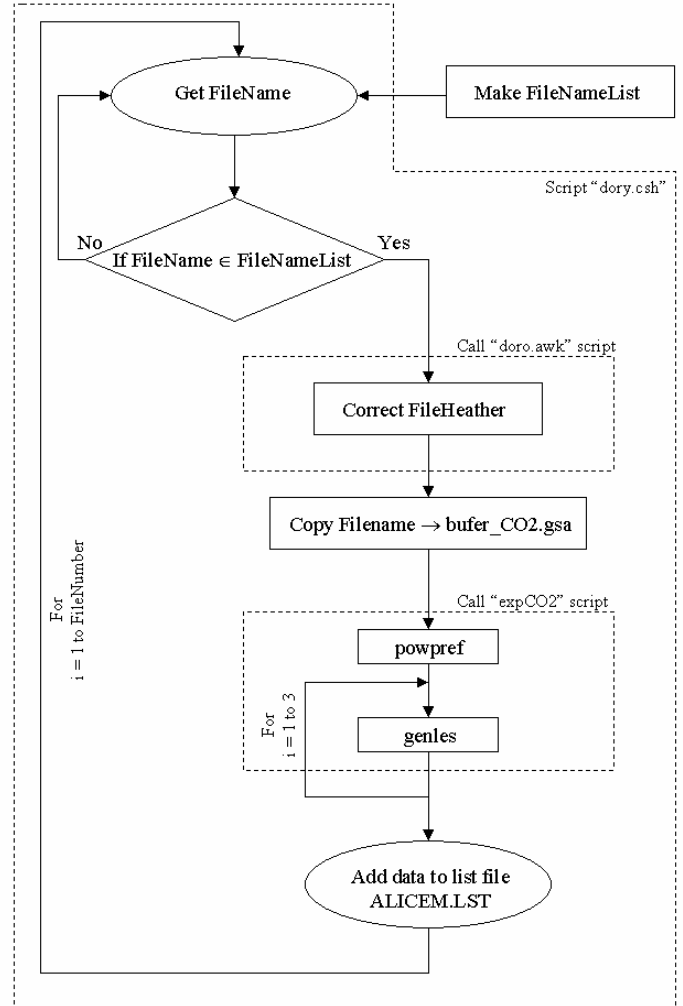


Fig. 2. Flowchart of the automatic processing of kinetic data

results of the Rietveld fit came out. Then the name of the refined data was written in the same LST file.

The procedure described above was repeated in a cycle until all data files were processed. The results of their refinement were collected in one LST file. Then the values of the gas hydrate and the ice weight fractions, corresponding to each refined diffraction pattern, were extracted from the LST file by the tools of the Linux shell. The automatically obtained gas hydrate fraction was plotted versus time and showed the trend of the hydrate formation.

§ 2. Image Processing

2.1. The approach

The image processing is an applied science born in the 60-es to restore, extract, understand and decode information hidden in digital images. This is any operation that acts to improve, correct, analyze, or in some way change an image. The necessity of such science arose in the early 60-es with the lunar program in NASA and the ranger program in NANA¹. Its importance increased in the late 60-es with the rapid development of the X-ray computer tomography (CT), magnetic resonance imagery (MRI), positron emission tomography (PET) and ultrasound imaging. Nowadays it is largely applied in fields like medical diagnostic imaging, biological research, materials research, remote sensing and Earth resources, space exploration and astronomy, defense and intelligence, etc. The software developers,

mathematical logicians and AI (Artificial Intelligence) specialists consider the IP as one of the most complicated problems to solve. That's why potentially very powerful AI methods like PCNN (Pulse Coupled Neuron Network) find their application there. Here the artificial neuron networks will not be discussed because such were not used at this preliminary stage of the studies. Therefore, the impact will be on the more common but not ineffective techniques for IP, implemented here.

The IP in this work is based on processing bitmap files by noise filtration, thresholding and obtaining binary images. The further analysis includes filtration of the binary images, obtaining the 0th

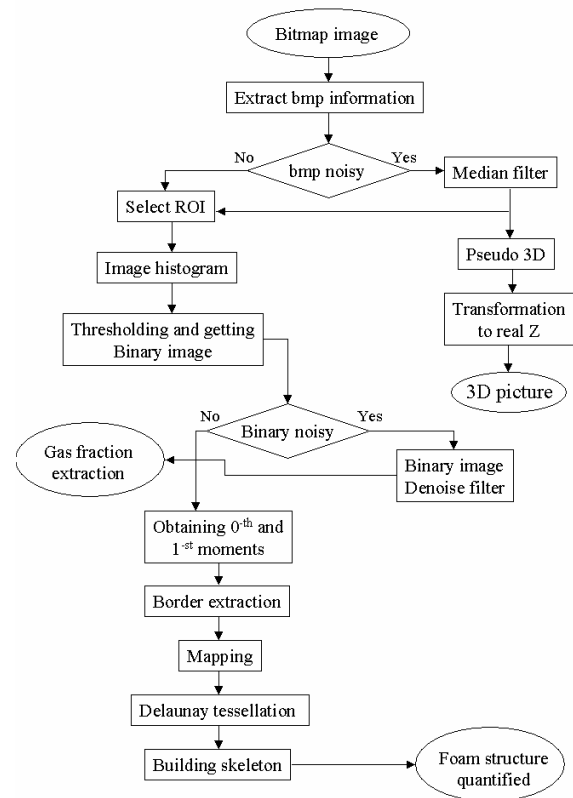


Fig.3 The algorithm

¹ The NANA Region, encompassing 38 000 square miles (or about the size of Indiana), is situated in Northwest Alaska. Most of the region is above the Arctic Circle.

(area) and 1st (center of mass) order moments of the explored objects and border extraction. The latter is to be used in a Delaunay tessellation procedure. It is supposed to provide a basis for implementing further procedures, like building the skeleton for quantifying of the hydrate foam structure. A general algorithm of this approach is given on **Fig. 3**.

2.2.The bitmap format

The Windows bitmap (bmp) files are stored in a device-independent bmp (DIB) format allowing windows to show them on any type of display. “Device independent” means the bmp specifies pixel color in a form independent of the method of displaying. Each bmp file contains file header, info header, color table and an array of bytes, defining the bits (**Fig. 4**).

The bmp file header contains information about the type, size and layout of a DIB. It is defined as BITMAPFILEHEADER structure.

The bmp info header specifies the dimensions, compression type, and color format for the bmp. It is defined as a BITMAPINFOHEADER structure.

The RGBQUAD array structure is a color table, containing as many elements as there are colors in the bmp. The color table is not present for bmps with 24 color bits, because each pixel there is represented by 24-bit RGB values in the actual bmp data area. The colors in the table appear in the order of importance. Thus the driver, using the biClrImportant member of the BITMAPINFOHEADER can render a bmp on a device that cannot display as many colors as there are in the bmp.

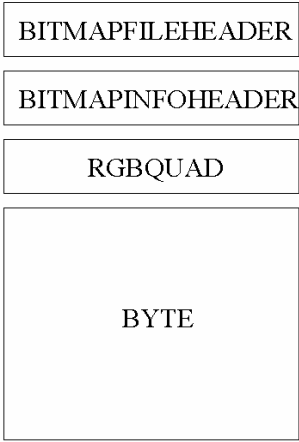


Fig. 4 The bitmap file

The BITMAPINFO structure is used to show combined bmp information (header and color table). The BYTE array contains the bmp bits. It represents the scan-lines of the bmp. Each scan-line consists of bytes representing the pixels in it in left-to-right order. The number of these bytes depends on the color format and on the width of the bmp in pixels. The scan-lines are stored from the bottom to the top. Thus, the first byte in the array represents the lower-left corner pixel and the last – the upper-right one.

The biBitCount member of the BITMAPINFOHEADER determines the number of bits defining each pixel and the maximum number of colors in the bmp. This member can have one of the following values:

- 1 - Monochrome bmp – the color table contains two entries. Each bit in the bmp array represents a pixel;
- 4 - 16 colors bmp. Each pixel in the bmp is represented by a 4-bit index in the color table;
- 8 - 256 colors bmp. Each pixel in the bmp is represented by 1 byte index into the color table;

$24 - 2^{24}$ colors bmp. The bmiColors (or bmciColors) member is NULL and each 3-byte sequence in the bmp array represents the relative intensities of red, green and blue for a pixel, respectively.

The biClrUsed member of the BITMAPINFOHEADER specifies the number of color indexes used in the bmp color table. If biClrUsed is 0, the bmp uses the maximum number of colors, corresponding to the value of the biBitCount member.

2.3. Image histogram, obtaining the binary image and its analysis

The histogram is a representation of the frequency of each color's intensity (red, green, blue or luminance) in one image. It is a fairly straightforward procedure to make the histogram of every image. One needs to count the intensities for every pixel in the image and store them into 256 member arrays. With this information one can perform histogram stretching, equalizing etc. Here the histogram is used in the production of binary images out of the grayscale SEM hydrate pictures.

The binary images (BI) are images quantumised to two values – typically black and white. The assignment is usually 0 for black and 1 or 255 for white. The BIs have found many applications since they are the simplest to process. At the same time they are such an impoverished representation of the image information that their use is not always possible. However, they are useful when the silhouette of the object provides all the needed information and when one can obtain this silhouette easily. Sometimes the output of other image processing techniques is represented in the form of a BI; for example, the output of border detection can be a binary image. BI processing techniques can be useful for subsequent processing of these output images. BI are typically obtained by thresholding a gray level image. Pixels with a gray level above the threshold are set to “white”, while the rest are set to “black”. This produces a white object on a black

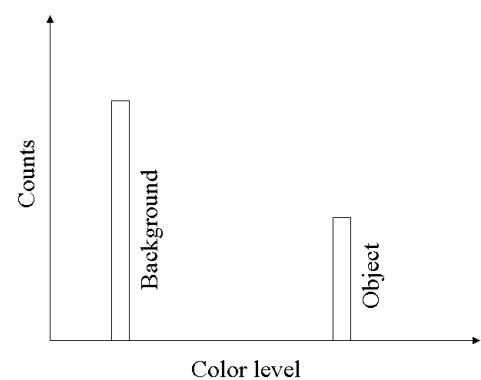


Fig. 5 Ideal histogram of a light object on a dark plain background

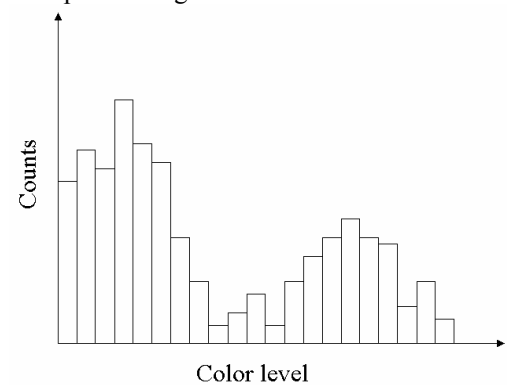


Fig. 6 Real histogram with background

background or vice versa, depending on the relative gray values of the object and the background. Of course, the “negative” of a binary image is also a binary image, where the pixel values have been reversed. However, choosing a threshold can be difficult, and is even considered by some authors to be a “black art” (Faugeras 1993). If one has a good fortune, the histogram will be bimodal and choosing a threshold will be easy. It may even be possible to construct an automatic procedure to determine it. Ideally, if one has a black object on a white background the histogram should appear as seen on **Fig. 5**. But there is the noise of the measurement. Then the real histogram is the result of

convolving the “ideal” one with the probability distribution of the noise (see **Fig. 6**). If the gray levels of the object and the background are fairly close, the influence of the noise may result in the object only appearing as a “shoulder” in the histogram. In this case the histogram will be no longer bimodal and there will be no trivial way of choosing the threshold level. Repeated observations and averaging may help, but the spread of the histogram may be due to light or color variations in the background and in the object.

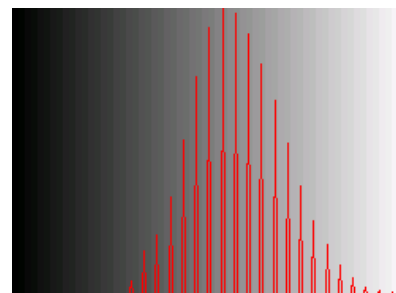
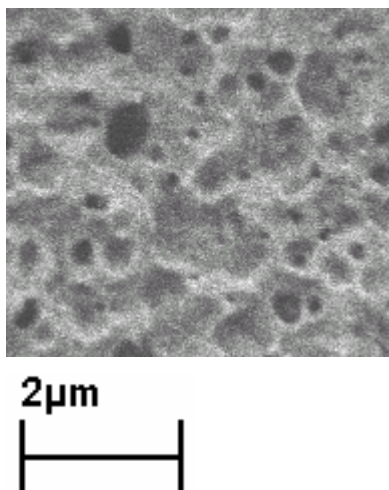


Fig. 7 The sample image and its histogram (Max at Gray scale 132)

What does the histogram give in the particular case of a picture of hydrate foam? From now on all the examples will be based on the image given in the next **Fig. 7**, where its grayscale histogram is also shown. Here comes one of the tricky moments in the whole story. Firstly the pictures here are considered flat. This means there are no other curvatures except the ones due to the bubbles. The second assumption is the electron beam is always perpendicular to the surface. Subsequently, in the image a reference line of zero altitude can be defined. Everything below this line is a “valley” and everything above is a “mountain”. This reference line corresponds to the histogram maximum. If one thresholds this image at luminance 132 (the maximum of this particular histogram) will get the picture on **Fig. 8**. The high level of noise is easily visible but this is something I will deal with later when the story goes about the applied filters. This image corresponds to a cut-off view of the structure or to its 2D projection. The black spots are the bubbles (gas fraction) and the white area is the dense fraction. From this image one can easily extract the gas fraction in the 2D foam in %. Usually for such highly homogeneous structures is assumed that the 2D picture can be expanded into the third dimension. At this point, one could start thinking everything is finished and there is no need to do anything else. But the ultimate goal here is not only to find the gas fraction but also to extract the bubble distribution in the foam. This would eventually help the subsequent modeling of the heat and noise transport through the hydrate foam.

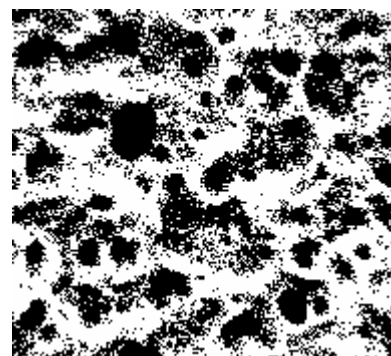


Fig. 8 Result of the thresholding of the image at luminance level 132

Usually the aim is to determine various characteristics of the objects in the image with the goal of using them to identify the objects, to determine their position and orientation or to follow the change in there size. The characteristic function of an object in one image is:

$$b(x, y) \begin{cases} = 1, & \text{for points belonging to the object} \\ = 0, & \text{for background points} \end{cases}$$

Lets suppose the object is continuous (it has infinite resolution). Then the area is given by its 0th moment:

$$S = \iint b(x, y) dx dy \quad (\text{AppV.7})$$

Its center of mass, (\bar{x}, \bar{y}) is given by the 1st moments:

$$\bar{x} = \frac{\iint x b(x, y) dx dy}{\iint b(x, y) dx dy} \quad (\text{AppV.8})$$

$$\bar{y} = \frac{\iint y b(x, y) dx dy}{\iint b(x, y) dx dy}$$

This is certainly very beautiful but at the same time too complicated because the considered objects have smooth boundaries. When one processes pixilated pictures, all the objects consist of large numbers of small squares (pixels). This allows for transforming the above equations to something much simpler, i.e.

$$\begin{aligned} S &= \sum_i b(x_i, y_i) \\ \bar{x} &= \frac{\sum_i x_i b(x_i, y_i)}{\sum_i b(x_i, y_i)} \\ \bar{y} &= \frac{\sum_i y_i b(x_i, y_i)}{\sum_i b(x_i, y_i)} \end{aligned} \quad (\text{AppV.9})$$

where $b(x_i, y_i)$ is the characteristic function of one single pixel.

Having the area of the object one can calculate its equivalent average radius, r_{av} :

$$S = \sum_i b(x_i, y_i) = \pi r_{av}^2 \quad (\text{AppV.10})$$

2.4. Filters and border extraction

Median filter²

As it became clear from **Fig. 8**, a lot of noise appeared after the thresholding. *De facto*, it had not appeared at all. It had been there before. This is mainly a noise from the equipment, essentially due to the amortization of the Shotky gun of the FE-SEM and when the lowest possible scan-velocity appears to be too high (because of charging). There are five approaches to solve this problem: (1) change the diode (the expensive one, which will not necessarily work), (2) filtration of the initial

² More information at URL <http://www.dai.ed.ac.uk/HIPR2/filtops.htm> and many others.

image, (3) filtration of the binary image, (4) both filtrations and (5) all together (even more expensive). Here the filtration of the initial image is discussed. The one of the binary image will be considered later on.

Image processing filters are mainly used to suppress either the high frequencies in the image (smoothing), or the low ones (enhancing or detecting edges). One image can be filtered either in the frequency³ or in the spatial domain⁴. The first involves transforming the image into the frequency domain, multiplying it with the frequency filter function and re-transforming the result into the spatial domain. The corresponding process in the spatial domain is to convolve the input image $f(i,j)$ with the filter function $h(i,j)$, i.e.:

$$g(i, j) = h(i, j) \otimes f(i, j)$$

The results of the digital implementations vary, since one has to approximate the filter function with a discrete and finite convolution

kernel, which is a small matrix of numbers used to perform filtering operation on each pixel in one image (**Fig. 9**). Most kernels have 3 rows and 3 columns but there is no size limitation. However, the larger the kernel the longer it takes to perform the filtration. The word “kernel” is also commonly used as a synonym for “structuring element”, which is a similar object used in mathematical morphology. A structuring element differs from a kernel in that it also has a specified origin.

The median filtering is a non-linear signal enhancement technique for smoothing signals, suppression of impulse noise and preserving the edges. It is used to reduce the noise, somewhat like the mean filter. However, it usually does a better job than the mean filter in preserving useful details in the image. Like the mean filter, the median one considers each pixel in the image and looks at its neighbors to decide whether or not it is representative of its surroundings. Instead of replacing the pixel value with the mean of neighboring pixel values, it replaces it with their median. First sorting all the pixel values from the surrounding neighborhood into numerical order and then replacing the considered pixel with the middle pixel value, calculate the median. (If the neighborhood under consideration contains an even number of pixels, the average of the two middle pixel values is used).

Fig. 10 illustrates one example calculation (after <http://www.dai.ed.ac.uk/HIPR2/filtops.htm>).

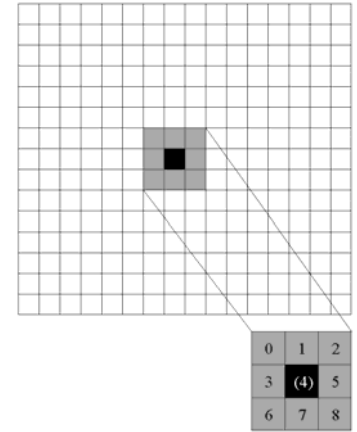


Fig. 9 Convolution kernel for a mean filter with 3×3 neighborhood

123	125	126	130	140
122	124	126	127	135
118	120	150	125	134
119	115	119	123	133
111	116	110	120	130

Neighbourhood values:

115, 119, 120, 123, 124
125, 126, 127, 150

Median value: 124

Fig. 10 Example calculation of the median. The central pixel value of 150 is unrepresentative of the surrounding pixels and is replaced with the median value: 124. A 3×3 square neighborhood is used here. Larger neighborhoods will produce more severe smoothing.

³ The *frequency domain* is a space where each image value at image position F represents the intensity variation in the image over a specific distance related to F .

⁴ The *spatial domain* is the normal image space. In most cases, the Fourier Transform will be used to convert images from the spatial domain into the frequency one.

The noise reduction technique realized in this work is also known as “Pseudo median filtering” - a form of median filtering. For fuller discussion of the original algorithm one can refer to Pratt (1991). This algorithm also performs a neighborhood inspection on sequences of pixels in horizontal and vertical directions. By default a 5 x 5 filter lattice is implemented with horizontal pixels, labeled: a, b, c, d, e and vertical ones labeled: f, g, c, h, i (see **Fig. 11**). This sequence is further subdivided into groups of 3 pixels i.e. (a, b, c), (b, c, d), (c, d, e), (f, g, c), (g, c, h) and (c, h, i). Two passes over the image are done. In the first one the maximum values of each subsequence are taken and their minimum is gotten. This is stored in an array and the second pass runs over this array finding the minimums of each subsequence. Then the maximum of those minimums is taken and this gives already the filtered image.

		f		
		g		
a	b	c	d	e
		h		
		i		

Fig. 11 The 5 x 5 filter mesh used in the current work

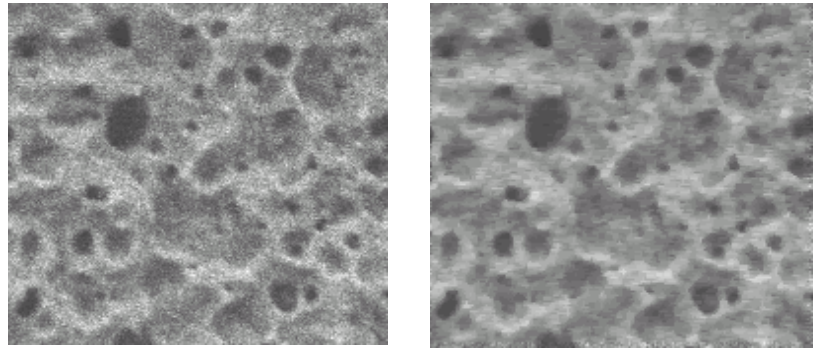


Fig. 12 Comparison between the original noisy image (left) and the result of the treatment with the filter (right).

Obviously, this is quite a complex state of affairs. The first pass gets rid of the dark areas of noise and the second one – of the bright ones. At the end on **Fig. 15** is given the algorithm of the filter, which will probably help for a better understanding. On **Fig. 12** is shown the result of its use.

Now let us consider the problems arising from the use of this filter. First of all, the use of any filter leads to some loss of information besides the noise correction. The losses may be loosing contrast, blurring more or less the whole image, blurring more or less the edges etc. There are many different types of filtering algorithms, which are characterized with different degrees of denoising and worsening the image. It is clear when choosing an algorithm one must compromise between both positive and negative effects. Here I have chosen the pseudo-median filter because it has the best performance in preserving the edges (which are the most important part of the image for this work) and at the same time performs very good denoising (**Fig. 12**). Still, when saying that it has “the best performance” it

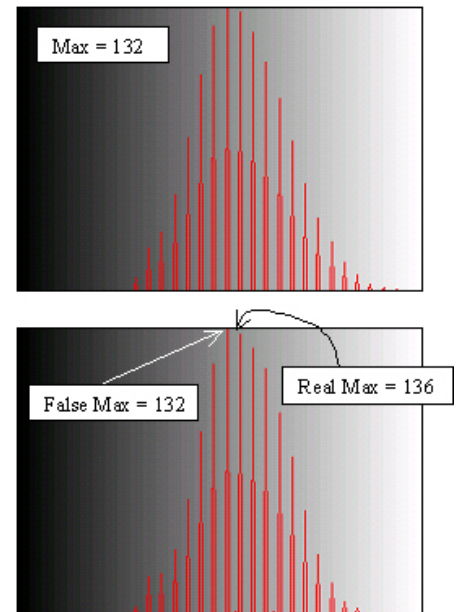


Fig. 13 Comparison between the histograms of the raw image (upper one) and the treated image (bottom). It shows the appearance of the false maximum in the treated image histogram.

does not mean that information is not lost. Also, in some cases it appears its use leads to a change in the histogram of the denoised image. It results in possible shifting the real histogram maximum to the right or more to the bright colors, as well as, in its slight asymmetrisation and shrinkage. Sometimes it gives significant rise to the color, which corresponds to the maximum of the raw image histogram, creating a false maximum there (**Fig. 13**). This must be kept in mind when thresholding the filtered image. In this case the reference level will be represented by the real histogram maximum. Another problem is the edge effect. Using this filter, as it is given here, will lead to a frame two pixels wide, which will stay denoised. There are two ways to deal with this problem; first to implement another filtering procedure for denoising the edges or second – to cut the edges. Here the second one is chosen.

Binary image denoise filter

As it is visible from **Fig. 14**-top the binary image obtained as a result of the thresholding the raw image with threshold level 132 is quite noisy. To get rid of the noise here I invented the “Binary image denoise filter”. It inspects the pixel’s nearby neighbors and decides whether or not to change its values to the negative one. It works with the, so called here, single pixel definition (SPD). SPD tells the computer what to consider as a single pixel (SP). The most straightforward idea is that a SP is a pixel surrounded entirely by pixels of the negative color. But here also the edge effect appears. The procedure this time is not to cut the noisy frame but to treat it. The SPD for the corner pixels, assumed in this algorithm, defines a SP as one having more than one neighbor of the negative color or this pixel will be inverted if two or three of its neighbors are negatively colored. The corresponding definition for the filtration of the edges (without the corners) stays that a SP has more than two neighbors of the negative colors. Up to here becomes clear the inversion of a corner pixel takes place if more than 33 % of the neighbors are colored negatively and for the edge pixels the number is – more than 20 %. Already the problem becomes visible. The treatment of the corners and the edges is not equivalent. This leads to the question: what SPD to choose for processing the bulk image? I decided to give more flexibility and to allow for choosing the number of the neighbors colored negatively, above which, the considered pixel is to be treated. One can choose between four possibilities: 0 – SP is the pixel whose neighbors are colored negatively; 1 (2 or 3) – SP is the one which has only one (2 or 3) neighbor(s) with the same color. It is clear that by choosing option 2, the considered pixel will be transformed if more than 25 % of the neighbors are colored negatively. This seems to be the most appropriate choice. Anyway, a program of this type without AI involved cannot decide itself which variant is the best. This is still necessary to be done by a human. A comparison between the results of the four different ways of treating the image is given on **Fig. 14**.

Thus, three different denoising procedures appeared on the horizon: (1) denoising the four corners, (2) the four edges and (3) the body of the picture. The third one is done twice (two passes);

from the top left corner to the bottom right and from bottom right to top left. A better idea about how this algorithm works can be obtained by observing the flowchart on **Fig. 16**.

The border extraction is always considered as a very tricky business. Different algorithms based on convolution kernels exist. But having a binary image the procedure allows for simplification. If one has black objects placed on white background or vice-versa, every pixel, which has at least one neighbor of the negative color, is a border one. The process chosen here is very similar to the one of the Binary image denoise filter. Again the nearby pixels are checked and if only one of them is negatively colored, the considered pixel is classified as a border one. Easily, it may appear that such a border encloses a zero area. This would lead to unpredictable triangulation results afterwards. One has to think about a procedure for hunting and eliminating zero surfaces.

After obtaining the satisfactory starting binary image and extracting its edges, a Delaunay tessellation procedure needs to be applied helping to describe the foam structure using either Voronoi or Johnson-Mehl structure models. The former assumes that nuclei of gas bubbles are randomly distributed with a density specified a priori. Nucleation of bubbles occurs at all sites simultaneously and all bubbles grow at the same rate. In contrast, the nucleation in a Johnson-Mehl model is continuous and follows the Poisson process. Here the nuclei of bubbles appear randomly in space and time and grow at a constant rate. Furthermore, calculations for the thermal transport through the hydrate cellular structure analogical to those made for the metal foams (e.g. Lu & Chen 1999) can be performed.

And to conclude I will say a few words on the possibility for extracting real Z information from the SEM pictures. If the light source is situated right in the zenith and the detector is at the same point then the luminance levels in the image carry direct information for the altitudes in it. In the case of SEM, if one succeeds to find a surface perpendicular to the electron beam, exactly such geometry is established⁵. Having this information one can make a plot in coordinates (X, Y, Luminance). This would look exactly an AFM image with the only disadvantage that a calibration “Color – Real Z” does

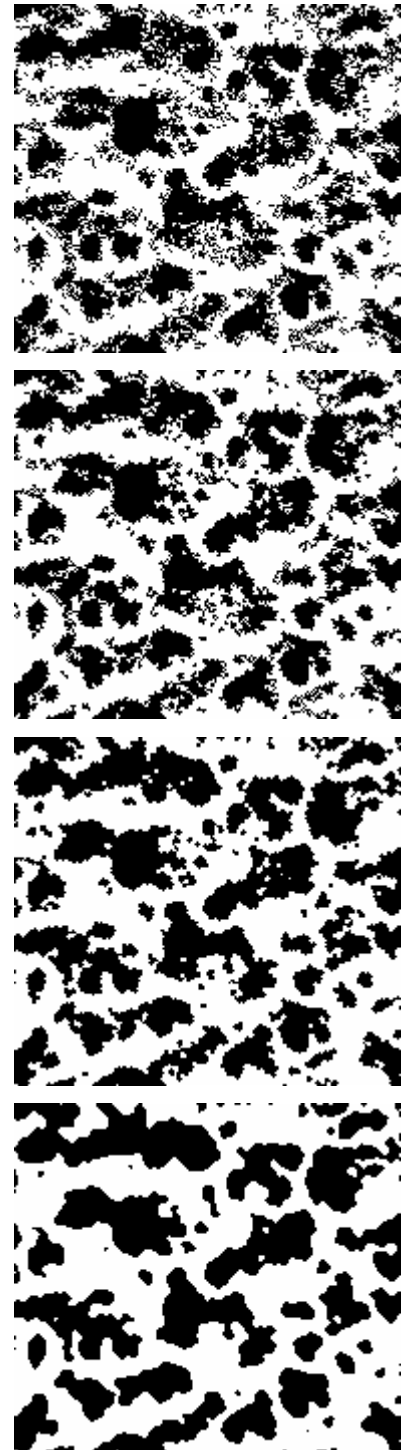


Fig. 14 Results of the filtration of the initial binary image choosing SPD 0 (top), 1, 2 and 3 (bottom)

⁵ Because of the physics staying behind the detection of all “reflected” by the surface electrons, the position of the detector does not play any role.

not exist. But if a sample of mica, prepared in a special way, is observed first in the AFM and then in the SEM machine such calibration may appear possible (Till Heinrichs private communication). Unfortunately, this is not foreseen for the near future.

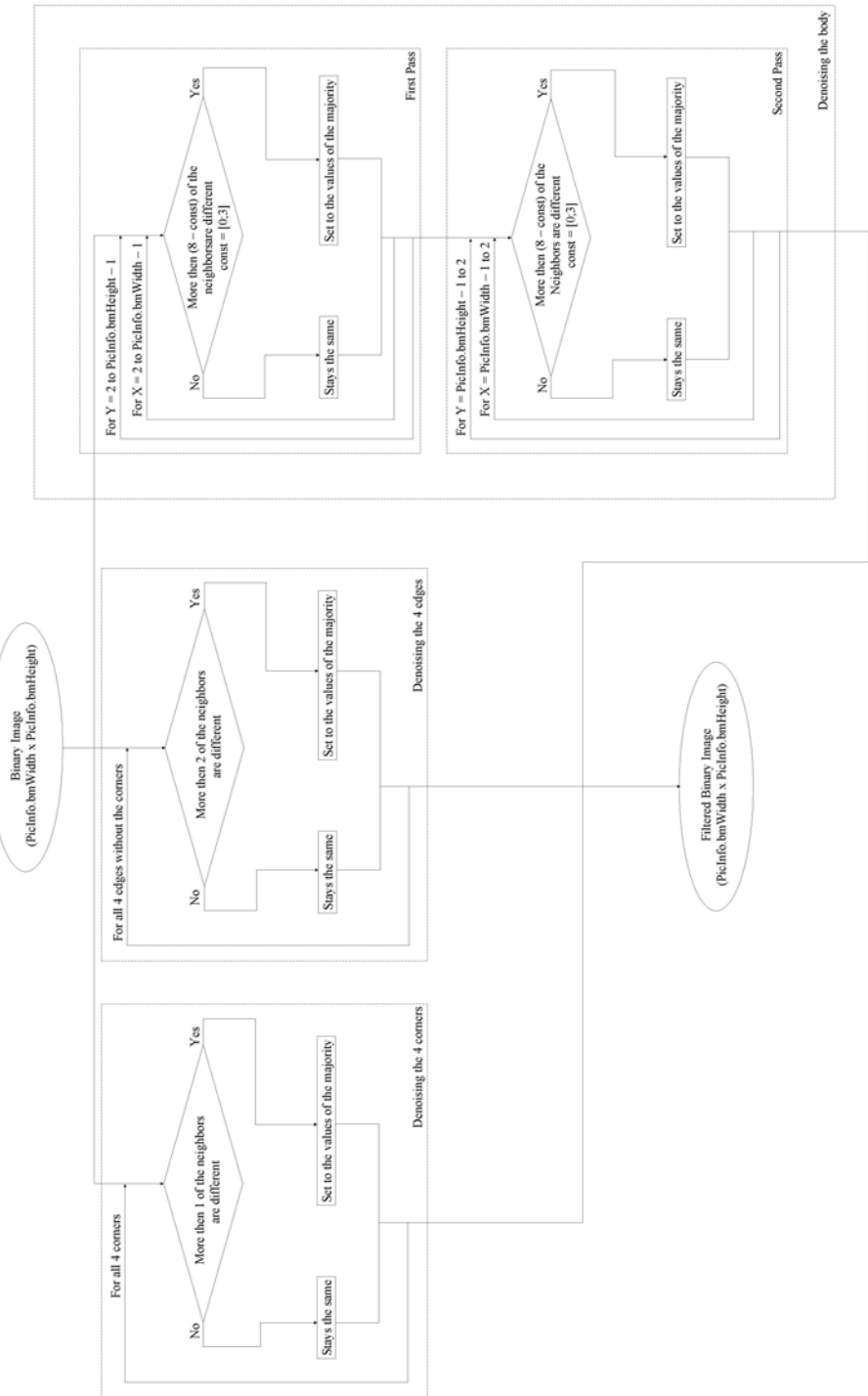


Fig. 15 The Binary Image Denoise filter flowchart

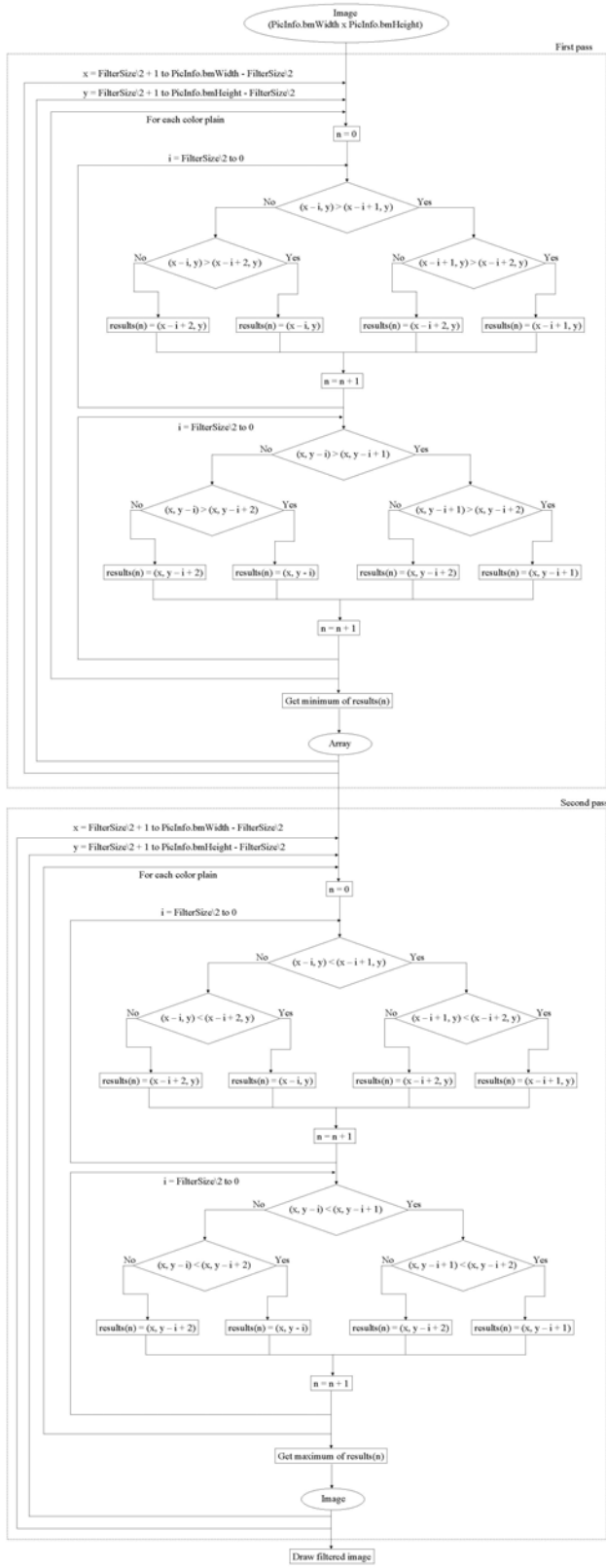


Fig. 16 The median filter flowchart

Acknowledgements

I am especially grateful to my supervisor Prof. Dr. Werner F. Kuhs for the invaluable supervision and help in producing the experimental results for this thesis, as well as for the very productive discussions on the theoretical descriptions and model interpretations. His administrative support throughout my stay here in Goettingen is not forgotten either.

Doroteya Staykova is gratefully acknowledged for introducing me into the GSAS software, for the nice discussions and also for the help upon my arrival in Goettingen.

I would like to thank Viorel Chihaiia, Andreas Zeller and Evgeny Goreschnik, for the useful discussions and technical support.

I am also thankful to Andrey Salamatina for the discussions on the multistage model.

Thanks to Till Heinrichs (GZG, Abt. Angewandte Geologie) and Kirsten Techmer for teaching me in electron microscopy.

I would like to thank Heiner Bartels, Klaus Haepe and Eberhard Hensel for the hardware and software support.

I am grateful to Thomas Hansen, Louis Melesi and Jean-Luc Laborier (ILL, Grenoble) for the help in performing the experiments on D20 and ILL for the beam time and support.

And not on the last place, I would like to thank all my colleagues from the Institute of Crystallography for the incredible working atmosphere. I had really nice time here.

This work was supported by the DFG grant **Ku 920/11**

Lebenslauf

Name: Georgi Yordanov Genov

Anschrift: Leinestr.1, 37073 Göttingen

Geburtstag: 03.08.1975

Geburtsort: Varna, Bulgaria

Staatsangehörigkeit: Bulgarisch

Schulbildung: 1994 Technische Schule des Maschinenbauwesens und der Elektronik, Varna

Hochschulbildung: 1999 Universität Sofia, Physikalische Fakultät
Studienrichtung: Physik
Abschluß: Diplom-Physiker
Thema der Diplomarbeit: Thermodynamic parameterization of multihadron production
2004 Doktorat am Geowissenschaftlichen Zentrum der Universität Göttingen Abt. Kristallographie
Thema der Promotion: Physical processes of the CO₂ hydrate formation and decomposition at conditions relevant to Mars

Göttingen, den 04.11.2004

Experimental studies on the formation of porous gas hydrates

GEORGI GENOV,^{1,*} WERNER F. KUHS,¹ DOROTEYA K. STAYKOVA,¹ EVGENY GORESHNIK,¹ AND ANDREY N. SALAMATIN^{1,2}

¹GZG Abt. Kristallographie, Georg-August-Universität Göttingen, Göttingen 37077, Germany

²Department of Applied Mathematics, Kazan State University, Kazan 420008, Russia

ABSTRACT

Gas hydrates grown at gas-ice interfaces were examined by electron microscopy and found to have a sub-micrometer porous structure. In situ observations of the formation of porous CH₄- and CO₂-hydrates from deuterated ice Ih powders were made at different pressures and temperatures, using time-resolved neutron diffraction data from the high-flux D20 diffractometer (ILL, Grenoble) as well as in-house gas consumption measurements. The CO₂ experiments conducted at low temperatures are particularly important for settling the open question of the existence of CO₂ hydrates on Mars. We found that at similar excess fugacities, the reaction of CO₂ was distinctly faster than that of CH₄. A phenomenological model for the kinetics of the gas hydrate formation from powders of spherical ice particles is developed with emphasis on ice-grain fracturing and sample-consolidation effects due to the outward growth of gas hydrate. It describes (1) the initial stage of fast crack-filling and hydrate film spreading over the ice surface and the two subsequent stages which are limited by (2) the clathration reaction at the ice-hydrate interface and/or by (3) the diffusive gas and water transport through the hydrate shells surrounding the shrinking ice cores. In the case of CO₂-hydrate, the activation energies of the ice-surface coating in stage 1 are estimated to be 5.5 kJ/mol at low temperatures and 31.5 kJ/mol above 220 K, indicating that water molecule mobility at the ice surface plays a considerable role in the clathration reaction. Comparable activation energies of 42.3 and 54.6 kJ/mol are observed in the high temperature range for the reaction- and diffusion-limited stages 2 and 3, respectively.

INTRODUCTION

Gas clathrate hydrates are non-stoichiometric inclusion compounds encaging small, usually apolar guest molecules in a host-framework of hydrogen bonded water molecules. They exist as a stable solid phase at high gas pressures and/or low temperatures (van der Waals and Platteeuw 1959). Two main crystallographic structures of gas hydrates, the von Stackelberg cubic structures I and II, are distinguished, both consisting of two types of cavities, small and large cages, that can be occupied by guest molecules (Sloan 1998). It is generally assumed that the encaged gas molecules cannot exchange with the environment after formation. Rather, the guest molecules have to be built into the crystal structure during the growth process according to their chemical activity at the reaction site.

Since the 1950s, many gas hydrate systems have been studied. Still, some physico-chemical properties of gas hydrates as well as their formation and decomposition kinetics are neither well known nor properly understood, though they are of primary importance for several reasons (Sloan 1998). With traces of water in gas and oil transport systems hydrate stability conditions are met leading eventually to complete blockages of pipelines. Likewise, the kinetics of CH₄-hydrate formation and decomposition is of major significance in geological settings, for our understanding of the role of methane gas in climate change, for the possible use of natural gas hydrate deposits as a future

source of energy, or simply for a more economic transport and storage of gas. CO₂ clathrate hydrates could also be a possible way to sequester CO₂ into the ocean to reduce global warming (Warzinski et al. 2000). They may also play a major role in some terra-forming processes on Mars (Cabrol et al. 1997; Komatsu et al. 2000; Wilson and Head 2002). In addition, they could affect the rheological properties of the polar ice layers at the north and south Martian poles (Brightwell et al. 2003; Durham 1998; Kargel 1998; Kargel and Tanaka 2002; Kreslavsky and Head 2002; Milkovich et al. 2002). Moreover, the higher the amount of CO₂ hydrate in the caps, the longer the period needed for establishing a steady-state geothermal gradient in their inner parts, which would affect basal melting (Kargel and Tanaka 2002; Kreslavsky and Head 2002). Not much is known about the formation kinetics of CO₂ hydrates under Martian conditions, and the present work partly intends to establish a solid physico-chemical basis for the hypotheses listed above. In this context, the most relevant formation process is the reaction of ice Ih with CO₂ gas to hydrate. A strong dependence of the transformation rates on the surface area of the gas-ice contact was demonstrated by Barrer and Edge (1967). Later, Hwang et al. (1990) studied methane-hydrate growth on ice as a heterogeneous interfacial phenomenon and measured the clathrate formation rates during ice melting at different gas pressures. Sloan and Fleyfel (1991) discussed molecular mechanisms of the hydrate-crystal nucleation on ice surfaces, emphasizing the role of the quasi-liquid-layer (QLL). Takeya et al. (2000) made in situ observations of CO₂-hydrate

* E-mail: ggenov@gwdg.de

growth from ice-powder for various thermodynamic conditions using laboratory X-ray diffraction. They distinguished the initial ice-surface coverage stage and a subsequent stage, which was assumed to be controlled by gas and water diffusion through the hydrate shells surrounding the ice grains. This process was modeled following Hondoh and Uchida (1992) and Salamatin et al. (1998) with a single ice particle approximation. The respective activation energies of the ice-to-hydrate conversion were estimated as 0.2 and 0.4 eV (19.2 and 38.3 kJ/mol). The first in situ neutron diffraction experiments on kinetics of clathrate formation from ice-powders were presented by Henning et al. (2000). They studied CO₂-hydrate growth on D₂O ice Ih, using the high intensity powder diffractometer HIPD at Argonne National Laboratory at temperatures ranging from 230 to 263 K and at a gas pressure of approximately 900 psi (6.2 MPa). The starting material was crushed and sieved ice with unknown but most likely irregular grain shapes. To interpret their results at a later stage of the hydrate formation process, the authors applied a simplified diffusion model for flat hydrate-layer growth, developed for the hydration of concrete grains (Berliner et al. 1998; Fujii and Kondo 1974), and obtained an activation energy of 6.5 kcal/mol (27.1 kJ/mol). This work was continued by Wang et al. (2002), who studied the kinetics of CH₄-hydrate formation on deuterated ice particles. A more sophisticated shrinking ice-core model (Froment and Bischoff 1990; Levenspiel 1999) reduced to the diffusion model of Takeya et al. (2000, 2001) was used to fit the measurements. A higher activation energy of 14.7 kcal/mol (61.3 kJ/mol) was deduced for methane hydrate growth on ice. Based on Mizuno and Hanafusa (1987), the authors suggested that the quasi-liquid layer of water molecules at the ice-hydrate interface may play a key role in the (diffusive) gas and water redistribution although a definite proof could not be given.

One of the recent and most intriguing find is that, at least in cases where the guest species are available as excess free gas, some gas hydrate crystals grow with a nanometric porous microstructure. Using cryo field-emission scanning electron microscopy (FE-SEM), direct observations of such sub-micrometer porous gas hydrates have now been made (Klapproth 2002; Klapproth et al. 2003; Kuhs et al. 2000; Staykova et al. 2002, 2003). Hwang et al. (1990) reported that the methane hydrates formed from ice in their experiments were bulky and contained many voids. Rather interestingly, there is evidence that besides dense hydrates, some natural gas hydrates from the ocean sea floor also exhibit nanometric porosity (Suess et al. 2002). Based on experimental studies (Aya et al. 1992; Sugaya and Mori 1996; Uchida and Kawabata 1995) of CO₂ and fluorocarbon hydrate growth at liquid-liquid interfaces, Mori and Mochizuki (1997) and Mori (1998) proposed a porous microstructure for the hydrate layers between the two liquid phases and suggested a phenomenological capillary permeation model of water transport across the films. Although the general physical concepts of this phenomenon in different situations may be quite similar, we still do not have sufficient data to develop a unified theoretical approach to its modeling (Mori 1998). The study presented here is confined to the particular thermodynamic conditions of gas hydrate formation from ice in a single-component gas atmosphere at pressures well exceeding the dissociation pressure at constant temperatures below the quadruple point.

In accordance with numerous experimental observations (Henning et al. 2000; Kuhs et al. 2000; Staykova et al. 2002, 2003; Stern et al. 1998; Takeya et al. 2000; Uchida et al. 1992, 1994), a thin gas hydrate film rapidly spreads over the ice surface at the initial stage of the ice-to-hydrate conversion. This stage of surface coverage was labeled stage I in our previous publications (Staykova et al. 2002, 2003). Subsequently, the only way to maintain the clathration reaction is the transport of gas molecules through the intervening hydrate layer to the ice-hydrate interface and/or of water molecules from the ice core to the outer hydrate-gas interface. As mentioned above, diffusion-limited clathrate growth was assumed for this second stage as described by Takeya et al. (2000), Henning et al. (2000), and Wang et al. (2002) on the basis of the shrinking-core models formulated for a single ice particle, without taking explicit account of a surface coverage stage. However, in the case of porous gas hydrates, gas and water mass transport through the hydrate layer becomes much easier, and the clathration reaction itself together with the gas and water transfer over the phase boundaries may be the rate-limiting step(s) that follows the initial coverage. This process should be modeled simultaneously with the ice-grain coating (Salamatin and Kuhs 2002). We have labeled this reaction-limited stage as stage II. Certainly, we can still expect the onset of a diffusion-limited stage (stage III in our nomenclature) of the hydrate formation process completely or, at least, partly controlled by gas and water diffusion through the hydrate phase, especially when a highly consolidated ice-hydrate structure develops with thick and dense hydrate shells surrounding ice cores and/or when the nanometric porosity is predominantly closed. As a result, the hydrate-phase growth and expansion beyond the initial ice-grain boundaries into the sample voids and the corresponding reduction of the specific surface of the hydrate shells exposed to the ambient gas can be a principal factor which slows down the hydrate formation rates at the later stages of the clathration reaction, as predicted by Staykova et al. (2003).

Here, we continue previous studies presented in Salamatin and Kuhs (2002) and Staykova et al. (2002, 2003) and attempt to quantitatively describe all the subsequent stages of the formation process of CH₄ and CO₂ gas hydrates as followed by in situ neutron diffraction and gas consumption experiments, starting from a well-characterized ice powder of known structure, grain size, and specific surface area. While neutron experiments give unique access to the fast initial part of the clathration reaction, in-house gas consumption experiments are indispensable for the much slower later stages of hydrate formation. Together with our kinetic diffraction studies, ex situ FE-SEM observations of the formation of porous gas hydrates proved to be helpful in understanding the initial coating phenomenon and the evolution of ice-powder structure during the clathration reaction and to construct a phenomenological multi-stage model of gas hydrate growth from ice powders. In particular, recent SEM images clearly show that the clathration reaction often starts in cracks of the ice grains formed during the preparation of the starting material. Thus, special attention will be paid here to the crack-filling sub-stage, which precedes or accompanies coverage of the spherical ice grain surfaces. A model for crack-filling is presented here for the first time and is applied to fit and interpret the experimental data.

EXPERIMENTAL METHODS AND SAMPLE PREPARATION

Diffraction instrumentation and gas-consumption technique

Neutron diffraction techniques are well suited to investigate gas hydrate formation kinetics as the strong penetration of neutrons allows for the use of thick-walled high-pressure gas equipment for cryogenic devices. We performed in situ neutron diffraction experiments at various pressures and temperatures with CH_4 and CO_2 gas on the high-intensity 2-axis D20 neutron diffractometer at ILL, Grenoble. D20 is a medium to high-resolution diffractometer providing a high flux at the sample position. It has 1536 detection cells in a stationary, curved linear position sensitive detector (PSD) covering a 2θ range of 153.6° . This makes D20 an ideal tool for in situ diffraction studies with acquisition times under one second, which makes it possible to follow fast changes in the sample. More details about the instrument can be found at <http://www.ill.fr/YellowBook/D20> and in Convert et al. (1998, 2000).

The beam-time allocation of neutron sources is typically limited to a few days. Therefore, the reaction kinetics at longer time scales can not usually be investigated by in situ neutron diffraction. At lower temperatures in particular, the reaction can take several weeks to several months. Therefore, we have also designed and employed an in situ technique based on gas consumption during the formation reaction. Different arrangements are used for pressures above and below 0.1 MPa shown in Figures 1 and 2 respectively. Using a gas pressure cell made of a high-strength aluminum alloy with a typical volume of 2 cm^3 and a low-temperature bath, the reaction is followed by recording the drop of gas pressure in the system. The pressure in the system is adjusted manually from time to time in order to maintain the pressure within typically a few percent fraction of the target pressure. As the pressure drop depends on the amount of ice in the pressure cell as well as on the free gas volume of the specific arrangement, calibration is necessary at the end of each experiment. This is achieved by measuring the ratio of unreacted ice Ih to newly formed gas hydrate by means of X-ray powder diffraction. As laboratory X-ray sources lack the penetration power to allow for in situ measurements, the samples are recovered at liquid nitrogen temperatures and investigated at 80 K in a custom-made Philips MRD diffractometer equipped with an APD helium

closed-cycle cryostat. The measured X-ray pattern is then analyzed using a full pattern Rietveld refinement technique with GSAS (Larson and von Dreele 1990). Occasional checks with samples measured previously by in situ neutron diffraction confirmed the reliability of the recovery method.

Sample preparation

Spherical D_2O ice Ih grains with a typical diameter of several tens of μm were prepared (see Fig. 3a) in our laboratory in Göttingen using a spraying technique. In order to quantify the morphology of the starting material, a representative part of the sample was investigated by FE-SEM. The pictures obtained were used to estimate the size distribution of the ice spheres. Measurements on different batches showed that the size distribution of ice spheres sprayed with the same nozzle is well reproducible and has a lognormal shape. The mean radius has been determined as $27 \mu\text{m}$ with a relative standard deviation of 0.8; for the first neutron experiment at 272 K ice spheres with a larger radius of $38.5 \mu\text{m}$ were used. The main characteristics of the ice samples and gas hydrates are presented in Table 1.

For the neutron diffraction experiments the samples were poured into thin-walled Al cans and transported in a dry- N_2 dewar to ILL/Grenoble. The estimated initial macro-porosity of $\epsilon_{\text{est}} \approx 30\text{--}35\%$ corresponds to a packing density of about 65–70% in the Al cans. Two high-strength auto-frettaged aluminum gas pressure cells were manufactured in Göttingen and adapted to an ILL sample holder. Temperature readings were obtained from a calibrated sensor fixed to the pressure cell wall. The Al cans were inserted into the pressure cell, already attached to the sample holder, and the Bridgman seal was closed. This filling operation was performed with a small stream of gas to ensure complete filling of the system. Subsequently, the pressure cell was inserted into the cryostat and the temperature was equilibrated at the chosen value. The desired gas pressure was applied within a few seconds while data collection was initiated. In our experiments, we did not observe an induction time except for temperatures below 200 K; reactions at higher temperatures began immediately (within the diffractometer time-resolution of a few seconds) after application of gas pressures higher than the decomposition pressure.

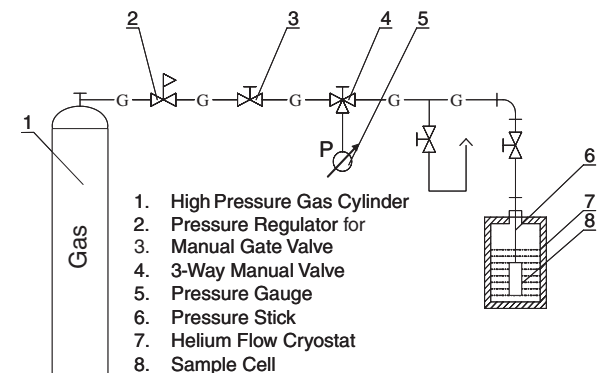


FIGURE 1. Schematic drawing of the set up for gas consumption measurement ($>0.1 \text{ MPa}$)

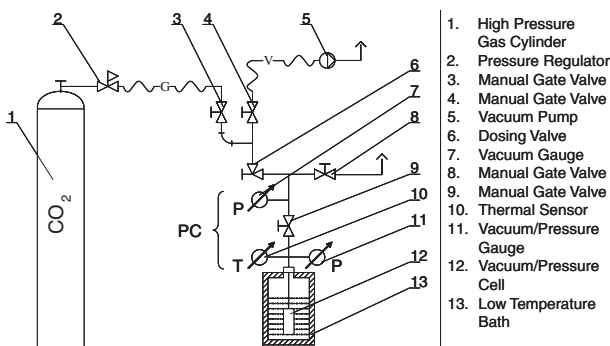


FIGURE 2. Schematic drawing of the set up for gas consumption measurement ($<0.1 \text{ MPa}$)

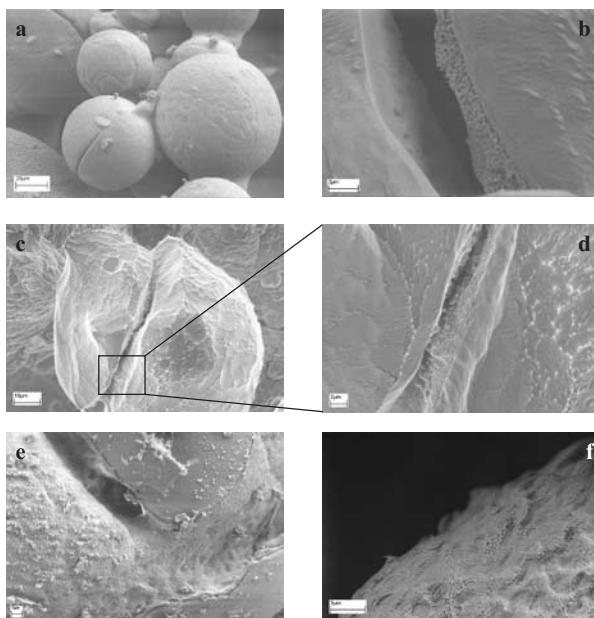


FIGURE 3. Field-emission scanning electron images of the starting ice-Ih material as well as samples quenched at various stages of the CO_2 -hydrate formation process: (a) initial ice-Ih material, consisting of spheres with average diameter of $40\text{--}60 \mu\text{m}$; (b) CO_2 hydrate formation on crack surface after 3 h of reaction at 193 K and 0.05 MPa; (c) view of a crack and a higher-magnification view into the crack (d) showing the crack surface coverage under the same conditions after 8 h of reaction; (e) reaction which started in the crack and spread over the grain surface (185 K, 0.036 MPa, 21 h); (f) surface coverage on a deuterated ice sphere after 52 min of reaction at 3 MPa and 275 K.

TABLE 1. Characteristics of ice samples and gas hydrates

Parameters and denotations	Values
Ice samples	
Ice density ρ_i , kmol/m ³	51
Typical (mean) grain size r_{0i} , μ m	25–40
Relative standard deviation of grain radii	0.8
Specific surface area S_{0i} , m ² /mol	1.5–2.1
Average crack opening angle β , rad	0.06
Macro-porosity ϵ_{m0}	0.33
Coordination number Z_0	7
Random density slope of particle distribution C	15.5
Gas hydrates	
Water density in hydrate phase ρ_{hw} , kmol/m ³	45
Sub-micrometer porosity of CH ₄ - (CO ₂ -) hydrates ϵ_h	0.15 (0.1)

Diffraction data collection and processing

To observe changes in the diffraction patterns during gas hydrate formation we used D20 at its highest intensity setting and a wavelength of $\lambda = 2.414$ Å. The reaction of gas (at constant pressure and temperature) with the ice grains was followed over a period of typically 10 to 20 h. The data presented here were collected with a time resolution of 30 s or 1 min for the initial fast reaction and with a resolution of 5 min for the slower later part of the reaction. In this way data of good statistical precision were obtained, suggesting that even times of several seconds would deliver useful information. An efficiency correction and a background subtraction were applied to all data. Subsequently, the measurements were analyzed with the GSAS Rietveld refinement program (Larson and von Dreele 1990), which gave quantitative information on the amount of gas hydrate formed as a function of time with an accuracy of about 0.1%. A two-phase (ice Ih + gas hydrate) Rietveld fit of the powder diffraction pattern obtained for each time interval was performed. Refined parameters were the lattice constants for ice Ih and gas hydrate, the phase fractions, and five to six background parameters; the scale factor and absorption coefficient were fixed. The atomic positions and displacement parameters for D₂O ice Ih and CH₄- or CO₂-hydrate phases were taken from Klapproth (2002) and were also kept fixed. The weight fraction of the clathrate phase α (mole fraction of ice converted to the gas hydrate) was extracted from the refinement for each time interval and was plotted as a function of time.

FE-SEM observations and SSA measurements

We restrict our phenomenological model developed in the theoretical section below to previous (Klapproth 2002; Klapproth et al. 2003; Kuhs et al. 2000; Staykova et al. 2002, 2003; Suess et al. 2002) as well as recent ex situ FE-SEM observations of porous gas hydrates recovered at various stages of the formation process. From a few hundred electron micrographs we have selected typical examples of the early stages of the reaction shown in Figure 3. Additionally, measurements of the specific surface area (SSA) of the starting material and partly reacted samples were made (Kuhs et al. 2004) using a BET adsorption method originally developed for SSA measurements of snow (Legagneux et al. 2002, 2003) in order to check the extent to which the nanometric pores are interconnected. Based on these observations in combination with general physical and mechanical concepts, we can formulate the following statements: (1) The starting material (ice Ih powder) consists of spherical grains several tens of micrometers in diameter (Fig. 3a). The arrangement of the ice grains in the sample is close to a random dense packing with a packing porosity of about 30–35%. The measured specific ice surface indicates minimum contact areas between grains. The typical time scales of the heat and mass transfer processes in the ice-powder samples are small (~5–10 min). The temperature in the pressure cell is essentially uniform, and all substances and energy are rapidly redistributed within the open space of the sample volume. (2) The initial stage of crack-filling and ice-grain surface coverage by a gas hydrate film is clearly distinguished from the subsequent stage(s) of growth of the hydrate shell into the shrinking isolated ice cores. Different mechanisms are generally involved in the coating process, such as preferential and relatively fast filling of cracks in the grains (Figs. 3b, 3c, and 3d), formation (nucleation) of hydrate patches on the ice surfaces, and lateral spreading of the hydrate film (Figs. 3e and 3f). At lower temperatures crack filling generally precedes surface coverage, while at temperatures above 230 K the surface coverage becomes more rapid and usually overlaps with filling of the cracks. Subsequently the porous gas hydrate shell grows and covers the ice surface to a large extent, leading to a consolidated sample in which the original ice grain structure can still be recognized. The intermediate stage II is thought to be limited by the clathration reaction (including gas and water redistribution across the phase boundaries) while stage III is assumed to be influenced (or fully

controlled) by water- and gas-mass transport through the hydrate layers from and to the inner parts of the original ice grains, respectively. (3) The SSA measurements show increasing SSA, mainly during the surface coverage stage I until it reaches a limiting value, which suggests that the porosity is only partly open over a scale of a few micrometers. Hence, it is likely that only the initial hydrate film spreading over the ice-grain surface retains a high permeability. The time scale of the coating process ranges from several hours to several days, depending on thermodynamic conditions (see also section 4). As the thicker clathrate layers develop further, the pores (at least partly) lose their interconnectivity inside the hydrate at longer distances. Therefore, mass transport at the later stages of the clathration reaction cannot be achieved via the predominantly closed sub-micrometer pores. Rather, it must occur by bulk diffusion. Stages II and III can be observed in the FE-SEM only after breaking the consolidated sample to provide some inner surfaces. (4) All our FE-SEM pictures show that the hydrate crystallites grown from ice are rather small (from a few to some tens of micrometers). Typically, single crystals of hydrates have an isotropic, porous structure with a mean pore size on the order of several hundred nm for CH₄-, Ar-, and N₂- (*macropores*) in the generally accepted terminology of porous materials), and several tens of nm for CO₂-hydrate (*mesopores* in this terminology), although non-porous gas hydrates are also observed in our SEM micrographs. There is no obvious dependency of the pore size on either pressure and temperature or on the time of reaction. From the SEM photographs, the internal meso- to macro-porosity of the hydrate phase is visually estimated as 10–20%. The diffraction data suggest a good crystallinity of the hydrate crystals, indicating a coherent “inward” growth of the hydrate shells without any appreciable deformation. This is also confirmed by the FE-SEM pictures, which show that the growth process generally does not perturb the initial setting of crystallites. (5) The density of water in the crystalline hydrate lattice of both types I and II is noticeably less than that of ice. Thus, the excess water molecules must be partly “evacuated” from the ice-hydrate contact area to provide additional space for the newly formed porous clathrate hydrates. This water (~20–30%) is transported toward the outer hydrate surface where it reacts with the ambient gas, leading to expansion of the hydrate layer into the open space between the initial ice grains and to a reduction of the pore surface area between them (see Figs. 3c–f). However, specific surface area measurements (see above) indicate that the total area of the gas hydrate interface does not decrease with time during the initial stage of the reaction. Consequently, as also confirmed by SEM micrographs, some of the nanometric porosity in the hydrates remains open. The higher the mean size of the ice grains, the less complete is the ice-to-hydrate transformation in a given time, presenting further evidence that thick hydrate layers gradually lose some of their permeability and/or closure of the open voids between the original ice grains occurs. The final consolidated stage is clearly born out by the compact nature of the product with irregular shapes of the ice-hydrate particles and little open pore space visible in the FE-SEM after breaking the sample.

THEORY

Principal notions

Because a clear molecular picture of the clathrate formation process is lacking, the primary goal of our study is the development of a phenomenological model for the different, partially overlapping stages of the clathration reaction in order to interpret the experimental kinetic data. In accordance with recent observations, ice spheres in the starting material may have cracks (see Figs. 3c and 3d) most probably caused by thermal strains which arise during ice-powder preparation by means of water droplets freezing in liquid nitrogen. Therefore, we continued our previous work (Salamatin and Kuhs 2002; Staykova et al. 2003) and additionally introduced a description for the crack-filling part of the initial surface coverage, which appeared in our FE-SEM micrographs as the prominent first step of the clathration reaction, especially at lower temperatures. Following Staykova et al. (2003), the geometry of the ice-powder structure is described in a monosize (or monodisperse) approximation, in terms of the mean-volume ice grain (core) radius r_i and the specific surface area of ice grains (cores) per mole of water molecules S_i (with

r_{i0} and S_{i0} indicating initial values). The degree of the reaction (the mole fraction of ice converted to hydrate phase) α is the principal characteristic of the hydrate formation process developed in time t . Correspondingly, the total crack-void fraction of ice grains in a sample is designated as ϵ_f , and the degree of crack-volume-filling in ice spheres of an initial radius of r_{i0} is χ . Hereinafter, we consider ϵ_f to have values of ~ 0.01 – 0.03 .

Some of the ice grains in the sample may be connected by bonds. Nevertheless, in accordance with our observations, we assume that S_{i0} is equal to the sum of the spherical grain surfaces and, by definition,

$$S_i = \frac{3r_i^2}{\rho_{i0}^3}, \dots, \alpha = \frac{1}{1 - \epsilon_f} \left[\left(1 - \frac{r_i^3}{r_{i0}^3} \right) \left(1 - \epsilon_f \frac{1 + E}{E} \right) + \chi \frac{\epsilon_f}{E} \right] \quad (1)$$

Here ρ_i is the molar density of ice. The hydrate-phase expansion coefficient E is the proportion of the hydrate volume excess with respect to the consumed ice volume

$$E = \frac{\rho_i}{\rho_{hw} (1 - \epsilon_h)} - 1$$

expressed via the mole density of water ρ_{hw} in hydrate and mesoporosity ϵ_h of the clathrate phase.

In accordance with Equation 1, the problem of modeling the gas-hydrate formation (reaction degree α) from monosize-sphere powders is reduced to a mathematical description of the principal parameters r_i and χ of a reference grain among densely packed identical neighbors with a given crack-volume fraction. The monodisperse approximation of the ice-sample structure was shown by Staykova et al. (2003) to be quite appropriate for the initial period of hydrate formation ($\alpha < 0.3$ – 0.4) until the volumetric expansion and geometric interaction of the growing hydrate shells become principal factors controlling the reaction rate. In this case, the extension of the theory to polydispersed powders with an experimentally well-established log-normal distribution of ice-sphere radii is rather straightforward: expression 1 for S_i should be additionally divided by the factor $1 + \sigma_0^2$, where σ_0 is the relative standard deviation of the grain size. The general model for hydrate formation from polydisperse powders of randomly packed ice spheres valid for the later part of the reaction will be presented elsewhere.

Ice-core model

Now, we introduce (after Staykova et al. 2003) the rate of the ice sphere surface-coating ω_s and the rate of subsequent volume ice-to-hydrate transformation ω_v outside of cracks. The former quantity can be defined as the fraction of the open (exposed to the ambient gas) ice surface which becomes covered by the initial hydrate film (hydrate patches) during a unit time period, while the latter is the number of ice moles transformed to hydrate phase per unit of time on a unit area of ice surface after coating. We also designate as δ_0 the thickness of the ice layer converted in the coating process relative to the initial hydrate film of thickness $d_0 = \delta_0(1 + E)$. Parameter δ_0 (and d_0) is small compared to the mean grain size r_{i0} , whereas the rate of the initial hydrate film formation is assumed to be much higher than that of the hydrate layer growth on the coated surface ($\omega_s \gg S_{i0}\omega_v$). Thus, the ice surface area remains practically constant

($S_i \approx S_{i0}$) during stage I.

Consequently, in accordance with Salamatin and Kuhs (2002), the radius of the shrinking ice core r_i in the sample is governed by the following mass balance equation

$$\frac{dr_i}{dt} \left(1 - \frac{r_i^3}{r_{i0}^3} \right) = S_i \left[\rho_i \delta_0 \omega_s e^{-\omega_s t} + \omega_v (1 - e^{-\omega_s t}) \right] \quad (2a)$$

or, identically, in monodisperse approximation for S_i given by Equation 1

$$\frac{dr_i}{dt} = -\delta_0 \omega_s e^{-\omega_s t} - \frac{\omega_v}{\rho_i} (1 - e^{-\omega_s t}). \quad (2b)$$

The driving force of the hydrate formation is the supersaturation of the gas-ice-hydrate system, $\ln(f/f_d)$, expressed via fugacities f and f_d of the gaseous phase and decomposition pressures p and p_d at a given temperature T . For each stage, this driving force determines the clathration kinetics and contributes to the different steps in the ice-to-hydrate conversion in proportion to their apparent resistances, namely, k_s^{-1} for the initial hydrate film spreading over the ice surface, and k_R^{-1} and k_D^{-1} for the clathration reaction and gas/water permeation through the hydrate layer, respectively.

Hence, we conventionally write

$$\omega_s = k_s \ln \frac{f}{f_d}, \quad \omega_v = \frac{k_R k_D}{k_R + k_D} \ln \frac{f}{f_d} \quad (3)$$

Depending on the rate-limiting step of the hydrate formation process, ω_v describes either the rate of the clathration reaction (ω_R) in stage II (when $k_D \gg k_R$) or the rate of gas and water mass transfer through the hydrate shell (ω_D) in stage III (when $k_D \ll k_R$). For comparable values of k_R and k_D in the latter part of Equation 3, both steps are important.

The clathration rate constants are assumed to be the Arrhenius-type functions of temperature:

$$k_J = k_J^* \exp \left[\frac{Q_J}{R_g} \left(\frac{1}{T^*} - \frac{1}{T} \right) \right], \quad J = S, R, D, \quad (4)$$

where k_J^* and Q_J are the clathration rate constant at the reference temperature T^* and the activation energy of the J -type step; R_g is the gas constant.

Phenomenological Equations 1–4 are considered to be a theoretical basis for the detailed analysis of the different stages of hydrate formation and interpretation of the neutron diffraction data. Actually, each J -th step, explicitly presented in the model, may be further divided into a sequence of sub-steps characterized by their own resistances, the sum of which is k_J^{-1} . Nevertheless, for a fixed temperature k_s and k_R can still be used as tuning parameters, but the permeation rate constant k_D depends on geometrical characteristics of the hydrate layers growing around shrinking ice cores and must be related to r_i to complete Equations 2 and 3.

Permeation resistance of the hydrate layer

Here we follow the geometrical description of powder-particle growth developed by Arzt (1982) for a random dense packing of monodisperse spheres on the basis of the concept of Voronoi cells associated with the initial powder structure. The build-up of the starting material is characterized by the average

number of contacts per particle (coordination number) Z_0 and the relative slope C of the random packing density function. Experimental estimates for these parameters deduced by Arzt (1982) are given in Table 1 and are consistent with the observed porosity of our ice-powder samples.

As shown schematically in Figure 4, the shape of each hydrate layer formed from a single spherical ice grain is represented as a truncated sphere of radius r_h . The ice core shrinks, and its radius r_i decreases due to inward growth of the hydrate layer. However, because of the lesser density of water in the porous hydrate phase, the excess water molecules must be transported to the outward hydrate surface exposed to the ambient gas, and the hydrate layer simultaneously expands into the open space between the original ice grains, eventually filling most of the initial open space. The existing contact areas between neighboring hydrate shells (ice-hydrate particles) increases and additional contacts are formed as r_h grows. Correspondingly (see Appendix A for details), the fraction s of the free hydrate surface area exposed to the ambient gas, the specific surface area of the macro-voids S_m , and the macro-porosity of the sample ϵ_m decrease. Finally, the current sample geometry is related to the ice core radius r_i by means of the hydrate-volume expansion factor E .

The fictitious spherical boundary of radius r in Figure 4 divides the hydrate shell into two sub-layers 1 and 2: from r_i to r and from r to r_h , respectively. The permeation (diffusion) resistance of the spherical sub-layer 1 is known from diffusion theory (Crank 1975). To estimate the resistance of the truncated sub-layer 2, we assumed (Staykova et al. 2003) that locally the mass-transfer process in the layer is similar to diffusion through a concave spherical layer of the same thickness with the same total areas of bounding surfaces. Finally, we arrived at the following relation for the permeation rate constant in Equation 3:

$$k_D = \frac{\rho_i D}{r_{i0}} \sigma, \quad \sigma = \frac{\sqrt{s} R_h R}{R_i \left[\sqrt{s} R_h (R - R_i) + R_i (R_h - R) \right]} \quad (5)$$

Here D is the apparent gas/water mass transfer (permeation) coefficient proportional to that introduced in Salamatina et al. (1998), and σ is the complex geometrical characteristic of the developing sample structure expressed via normalized parameters

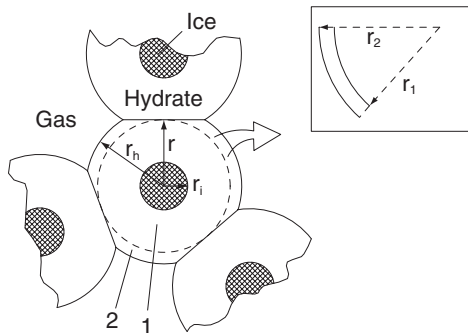


FIGURE 4. Schematic diagram of gas hydrate expansion into the voids between the ice spheres during the growth of hydrate shells around the shrinking ice cores. In the diffusion model (see text) the permeation resistance of the convex sub-layer 2 surrounding the inner spherical hydrate layer 1 is assumed to be similar to that of the concave spherical layer shown in the insert. See text for further details.

$R = r/r_{i0}$, $R_i = r_i/r_{i0}$, and $R_h = r_h/r_{i0}$. The temperature dependence of the permeation coefficient follows Equation 4 with k_D^* corresponding to D^* at the reference temperature T^* in Equation 5.

If the expansion effect is neglected ($E = 0$), the hydrate shells in the sample remain within the initial ice-grain boundaries, R_h and s equal unity, and Equation 5 is reduced to the diffusive shrinking-core model for a single particle employed by Takeya et al. (2000) and Wang et al. (2002). Actually, in the case of a dense packing of the ice-powder, such an approximation might be valid only in the very beginning of the hydrate formation process when $R_h - R_i \rightarrow 0$ in Equations 5 and $\sigma \rightarrow \infty$ (i.e., $k_D \rightarrow \infty$). Consequently, in accordance with Equations 2 and 3, the kinetics of the ice-to-hydrate conversion passes, at least initially, through stages I and II as controlled by the ice surface coverage process and/or by the clathration reaction—and not by diffusion. Thus, the simplified models used in Henning et al. (2000), Takeya et al. (2000), and Wang et al. (2002) are neither applicable for an interpretation of the initial stage of the clathration reaction, nor are they valid for the final phase of sample consolidation.

Gas hydrate growth in a crack of an ice grain

The fissures were in SEM images (see Figs. 3c and 3d) of the starting material (ice samples), although rather narrow, are open and usually penetrate deep into the powder particles. The observed process of fast initial hydrate growth in the ice-grain cracks, schematically shown in Figure 5, is assumed to develop simultaneously with the hydrate film patches spreading over the spherical surface of the reference grain as an independent, relatively short counterpart (sub-stage) of the initial stage I. To calculate the degree of volume-filling χ in a reference ice grain of initial radius r_{i0} , we write analogues of Equations 2 and 3 for hydrate formation on the crack surface (see Appendix B), designating all corresponding characteristics by primes. Thus, for example, the thickness δ'_0 of the ice layer converted to the initial hydrate film spreading over the crack sides is introduced together with the respective rates ω'_s and ω'_k of the crack surface coating and clathration reactions, the latter being related to the temperature-dependent rate constants k'_s and k'_k with activation energies Q'_s and Q'_k . Then, as explained in Appendix B, for the mean crack-opening angle β the average height h of the crack-filling (see Fig. 5) normalized by r_{i0} can be explicitly expressed (at constant ω'_k) vs. time t :

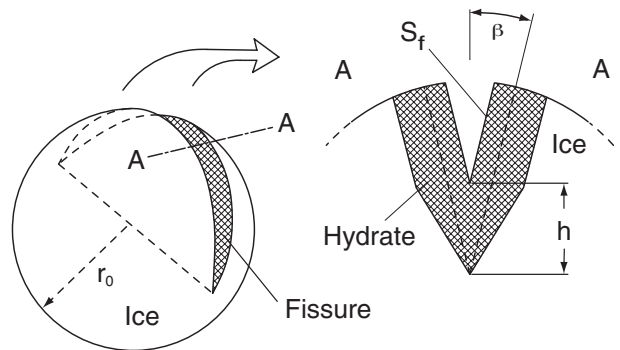


FIGURE 5. Schematic diagram of the hydrate formation in an ice-grain fissure and its A-A cross-section. The ice at the cleavage sides S_f is converted to hydrate at constant rate ω'_k and the height h linearly increases with time. See text for further details.

$$\xi = h/r_{i0} = A'(1 - e^{-\omega_s t}) + B't, \quad h < r_{i0}, \quad (6a)$$

$$A' = \frac{E}{\beta r_{i0}} \left(\delta'_0 - \frac{\omega'_R}{\rho_i \omega'_s} \right), \quad B' = \frac{E \omega'_R}{\beta \rho_i r_{i0}},$$

until complete filling is reached at $h = r_{i0}$, i.e., $\xi = 1$.

The area S_f of each crack side exposed to the ambient gas decreases as the hydrate fills the fissure. The volume of hydrate growing in the crack is calculated in Appendix B by integration of the incremental mean hydrate layers with respect to h , which yields the degree of filling term χ in the following form:

$$\chi = \frac{3}{4} \pi \xi - \frac{3}{2} \xi \arcsin \xi - \frac{3}{2} (1 - \xi^2)^{1/2} + \frac{1}{2} (1 - \xi^2)^{3/2} + 1, \quad \xi < 1, \quad (6b)$$

and $\chi \equiv 1$ for $\xi > 1$.

Although this relationship is derived for a crack penetrating to the center of a reference grain, it has a general structure and after substitution of Equation 6, can be tuned to any lesser mean initial relative depth of cracks by appropriate correction of A' and B' (e.g., by β).

Qualitative analysis of the model

Solutions of the general models 1–6 can be obtained only numerically, but for fixed pressure and temperature conditions, during stages I and II, at least in the beginning of the clathration reaction when $k_D \gg k_R$, quantities ω_s and ω_V given by Equation 3 can be considered as constant values ($\omega_V = \omega_R$), and Equation 2 can be integrated analytically. This yields an analogue of the asymptotic solution which was derived at $k_D \rightarrow \infty$ in Salamatin and Kuhs (2002).

$$r_i/r_{i0} = 1 - A(1 - e^{-\delta_0 t}) - Bt \quad (7)$$

where

$$A = \frac{\delta_0}{r_{i0}} - \frac{B}{\omega_s}, \quad B = \frac{\omega_R}{r_{i0} \rho_i}$$

Parameter A is the difference of two small terms and, hence, its absolute value is expected to be small although the quantity itself can be either positive or negative.

Neglecting terms of the order of magnitude of $O(\varepsilon_f^2 / E^2)$ and combining the latter Equation 7 with Equations 1 and 6, one obtains a generalized asymptotic relation for the reaction-limited kinetics of the hydrate formation process valid for small values of α :

$$(1 - \alpha)^{1/3} \approx 1 - \frac{\varepsilon_f}{3E} \chi(\xi) - A(1 - e^{-\omega_s t}) - Bt. \quad (8)$$

As noted in Staykova et al. (2003), Equation 8 requires that the graph of $(1 - \alpha)^{1/3}$ vs. time t for the earlier phase of hydrate formation during stage II and limited by the clathration reaction for $t \gg \omega_s^{-1}$ should be a straight line with slope B and intercept $1 - A - \varepsilon_f / (3E)$. This also gives us an insight into how the model parameters can be constrained by the kinetic measurements. First, via Equations 7 and 8, the asymptotic slope B is directly linked to the bulk ice-to-hydrate transformation rate and, for a given estimate for the grain-surface-coating rate ω_s , coefficient A (and, hence, δ_0) is determined, while ω_s can also be somewhat cor-

rected so as to follow back in time the preceding adjacent part of the reaction data. Then, the intercept of curve 8 directly delivers the crack void fraction ε_f . Finally, parameters A' and B' (i.e., δ'_0 and ω'_R for a given estimate for ω'_s) in Equations 6 and 8 can be adjusted to fit the very beginning of the kinetic curve which is mainly affected by the crack-filling process. Due to the difference in time scales ($\omega'_s \gg \omega_s$), the two sub-stages of the initial stage I are well distinguished, especially at low temperatures. The latter conclusion was demonstrated in Staykova et al. (2003), where a noticeable mismatch between Equation 7 and experimental data was observed at the very beginning of the clathration reaction (see Fig. 8 in this paper).

In the general case, the rate of the hydrate phase growth ω_V in Equations 2 and 3 may be significantly influenced or even limited by gas and water diffusion through the hydrate layer. Substitution of Equation 5 into the last part of Equation 3 yields

$$\omega_V = \omega_R \left(1 - \frac{1}{1 + F\sigma} \right), \quad F = \frac{D\rho_i}{r_{i0} k_R}. \quad (9)$$

The dimensionless complex F in Equation 9 is the principal parameter responsible for the onset of stage III controlled (or influenced) by gas/water mass transfer through hydrate shells surrounding the shrinking ice cores. As explained above, the normalized factor σ changes from infinitely large values in the beginning of the clathration reaction to the first order of magnitude in the later phase of the gas hydrate formation. Thus, the ice-hydrate system can never pass to stage III at large F , and $\omega_V \approx \omega_R$ in Equations 3 and 9. For $F \ll 1$ stage II becomes extremely short and ends up, together with stage I, being directly replaced by the diffusion-limited stage III. The intermediate values of $F \sim 1$ correspond to the onset of stage III simultaneously controlled by both (reaction and diffusion) steps.

For the hydrate formation process influenced by gas and water transport through the hydrate layers, the time behavior of the quantity $(1 - \alpha)^{1/3}$ becomes non-linear. Correspondingly, after some time t^* in the beginning of the diffusion-limited stage III described (for small α) by the simplified diffusion theory of Fujii and Kondo (1974), the relative ice-core radius r_i/r_{i0} is proportional to $(t - t^*)^{1/2}$. More elaborate models (Salamatin et al. 1998; Takeya et al. 2000; Wang et al. 2002) predict even higher non-linearity due to the decrease in the ice-core surface S_i . However, they do not take into account the initial stage I, as well as the sample compaction and the reduction of the macro-pore surface S_m in the course of the ice-to-hydrate transformation, as described by Equation 5. The latter effects additionally suppress the gas and water fluxes through the hydrate shells to and from the ice cores and slow down the reaction. However, as shown by Staykova et al. (2003), the difference between the reaction- and diffusion-limited kinetics of hydrate formation becomes noticeable only at the final phase of the clathration reaction (for $\alpha > 0.5$ –0.6). Before this, the α -curves can be equally well approximated by both limiting scenarios. Another peculiarity of the diffusion-limited conversion of ice powders to clathrate hydrates confirmed by Equations 1–3 and 5 and discussed in Staykova et al. (2003) is that the hydrate-growth rate in this case is inversely proportional to r_{i0}^2 , being in contrast to the first two stages with A and B inversely proportional to r_{i0} in Equations 7 and 8. Thus, the stages controlled by different rate-limiting steps

(clathration reaction or gas/water transport through the hydrate shells) can be distinguished from each another. This may also help to recognize the formation of porous gas hydrates in the analysis of kinetic data.

As mentioned above, at the beginning of the hydrate formation process (for $\alpha < 0.3$ –0.4) the monosize description of the ice-sample structure can be directly extended to polydispersed powders with log-normal distribution of ice-sphere radii. The necessary correction of Equation 1 for S_i presumes that the right-hand side of Equation 2₂ and coefficients A' , B' and A , B in Equations 6, 7, and 8 should also be divided by the factor $1 + \sigma_0^2$.

RESULTS AND DISCUSSION

CO₂-hydrate formation

Two series of in situ neutron diffraction experiments were previously conducted with D₂O-ice and a third one with H₂O-ice. Some of these results, in particular for methane, were presented in Staykova et al. (2003) where it was also shown that the deuterated and hydrogenated systems were essentially identical. Recently, a new series of in situ diffraction experiments with D₂O-ice as well as in-house measurements of CO₂-gas hydrate formation have been performed. Here we apply the model developed above to continue our study of hydrate formation from ice powders with special emphasis on crack filling during the initial stage I and CO₂-hydrate formation over a broad range of temperatures, including those related to Martian conditions (see Table 2).

In neutron-diffraction measurements, the gas hydrate growth reveals itself by an increase of the Bragg intensities originating from the gas hydrates which starts immediately after the application of gas pressure and increases with time while the amount of ice Ih decreases. The repeatedly reported induction period (Sloan 1998) was observed only at temperatures below 200 K and is not discussed here. A series of three experiments at 263, 253, and 230 K was performed with deuterated samples (see Fig. 6a). The reactions lasted between 17 and 26 h (see Table 2), resulting in 13–37% ice-to-hydrate conversion. An experiment performed with larger ice grains at 272 K (Fig. 6b) reported by Staykova et al. (2003) with a total reaction degree of about 56% was also used and is re-analyzed here. Likewise, the methane 230 K data up to 5%-degree transformation obtained previously (Staykova et al. 2003) have been re-examined with the improved model and are shown in Figure 6c along with the 230 K CO₂ data.

Another series of experiments were performed at 223, 203, and 193 K using our in-house gas consumption technique (described in section 2), also starting with deuterated ice. The reac-

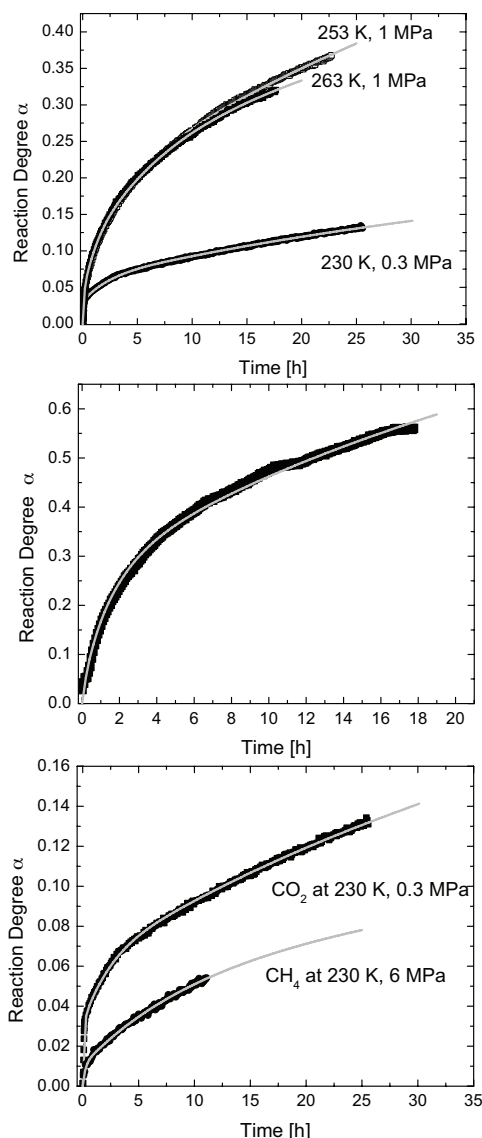


FIGURE 6. Plots of the data obtained during the neutron diffraction experiments, showing the temperature and pressure dependency of the growth kinetics: (a) comparison of the growth of CO₂ hydrate from deuterated ice under different thermodynamic conditions; (b) the most complete neutron kinetic experiment of CO₂ hydrate formation from deuterated ice at 272 K and 2 MPa; (c) comparison of the hydrate formation rates of CO₂ (0.3 MPa) and CH₄ (6 MPa) at 230 K. The light gray lines are the model fits.

TABLE 2. Conditions of experiments and kinetic parameters of gas hydrate formation

Conditions of experiments							Parameters of diffusion (D) and reaction (k_R) limited kinetics							
Ice	r_{0i} μm	Gas	T , K	p (f_i), bar	p_d (f_d), bar	Time, h	k'_s , 1/h	k'_R , $\text{kmol/m}^2\text{h}$	δ_{0i} , μm	k_s , 1/h	k_R , $\text{kmol/m}^2\text{h}$	D , m^2/h	δ_{0a} , μm	ϵ_i
D ₂ O	27	CH ₄	230	60 (46.2) 3 (2.9)	5.9 (5.8) 1.86 (1.82)	11 26	2 20	1.2·10 ⁻⁵ 2·10 ⁻⁴	1.4 3.7	1.2·10 ⁻² 8·10 ⁻²	— 2.6·10 ⁻⁶	— 1.4·10 ⁻¹³	1.6 1–1.8	1.2·10 ⁻² 1.5·10 ⁻²
			193	0.5 (0.495)	0.22 (0.219)	126	0.7	7·10 ⁻⁵	2.3	2.2·10 ⁻²	—	—	1.9	1.8·10 ⁻²
			203	0.89 (0.88)	0.433 (0.43)	48	5	2.3·10 ⁻⁴	2.3	2.7·10 ⁻²	—	—	1.9	1.8·10 ⁻²
			223	1.95 (1.9)	1.3 (1.28)	239	1.8	(0.85–1.5)·10 ⁻⁴	2.3	3.5·10 ⁻²	3.7·10 ⁻⁷	1.9·10 ⁻¹⁴	1.4	(1.6–1.9)·10 ⁻²
			253	10 (9.1)	5.1 (4.9)	22.5	20	4·10 ⁻⁴	3.3	0.35	1.4·10 ⁻⁵	1.5·10 ⁻¹²	2.2–3.4	1.6·10 ⁻²
			263	10 (9.3)	7.5 (7.1)	17.5	30	8·10 ⁻⁴	3.3	0.49	1.9·10 ⁻⁵	2·10 ⁻¹²	3.5–4.2	2.2·10 ⁻²
	38.5	272	20 (19.7)	11.4 (11.3)	18	5	4·10 ⁻⁵	3.3	0.85	3.5·10 ⁻⁵	6.4·10 ⁻¹²	4–5.6	(1.6–1.8)·10 ⁻²	

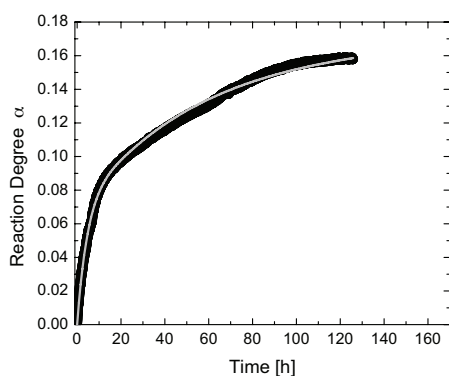


FIGURE 7. CO₂ hydrate formation reaction at 193 K and 0.5 MPa performed by the *pVT* method (see Fig. 2). The light gray line is the model fit.

tion degree did not exceed 17%. All these experiments covering the temperature range from 193 to 272 K were used to obtain the tuned model parameters listed in Table 2; examples are shown in Figures 6 and 7.

At high temperatures, the reduced (excess) fugacity ($f - f_d$) / f_d clearly influences the rate of CO₂-hydrate formation (see Fig. 6a and Table 2). During the first 6–7 hours both reactions at 253 and 263 K run closely together; only at a later stage does the reaction at 253 K significantly exceed the one at 263 K. This is due to a counterbalancing of the effects of temperature and excess fugacity. To reach the same reaction degree of 10%, a time of about 1 h is needed at 253 K; this is approximately 15 h at 230 K and exceeds 24 h at 193 K (compare Figs. 6a and 7). In all experiments the kinetic curve for the initial stage shows a strongly non-linear development in time and flattens in later stages while keeping a smooth overall shape. Our electron microscopic observations of the porous hydrate layer during stage I show that the coating process preferentially starts in cracks (see Figs. 3b, c, and d) with a subsequent spreading over the spherical grain surface. This suggests dividing stage I into two sub-stages: stage Ia (crack-filling) and stage Ib (surface-coating). The formation and spreading of hydrate patches is much slower than the filling of the cracks. Even at high temperatures, the ice surface is not fully covered with a hydrate shell after several hours, although the cracks in grains are completely filled.

Based on these observations the theoretical model described in section 3 was used to interpret the gas-consumption and diffusion data. An interactive computer program was developed to perform all necessary simulations. A least-squares procedure under user control was used to iteratively fit the model to measurements within the framework of the general strategy described at the end of section 3. The same approach was successfully employed previously in Staykova et al. (2003), and all previous simulations showed that certain parts of the kinetic curves were selectively sensitive to different groups of tuning parameters. Experimental constraints on the coating rate constants k_s and k'_s in Equations 3 and 6 derived from our SEM images in experiments interrupted at various temperatures were also taken into account, together with the estimate of the average crack opening angle $\beta \sim 0.06$. The most complete ice-to-hydrate conversion (up to 56%) was observed in the CO₂-D₂O clathration reaction (see Fig. 6b) at 272 K with a radius of the unreacted ice core shrunk to an

averaged value of $\approx 29 \mu\text{m}$. This makes the latter set especially valuable for model validation (Staykova et al. 2003).

The typical time scale (ω_s^{-1}) of stage I (stage Ia + stage Ib) is proportional (see Eqs. 3) to the reciprocal value of the ice-grain coating rate constant k'_s which increases from about 1 to approximately 12 h as the temperature decreases from 272 to 230 K (see Table 2). At 193 K it takes about 45 h. In these terms, for the thermodynamic driving force $\ln(f/f_d) \sim 1$, the reaction at 193 K can be interpreted as pure crack-filling during the first 5–7 h, followed by a transition period and surface-coating until approximately 150 h. The reaction curves at high temperatures are smoother, making it difficult to easily discern different sub-stages. This is in agreement with our SEM observations that at higher temperatures different stages may develop locally (grain-wise and even on one grain) with different speed and occur partly concomitantly when the whole sample is considered. As expected, the overall rates are much faster and complete surface coating at 272 K takes only about 6 h.

In all CO₂ experiments presented here the surface-coating stage was sufficiently well developed to obtain reliable values for the coating rate constant k_s . Thus, we are able to extract the activation energy Q_s of this process (see Fig. 8a). Obviously, two different regions can be considered, above and below 220–230 K. For the high temperature region, the value of the activation energy is 31.5 kJ/mol while it is 5.5 kJ/mol for the lower range. At low temperatures, the formation reactions should be followed for several months in order to get a robust result for the reaction rate constant k_R and/or permeation coefficient D . Such long-term experiments have not yet been completed and will be presented elsewhere. Nevertheless, at higher temperatures the reactions definitely reach stages II and/or III and allow for a reliable model interpretation, although, as discussed by Staykova et al. (2003), the reaction degree is still too low to distinguish between the controlling steps. The values of the reaction rate constant k_R and permeation coefficient D deduced under the assumption that the hydrate formation is either limited by reaction or diffusion are given in Table 2. They should be considered as lower estimates of these parameters if both steps are equally presented in the clathration process. The activation energy of the diffusion-limited process obtained for the 223 to 272 K range is 54.6 kJ/mol (Fig. 8b), while for the reaction-limited process an energy of 42.3 kJ/mol results from our analysis (Fig. 8c). The inferred permeation coefficient of the gas- and water-mass transfer in CO₂-hydrate formed from deuterated ice-powder is $6.4 \times 10^{-12} \text{ m}^2/\text{h}$ at 272 K, and is in good agreement with the estimate of about $8 \times 10^{-16} \text{ m}^2/\text{s}$ ($3 \times 10^{-12} \text{ m}^2/\text{h}$) obtained by Takeya et al. (2000) at 269 K for H₂O ice. This provides additional evidence that the isotopic properties of ice do not significantly affect gas hydrate growth and that the observed kinetics are similar. Unfortunately, the mean particle size in ice powders used by Henning et al. (2000) was not reported and a comparison with their experimental data cannot be made.

Concerning the initial crack-filling sub-stage, one can deduce from k'_s and k'_R listed in Table 2 that, in general, this process is more rapid at high temperatures, but the surface coverage, being several orders of magnitude slower at low temperatures, accelerates to a much higher degree and becomes hardly distinguishable from the crack-filling coverage (compare k'_R and k_R) at the melting

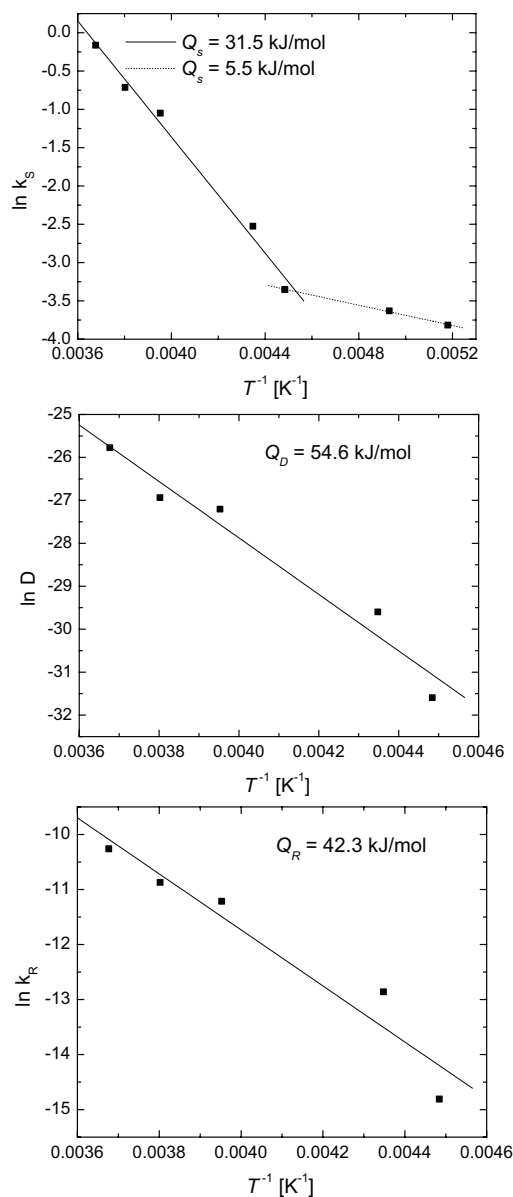


FIGURE 8. Arrhenius plots of the various stages of the CO_2 hydrate formation at temperatures above 223 K with (a) the surface coverage stage, (b) the diffusion-limited stage, and (c) the reaction-limited stage, as deduced from the best-fit model parameters (see Table 2).

point. This is in good agreement with our SEM observations. As a consequence, at lower temperatures the crack-filling stage is much more easily separated from a subsequent surface-coating sub-stage. From the model fits typically several μm are obtained for the thickness δ'_0 of the ice layer converted to the initial hydrate film on the crack walls, which compares well with the thickness δ_0 of the coating layer on the ice grain surface, being entirely consistent with the observations from electron microscopy.

CH_4 -hydrate growth from ice-powders

These experiments were reported in detail in Staykova et al. (2003). The latter paper also presented kinetic data interpreta-

tion, albeit under the assumption that ice grain surface-coating was the only process taking place in stage I of the reaction. A noticeable discrepancy between the observations and model fits at the very beginning of the kinetic curves (Staykova et al. 2003; Fig. 8) most likely was due to ignoring the crack-filling phenomenon. On the other hand, our SEM studies of methane hydrate formation suggest that at high temperatures the filling of cracks in ice grains may additionally overlap with particle necking, as well as the formation and lateral spreading of hydrate patches on the spherical ice grain surfaces. Therefore, in light of our low-temperature SEM observations when crack-filling is clearly distinguished from the much slower surface coverage, only the methane kinetic neutron data at 230 K presented in Figure 6□ have been reconsidered here. Taking into account a separate crack-filling stage improved the fit considerably and modified somewhat the remaining parameter set established in our earlier work (Staykova et al. 2003). Based on the new theoretical model we can see that this experiment was rather short and did not extend beyond stage I. Reaction and diffusion rates (parameters k_R and D) were too low to be reliably determined and are not given in Table 2. Comparison of these data in Figure 6c with those for CO_2 -hydrate formation at the same temperature of 230 K allows us to estimate and compare the ice-grain coating and crack-filling rates for the CH_4 - and CO_2 -clathration reactions. To do this one should note that in our case (see Table 2) the excess fugacity $(f - f_d) / f_d$ for the CH_4 -hydrate reaction at 230 K was about 12 times that for CO_2 . Even at this much higher driving force methane reacts two to three times slower than carbon dioxide. The actual scales of the crack-filling and coating rates at equal thermodynamic conditions are characterized by the respective reaction rate constants k_s^i and k_s . At 230 K (see Table 2), they are approximately one order of magnitude higher for CO_2 than for CH_4 . Thus, the tendency of the clathration reaction on ice to be much slower for methane than carbon dioxide at 272 K (Staykova et al. 2003) appears to be even more pronounced at lower temperatures.

ACKNOWLEDGMENTS

The authors are grateful to L. Melesi and J.-L. Laborier (ILL, Grenoble) for their help in preparing the high pressure equipment. Likewise we thank T. Hansen (ILL, Grenoble) for his competent help in performing the D20 experiments and the ILL for beam time and support. We also thank A. Klapproth and S. Klapp (Göttingen) for discussions and help during sample preparation and data analysis. L. Legagneux and F. Dominé (LGGE, Grenoble) as well as A. Zeller (Göttingen) are gratefully acknowledged for performing the measurement of the specific surface area of the ice-powder and porous gas hydrates. This study was supported by DFG grants Ku920/9-1 and Ku920/11-1. Likewise, part of this work was supported by grant 03G0553A of the BMBF in its programme GEOTECHNOLOGIEN of which this publication is paper No. GEOTECH-56. The financial support of both DFG and BMBF is gratefully acknowledged here.

REFERENCES CITED

- Arzt, E. (1982) The influence of an increasing particle coordination on the densification of spherical powders. *Acta Metallurgica*, 30, 1883–1890.
- Aya, K., Yamane, K., and Yamada, N. (1992) Stability of clathrate hydrate of carbon dioxide in highly pressurized water. In P.E. Kroeger and Y. Bayazitoglu, Eds., *Fundamentals of Phase Change: Freezing, Melting, and Sublimation—1992 HTD*, p. 17–22. The American Society of Mechanical Engineers, New York.
- Barrer, R.M. and Edge, A.V.J. (1967) Gas hydrates containing argon, krypton and xenon: kinetics and energetics of formation and equilibria. *Proceedings of the Royal Society London*, A 300, 1–24.
- Berliner, R., Popovici, M., Herwig, K.W., Berliner, M., Jennings, H.M., and Thomas, J.J. (1998) Quasielastic neutron scattering study of the effect of water-to-cement ration on the hydration kinetics of tricalcium silicate. *Cement and Concrete Research*, 28, 231–243.

- Brightwell, S.N., Kargel, J.S., and Titus, T.N. (2003) Martian south polar deformation and sublimation processes. In *Lunar and Planetary Science XXXIV*: Papers presented to the 34th Lunar and Planetary Science Conference, March 17–21, 2003. Lunar and Planetary Institute, no. 2077, League City, Texas.
- Cabrol, N.A., Grin, E.A., Landheim, R., and McKay, C.P. (1998) Cryovolcanism as a possible origin for pancake-domes in the Mars 98 landing site area: relevance for climate reconstruction and exobiology exploration. In *Lunar and Planetary Science XXXIX*: Papers presented to the 29th Lunar and Planetary Science Conference, 16–20 March 1998. Lunar and Planetary Institute, no. 1249, Houston, Texas.
- Convert, P., Hansen, T., Oed, A., and Torregrossa, J. (1998) D20 high flux two axis neutron diffractometer. *Physica B*, 241–243, 195–197.
- Convert, P., Hansen, T., and Torregrossa, J. (2000) The high intensity two axis neutron diffractometer D20—first results. *Materials Science Forum*, 321–324, 314–319.
- Crank, J. (1975) *The Mathematics of Diffusion*. Clarendon Press, Oxford.
- Demirdjian, B., Ferry, D., Suzanne, J., Toubin, S., Picaud, S., Hoang, P.N.M., and Girardet, C. (2002) Structure and dynamics of ice Ih films upon HCl adsorption between 190 and 270 K. I. Neutron diffraction and quasielastic neutron scattering experiments. *Journal of Chemical Physics*, 116, 5143–5149.
- Durham, W.B. (1998) Factors affecting the rheologic properties of Martian polar ice. *First International Conference on Mars Polar Science*, no. 3024.
- Froment, G.F. and Bischoff, K.B. (1990) *Chemical Reactor Analysis and Design*. Wiley, New York.
- Fujii, K. and Kondo, W. (1974) Kinetics of hydration of tricalcium silicate. *Journal of the American Ceramic Society*, 57, 492–497.
- Henning, R.W., Schultz, A.J., Thien, V., and Halpern, Y. (2000) Neutron diffraction studies of CO₂ clathrate hydrate: formation from deuterated ice. *Journal of Physical Chemistry*, 104, 5066–5071.
- Hondoh, T. and Uchida, T. (1992) Formation process of clathrate air-hydrate crystals in polar ice sheets. *Teion Kagaku (Low Temperature Science)*, A51, 197–212.
- Hwang, M.J., Wright, D.A., Kapur, A., and Holder, G.D. (1990) An experimental study of crystallization and crystal growth of methane hydrates from melting ice. *Journal of Inclusion Phenomena*, 8, 103–116.
- Kargel, J.S. (1998) Possible composition of Martian polar caps and controls on ice-cap behavior. In *First International Conference on Mars Polar Science*: Papers presented to the First International Conference on Mars Polar Science, October 19–22, 1998. Lunar and Planetary Institute, no. 3048, Houston, Texas.
- Kargel, J.S. and Tanaka, K.L. (2002) The Martian south polar cap: glacial ice sheet of multiple interbedded ices. In *Lunar and Planetary Science XXXIII*: Papers presented to the 33rd Lunar and Planetary Science Conference, March 11–15, 2002. Lunar and Planetary Institute, no. 1799, Houston, Texas.
- Klapproth, A. (2002) Strukturuntersuchungen an Methan- und Kohlenstoffdioxid-Clathrat-Hydraten. GZG, Abteilung Kristallographie. Georg-August-Universität, Göttingen.
- Klapproth, A., Goreschnik, E., Staykova, D.K., Klein, H., and Kuhs, W.F. (2003) Structural studies of gas hydrates. *Canadian Journal of Physics*, 81, 503–518.
- Komatsu, G., Kargel, J.S., Baker, V.R., Strom, R.G., Ori, G.G., Mosangini, C., and Tanaka, K.L. (2000) A chaotic terrain formation hypothesis: explosive outgas and outflow by dissociation of clathrate on Mars. In *Lunar and Planetary Science XXXI*: Papers presented to the 31st Lunar and Planetary Science Conference, March 13–17, 2000. Lunar and Planetary Institute, no. 1434, Houston, Texas.
- Kreslavsky, M.A. and Head, J.W. (2002) Conditions and principal time scales for basal melting of Martian polar caps. *Lunar and Planetary Institute*, no. 1779.
- Kuhs, W.F., Klapproth, A., Gotthardt, F., Techmer, K., and Heinrichs, T. (2000) The formation of meso- and macroporous gas hydrates. *Geophysical Research Letters*, 27, 2929–2932.
- Kuhs, W.F., Genov, G., Goreschnik, E., Zeller, A., Techmer, K.S., and Bohrmann, G. (2004) The impact of porous microstructures of gas hydrates on their macroscopic properties. *Proceedings of the 14th International Offshore Polar Engineering Conference*, ISOPE-2004, Toulon, France.
- Larson, A.C. and von Dreele, R.B. (1990) Los Alamos National Laboratory. Report LAUR 86-748.
- Legagneux, L., Cabanes, A., and Dominé, F. (2002) Measurement of the specific surface area of 176 snow samples using methane adsorption at 77K. *Journal of Geophysical Research*, 107, 4335.
- Legagneux, L., Lauzier, T., Dominé, F., Kuhs, W.F., Heinrichs, T., and Techmer, K. (2003) Rate of decay of specific surface area of snow during isothermal experiments and morphological changes studied by scanning electron microscopy. *Canadian Journal of Physics*, 81, 459–468.
- Levenspiel, O. (1999) *Chemical Reaction Engineering*. Wiley, New York.
- Milkovich, S.M., Head, J.W., and Kreslavsky, M.A. (2002) Variations in layered deposits at the North Pole of Mars: stratigraphy along a single trough and evidence for CO₂ loss. In *Lunar and Planetary Science XXXIII*: Papers presented to the 33rd Lunar and Planetary Science Conference, March 4–8, 2002. Lunar and Planetary Institute, no. 1713, Houston, Texas.
- Mizuno, Y. and Hanafusa, N. (1987) Studies of surface properties of ice using nuclear magnetic resonance. *Journal de Physique, Colloque C1, Supplement au N3*, 48, C1-511–C1-517.
- Mori, Y.H. (1998) Clathrate hydrate formation at the interface between liquid CO₂ and water phases—A review of rival models characterizing “hydrate films”. *Energy Conversion and Management*, 39, 1537–1557.
- Mori, Y.H. and Mochizuki, T. (1997) Mass transport across clathrate hydrate films—a capillary permeation model. *Chemical Engineering Science*, 52, 3613–3616.
- Salamatin, A.N. and Kuhs, W.F. (2002) Formation of porous gas hydrates. *Proceedings of the Fourth International Conference on Gas Hydrates*, Yokohama, May 19–23, 2002, Yokohama, p. 766–770. <http://hydrate.welcome.to/pdf/ICGH766.pdf>
- Salamatin, A.N., Hondoh, T., Uchida, T., and Lipenkov, V.Y. (1998) Post-nucleation conversion of an air bubble to clathrate air-hydrate crystal in ice. *Journal of Crystal Growth*, 193, 197–218.
- Sloan, E.D. Jr. (1998) *Clathrate Hydrates of Natural Gases*. Dekker, New York.
- Sloan, E.D. Jr. and Fleyfel, F. (1991) A molecular mechanism for gas hydrate nucleation from ice. *Institute of Chemical Engineering Journal*, 37, 1281–1292.
- Staykova, D.K., Hansen, T., Salamatin, A.N., and Kuhs, W.F. (2002) Kinetic diffraction experiments on the formation of porous gas hydrates. *Proceedings of the Fourth International Conference on Gas Hydrates*, Yokohama, May 19–23, 2002, 2, Yokohama, p. 537–542. <http://hydrate.welcome.to/pdf/ICGH537.pdf>
- Staykova, D.K., Kuhs, W.F., Salamatin, A.N., and Hansen, T. (2003) Formation of porous gas hydrates from ice powders: Diffraction experiments and multi-stage model. *Journal of Physical Chemistry B*, 107, 10299–10311.
- Stern, L.A., Hogenboom, D.L., Durham, W.B., Kirby, S.H., and Chou, I.M. (1998) Optical-cell evidence for superheated ice under gas-hydrate-forming conditions. *Journal of Physical Chemistry B*, 102, 2627–2632.
- Suess, E., Bohrmann, G., Rickert, D., Kuhs, W.F., Torres, M.E., Trehu, A., and Linke, P. (2002) Properties and fabric of near-surface methane hydrates at Hydrate Ridge, Cascadia Margin. *Proceedings of the Fourth International Conference on Gas Hydrates*, Yokohama, May 19–23, 2002, Yokohama, p. 740–744. <http://hydrate.welcome.to/pdf/ICGH740.pdf>
- Sugaya, M. and Mori, Y.H. (1996) Behavior of clathrate hydrate formation at the boundary of liquid water and fluorocarbon in liquid or vapor state. *Chemical Engineering Science*, 51, 3505–3517.
- Takeya, S., Hondoh, T., and Uchida, T. (2000) In-situ observations of CO₂ hydrate by X-ray diffraction. *Annals of the New York Academy of Sciences*, 912, 973–982.
- Takeya, S., Shimada, W., Kamata, Y., Ebinuma, T., Uchida, T., Nagao, J., and Narita, H. (2001) In situ X-ray diffraction measurements of the self-preservation effect of CH₄ hydrate. *Journal of Physical Chemistry A*, 105, 9756–9759.
- Toubin, C., Picaud, S., Hoang, P.N.M., Girardet, C., Demirdjian, B., Ferry, D., and Suzanne, J. (2002) Structure and dynamics of ice Ih films upon HCl adsorption between 190 and 270 K. II. Molecular dynamics simulations. *Journal of Chemical Physics*, 116, 5150–5157.
- Uchida, T. and Kawabata, J. (1995) Observations of water droplets in liquid carbon dioxide. *Proceedings of the MARIENV 95 Conference*, September 1995, Tokyo, p. 906–910.
- Uchida, T., Hondoh, T., Mae, S., Duval, P., and Lipenkov, V.Y. (1992) In-situ observations of growth process of clathrate air-hydrate under hydrostatic pressure. In N. Maeno and T. Hondoh, Eds., *Physics and Chemistry of Ice*, p. 121–125. Hokkaido University Press, Sapporo.
- — — (1994) Effects of temperature and pressure on transformation rate from air-bubbles to air-hydrate crystals in ice sheets. *Annals of Glaciology*, 20, 143–147.
- van der Waals, J.H. and Platteeuw, J.C. (1959) Clathrate solutions. *Advances in Chemical Physics*, 2, 1–57.
- Wang, X., Schultz, A.J., and Halpern, Y. (2002) Kinetics of ice particle conversion to methane hydrate. *Proceedings of the Fourth International Conference on Gas Hydrates*, Yokohama, May 19–23, 2002, Yokohama, p. 455–460.
- Warzinski, R.P., Lynn, R.J., and Holder, G.D. (2000) The impact of CO₂ clathrate hydrate on deep ocean sequestration of CO₂. *Annals of the New York Academy of Sciences*, 912, 226–234.
- Wilson, L. and Head, J.W. (2002) Volcanic eruption styles on Mars due to shallow interactions between magma and volatiles. In *Lunar and Planetary Science XXXI*: Papers presented to the 31st Lunar and Planetary Science Conference, March 13–17, 2000, Houston, Texas, Lunar and Planetary Institute, no. 1275.

MANUSCRIPT RECEIVED OCTOBER 3, 2003

MANUSCRIPT ACCEPTED APRIL 21, 2004

MANUSCRIPT HANDLED BY BRYAN CHAKOUMAKOS

APPENDIX A. SAMPLE STRUCTURE DESCRIPTION

As suggested by Arzt (1982), in random dense packing without particle rearrangement, the current coordination number Z can be expressed as a linear function of the relative hydrate shell radius $R_h = r_h/r_0$:

$$Z = Z_0 + C(R_h - 1) \quad (\text{A1})$$

where the coordination number of the initial ice-powder $Z_0 \sim 7$, and the slope of the random density function $C \sim 15.5$.

The normalized volume of a reference ice-hydrate particle schematically depicted in Figure 4 is directly related (Arzt 1982) to the relative ice-core radius $R_i = r_i/r_0$

$$R_h^3 - \frac{Z_0}{4}(R_h - 1)^2(2R_h + 1) - \frac{C}{16}(R_h - 1)^3(3R_h + 1) = 1 + E(1 - R_i^3) \quad (\text{A2})$$

The fraction s of the free hydrate surface area (in units of $4\pi r_h^2$) exposed to the ambient gas is (Arzt 1982)

$$s = 1 - \frac{Z_0}{2} \frac{R_h - 1}{R_h} - \frac{C}{4} \frac{(R_h - 1)^2}{R_h} \quad (\text{A3})$$

The geometrical model A1–A3 fully describes the sample packing development during the ice to hydrate conversion. The initial macro-porosity of the ice-powder ε_{m0} is directly linked to the packing parameters Z_0 and C in Equation A1, the quantity $(1 - \varepsilon_{m0})^{-1}$ being equal to the maximum normalized volume of the reference ice-hydrate particle, i.e., to the value of the left-hand side of Equation A2 at $s = 0$ in Equation A3. Accordingly, the current porosity ε_m and the normalized surface area of the macro-pore space are

$$\varepsilon_m = \varepsilon_{m0} - E(1 - \varepsilon_{m0})(1 - R_i^3), \quad S_m = sR_h^2S_{r0}.$$

The area of the spherical cap surface of radius r_h cut by one average contact from the truncated hydrate shell in Figure 4 can be calculated in two different ways:

$$2\pi r_h(r_h - r) = 4\pi r_h^2(1 - s)/Z$$

thus yielding the distance r from the ice core center to an average contact plane

$$r = r_h \left[1 - \frac{2(1 - s)}{Z} \right]$$

APPENDIX B. GAS HYDRATE FORMATION IN A CRACK

We assume that on average the initial fissure in a reference ice grain of radius r_0 has the form of a cleft penetrating to the sphere center with the angle 2β between its sides S_f (see Fig. 5). Most probably due to numerous physical defects, the process of gas hydrate formation in the cracks is much faster in comparison with the growth of hydrate layers around the shrinking ice cores. Nevertheless, SEM observations show that in general the crack-filling passes through the two analogous stages of (1) hydrate film coating the crack surface and (2) reaction-controlled growth of the hydrate layer on the two crack sides. Thus, per unit time, additional fraction $\omega'_s e^{-\omega'_s t}$ of the crack surface is covered with the initial hydrate film, formed of an ice layer with thickness δ'_0 , and on the coated area exposed to the ambient gas, the ice layer of ω'_R/ρ_f -thickness transforms to hydrate. In each case, the newly formed porous hydrate layer is $1 + E$ times thicker than the consumed ice. The incremental excess hydrate volume intrudes into the cleft from both sides and leads to an increase in the average height h of the crack-filling. The above process is governed by an equation that copies Equation 2₂

$$\beta \frac{dh}{dt} = E\delta'_0 \omega'_s e^{-\omega'_s t} + E \frac{\omega'_R}{\rho_i} (1 - e^{-\omega'_s t})$$

and results in Equation 6₁.

Simultaneously, the cleavage-side area (initially equal to $\pi r_0^2/2$) decreases

$$\frac{dS_f}{dh} = -2\sqrt{r_0^2 - h^2},$$

whereas the hydrate volume v_f formed in and around the crack increases

$$\frac{dv_f}{dh} = 2\beta S_f \frac{1 + E}{E}.$$

The sequential integration of the latter equations with respect to h from 0 to h yields

$$S_f = \frac{\pi r_0^2}{2} \left(1 - \frac{2}{\pi} \arcsin \frac{h}{r_0} \right) - h\sqrt{r_0^2 - h^2}$$

and

$$v_f = 2\beta r_0^3 \frac{1 + E}{E} \left[\frac{\pi}{2} \xi - \xi \arcsin \xi - (1 - \xi^2)^{1/2} + \frac{1}{3} (1 - \xi^2)^{3/2} + \frac{2}{3} \right], \quad \xi = h/r_0.$$

The total hydrate volume which completely fills the crack corresponds to $\xi = 1$, and the last relation determines the current filling degree $\chi = v_f/v_f(\xi = 1)$ given by Equation 6₂.

Ice perfection and onset of anomalous preservation of gas hydrates

W. F. Kuhs,^{*a} G. Genov,^a D. K. Staykova^a and T. Hansen^b^a GZG, Abt. Kristallographie, Universität Göttingen, Goldschmidtstr. 1, 37077 Göttingen, Germany. E-mail: wkuhs1@gwdg.de; Fax: +49 551 39-9521; Tel: +49 551 39-3891^b Institut Laue Langevin, B. P. 156X, 38042 Grenoble Cedex, France. E-mail: hansen@ill.fr; Fax: +33 476483906; Tel: +33 476207044

Received 20th August 2004, Accepted 5th October 2004

First published as an Advance Article on the web 13th October 2004

Anomalous preservation is the well-established but little-understood phenomenon of a long-term stability of gas hydrates outside their thermodynamic field of stability. It occurs after some initial decomposition into ice in the temperature range between 240 and 273 K. *In situ* neutron diffraction experiments reveal that the low-temperature on-set of this effect coincides with the annealing of stacking faults of the ice formed initially. The defective, stacking-faulty ice below 240 K apparently does not present an appreciable diffusion barrier for gas molecules while the annealed ordinary ice I_h above this temperature clearly hinders gas diffusion. This is supported by further experiments showing that the so-called ice I_c formed from various high-pressure phases of ice, gas hydrates or amorphous ices does transform fully to ordinary ice I_h only at temperatures near 240 K, *i.e.* at distinctly higher temperatures than generally assumed. In this light, some quite disparate observations on the transformation process from ice I_c to ice I_h can now be better understood. The transformation upon heating is a multistep-process and its details depend on the starting material and the sample history. This 'memory' is finally lost at approximately 240 K for laboratory time-scale experiments.

'Anomalous preservation' (sometimes also called 'self-preservation') of gas hydrates is a very intriguing phenomenon of considerable scientific and practical interest. Early observations of this effect were made independently by Davidson *et al.*¹ and, more detailed, by Yakushev and Istomin.² These authors observed an unexpected persistence when gas hydrates were brought outside their field of stability at temperatures below the melting point of ice. More recently, Stern *et al.*³ and Takeya *et al.*⁴ have investigated the temperature dependency of the effect for the case of methane hydrate and found that the effect also had a lower limit. According to Stern *et al.*,³ the 'anomalous preservation window' extends from 240 K to the melting point of ice, while at temperatures below 240 K the decomposition is rapid and appears to be thermally activated. Within this window, the decomposition rates vary considerably by several orders of magnitude in a reproducible way (Fig. 1) with two minima at around 250 and 268 K. Takeya *et al.*⁵ confirmed this effect and suggested a diffusion limitation to explain the slow decomposition kinetics of gas hydrates within the anomalous preservation window. A similar, but not identical behaviour was observed for CO_2 hydrate.⁶ Still, the deeper physical origin of 'anomalous preservation' remains obscure and the controlling parameters elusive.⁷⁻⁹ The effect is of potential economic interest as it would allow for a low-cost compact and normal-pressure storage of gas in the form of hydrate by simple cooling to temperatures below 0 °C.¹⁰ Here we report on neutron diffraction experiments on both the change of crystalline perfection in going from ice I_c to ice I_h

upon heating as well as on the decomposition of gas hydrate, revealing for the first time the importance of the crystallographic state and perfection of ice as important ingredients in understanding anomalous preservation phenomena. To be able to appreciate this connection we first turn to a discussion of the solid-solid transition of condensed forms of H_2O into ice.

The decomposition of gas hydrates yields apparently normal ambient pressure hexagonal ice, so-called ice I_h as confirmed by Takeya *et al.*^{4,5} by laboratory X-ray diffraction. It is interesting to note that at lower temperatures various solid water phases transform not into ice I_h but into so-called cubic ice, ice I_c . This form of ambient pressure ice is produced from amorphous forms of water and from high-pressure ices when they are heated after a recovery at low temperature and ambient pressure.^{11,12} The transformation is ascribed to the on-set of mobility of Bjerrum defects promoting an ice-like crystal growth.¹³ It was noticed early on¹⁴ that the diffraction patterns for ice I_c obtained from different starting materials were different. These differences were explained by Kuhs *et al.*¹⁵ in terms of various degrees of stacking faulting for ice I_c from different origins. The faults were identified as deformation stacking faults, which in diffraction experiments lead to the appearance of broad reflections at Bragg angles typical for ice I_h as well as to high- and/or low-angle shoulders on the Bragg peaks at genuine ice I_c positions.¹⁵ The width of the cubic reflections was used to estimate the particle size of ice I_c produced from ice II as 160 Å. Stacking faults in ice I_h and their creation by rapid temperature changes were also described by other authors.¹⁶ Some authors have investigated the transition of ice I_c into the normal hexagonal ice (ice I_h) by diffraction, which was found to take place over a seemingly large temperature range starting slowly at 150 K with a rapid progress of the transformation between 190 and 210 K,¹⁷ at

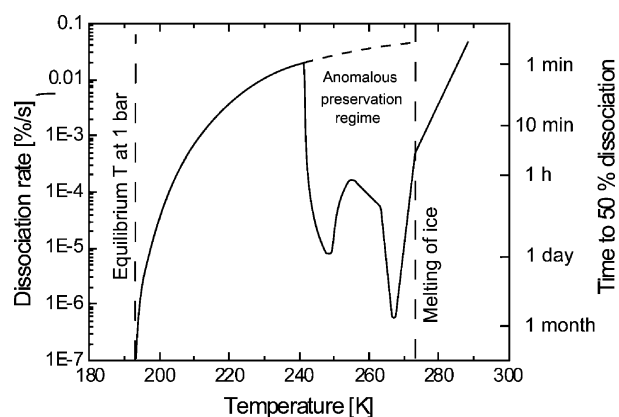


Fig. 1 Decomposition kinetics and extent of 'anomalous preservation' regime of methane hydrate (modified after Stern *et al.*³).

higher temperatures this work showed apparently pure ice I_h .¹⁸ Differential thermal analysis of the ice I_c –ice I_h transition revealed the main transition region again at 190–205 K, with small but detectable events starting at ≈ 176 K¹⁹ and ending at ≈ 240 K.²⁰ A change of activation energy was observed at 185 K, and the transformation was observed to be complete at 210 K by Sugisaki *et al.*²¹ Already an earlier review of the situation showed a confusing picture²² in which the ice I_c –ice I_h transition was located at temperatures between 160 and 205 K, a situation which has not much improved since. The reason for this variability of ice I_c –ice I_h transition temperatures are not clear, yet there are indications that in addition to the molecular arrangement of the parent phase mentioned above, the surface area of the ice I_c crystallites²³ has a significant influence. Thus it appeared worthwhile to look in some more detail at the transformation behaviour of ice I_c into ice I_h in the temperature range in question with a well-defined starting material. Diffraction is the most promising tool as it permits insight into changes of the molecular arrangement not only at long ranges but also into a number of more local defect structures. Moreover, time-resolved diffraction experiments allow for *in situ* studies of this transition and can give access to the transformation kinetics. Likewise, we have studied the crystallographic nature of the ice produced in decomposition of gas hydrates at temperatures below and within the anomalous preservation window by time-resolved neutron diffraction.

Neutron diffraction techniques were chosen as they allow for unrestricted work in the complex sample environment of high pressures at low temperature. Moreover, neutron diffraction is sensitive to proton arrangements in the various crystal structures, which could be important for some of the transitions. The experiments were performed on the high-resolution scanning powder diffractometer D2B (wavelength 1.6 Å) as well as the high-intensity powder diffractometer D1B and D20 equipped with a linear position sensitive detector (wavelength 2.4 Å) at the High-Flux-Reactor of the Institut Laue-Langevin in Grenoble, France. The first series of measurements consisted of studies of the ice I_c –ice I_h transition. The starting material used was the high-pressure ice V,²⁴ returned to ambient pressure at liquid nitrogen temperatures. Upon further heating at ambient pressure the recovered ice transformed into ice I_c at a temperature of 143 K within 15 h.²⁵ Further temperature increase led to a gradual transition into ice I_h . The main structural rearrangements took place at temperatures below 205 K in agreement with a number of previous observations.^{18,19,23} Detailed observations were made in the temperature range between 180 and 265 K. Consequently, for the experiment performed on D2B the temperature was increased at a rate of 10° h^{-1} in steps with a holding time of 30 min after reaching each target value. During both ramping and holding the temperature diffraction data were collected with a time resolution of 15 min. Any crystallographic changes are documented in the diffraction pattern. Particular attention was given to the peak intensity and peak shape of the cubic 111 reflection as well as the neighbouring and partly overlapping hexagonal 100, 002 and 101 reflections. Intensity changes of these reflections upon heating were observed to take place first rapidly, then slowing down and coming essentially to a hold. The time spent at each temperature was chosen to cover the period in which significant differences between adjacent data sets could be detected as established from exploratory runs on D20; with the good counting capability of D20, intensity changes of 1% were detectable. Fig. 2 shows a typical result of the detailed analysis of the first complex diffraction peak. The plot depicts the intensity ratio of the hexagonal 100 and 002 reflection highlighting the persistence of some cubic component at temperatures as high as 237 K. Following our earlier analysis,¹⁵ this is interpreted as cubic stacking sequences and represents the first unequivocal crystallographic evidence for the persistence of significant two-dimensional defects

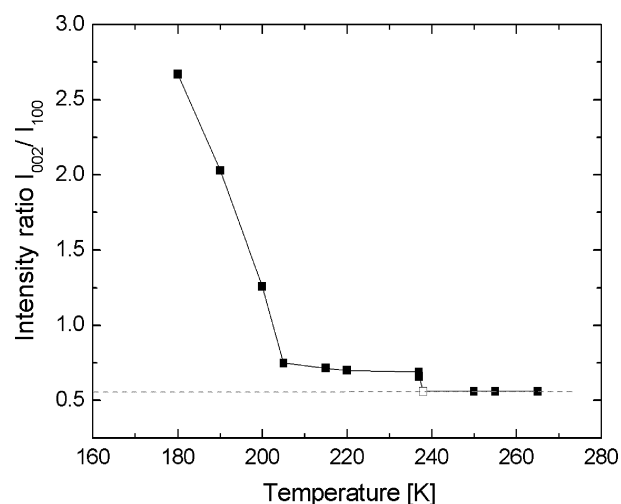


Fig. 2 The temperature dependency of the intensity ratio of the hexagonal 100 and 002 peaks during the transformation ice I_c into ice I_h . At 237 K the transition proceeds on a laboratory timescale; the open square is an extrapolated point. The broken lines gives the intensity ratio of the defect-free structure of ice I_h .

at temperatures above 205 K. Only at temperatures close to 240 K these imperfections finally disappear.

Independently, a number of time-resolved neutron diffraction runs were performed on the high-flux diffractometer D20 at ILL/Grenoble in order to study the decomposition behaviour of gas hydrates. Custom-made gas pressure cells were used which were filled with almost pure gas hydrates formed from hexagonal ice.²⁶ The samples were equilibrated at given pressure and temperature conditions. Concomitant with a pressure release to the designed end pressure, data collection was started. Complete diffraction patterns were recorded with a time resolution of 10 s up to 1 min for the initial part of the reaction and slower acquisition rates of typically 5 min for the later part of the decomposition process. The complete sample of typically 1 cm^3 was intercepted by the neutron beam. The analysis of the numerous diffraction data was performed in an automated fashion using the Rietveld program GSAS²⁷ similar to the approach described for the gas hydrate formation reactions.²⁶ Between 50 and 300 individual diffractograms were collected for each decomposition run as a function of time. Beam-time restrictions limited the duration of each run to typically less than half a day. Quantitative information on the progress of the reaction was obtained from the phase fractions of ice and gas hydrate for each data set. The results are shown in Fig. 3a and b for CH_4 - and CO_2 -hydrate, respectively. In agreement with earlier observations,^{3,4} the initial decomposition was always fast, but slowed down for temperatures above approximately 240 K in the anomalous preservation regime. A phenomenological model combining an initial reaction-limited and a later diffusion-limited process can quantitatively explain the decomposition. Similar successive processes also take place during the gas hydrate formation from ice.^{26,28,29} More interesting in the present context is the detailed nature of the ice formed below and above the onset of anomalous preservation. A detailed inspection of the diffraction features of the ice obtained upon gas hydrate decomposition clearly shows that imperfect ice I_h is formed. Indeed, there is unequivocal evidence for the existence of stacking faults in the ice I_h crystallites. They are clearly born out in shoulders of the main hexagonal diffraction peaks as well as in the non-ideal intensity ratio of the hexagonal 100 and 002 reflections shown in Fig. 4. Insufficient crystallite statistics or textural effects can be safely excluded as an explanation of the non-ideal intensity ratios. It is noteworthy that the non-ideal character of the hexagonal ice formed is more pronounced at lower temperatures and

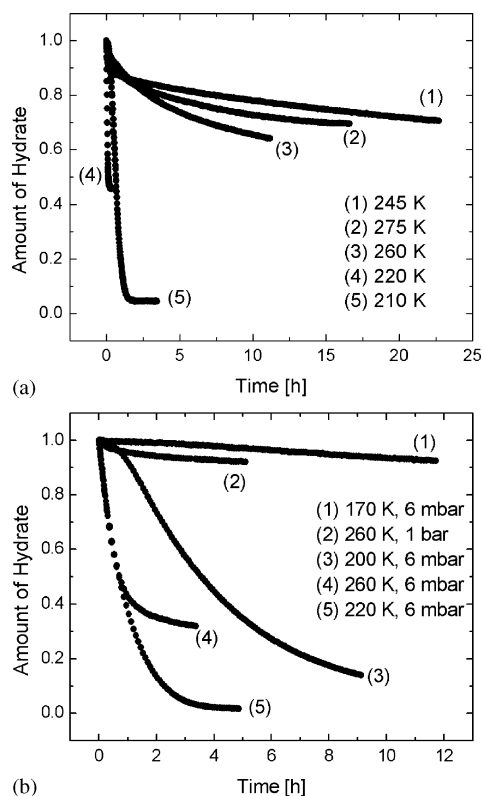


Fig. 3 Time dependency of the decomposition of gas hydrate into ice as established by neutron powder diffraction: (a) CH₄ hydrate; (b) CO₂ hydrate.

disappears completely for all data sets in the self-preservation regime. Moreover, ice formed from CO₂- and CH₄-hydrate appears to be different in that the latter shows more pronounced features for deformation stacking faults born out in the high-angle shoulders of the hexagonal 100 reflection.¹⁵

Cryo-scanning electron microscopy (cryo-SEM) was used to study different stages of the gas hydrate decomposition reaction. The set-up chosen for the decomposition runs was identical to the one for the *in situ* diffraction experiments described above. After a pressure release to the designed end pressure the decomposition reaction was allowed to proceed for a given time. Then, partly decomposed samples were obtained from a rapid recovery to liquid N₂ temperatures. The initial stages of the decomposition are particularly revealing as individual ice crystallites could be identified in location, shape and frequency of appearance. Fig. 5 shows some typical examples. Frequently the gas hydrate phase could be identified by its sub-micron porous appearance.³⁰ The newly formed ice crystallites exhibit frequently hexagonal symmetry and some show kinks on the prismatic faces (see Fig. 5a). These kinks are atypical for defect-free ice I_h crystals as found *e.g.* in prismatic snow crystals³¹ and appear to be a consequence of the stacking faults present in the crystallites. As judged from the number and distribution of ice crystallites the density of nucleation sites is quite high. Nevertheless, it is clear that a homogeneous coverage of the gas hydrate surface is not readily achieved at temperatures below 240 K. Rather, the ice cover is broken up into individual crystallites with gaps in between (see Fig. 5b) while at higher temperatures a contiguous coverage is developed. Clearly, the lower the temperature, the more inhomogeneous is the coverage leaving pathways for free diffusion between individual crystallites.

Combining the observations essentially based on diffraction data and supported by the SEM appearance, clear evidence is found that the ice formed upon gas hydrate decomposition at temperatures below the anomalous preservation window is defective. It forms small crystallites of a few μm , which do

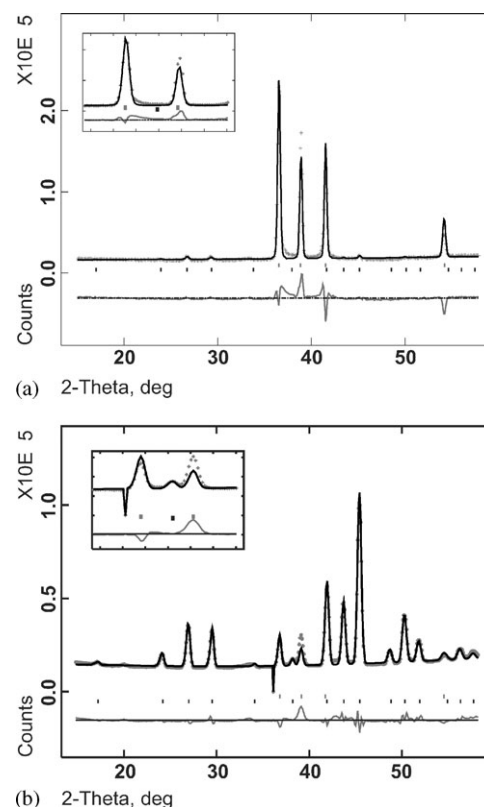


Fig. 4 Diffraction pattern and Rietveld-fit for various stages of the decomposition reaction showing the observed intensity data, a model fit assuming perfect ice I_h, the difference between observed and calculated profile as well as tick-marks indicating the reflection positions (top phase ice I_h, bottom phase hydrate). The insert shows the enlarged portion of the diffraction pattern with the 100 and 002 reflection of ice. Please note the misfit in particular for the 002 reflection at approximately 39° in 2 θ highlighting the existence of stacking fault imperfections in the formed ice. (a) CH₄ hydrate at 210 K and 1 bar after 3.5 h of decomposition (b) CO₂ hydrate at 170 K and 6 mbar after 12 h of decomposition.

not combine to larger, more homogeneous assemblies below 240 K. Appreciable annealing of stacking faults and grain growth of the ice crystallites sets in at temperatures of approximately 240 K. At the same temperature, the stacking faults present in hexagonal ice formed from ice I_c finally anneal as evidenced by the diffraction data. The initial degree of stacking-faulty sequences and the details of the step-wise disappearance of stacking-faults upon temperature increase apparently depend on the parent phase as well as the speed of transformation into ice. Remarkable differences in lattice defects were established earlier on for the various high-pressure ices as parent phases.¹⁴ In a similar way, differences in the degree of perfection were found for ice produced from decomposing CO₂ and CH₄ hydrate, with the latter showing more imperfections. As the water topology of both hydrates is identical (both form a cubic type I hydrate structure) the difference must arise from the different transformation kinetics, with the CO₂ hydrate decomposing distinctly slower.

It is intriguing in the present context that a number of spectroscopic properties of ice I_h show a change in behaviour near 240 K. The temperature dependency of the NMR spin-lattice relaxation time T_1 for pure ice I_h samples shows a change of slope³² as does the real part of dielectric permittivities³³ and the temperature dependency of the frequency of the translational lattice vibrations as observed by Raman spectroscopy.^{33,34} This suggests that intrinsic defects, most probable of the Bjerrum-type, reach such degrees of mobility and concentration that cooperative displacements of water molecules became possible on laboratory timescales at temperatures near 240 K. Such phenomena were discussed for the movement of

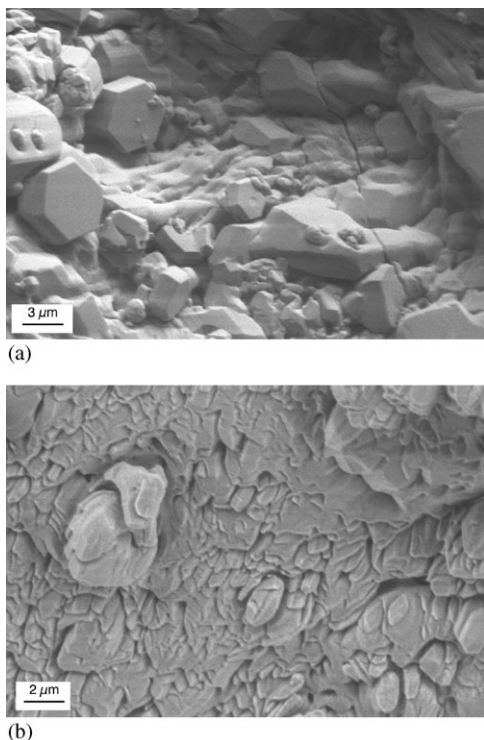


Fig. 5 Cryo-scanning electron microscopic images showing the surface of gas hydrate in the initial stage of decomposition: (a) CO₂ hydrate at 195 K and 6 mbar, (b) CH₄ hydrate at 220 K and 1 bar.

dislocations in ice.³⁵ Similar processes appear also to be operative for the annealing of stacking faults. The higher cooperative mobility of water molecules should lead to an annealing of defective crystallites with a resulting closing of existing pathways for gas diffusion. This in turn leads to the on-set of anomalous preservation. At this point, the gas molecules can only escape by solid-state diffusion, which slows down the decomposition reaction by orders of magnitude. It should be noted here that high gas pressures are not mandatory to stabilize the gas hydrate. What is needed is a chemical activity of the gas at the hydrate surface which corresponds to conditions inside the stability field. Correspondingly, we expect that changes in the microstructure of ice (*e.g.* a reduction of grain-boundaries due to Ostwald-ripening processes) is also at the origin of the complicated anomalous preservation features at higher temperatures.

Acknowledgements

We thank ILL/Grenoble for beam-time and support. We acknowledge the help of Frank Gotthardt and Evgeny Goreshnik (both at Göttingen) at an early stage of the data analysis and Kirsten Techmer as well as Till Heinrichs (both at Göttingen) for their assistance during the SEM analysis. The financial support of DFG (grants Ku920/9-1 and Ku920/11-1) and BMBF is gratefully acknowledged. This is publication No. GEOTECH-95 of the programme GEOTECHNOLOGIEN of BMBF, grant 03G0553A.

References

- 1 D. W. Davidson, S. K. Garg, S. R. Gough, Y. P. Handa, C. I. Ratcliffe, J. A. Ripmeester, J. S. Tse and W. F. Lawson, *Geochim. Cosmochim. Acta*, 1986, **50**, 619–623.
- 2 V. S. Yakushev and V. A. Istomin, in *Physics and Chemistry of Ice*, ed. N. Maeno and T. Hondoh, Hokkaido University Press, Sapporo, 1992, pp. 136–140.
- 3 L. A. Stern, S. Circone, S. H. Kirby and W. B. Durham, *J. Phys. Chem. B*, 2001, **105**, 1756–1762.
- 4 S. Takeya, W. Shimada, Y. Kamata, T. Ebinuma, T. Uchida, J. Nagao and H. Narita, *J. Phys. Chem. A*, 2001, **105**, 9756–9759.
- 5 S. Takeya, T. Ebinuma, T. Uchida, J. Nagao and H. Narita, *J. Cryst. Growth*, 2002, 237–239.
- 6 S. Circone, L. A. Stern, S. H. Kirby, W. B. Durham, B. C. Chakoumakos, C. J. Rawn, A. J. Rondinone and Y. Ishii, *J. Phys. Chem. B*, 2003, **107**, 5529–5539.
- 7 J. W. Wilder and D. H. Smith, *J. Phys. Chem. B*, 2002, **106**, 226–227.
- 8 L. A. Stern, S. Circone, S. H. Kirby and W. B. Durham, *J. Phys. Chem. B*, 2002, **106**, 228–330.
- 9 S. Circone, L. A. Stern and S. H. Kirby, *J. Phys. Chem. B*, 2004, **108**, 5747–5755.
- 10 A. Gudmundsson, V. Andersson, O. I. Levik and M. Mork, *Ann. N. Y. Acad. Sci.*, 2000, **912**, 403–410.
- 11 H. König, *Z. Kristallogr.*, 1943, **105**, 279–286.
- 12 J. E. Bertie, L. D. Calvert and E. Whalley, *J. Chem. Phys.*, 1963, **38**, 840–846.
- 13 P. J. Wooldridge, H. H. Richardson and J. P. Devlin, *J. Chem. Phys.*, 1987, **87**, 4126–4131.
- 14 G. P. Arnold, E. D. Finch, S. W. Rabideau and R. G. Wenzel, *J. Chem. Phys.*, 1968, **49**, 4365–4369.
- 15 W. F. Kuhs, D. V. Bliss and J. L. Finney, *J. Phys. Coll. (Paris)*, 1987, **48**, 631–636.
- 16 A. Higashi, *Lattice Defects in Ice Crystals. X-ray Topographic Observations*, Hokkaido University Press, Sapporo, 1988.
- 17 I. Kohl, E. Mayer and A. Hallbrucker, *Phys. Chem. Chem. Phys.*, 2000, **2**, 1579–1586.
- 18 L. G. Dowell and A. P. Rinfret, *Nature*, 1960, **188**, 1144–1148.
- 19 Y. P. Handa, D. D. Klug and E. Whalley, *J. Chem. Phys.*, 1986, **84**, 7009–7010.
- 20 E. Mayer and A. Hallbrucker, *Nature*, 1987, **325**, 601–602.
- 21 M. Sugisaki, H. Suga and S. Seki, *Bull. Chem. Soc. Jpn.*, 1968, **41**, 2591–2599.
- 22 P. V. Hobbs, *Ice Physics*, Clarendon Press, Oxford, 1974.
- 23 M. Kumai, *J. Glaciol.*, 1968, **7**, 95–108.
- 24 C. Lobban, J. L. Finney and W. F. Kuhs, *J. Phys. Chem.*, 2000, **112**, 7169–7180.
- 25 F. Gotthardt, PhD Thesis, 2001, Georg-August-Universität, Göttingen.
- 26 D. K. Staykova, W. F. Kuhs, A. N. Salamatina and T. Hansen, *J. Phys. Chem. B*, 2003, **107**, 10299–10311.
- 27 A. C. Larson and R. B. von Dreele, *General Structure Analysis System (GSAS)*, Los Alamos National Laboratory, 1994.
- 28 A. N. Salamatina and W. F. Kuhs, in *Proceedings of the Fourth International Conference on Gas Hydrates, Yokohama, May 19–23, 2002*, Yokohama, 2002, pp. 766–770. See <http://www.hydrate.welcome.to/pdf/ICGH766.pdf>.
- 29 G. Genov, W. F. Kuhs, D. K. Staykova, E. Goreshnik and A. N. Salamatina, *Am. Miner.*, 2004, **89**, 1228–1239.
- 30 W. F. Kuhs, A. Klapproth, F. Gotthardt, K. Techmer and T. Heinrichs, *Geophys. Res. Lett.*, 2000, **27**, 2929–2932.
- 31 F. Dominé, T. Lauzier, A. Cabanes, L. Legagneux, W. F. Kuhs, K. Techmer and T. Heinrichs, *Microsc. Res. Tech.*, 2003, **62**, 33–48.
- 32 K. Kume, *J. Phys. Soc. Jpn.*, 1960, **15**, 1493–1501.
- 33 T. Matsuoka, S. Mae, H. Fukazawa, S. Fujita and O. Watanabe, *Geophys. Res. Lett.*, 1998, **25**, 1573–1576.
- 34 H. Fukazawa, D. Suzuki, T. Ikeda and S. Mae, *J. Phys. Chem. B*, 1997, **101**, 6184–6187.
- 35 J. W. Glen, *Phys. Kondens. Mater.*, 1968, **7**, 43–51.